INFORMATION TO USERS

This manuscript has been reproduced from the microfilm master. UMI films the text directly from the original or copy submitted. Thus, some thesis and dissertation copies are in typewriter face, while others may be from any type of computer printer.

The quality of this reproduction is dependent upon the quality of the copy submitted. Broken or indistinct print, colored or poor quality illustrations and photographs, print bleedthrough, substandard margins, and improper alignment can adversely affect reproduction.

In the unlikely event that the author did not send UMI a complete manuscript and there are missing pages, these will be noted. Also, if unauthorized copyright material had to be removed, a note will indicate the deletion.

Oversize materials (e.g., maps, drawings, charts) are reproduced by sectioning the original, beginning at the upper left-hand corner and continuing from left to right in equal sections with small overlaps.

Photographs included in the original manuscript have been reproduced xerographically in this copy. Higher quality 6" x 9" black and white photographic prints are available for any photographs or illustrations appearing in this copy for an additional charge. Contact UMI directly to order.

Bell & Howell Information and Learning
300 North Zeeb Road, Ann Arbor, MI 48106-1346 USA

UMI®
800-521-0600

EXPERIMENTAL AND MODELLING STUDY OF THE PLASMA VAPOUR-PHASE SYNTHESIS OF ULTRAFINE ALUMINUM NITRIDE POWDERS

by

Antonio Carlos da Cruz

Department of Chemical Engineering
McGill University, Montreal
September 1997

Under the supervision of Prof. R. J. Munz

Thesis submitted to the Faculty of Graduate Studies and Research in partial fulfilment of the requirements of the degree of Doctor of Philosophy

0-612-44397-3

To Luzia and Marina ...

ABSTRACT

An experimental and theoretical study of the fundamentals of the vapour phase synthesis of ultrafine aluminum nitride (AlN) particles using thermal plasma was carried out. The study used the concept of a transferred-arc reactor which produces AlN ultrafine powders in two stages: evaporation of aluminum (Al) metal by the transferred-arc in non nitriding conditions; and the reaction between Al vapour and ammonia (NH_3) in a separate tubular reactor. A new version of this reactor concept was built in which the transferred-arc chamber and tubular reactor were vertically aligned. This reactor design allowed the study of both radial and axial mixing of ammonia with the plasma chamber off-gas. Ultrafine powders with a specific surface area (SSA) in the range of 38-270 m^2/g were produced in two plasma chamber off-gas temperature levels (1800 and 2000 K), with different quenching intensities, and two different plasma gas compositions (pure Ar and Ar/H_2 mixture). The dependence of the particle size and composition on the reactor operating conditions was investigated. Depending on the plasma gas composition, two different trends were observed for the SSA as a function of quenching intensity, with the radial injection of NH_3. A two-dimensional numerical model was developed for the nucleation and growth of ultrafine particles in this system, using the method of moments. A new equation for the nucleation rate for the AlN system was developed. This equation considers the effect of reaction on the surface of clusters of the new phase. This new modelling approach could explain the trends observed experimentally. The importance of the mechanisms for the gas-to-condensed phase transition in the AlN system were examined. The sinterability of the powder produced was examined. Sintering to full density was achieved at 1550 °C. Because of the high oxygen content of the powder, a second phase identified as aluminum oxynitride (ALON) was observed to form.

Key words: plasma synthesis; vapour phase synthesis; transferred-arc; plasma reactor; fine particles; aluminum nitride; nucleation and growth; method of moments.

RÉSUMÉ

Une étude expérimentale et théorique a été menée sur les fondements de la synthèse en phase gazeuse de particules ultrafines de nitrure d'aluminium (AlN) en utilisant un plasma thermique. L'étude a utilisé le concept d'un réacteur à arc transféré pour produire de la poudre ultrafine d'AlN en deux étapes: évaporation de l'aluminium métallique par un arc transféré dans des conditions sans azote et réaction entre la vapeur d'aluminium et l'ammoniac (NH_3) dans un réacteur tubulaire séparé. Une nouvelle version de ce concept de réacteur a été construite dans lequel la chambre de l'arc transféré et le réacteur tubulaire étaient alignés verticalement. Cette configuration a permis l'étude du mélange radial et axial du NH_3 avec l'effluent gazeux provenant de la chambre à plasma. De la poudre ultrafine avec une surface spécifique (SSA) de l'ordre de 38-270 m^2/g a été produite en utilisant deux températures de gaz à la sortie de la chambre à plasma (1800 et 2000 K), différentes intensités de trempe et deux différentes compositions de gaz plasmagène (argon pur et argon-hydrogène). La dépendance de la taille et de la composition des particules en relation avec les conditions d'opération a été étudiée. Dépendemment de la composition du gaz, deux tendances ont été observées pour la SSA en fonction de l'intensité de la trempe en utilisant l'injection radiale du NH_3. Un modèle numérique en deux dimensions utilisant la méthode statistique a été développé pour la nucléation et la croissance des particules ultrafines dans ce système. Une nouvelle équation du taux de nucléation pour le système AlN a été développée. Cette équation considère l'apport de la réaction à la surface d'agglomérats de la nouvelle phase. Cette approche de modélisation pourrait expliquer les tendances observées expérimentalement. L'importance des mécanismes de la transition gazeuse vers la phase condensée a été examinée. Le taux de frittage des poudres produites a aussi été étudié. Le frittage jusqu'à la densité maximale a été atteint a une température de 1550°C. Dû au contenu élevé en oxygène de la poudre, une deuxième phase identifiée comme de l'oxynitrure d'aluminium (ALON) a été observée.

ACKNOWLEDGMENTS

To Prof. Richard J. Munz I want to express my gratitude for his unconditional support, secure and enthusiastic guidance, and in special for his availability, dedication and patience.

I want to express my gratitute also to the many people who make a Ph.D. thesis a possible and enjoyable work to pursue:

The Chemical Engineering Machine Shop personnel: Mr. Alain Gagnon, M. Walter Greenland, and Mr. Charles Dolan, for their expertise, availability, friendship, and in special for providing me with the beautiful machine that was the plasma reactor (and for keeping it working...).

The Chemical Engineering staff: Mr. Ed Siliauskas, for his support in the many chemical analyses; Mr. Jean Dumont, who always had a friendly smile and helped me to find whatever I need to keep things running; Mr. Bill Habib, always a helping hand; Mr. Michael Harrigan, the friendly store keeper who knows about microscopy and photography; and Mr. Luciano Cusmich, who helped me to connect the right cables. The administrative staff, in special to Ms. Anne Prihoda, Ms. Pat Fong, and Ms. Joanne Terrasi.

Prof. D. Berk, for making available his lab facilities.

The members of Mining and Metallurgy: Mr. Slavec Poplawski, for the many XRD analysis and friendly chats; Prof. J. Szpunar, for discussing the XRD analysis; Prof. Robin A. L. Drew, for making available his ceramic lab facilities ; Carlos Leon Patino and José Lemus Ruiz, friendly Prof. Drew's Ph.D. students who shared their expertise in the conduction of the sintering experiments; and Ms. H. Campbell, for her assistance with the SEM analysis.

Dr. Hojatollah Vali, for his precious technical expertise in TEM, and in special for his availability and interest in discussing its results.

Mr. George Vielleux (INRS) for the XPS analyses; to Dr. Mark Ward (Department of Metallurgy and Materials Science, University of Toronto) for the oxygen analyses.

The members of the CRTP Plasma Group, past and present: Prof. J.-L. Meunier, Theodora Alexakis, Tony Addona, Sylvain Coulomb, Muftah H. El-Naas, Julie Filion, Munther Kandah, George Kim, Jan Kwak, Francisco J. Moura, Patrice Nadeau, Jorg Oberste-Berghaus, Hungsun Seon, and Karen Sum. In special, I want to thank Samer Awarage, for his laborious work on the nitrogen analysis of the AlN powder. It was exciting working with you and a great fun seeing all those plasma fire works inside and, sometimes, outside reactors.

Gratefully acknowledged are: the Conselho Nacional de Pesquisa Científica e Tecnológica (CNPq), Brazil, for the financial support received; the National Science and Engineering Research Council of Canada (NSERC) and the Fonds pour la Formation des Chercheurs et l'Aide a la Recherche (FCAR) of Quebec for sponsoring this research.

To my beloved wife Luzia, for her encouragement, caring and love, and our little daughter, Marina, whose radiant smile and happiness inspires my work.

TABLE OF CONTENTS

LIST OF FIGURES

LIST OF TABLES

Chapter 1

INTRODUCTION

A noticeable progress has been accomplished in the past few decades in the field of ceramic materials, based mainly on a better understanding of microstructure and its development during processing. This resulted in a new generation of ceramics often referred to in the literature as "advanced ceramics", which encompasses a broad range of materials made from refined naturally occurring mineral powders, or from new powder compositions synthesized to achieve unique properties[1],[2],[3].

Because the starting powder plays a key role in the determination of the properties of the finished component, it is seen as one of the most critical and challenging factors in advanced ceramics manufacture[4]. The powder properties of importance include particle size, particle morphology, particle size distribution, and purity, all of which may be controlled through the powder synthesis process. Many innovative synthesis routes have been proposed, addressing the fulfillment of these requirements. However, few of them are commercialized. Some of the barriers to be overcome[4] are yield improvement, powder lot to lot reliability, and high production cost .

One such route uses thermal plasma as the processing medium. The application of thermal plasma to produce powders of many different compositions has been demonstrated in laboratory scale since the early 60's[5],[6]. Its most explored feature in these applications is the ability to carry out high temperature reactions, followed by fast quenching resulting in the formation of finely dispersed powders. Other highly favorable factors are the reduced number of processing steps, and a clean processing environment that contributes to the production of high purity materials.

The application of thermal plasmas to the synthesis of refractory ceramic powders that invariably require high temperature processing is of particular interest. Literature reviews on this subject were carried out by Hamblyn[7] (1975), Fauchais et al.[5] (1983), Akashi[8] (1987), and

Kong and Lau[6] (1990). Notwithstanding the large amount of research work in this field, scaling up of plasma reactors from the few grams/hr of lab scale experiments to the rates needed for industrial scale production is still a major problem. Few successful industrial scale developments have been reported, e.g. the production of ultrafine TiO_2 pigment[9]. A major technological barrier encountered in these developments is the limited availability of gas-phase metal precursors[9]. The most commonly used reactants for plasma synthesis are solids which have to be evaporated. In order to improve productivity, evaporation at high rates is required. Another major obstacle is the still poor understanding of the mechanisms by which gas-to-condensed phase transition proceeds in these systems. To this respect, only more recently with the aid of numerical simulation, are the phenomena involving vapour phase nucleation and growth in these high temperature processes being better understood.

Amongst the various plasma generation techniques, transferred-arcs constitute relatively simple systems that can be efficiently used to melt and evaporate clean metal charges. However, steep temperature and concentration gradients surrounding the arc make gas-to-condensed phase conversion non uniform and the process difficult to control[10],[11]. The problems are exacerbated if chemical reaction is involved. To overcome these problems, a new transferred-arc reactor concept was proposed and successfully applied to the production of aluminum nitride (AlN) ultrafine powders[12]. Its main characteristic is the metal evaporation in an inert atmosphere, with the reaction being carried out outside the plasma chamber under well controlled operating conditions.

The present work introduced a new version of this reactor, and continued the research on the synthesis of AlN powder. Its overall objective was to investigate the fundamentals of the vapour-phase synthesis, looking forward the scale-up of this reactor concept. The research included simultaneous experimental and theoretical work based on modelling of particle nucleation and growth in the reaction portion of the reactor.

Experimental data on temperature and metal vapour concentration at the entrance of the reaction zone were used as boundary conditions for the numerical model. In return, the model results were used to interpret the experimental data on powder characteristic (particle size and powder composition). Once the model was developed for a particular operating condition, which involved the plasma chamber hot gas quenching by radially distributed impinging jets of cold reacting gas, it was used to simulate a modified hot/cold gas mixing arrangement aimed to producing a higher purity powder. The experimental results on this new configuration fully confirmed the theoretical predictions.

The thesis is divided into four main parts. The first part, which comprises Chapters 2 to 4, reviews the most important AlN powder synthesis methods. It includes the methods used for its commercial production and new developments. A separate review is made of the thermal plasma synthesis, with emphasis on the identification of the major barriers for the development of this technology. The previous work on the reactor concept used in the present study is introduced and the objectives of the research stated. The physical properties of AlN, specially those of interest for the development of the theoretical part of this research, are reviewed.

The second part (Chapter 5) refers to the experimental portion of the study, including equipment, procedures, and results. The techniques used for the characterization of the powder produced are described. The experimental results presented and discussed pertain to the measurement of Al vapour concentration and its dependence on gas temperature, and to the investigation of the influence of operating parameters on the powder characteristics.

The third part (Chapter 6) refers to the theoretical study of the gas-to-condensed phase transition mechanisms, and prediction of powder characteristics using a numerical model. A brief review is made of the previous work on the modelling of particle nucleation and growth in similar systems. The particle-number continuity equation is developed and each of its terms detailed. The framework of the conservation equations used to describe the particle nucleation and growth and the gas flow is introduced. A new formulation for the nucleation of particles in this reacting system is developed. A typical experimental condition is simulated for which the results of this new nucleation formulation are compared with results obtained using the previous proposition. The modelling results are used for the interpretation of the major trends observed in the experimental part of the work and to introduce modifications on the mixing of reacting species in order to improve Al conversion.

The last part (Chapter 7) involves a study of the sintering properties of the powder produced. A short review of the main sintering principles is given. The results of the sintering experiments and analysis of the sintered compacts are presented and discussed.

AlN is a covalent ceramic whose unique combination of properties has attracted a great deal of attention. Its current and future application potential were reviewed by Sheppard[3] (1989) and Mroz[13] (1993). AlN synthesis methods were reviewed by Selvaduray and Sheet[4] (1993).

The relatively high thermal conductivity and high electrical insulation characteristics of AlN make it a candidate material for the electronic industry in applications such as integrated circuit substrates, heat sinks, and semiconductor packagings. Its thermal expansion coefficient closely matches that of silicon. Conventional materials used for such applications are alumina (Al_2O_3) and beryllia (BeO). Alumina has a limited performance relative to heat dissipation as electronic components as circuits are made smaller and denser. Beryllia is known for its toxicity.

Because it exhibits high strength and high temperature stability, a variety of applications exist for AlN as structural ceramics: armours for aircrafts and vehicles are currently the predominant structural applications[4]. The property that makes AlN a potential armour material is its plastic deformation at high strain. Additionally, its density makes it lightweight compared with metallic materials. The primary technological barrier with respect to armour applications is the fabrication of large and uniform pieces.

Because AlN also exhibits corrosion resistance to a wide variety of molten metals and salts, it is finding increased application as crucibles and hardware for containing and processing corrosive materials[4]. In metals like aluminum, AlN can be used to strengthen the matrix. In polymers, AlN can be used to increase the stiffness, reduce the thermal expansion, or increase the thermal conductivity[4].

2.1. AlN powder synthesis methods

Salvaduray and Sheet[4] presented a classification of the several technologies reported for the production of AlN powders based on the synthesis principle. This classification is summarised in Figure 2.1. Only two of the methods reported are currently used for commercial production: carbothermal reduction and direct nitridation. Due to the requirement for higher quality AlN powders, several other methods are in development. A brief description of some of these methods is presented next, followed by a review of the application of thermal plasmas with emphasis on the previous work on the reactor principle presently developed.

2.1.1. Commercial production

Aluminum nitride powders have been produced commercially by direct nitridation of aluminum powders and by carbothermal reduction of alumina in the presence of nitrogen. The direct nitridation involves a liquid-gas reaction between molten aluminum powders and nitrogen, in a sequence of seven steps which ends with ball mill grinding for decreasing the average particle diameter. The whole sequence can take more than 20 hours. The carbothermal reduction process, on the other hand, involves a solid-solid reaction between alumina and carbon powders, and a subsequent conversion of alumina in a nitrogen atmosphere. The schematic diagram of the reduction process developed by Keramont Corp.[3] is shown in Figure 2.2.

The major advantages of conventional processes are:

- large availability of raw materials;
- large range of powder size characteristic that can be produced; and
- powders homogeneously sized and weakly aggregated.

At the same time, they present the following disadvantages:

- in the case of direct nitridation, full conversion to AlN is difficult to achieve;
- in the reduction process, carbon remains even after treatment (oxidation step) either free or combined in the AlN crystalline lattice;
- powders produced by the reduction process tend to give a higher oxygen content due to the presence of unreacted alumina and to the oxidation step.

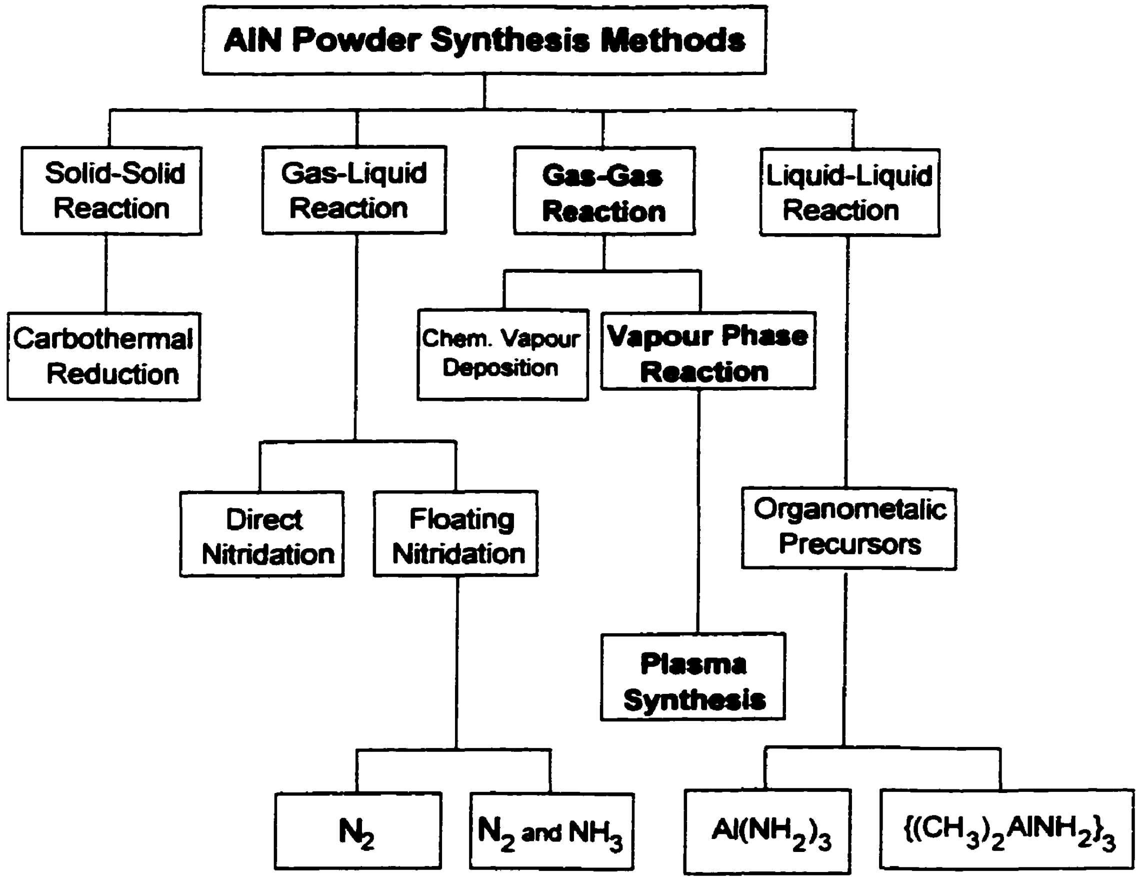

Figure 2.1 - Classification of the currently available methods for the synthesis of AlN powder; adapted from [4].

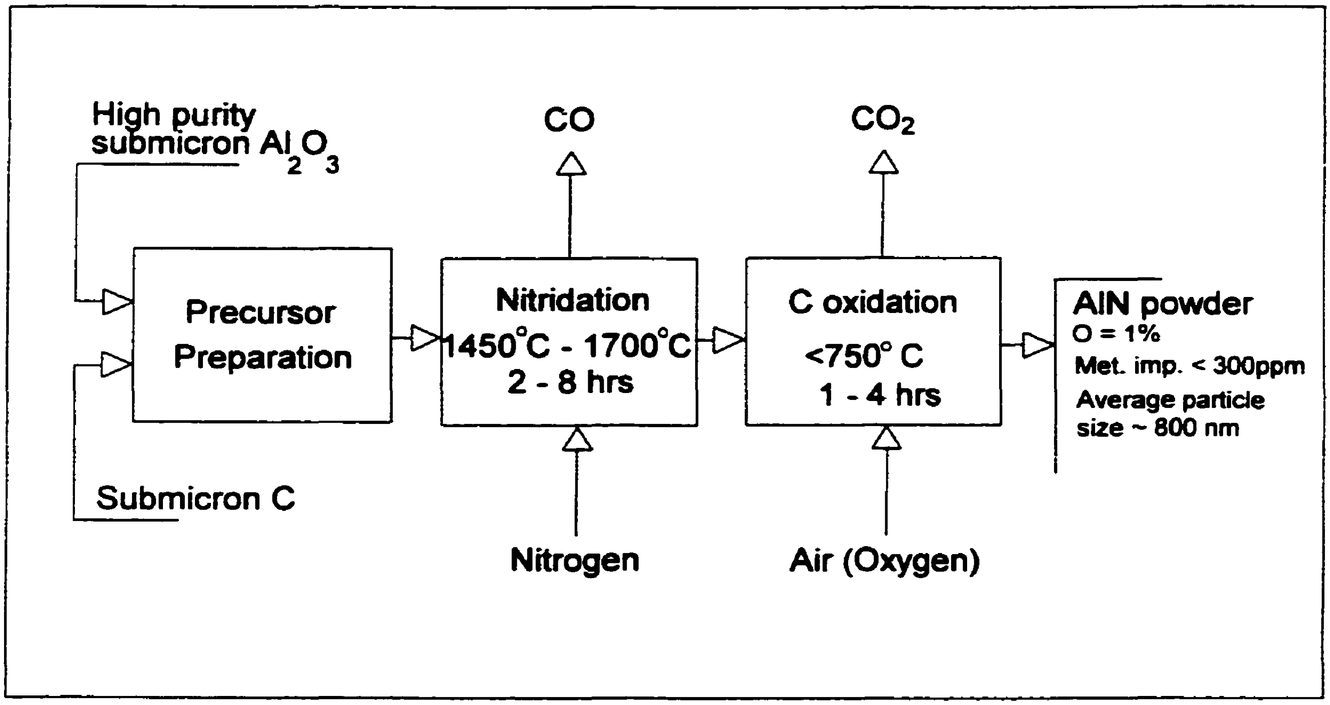

Figure 2.2 - Schematic diagram of the carbo-nitridation process for producing fine AlN powder developed by Keramont Corp. (U.S.); reproduced from [3].

2.1.2. The floating nitridation

The floating nitridation is a continuous process for the synthesis of AlN powders in which aluminum powder suspended in a gas stream is nitrided by a mixture of N_2/NH_3 at relatively low temperatures[14],[15]. This work is reviewed here in more detail since it offers some insight to the possible mechanism for the nitridation of liquid aluminum particles.

Kimura et al.'s[14] laboratory scale reactor was formed by a vertical alumina tube 42 mm internal diameter with a 1000 mm long heating zone operating between 1150 to 1300 °C. The N_2/NH_3 mixture with a maximum concentration of NH_3 of 20 % vol. is injected at the tube centreline below the central portion of the heating zone. Full conversion to AlN of aluminum particles of an average particle size of 15 microns was reported to occur using 5 % vol. NH_3 at 1250 °C. At this temperature, it was also reported that the increase of NH_3 concentration above

10 % vol. reduces the amount of conversion. Depending on particles diameter, residence times in the range of 15 to 50 sec were estimated for this type of reactor[15]. In this process the reactor temperature is insufficient to promote fast gas phase reaction, and full conversion of the Al in the core of a particle, resulting from diffusion of nitrogen from the particle surface, would require residence times longer than the ones estimated. Fully nitrided particles observed by scanning electron microscopy showed cracks on their surface, suggesting nitridation occurred between liquid aluminum erupting from inside of the particles and the N_2/NH_3 gas mixture. The same was observed by Chang et al.[15]. It was suggested by Kimura et al.[14] that these cracks might result from differential thermal expansion between the AlN layer formed on the surface of particles and the liquid aluminum in the particle. This cracking process might explain the high conversion observed.

Sinterability tests on the 100 % converted powder produced by this process produced transparent AlN ceramics by hot-pressing at 1900 °C without sintering aids.

2.1.3. Vapour phase synthesis

Vapour phase synthesis of ceramic materials invariably requires gas phase metal precursors whose availability is severely limited[6]. Aluminum nitride is no exception. A possible alternative is the use of solid metal reagent which has to be evaporated. This last method demands high energy sources coupled with an effective heat transfer between the source and the condensed phase metal, a requirement met by thermal plasma systems. Next, some of the processes reported in the literature concerning vapour phase synthesis of AlN are briefly reviewed. The specific application of thermal plasmas will be reviewed in more detail in a separate section.

AlN was synthesized by the reaction of aluminum chloride $AlCl_3$ and ammonia at moderate temperatures (993 to 1463 K)[16]. In this process, ammonium chloride (NH_4Cl) is formed as a by-product according to the following reaction:

$$AlCl_{3(g)} + 4NH_3 \rightarrow AlN + 3NH_4Cl \qquad (2.1)$$

The size of the particles produced by this method was in a range of 300 nm and 30 μm. Larger particle sizes were produced at higher process temperatures. This process rises environmental concerns since it involves hazardous reagents[4].

Another study dealt with the production of AlN by the thermal decomposition of triethyl aluminum ($Al(C_2H_5)_3$) in presence of ammonia[17]. The powder formed at a furnace temperature of 1373 K exhibited broad x-ray diffraction peaks corresponding to those of AlN. Particles produced had a diameter of less than 100 nm.

Pratsinis et al.[18] used an externally heated alumina tube to evaporate aluminum inside an alumina boat. The furnace atmosphere was formed by a main stream of argon. Ammonia was injected at the tube centre line upstream of the alumina boat. Pure AlN powders were produced at operating temperatures ranging from 1400 to 1873 K, in the presence of excess NH_3. Powder particle sizes evaluated from BET specific surface area analysis were in a range of 34 to 68 nm.

2.2. Thermal plasma synthesis

The vapour synthesis of aluminum nitride using thermal plasmas has been reported by several workers. Most of the research has been carried out using aluminum metal, either as a powder or as pieces which are melted and vaporized in the plasma and reacted with nitrogen species originating from nitrogen gas or ammonia. Both radio frequency (RF) and direct current (DC) arc plasmas have been used.

The use of RF plasmas with aluminum powder injected above the fire ball was reported by Canteloup and Mocellin[19] (1974), and by Wehling[20] (1991). In both works ammonia was introduced as nitriding reagent in the tail flame, at molar ratios N/Al ranging from 5 to 50. Baba et al.[21] (1987) opted to use pieces of aluminum in the form of small cubes of 10x10x10 mm.

These were lifted up into the flame. A common characteristic of these RF plasma systems was the use of argon for plasma generation with ammonia introduced in the tail flame.

Etemadi[10] (1991), Godin et al.[22] (1991), and Ageorges et al.[11] (1993) reported the use of DC transferred-arc plasmas having an aluminum melt as anode. All of those workers used a reactive plasma gas formed by pure nitrogen or mixtures nitrogen/ammonia. The aluminum nitride produced by these experiments ranged from ultrafine particles collected from the exhaust gases to large sintered crystals which grew around the anode.

Some of the plasma synthesis results presented in the literature are summarized in Table 2.1. A great scatter is observed in the particle size reported by different authors. A broader particle size range was reported for the experiments using transferred-arcs. Etemadi[10] (1991), who used a transferred-arc in a water cooled chamber, and the other authors who used RF equipment reported smaller particle sizes and more uniform particle size distributions. These data lead to the conclusion that previous investigations of the production of AlN using plasma systems were far more qualitative than quantitative. Because in the transferred-arc experiments the metal vaporization and reaction were carried out in the same chamber, longer residence times in the high temperature region, and possibly higher concentrations of metal vapour, were available. Both factors contribute to produce larger particles. But, due to larger temperature differences, the transferred-arc process is more difficult to control and broader size distributions were produced. In the RF experiments, on the other hand, because the contact between metal vapour and the reactant gas was made after the zone where plasma is generated, shorter residence times for particles to grow were available and smaller particles with a narrower particle size distribution were obtained. When metal powder is fed above the fire ball in a RF plasma, excessive feed rates can cause incomplete evaporation of metal particles. Given the limited feed rate and the greater gas flow rates reported for these systems, their smaller particle sizes could have resulted from a smaller vapour concentration (if compared with the greater metal vapour concentrations of transferred-arc systems). In either case, the effect of parameters such as temperature, metal vapour concentration, and cooling conditions on powder characteristics were not investigated.

Table 2.1 - Summary of experimental results reported in the literature for the plasma synthesis of AlN.

Author(s)	Type of plasma	Power (kW)	Plasma gas		Quenching gas (lpm)	Al(v) wt% (1)	NH3/Al molar ratio	SSA (m^2/g)	Part. size (nm)
			Comp.	Flow rate (lpm)					
Canteloup and Mocellin (1974)	RF	10	Ar	36	NH_3 10.5	0.4	50	220-260	7-8
Baba et al. (1987)	RF	20	Ar/N_2	42/18	NH_3 5~20	1.1	5-22	50-80	23-37
Wehling et al. (1991)	RF	13	Ar	40	$N_2/NH_3/Ar$ 75	0.15	N.A.	115	30
Etemadi (1991)	DC-TA	2	Ar/N_2 Ar/NH_3	18	Not used	N.A.	N.A.	N.A.	30
Godin et al. (1991)	DC-TA	350	Ar/NH_3 NH_3	N.A.	Not used	N.A.	10 max.	N.A.	<200
Ageorges et al (1993)	DC-TA	69	N_2/Ar	80/25	NH_3 (100)	N.A.	N.A.	12-16	135
Moura (1993)	DC-TA	8	Ar	15	NH_3/Ar 2/3.6	0.7	12	80-100	23

RF = Radio frequency induction coupled plasma.
DC-TA = Direct current transferred-arc.
(1) calculated based on reported data.

2.3. Previous work on the present reactor concept

Table 2.1 also includes the results of Moura[12] (1993) using the new concept of DC transferred-arc reactor developed at McGill University. Moura's research demonstrated the feasibility of producing aluminum nitride in a transferred-arc reactor having a different design than those reported in the literature. This previous work focused on the study of the process variables (arc current, arc length, and plasma gas flow rate) on AlN conversion, as well as on the aluminum evaporation rate.

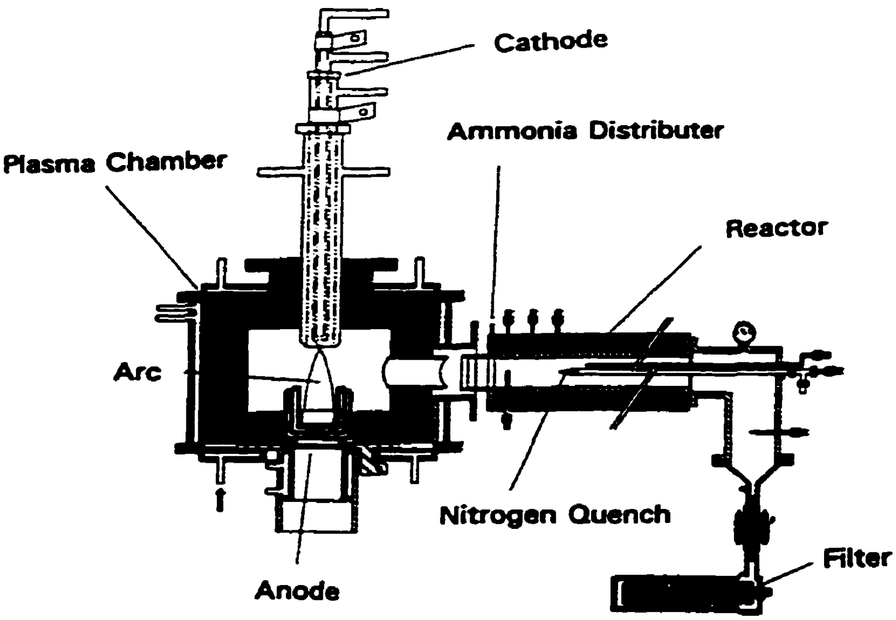

Figure 2.3 - Schematic diagram of the plasma reactor used for the synthesis of AlN ultrafine particles with the reaction carried out outside the plasma chamber; adapted from Moura[12], 1993.

In this reactor design, shown in Figure 2.3, the reaction between aluminum vapour and ammonia was carried out in a section formed by a stainless steel tube of 40 mm internal diameter, separated from the evaporation chamber. Pieces cut from an Al bar were placed in a graphite crucible (32 mm diameter x 35 mm deep) acting as anode. Argon was used as plasma gas and ammonia was injected either pure or mixed with argon as the nitriding reagent, immediately after the outlet of hot gases from the plasma chamber. The ammonia distributor consisted of 24 radial holes of 0.8 mm diameter. The reactor length was defined by the distance between the point where ammonia was introduced and the downstream point where nitrogen was injected to quench the reaction. The nitrogen injection device could be moved in order to change the reactor length. Typical operating conditions reported are shown in Table 2.2.

AlN conversion was studied as a function of the ratio Ar/NH_3 of the gas mixture injected in the reaction portion. The amount of aluminum evaporated was determined by weight difference of the aluminum in the graphite crucible before and after each experiment. From the data reported, the molar fraction of Al vapour carried with the plasma gas is estimated to be of the order of 1×10^{-2}. With the reactor layout shown in Figure 2.3 and the operating parameters shown in Table 2.2, it was demonstrated that full conversion to AlN could be achieved if the reactants were well mixed. Also, it was demonstrated that the effective reactor length is very short. Typical operating parameters used when full conversion was achieved were: 40 mm arc length; 994 K mixing zone temperature; nitriding gas formed either by pure ammonia at 6 lpm or by a mixture of 2 lpm of ammonia and 2.4 lpm of argon. The specific surface area of the powders produced, measured by the BET method, varied from 80 to100 m^2/g, corresponding to specific surface area average particle diameters ranging from 18 to 24 nm.

Because the previous reactor design was unable to produce a broad range of temperatures and aluminum vapour concentrations, the influence of these variables, as well as of the cooling conditions, on powder characteristics could not be investigated.

Table 2.2 - Typical operating parameters used in the production of AlN, as reported by Moura[12].

Plasma gas:	Argon
Plasma gas flow rate:	10 - 20 lpm
Arc length:	3 and 4 cm
Arc current:	240 and 260A
Arc power:	6.3 kW
Ammonia flow rate:	2 - 6 lpm
Argon mixed with ammonia:	0 - 2.5 lpm
Temperature at the mixing zone:	770 - 1090 K

Chapter 3

OBJECTIVES

The potential of the application of thermal plasmas to the synthesis of ultrafine particles is widely recognized. However, as it has been pointed out before, promoting higher yields and understanding the mechanisms involved in the gas-to-condensed phase transition characteristic of vapour-phase synthesis are still major barriers to overcome.

Continuing the research on the AlN system, the overall objective of the present work was to investigate the fundamentals of the vapour-phase synthesis of AlN ultrafine particles using a proposed new concept of plasma reactor. The study focused on the understanding of the phase transition mechanisms associated with this particular system, and on the influence of its main operating parameters on the properties of the powder produced. The specific objectives which were established to reach this target are:

- To carry an experimental investigation of the dependence of powder properties on the reactor operating conditions, particularly the effect of temperature, metal vapour concentration, and cooling conditions on particle size and composition.

- To simultaneously carry a theoretical investigation, supported by experimental results, on the gas-to-condensed phase transition in this reacting system.

- To design and construct a new version of this plasma reactor concept.

- To develop a gas sampling probe for the determination of metal vapour concentration at the entrance of the reaction zone.

- To evaluate of the sintering properties of the powder produced.

4.1. Crystal structure

Aluminum nitride (AlN) is a semiconducting compound. It crystallizes with a wurtizite like hexagonal structure (2H) whose unit cell[1] is shown in Figure 4.1. Its crystal structure can be visualized as a network of four close packed planes of Al and N atoms stacked in the (001) direction, indicated as A,B,C, and D in the figure. The planes are shifted with respect to each other in such a way that each aluminum atom is the center of a tetrahedron of nitrogen atoms. The unit cell parameters are: a_0 = 0.311 nm and c_0 = 0.498 nm[23]. The theoretical density determined from the above cell parameters is 3.26 g/cm^3. Pure AlN crystals are hard, colourless, and optically transparent[24]. Pure AlN does not present polytypisms (ability of a chemical compound to crystallize in a large number of crystal structures, all of which can be regarded as build up by stacking nearly identical layers on top of each other and differ only in the stacking sequence of layers)[24]. On the other hand, with the addition of impurity elements its crystal structure can be modified into a variety of polytypes[13].

4.2. Melting point

At the pressure of 1 atm (100 kPa), AlN does not melt, but dissociates significantly above 2500 K[24]. At a 100 atm pressure ($1x10^4$ kPa) of N_2, the first liquid phase is observed at 3073 K, probably resulting from the dissociation into liquid Al saturated with nitrogen and N_2 gas[24].

4.3. Reactivity with moisture and oxygen

Like aluminum, aluminum nitride reacts with moisture and/or oxygen in the air to form a surface layer of aluminum oxide; this layer is protective and retards further oxidation. Taylor and

Lenie[25] (1960) investigated the stability of 6.35x12.7x12.7 mm AlN hot pressed specimens in various atmospheres. The effect of air and oxygen at temperatures up to 1673K, or dry steam up to 1273 K, after 30hr is slight - conversions to aluminum oxide from 0.3 to 1.3 % were observed. Oxidation in air starts at 973 K but is slow up to 1673 K because of the formation of a protective oxide layer (after 24 hr at 1673 K, an oxide surface film of the order of 40 μm thick was observed). However, at 1973 K in air, the rate of oxidation becomes rather rapid. Slack and McNelly[24] (1976) reported that, at room temperature, AlN high surface area powder typically develops an oxide layer of 50 to 100 Å in one day.

4.4. Thermal conductivity

The theoretical thermal conductivity of aluminum nitride has been estimated to be 320 W/m.K, which has been measured only in single crystals. Conventional AlN ceramics do not exhibit such high values; the highest thermal conductivity reported for translucent polycrystalline AlN is 260 W/m.K [3],[26].

Oxygen and metallic impurities such as silicon, iron, and magnesium, even in amounts as little as 200 ppm, are proven to significantly reduce the thermal conductivity[26]. Sintering aids such as rare earth and alkaline earth metal oxides and fluorides are commonly used for improving both sinterability and thermal conductivity. Oxygen is present in AlN powders as alumina either on the particle surface or inside the particle as a solid solution. Yttria (Y_2O_3) and calcium oxide (CaO) are believed to retain the alumina at interstitial sites among grains after the sintering process, thus improving the thermal conductivity from 50 to 200 W/m.K [2].

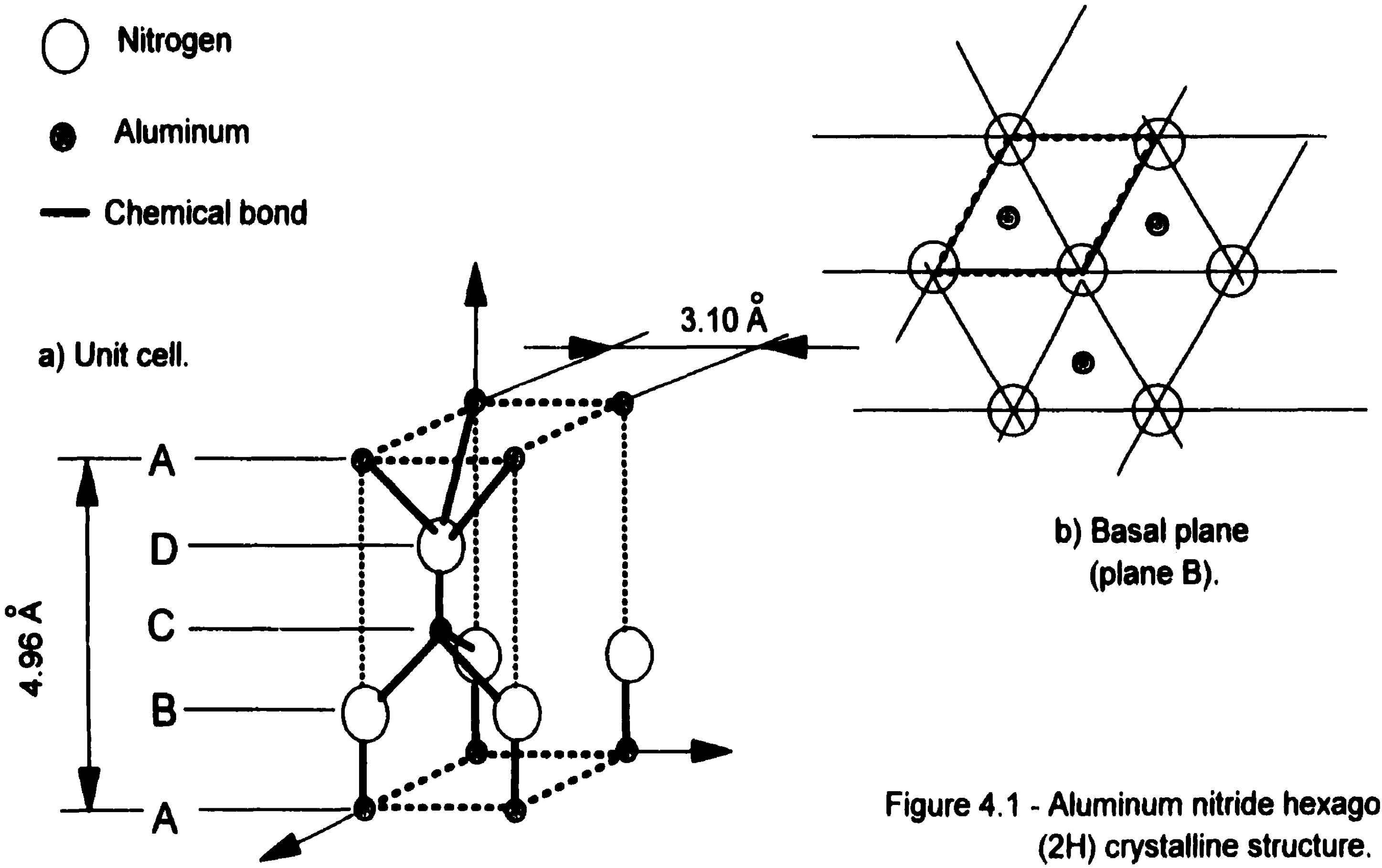

a) Unit cell.

b) Basal plane (plane B).

Figure 4.1 - Aluminum nitride hexagonal (2H) crystalline structure.

4.5. Thermal expansion

The thermal expansion measured parallel to the direction of pressing[25], on a sintered AlN bar of 6.35 mm diameter and 76.2 mm long, is shown in Table 4.1. The thermal expansion exhibited by AlN is in the range characteristic of ceramic materials, being only slightly higher than the thermal expansion of silicon carbide.

Table 4.1 - Thermal expansion of hot pressed AlN[25].

Temperature interval (°C)	Linear expansion (cm/cm/°C)
25-200	$4.03\text{x}10^{-6}$
25-600	$4.84\text{x}10^{-6}$
25-1000	$5.64\text{x}10^{-6}$
25-1350	$6.09\text{x}10^{-6}$

4.6. Thermodynamics of the AlN vapour phase synthesis

A study of the thermodynamic of the vapour synthesis of AlN by nitridation of metallic aluminum and of its halides was carried out by Hashman and Pratsinis[27]. The effects of reactant ratio, temperature, and pressure on reactant conversion and product purity were estimated. In case of nitridation of metallic aluminum, this study concludes that nitridation by ammonia in the presence of nitrogen results in the highest reactant conversion and AlN purity. Although favorable from the thermodynamic point of view, nitridation using N_2 might be rather slow at temperatures below 2000 K, as demonstrated by the results of some of the studies using this gas at this temperature range[12],[19]. However, the use of N_2 as a plasma gas in transferred-arc reactors may be troublesome in the sense that large lumps of AlN may form[10],[11], rather than ultrafine particles. This is caused by the far higher temperatures and extended periods of contact with the molten Al anode.

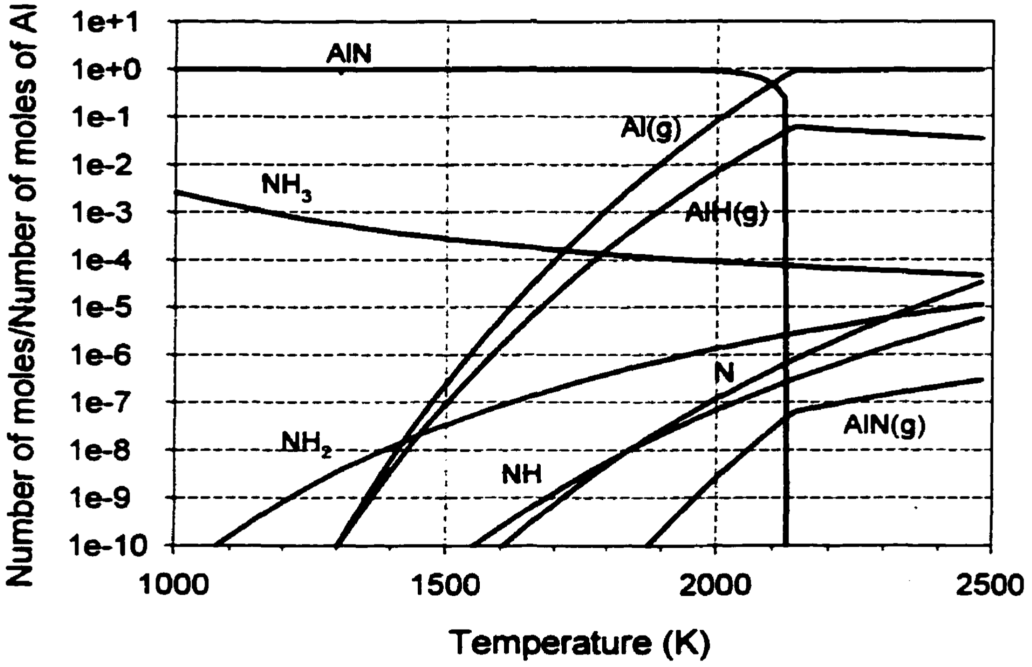

Figure 4.2 - Equilibrium compositions of a carrier gas formed by 20 lpm Ar, Al mole fraction of $2x10^{-3}$, and quenching jet formed by 2 lpm of NH_3 and 5 lpm of Ar.

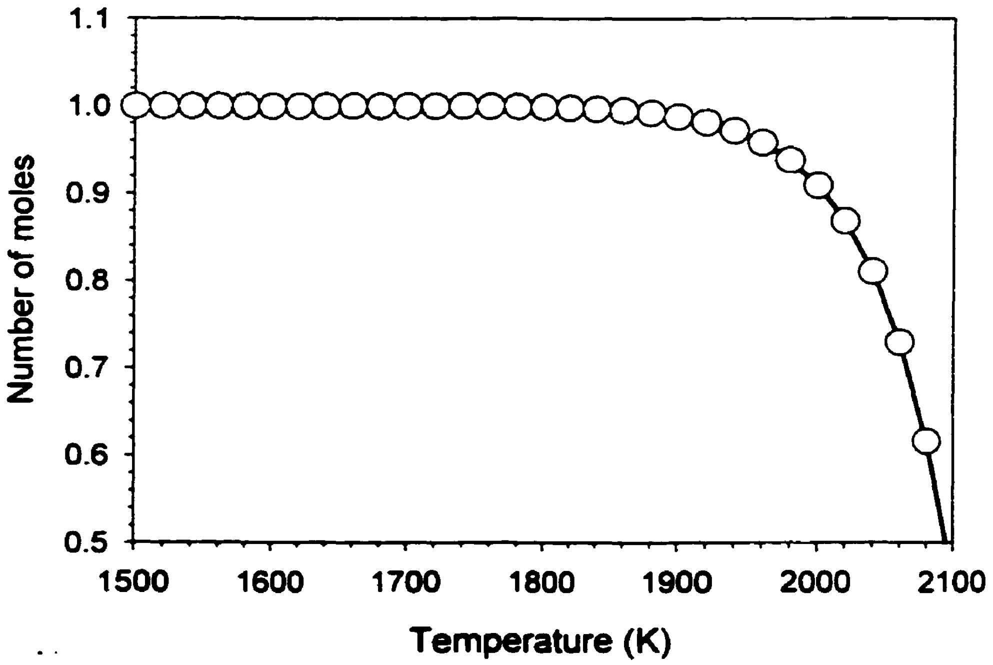

Figure 4.3 - Aluminum conversion as a function of temperature.

The computer code HSC - Chemistry[28] was used to evaluate the thermodynamic equilibrium of the various species present in the Al-N-H-Ar system at the range of temperature and gas composition characteristic of the present reactor. The calculations were based on data supplied by JANAF thermochemical tables[29].

The equilibrium mole fraction for a typical operating condition is presented in Figure 4.2, considering a plasma gas composed of pure argon, assuming an aluminum mole fraction at the entrance of the reactor of $2x10^{-3}$, to be mixed with a reacting gas formed by 2 lpm of ammonia and 5 lpm of argon (flow rates measured at room temperature of 298 K, and 100 kPa pressure). It is observed from this figure that AlN is by far the most stable phase at temperatures below 2000 K. H_2 and N_2 resulting from the NH_3 decomposition exceed the concentration range plotted. Because Al concentration is highly dilute, this diagram does not show liquid aluminum resulting from the AlN decomposition above 2000 K (at approximately 2100 K, the Al vapour pressure is reached). Considering the use of Ar/H_2 plasma gas in this study, the equilibrium composition for a Ar/10 % H_2 vol. mixture was also evaluated. The result obtained showed practically no difference in comparison with the pure Ar diagram. The maximum possible conversion of Al to AlN as a function of temperature is shown in Figure 4.3. It is observed that for the assumed overall gas mixture compositions, Al conversion sharply decreases for temperatures above 1800K.

The effects of possibly occurring carbon and oxygen contamination in the processing gas were also analyzed. The equilibrium diagram in Figure 4.4 shows that a slight amount of oxygen in the mixture leads to the formation of Al_2O_3 at the expense of AlN at temperatures up to 1300 K. Above this temperature, formation of CO is favored. If hydrogen is present, at low temperatures carbon preferably forms CH_4.

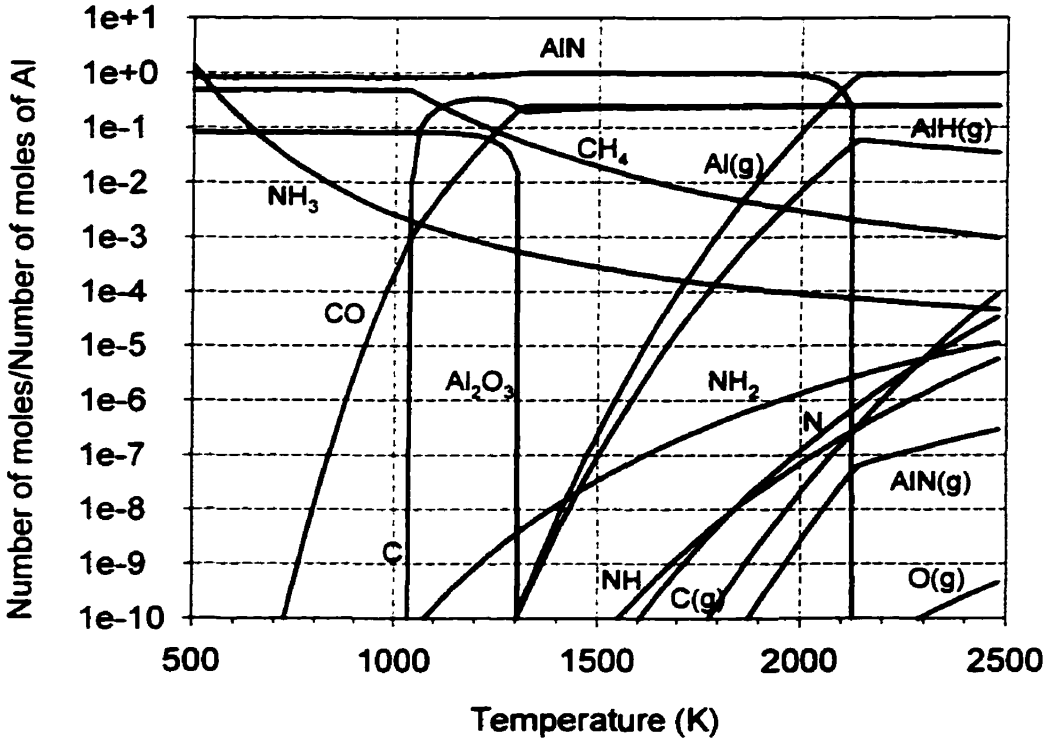

Figure 4.4 - Equilibrium composition of a carrier gas formed by 20 lpm of Ar, Al mole fraction of 2×10^{-3}, assumed mole fractions of elemental carbon and oxygen impurities of 10^{-3} and 5×10^{-4}, respectively, and a quenching jet formed by 2lpm of NH_3 and 5 lpm of Ar.

Chapter 5

EXPERIMENTAL

5.1. Experimental setup

The experimental apparatus used in the present research is shown in the photograph of Figure 5.1. Its schematic diagram is shown in Figure 5.2. The setup included the plasma generating system, gas supply, cooling water supply, reactor, gas sampling accessories, and data acquisition.

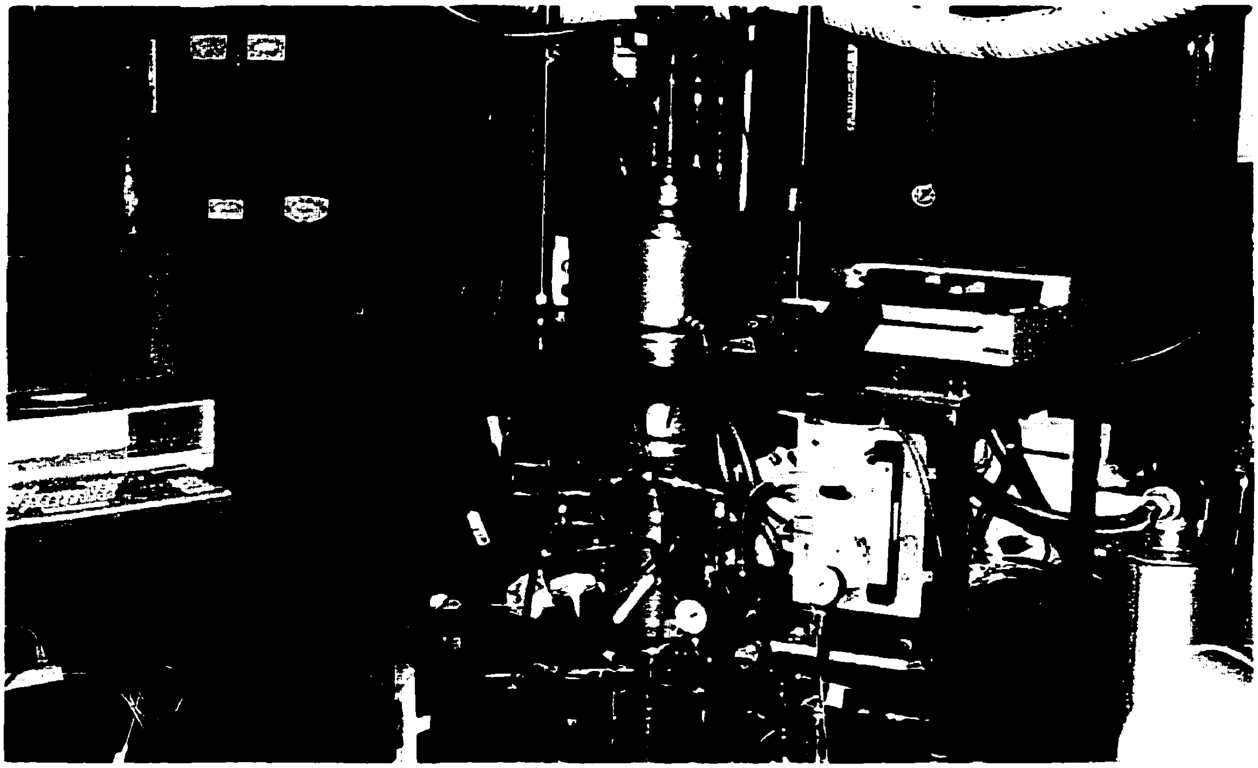

Figure 5.1 - Photograph of the experimental apparatus.

The plasma generating system comprised the following items: a home made cathode assembly; a D.C. power supply; a control console including a radio-frequency starter; and a start up resistor and switch connecting the cathode nozzle to the anode. The cathode was made of a W-2%Th rod, 6.35 mm diameter, surrounded by a gas nozzle. Both the cathode and nozzle were water cooled. The nozzle was electrically insulated from the cathode. Electrical energy was supplied to the system by a Thermal Dynamic rectifier, model TDC IA-40, with rated power of 40 kW, open circuit voltage taps for 80, 160 or 320 VDC, and maximum operating current of 500A.

The plasma gas and the quenching gas were supplied from high pressure cylinders, and the gas flow rates controlled by means of calibrated rotameters.

Water from the laboratory service water circuity was used for cooling both the cathode assembly and the reactor walls.

Gas sampling was carried out in order to evaluate the aluminum vapour content in the plasma chamber off-gas and the degree of ammonia decomposition. For this purpose, a gas sampling aparatus and analysis procedure were developed and adapted for each case.

Temperature, arc voltage and arc current data acquisition was performed using a data logger, Omega model DPS-800, connected to a computer, and a strip chart recorder.

5.2. Reactor design and operation

A new reactor was built to carry out the experimental part of this study. As in the previous version, the reaction zone was separated from the plasma chamber. Modifications were introduced to produce evaporation of aluminum over relatively long periods of time, to promote a homogeneous outflow of the hot gas from the plasma chamber, and to provide space for the introduction of a high temperature gas sampling probe for the measurement of the aluminum vapour concentration.

The schematic diagram of the reactor is shown in Figure 5.3. As shown in Figure 2.2, the previous version had the crucible placed on top of a water cooled anode, the gas outlet on the side of the plasma chamber, and the reaction tube placed with its axis on the horizontal direction. The new reactor, on the other hand, has the reaction zone vertically aligned with the plasma chamber. The crucible is hold by three graphite rods, equally spaced, which are attached to an external graphite ring. The plasma chamber off-gas outlet is formed by the annular space between the external ring and the crucible.

A 76.2 mm diameter Al disk (Aluminum Association Grade 1100, 99% Al) was melted and evaporated inside the graphite crucible. The reaction zone comprised a graphite tube (40 mm internal diameter).

In this arrangement, the plasma gas laden with Al(v) flows through the anular space between the crucible and the plasma chamber wall into the reaction tube where it is mixed with NH_3 and quenched by a radial jet of cold gas. Two geometries of gas mixing were used which characterized two distinct steps in the development of this research project. In the first step, experiments for the production of AlN powder were carried out in which ammonia mixed with argon was introduced in the form of radial jets at an axial position 175 mm distant from the entrance of the reaction tube. The results of this set of experiments were used for the development of a model for the nucleation and growth of AlN ultrafine particles. Because full conversion of Al to AlN could not be accomplished using the radial configuration, this model was used to simulate the axial feeding configuration, which was further implemented. The radial injection of NH_3 mixed with Ar is shown in Figure 5.3(a). Figure 5.3(b) shows the axial injection modification, upstream of the radial jet of pure inert gas. In this case two injection locations were studied: NH_3 feeding right at the entrance of the tubular reactor (T2 position); and at a higher position (T1), 45 mm above the entrance to the tubular reactor. In case of axial injection, the radial quenching was kept to cool the exit gas below 600 K before it leaves the reactor.

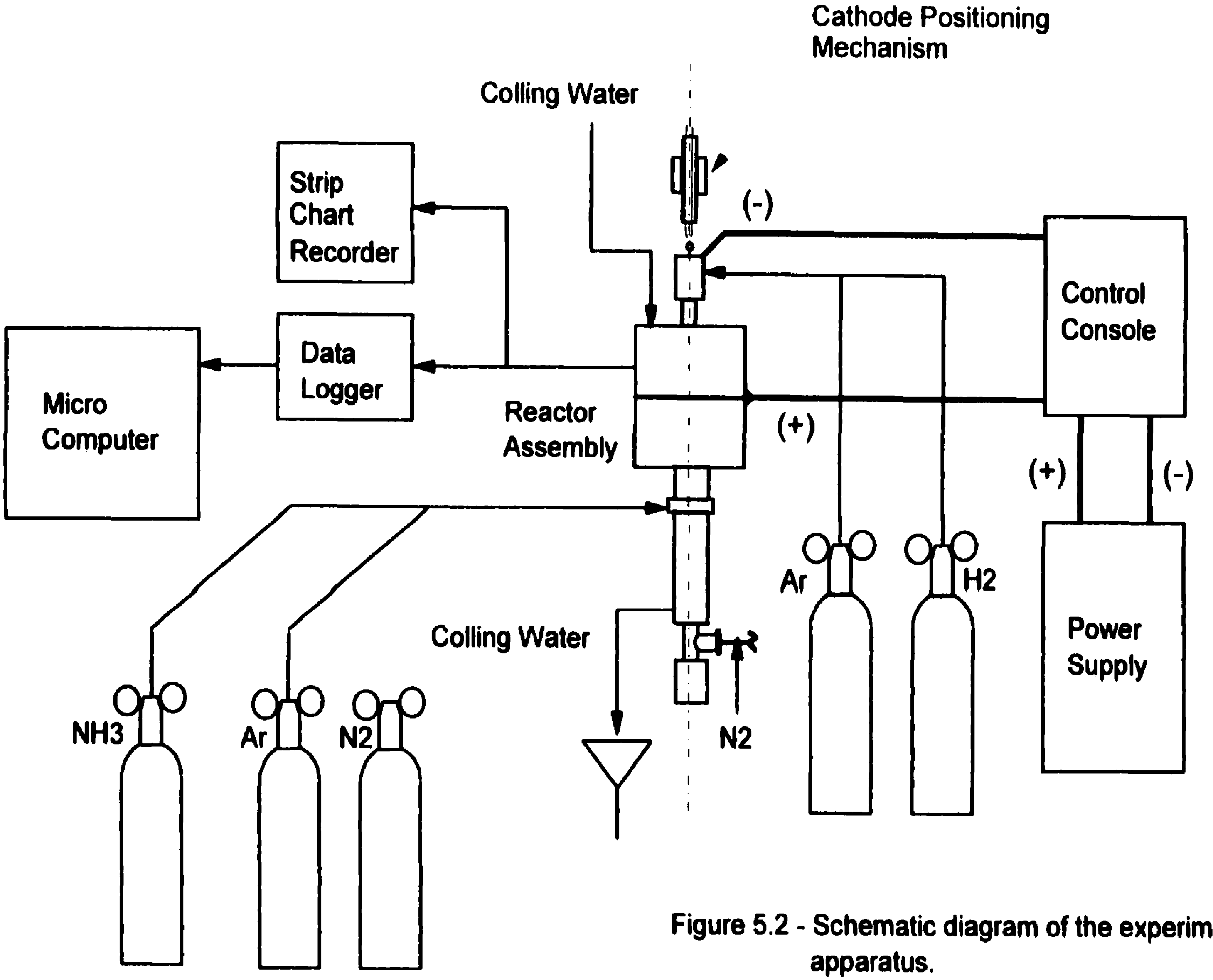

Figure 5.2 - Schematic diagram of the experimental apparatus.

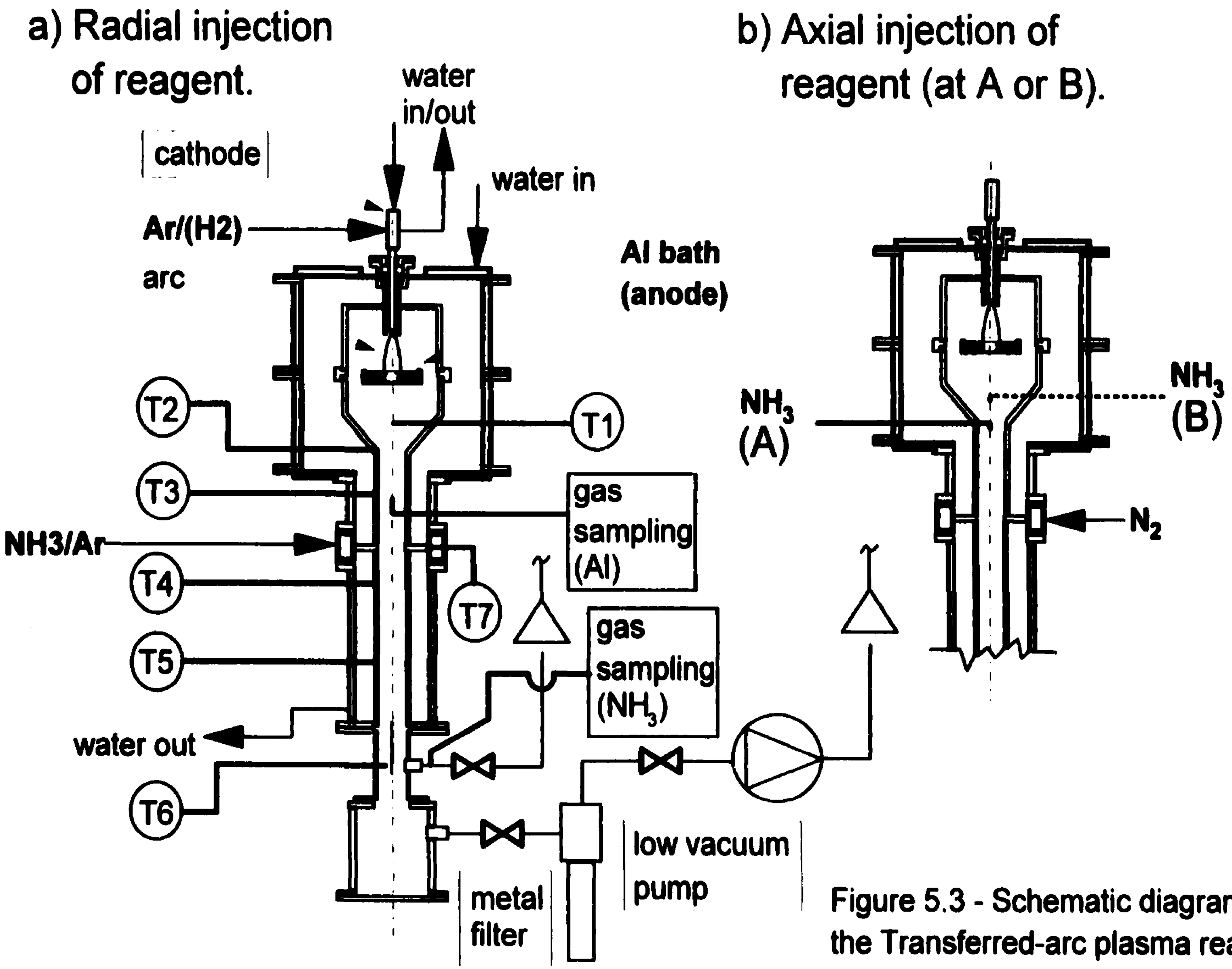

Figure 5.3 - Schematic diagram of the Transferred-arc plasma reactor for AlN ultrafine powder synthesis.

The radial gas injector was formed by a ring of 24 holes of 0.8 mm diameter each. Following the results of Moura's[12] study on the effect of different combinations of NH_3 and Ar flow rates on AlN conversion, for most part of the radial injection experiments, the NH_3 flow rate was kept constant at 2 lpm (see note).

An closed end alumina tube 6.35 mm o.d. x 3.175 mm i.d. with a single hole cut perpendicular to its axis at 10 mm from the end was used for the axial injection of NH_3.

With the exception of the radial gas injector, which was fabricated of stainless steel, graphite was used for the construction of all internal parts in contact with the hot gas because of its high temperature resistance and relatively low cost. Inside, the reactor was heavily insulated to minimize heat losses and keep the plasma chamber off-gas as hot as possible until it could reach the mixing zone. The reactor outer shell consisted of many parts made of stainless steel. These were tightly sealed by 'o' rings in order to prevent gas leaks. A water jacket cooled the outer shell for dimensional stability. The cathode assembly entered the top of the reactor, at its axis of symmetry. The cathode could be axially displaced to adjust the arc length.

Before each run, the reactor volume was purged with Ar by successively rising and lowering its internal pressure using a gas cylinder and a vacuum pump. Typically, the reactor was heated for about fifty minutes until steady state could be reached. In total, each experiment lasted from two to five hours.

As indicated in Figure 5.3(a), temperature was monitored in several points of the reactor. The hot gas temperature was measured beneath the anode and close to the reactor centre line, before gas entered the tubular reactor (T1). In the tubular reactor internal wall, the temperature was measured at two points upstream and two points downstream of the quenching gas injector (T2, T3, T4, and T5). The temperatures at the points T1 and T2 were measured using W-5% Re thermocouple wire (0.25 mm diameter), isolated by a 1.59 mm alumina two holes tube. These thermocouple assemblies were placed inside a 6.35 mm o.d. x 3.175 mm i.d. high alumina protection tube, closed at the end. All other points were measured using type K thermocouples sets, 1.59 mm diameter, with exposed junction.

Gas flow rates were measured with rotameters. Experiments were carried out using either Ar or an Ar/H_2 mixture as plasma gas. The nitriding gas mixture was fed at room temperature. Ammonia decomposition was evaluated by sampling small volumes of gas at the bottom of the tubular reactor.

For each set of operating conditions, the powder produced was sampled by a 10 μm stainless steel metal filter downstream of the reaction zone. The powder collected was transferred to vials which were kept in a dissecator. Because the pressure drop through the filter increased as a function of the amount of powder deposited on the filter's surface, a water sealed vacuum pump was used to maintain the pressure inside the reactor constant at 100 kPa during the sampling operation. Typically, powder collection lasted for 10 to 20 minutes.

5.3. Gas sampling and analysis

Small amounts of gas were collected for measurement of Al concentration in the hot gas, prior to mixing with ammonia, and for the evaluation of the quantity of NH_3 that decomposes in the process. The schematic diagram of the apparatus used for this purpose is shown in Figure 5.4.

Note: Unless otherwise indicated, liters per minute (lpm), referred to 298 K temperature and 100 kPa pressure, will be used through out the text as gas flow rate unit.

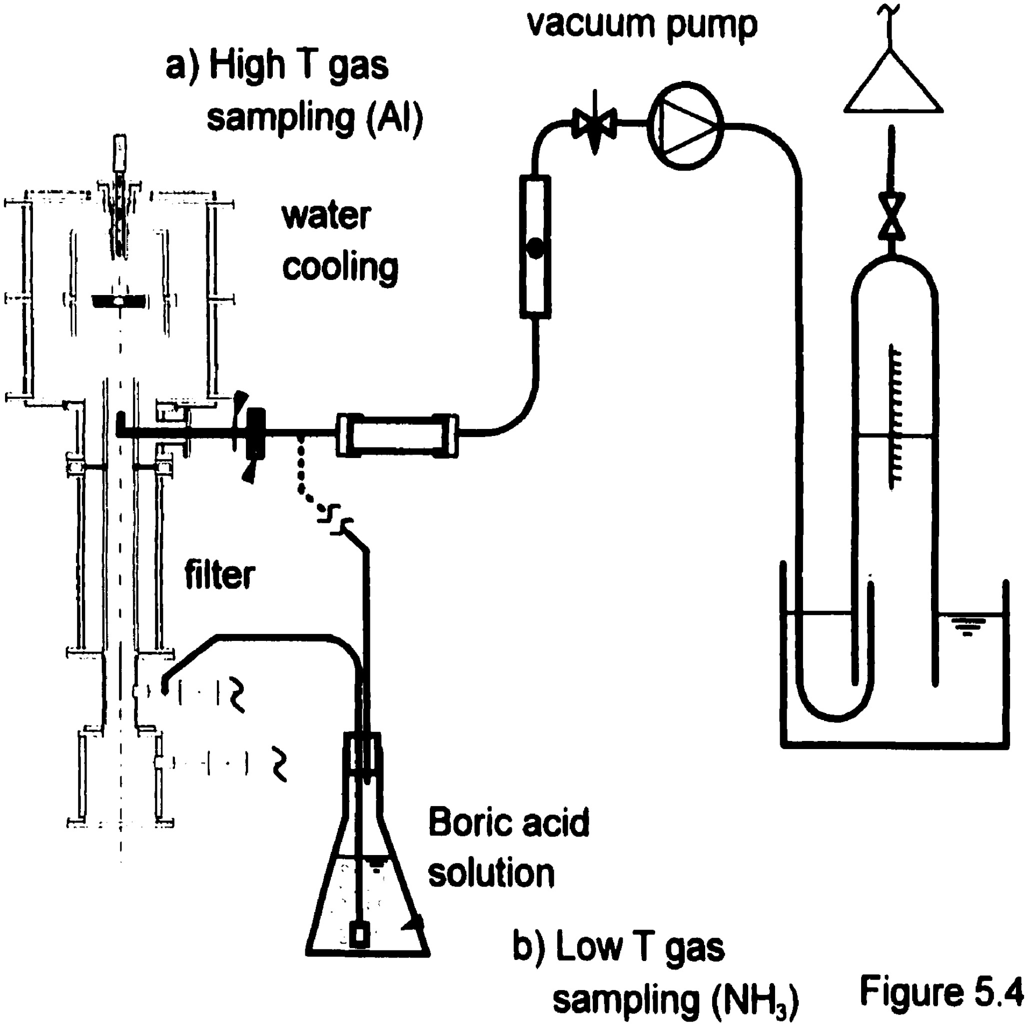

Figure 5.4 - Schematic diagram of the gas sampling device.

5.3.1. Measurement of Al vapour concentration

A small volume of the carrier gas (between 1000-2000 ml) was isokinetically sampled near the entrance, and at the centreline, of the tubular reactor by a water cooled probe (3.2 mm I.d.). The probe assembly shown in Figure 5.4 (a) included a filter, a low flow rate vacuum pump, a rotameter with high precision flow control valve, and a shutoff valve. An inverted burette was used to measure the total gas volume by water displacement.

The probe was introduced 82 mm upstream of the reacting gas injector, when operating at steady state and without injection of the nitriding gas mixture. The Al retained inside the probe was dissolved in a known volume of hydrochloric acid (HCl) solution (5%vol.), typically 150 ml, and the solution analyzed by atomic absorption for Al content.

5.3.2. Measurement of NH_3 decomposition

The thermal decomposition of ammonia was evaluated experimentally by sampling small volumes of gas at the bottom of the reactor using the gas sampling probe assembled as shown in Figure 5.4 (b). The volume sampled was bubbled through 500ml of 0.05M boric acid (H_3BO_3) solution contained in an elemeyer. The total gas volume was measured using the same procedure as in the Al concentration case, using the inverted burette. The boric acid solution was titrated with a 0.05M HCl solution and the amount of NH_3 determined using a calibration curve. The calibration curve was obtained using a similar procedure, with the introduction of known volumes of NH_3 gas into an Ar gas stream.

5.4. Powder characterization

5.4.1. Specific surface area

The specific surface area of the powders produced was analyzed by the Brunner-Emmett-Teller method (BET) using a FLOWSORB II 2300, Micromeritics Instrument Corporation. The samples were degassed in a glass sample tube, heated to 250 °C for approximately 2 hr, until no change in the sample weight could be observed. The same He/30%vol.N_2 gas flow used for surface area measurement passed through the glass tube at this point. Following the degassing step, the glass sample tube was positioned in a surface area measuring station and a Dewar containing liquid N_2 was placed around it. After reaching equilibrium, the Dewar was replaced by a water container to heat the glass sample tube back to room temperature. The whole operation was monitored by measuring the change in the thermal conductivity of the He/30%vol.N_2 gas mixture. The surface area of the powder in the glass tube was measured by determining the quantity of N_2 that adsorbs as a single layer of molecules on the surface of the particles. The equipment calibration was periodically verified by injecting a known volume of N_2 in the gas line (1 cm^3 of N_2 being equivalent to 2.84 m^2 of surface area). The specific surface area (m^2/g) was calculated by dividing the surface area reading by the weight in grams of the degassed sample.

5.4.2. X-ray diffraction

The identification of crystalline AlN was performed using x-ray diffraction (XRD) patterns (Rigaku - Rotating Anode Diffractometer). Small samples of the powders were deposited on a quartz blade coated with silicone grease. The sample was exposed to Cu-$K\alpha$ radiation at an accelerating voltage of 50 kV and a beam current of 150 mA. The free Al content was determined by comparison of the relative intensities of the Al peak at 44.7° and the AlN peak at 49.8 ° with Al/AlN calibration mixtures.

5.4.3. Transmission electron microscopy

Samples of the powder were examined at high magnification by transmission electron microscopy (TEM), for observation of particle size and morphology. Also, the sintered compacts, which were produced as described in Chapter 7, had their microstructure examined using this technique. The powder samples were prepared from a dilute suspension of powder in anhydrous isopropanol. After using an ultrasonic bath to break large aggregates, a drop of the suspension was deposited on a 200 mesh copper grid, coated with a 20 - 30 nm thick support C film. TEM imaging was performed with a JEOL 100 CX, at an accelerating voltage of 80 kV.

5.4.4. Chemical analysis

5.4.4.1. Nitrogen analysis

Chemical analysis was used to determine the nitrogen content of the powders produced. The procedure consisted of dissolving about 20 mg of powder in 5 ml of HCl solution (38%wt) in a closed vial. The vial was then heated to approximately 80 °C for 1 to 2 hours. The products of the digestion were $AlCl_3$ in solution and NH_4Cl crystal precipitate. The 5 ml concentrate was then diluted to 100 ml. At this step, the NH_4Cl precipitate completely dissolves, forming a crystal clear solution. An ultrasonic bath was used to accelerate the dissolution. Nitrogen analysis was then carried out using a procedure developed from the Kejldahl method[30].

The following solutions were used in the analysis:

- Saturated sodium carbonate solution (Na_2CO_3): anhydrous sodium carbonate powder (Fisher Scientific), having a solubility of 22 g per 100 ml of distilled water.
- Boric acid solution (H_3BO_3): 1%wt boric acid solution prepared by mixing 5 g of anhydrous boric acid powder (Fisher Scientific) with 500 ml of distilled water.

- Ammonium chloride solution (NH4Cl): 5 standard solutions ranging from 10 to 50 ppm were prepared for calibration using 99.9 % pure NH_4Cl anhydrous powder (Fisher Scientific).
- Hydrochloric acid solution (HCl): 0.04 M, used for titration.
- Indicator: 50 ml of solution containing 0.1 %wt. bromocresol green, 0.02 %wt methyl red in 85 %wt methyl alcohol, and reagent I water (Aldrich), mixed with 50 ml of 1%wt boric acid solution.

The analysis apparatus consisted of a small Teflon base with two concentric circular chambers, and a plastic cover. The analysis procedure consisted of placing 1 ml of boric acid solution mixed with the indicator in the central chamber. In the outer chamber 1 ml of sodium carbonate solution and 0.5 ml of the solution to be analyzed were placed diametrically opposed from each other. The dish was then closed using silicone vacuum grease as a sealant between the base and the cover. The dish was slowly rotated to promote the mixing between the two solutions in the outer chamber. The preparation was let to rest for a minimum of 5 hours. Next, the boric acid solution in the inner chamber, then turned green, was titrated with the 0.04 M HCl solution using a 2 ml micro-syringe (Gilmont) until its color returned to the original red. The volume of HCl solution required is directly proportional to the concentration of ammonium ions in the original sample. The sample concentration was determined using a calibration curve obtained from the analysis of dissolved NH_4Cl samples of known concentration.

The following are the reactions involved in the whole analysis:

$$AlN + 3HCl_{(aq)} \rightarrow AlCl_{3(aq)} + NH_{3(g)} \tag{5.1}$$

$$NH3_{(g)} + HCl_{(aq)} \rightarrow NH_4Cl \tag{5.2}$$

$$NH_4Cl + Na_2CO_3 \rightarrow NaCl + NaHCO_3 + NH_{3(g)} \tag{5.3}$$

$$NH_{3(g)} + H_3BO_3 \rightarrow NH_4^+ + H_2BO_3^- \tag{5.4}$$

5.4.4.2. Oxygen analysis

The total oxygen in the AlN powder was analyzed by the Department of Metallurgy and Materials Science of the University of Toronto using a TC136 LECO OXYGEN ANALYZER. In this method, about 15 mg of the analysis sample is weighed and compressed into a tin capsule (LECO PART #501-059) weighing approximately 180 mg. The capsule is inserted into a nickel basket (LECO PART #763-065) weighing approximately 1.00 g. This basket is then placed into a graphite crucible. The whole assembly is heated up to 2600 °C under a He flow. As the metal melts and the AlN decomposes, oxygen reacts with the crucible material to form carbon monoxide. The CO carried away with the He is analyzed by an infra-red (IR) detector. The IR analyzer signal is integrated over a period of time to give the total CO, and thus the oxygen content of the sample.

5.4.4.3. Atomic Absorption Spectroscopy

The determination of the Al vapour concentration in the plasma chamber off-gas and the Al content of some of the powder produced were carried out using atomic absorption analysis (Thermal Jarrell Ash Smith-Hieftje 11 Spectrophotometer).

By this method, a parallel beam of continuous radiation (produced by a hollow cathode lamp) of a given intensity passes through a flame in which the analyte solution is atomized. The frequency of radiation used is chosen to match the absorption line of the atomic species under analysis. A sensor in the opposite side of the emitting source detects the amount of radiation with passes through the flame. The amount of radiation absorbed is proportional to the concentration of the analyte in the flame.

The sample to be analyzed was dissolved in a HCl solution. An Al hollow cathode lamp and nitrous oxide-acetylene were used. The instrument was adjusted for a 309.3 nm wave length. The Al concentration was determined using a linear calibration curve.

5.4.4.4. Fourier Transform Infra-Red Spectroscopy

Fourier Transform Infra-Red Spectroscopy (FTIR) was used to determine the presence of Al-O and O-H bonds in the surface of the particles of the powder produced. Aluminum hydroxide ($Al(OH)_3$) and alumina (Al_2O_3) powders were used as reference for comparing the sample powder peaks. The sample preparation consisted of grinding and mixing 5% of powder sample with potassium bromide (Kbr) powder. All the powders were dried at 120 °C for a minimum of 12 hours prior to mixing. The analysis was carried out in a Bomen-Michelson 100 analyzer. The transmitance was determinded using pure KBr as a reference material.

5.4.4.5. X-Ray Photoelectron Spectroscopy

XPS, X-ray Photoelectron Spectroscopy, also known as ESCA, Electron Spectroscopy for Chemical Analysis, was used to determine the surface composition of the AlN powder produced, and also to analyze the microstructure of fracture surfaces of the sintered pellets formed using the powder produced (VG Scientific, ESCALAB 220i-XL). This analysis is accomplished by irradiating a sample with monoenergetic soft x-rays and analyzing the energy of the detected electrons[31]. Al-$K\alpha$ (1486.6 eV) and also Mg-$K\alpha$ (1253.6 eV) x-rays are usually used. These photons, which have limited penetrating power in a solid, interact with atoms in the surface region causing electrons to be emitted by photoelectric effect. Emitted electrons have a kinetic energy (KE) which is given by

$$KE = h\nu - BE - \phi_s \tag{5.6}$$

where $h\nu$ is the photon energy, BE the binding energy taken as the energy difference between the initial and final states after the photoelectron has left the atom, and ϕ_s the spectrometer work function. Liberated photoelectrons are detected as a function of energy by an electrostatic spherical sector analyzer. The XPS spectrum consistis of a plot of electron counts (or intensity) vs kinetic or bonding energy. Sharp lines of intensity reflect the origin of photoelectrons in orbits around the atomic nucleus. Because each element has a unique set of binding energies, XPS can be used to identify and determine the concentration of the elements on the surface.

5. 5. Experimental results and discussion

The experimental results presented next were divided into two classes: (i) the results related to the reactor operating parameters, which includes gas temperature measurement, Al vapour concentration, and NH_3 decomposition measurement after the reaction zone; and (ii) powder characterization, which includes size analysis and composition.

The results of Al concentration were correlated with the temperature measurement at the entrance of the tubular reactor. The powder particle size (determined from specific surface area measurement) and powder composition were correlated with the plasma chamber off-gas temperature and composition, and quenching intensity.

Because of its ease of operation, high reproducibility, and the fact that it is widely used for the characterization of ultrafine particles, BET surface analysis was extensively used in this work for particle size evaluation. Samples of all of the powders which were produced were analyzed using this technique. The equivalent specific surface area sphere diameter (d_{BET}) determined from BET measurement was combined with visual inspection of TEM micrographs.

5.5.1. Reactor operating parameters

The typical operating parameters of the transferred-arc used in the study of Al concentration and powder production using the radial injection of NH_3 are given in Table 5.1. During preliminary experiments the reactor was operated in a temperature range between 1500 and 2000 K (measured at the entrance of the vertical tube). Because little amount of powder could be collected in the metal filter with temperatures lower than 1800 K, two temperature levels were chosen for carrying out the experimental study on the production of AlN powder: 1800 K and 2000 K.

5.5.1.1. Temperature measurement

A typical plot of the temperature data recorded during an experimental run is given in Figure 5.5 for the 2000 K temperature operating level, pure Ar plasma gas. The points indicated are located as shown in the schematic representation of Figure 5.3(a). Approximately 50 min were necessary to reach steady state at the 1800 K temperature operating level, and approximately 70 min to reach steady state at the 2000 K level.

For modelling purposes, the temperature measured at the point T1 was considered as the gas temperature at the entrance of the tubular reactor. The thermocouple was assembled with its junction inside an alumina protection tube (6.35 x 3.125 mm dia.), approximately 10mm from the tube end. It was considered that the tube end would be in close thermal equilibrium with the gas and thus, by shielding the thermocouple tip from the radiation emanating from the bottom of the crucible, the reading would reflect the true gas temperature. The reading error was evaluated by sucking a small amount of gas through the protection tube, at a flow rate of 0.4 lpm. As shown in Figure 5.6, the temperature change observed was about 4K higher than the reading without gas sucking. All other thermocouples were placed in contact with the tube wall.

Table 5.1 - Typical operating parameters of the transferred-arc plasma and reactive radial gas quenching.

Plasma gas composition	Ar	Ar		Ar/H$_2$	
Plasma gas flow rate (lpm, 298 K)	20	20		18/2	
Temperature T1[1] (K)	1,500	1,800	2,000	1,800	2,000
Temperature T3[1] (K)	1,070	1,270	1,410	1,190	1,330
Arc length (cm)	5	7	7	5	5
Arc voltage (V)	29	30	34	50	55
Arc current (A)	185	275	360	180	250
Arc Power (kW)	5.4	8.3	12.2	9.0	13.8
Quenching:					
Ar (lpm, 298 K)	-	2 to 7			
NH$_3$ (lpm, 298 K)	-	2			
Pressure	100 kPa				

[1] Thermocouples were positioned according to Figure 5.3(a).

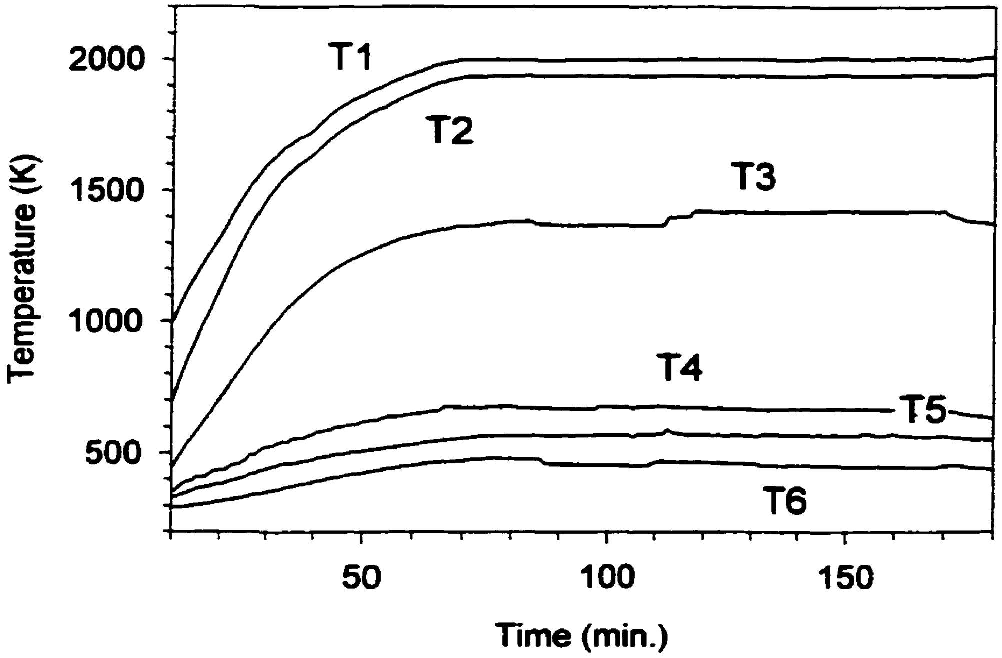

Figure 5.5- Development of temperature in time at several points of the reactor for the 2000 K temperature operating level, pure Ar plasma gas.

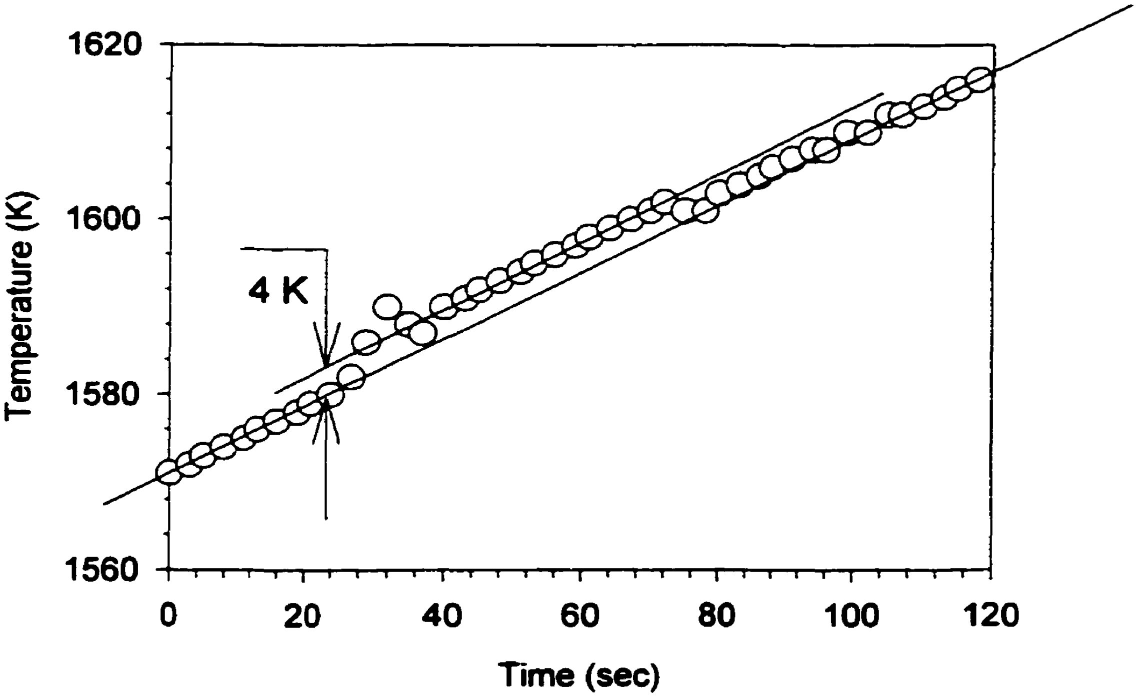

Figure 5.6 - Temperature change upon gas aspiration through the thermocouple (T1) protection tube.

5.5.1.2. Al vapour concentration

The aluminum content in the plasma chamber off-gas, measured using the water cooled gas sampling probe previously described, is shown in Figure 5.7. The Al mole fraction is plotted against the gas temperature measured before the entrance of the tubular reactor (T1), for both pure Ar and Ar/10%vol.H_2 plasma gas compositions. The different values plotted for a same temperature result from experimental scatter.

The amount of Al collected in the probe was converted to Al vapour concentration assuming that no relevant phase transition had occurred upstream the sampling point. It is observed from the data plotted that:

(i) Below 1800 K, the Al concentration measured is above saturation; little change of Al concentration with temperature is observed in this temperature range;

(ii) At higher temperatures (>1800 K), the Al concentration stays under the saturation line; and

(iii) The change in the plasma gas composition has little effect on the Al concentration.

In Figure 5.8, the aluminum concentration which would be calculated based on the total mass of aluminum evaporated, calculated by difference of the mass of the crucible filled with metal before and after the experiment, is plotted as a function of gas temperature (T1). These data represent the estimated concentrations which would be found inside the plasma chamber, before the gas flowing above the metal bath contacts the chamber walls and the cathode nozzle. Those values are about an order of magnitude greater than the actual measured concentrations at the exit of the plasma chamber shown in Figure 5.7, for a same gas temperature.

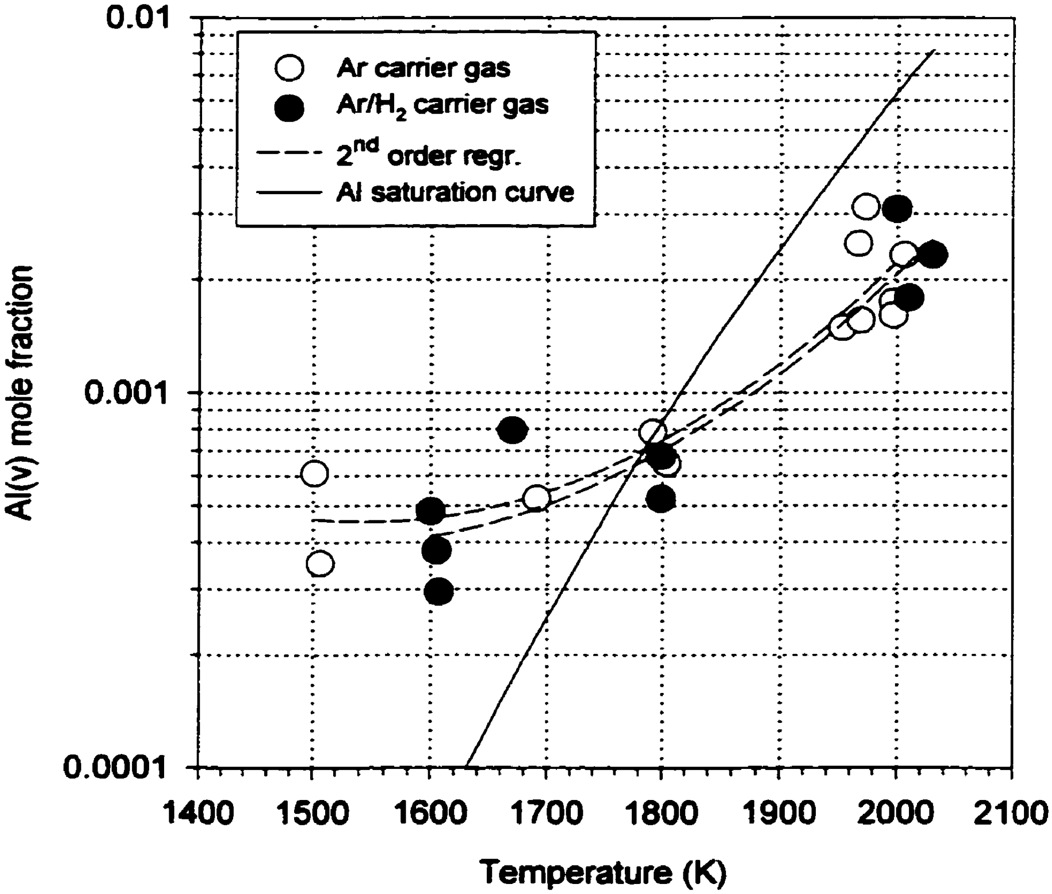

Figure 5.7 - Al vapour mole fraction plotted as a function of carrier gas temperature. Based on gas sampling measurement, for pure Ar and Ar/H_2 gas mixture.

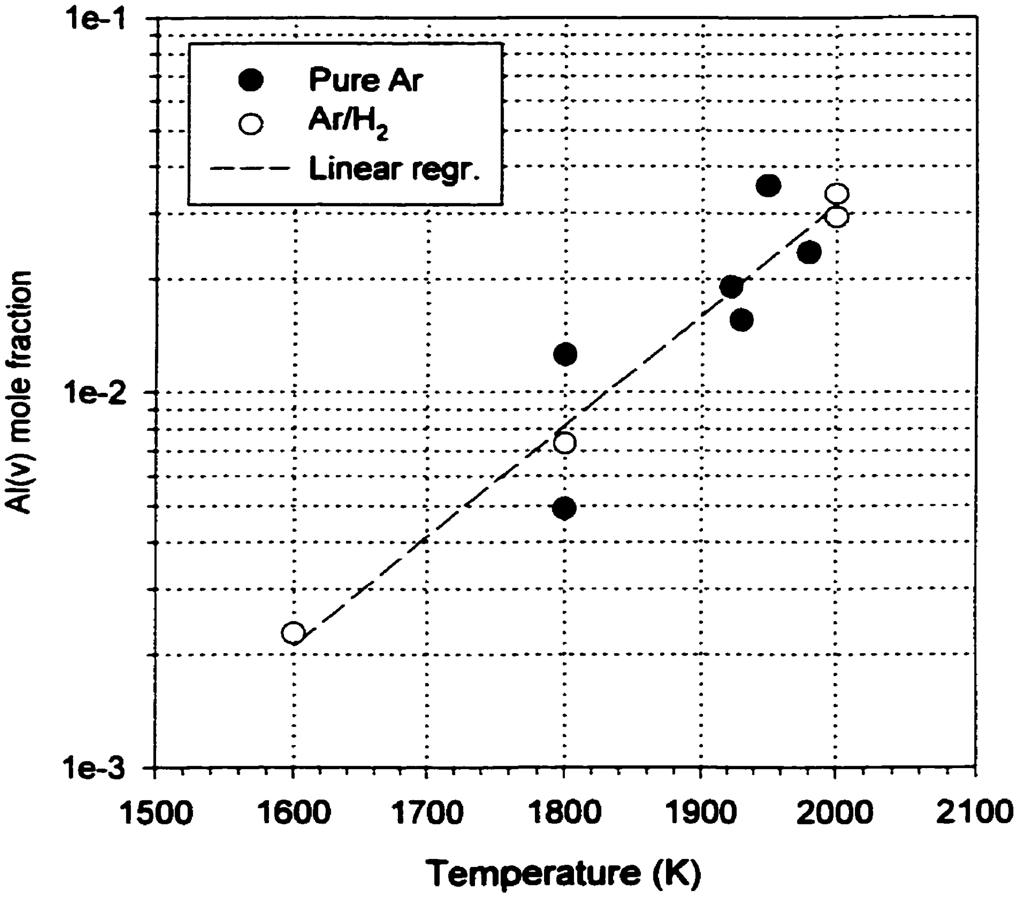

Figure 5.8 - Al vapour mole fraction plotted as a function of the carrier gas temperature. Based on the total aluminum evaporated from the crucible, for pure Ar and Ar/H$_2$ gas mixture.

5.5.1.2.1. Influence of gas temperature

The gas temperature is the result of the combined and interdependent effects of input power, heat losses, gas composition and flow rate. On the other hand, the amount of Al transported into the tubular reactor is the net result of the amount of Al evaporated in the anode minus the Al that condenses within the plasma chamber. Because Al condensation occurs on the water cooled cathode nozzle and on the plasma chamber walls, the Al concentration measurements which are plotted in Figure 5.7 suggest that lower power operation (lower temperature), which results in less recirculation within the plasma chamber, is more efficient for the transportation of the evaporated metal to the reaction zone. In case of a lower recirculation inside the plasma chamber, the contact between the Al vapour and the chamber walls (including the cathode nozzle) is restricted to diffusion transport. However, the production rate of powder at low temperatures is considerably smaller than at high temperature. Very little powder could be collected for analysis in the temperature range below 1800 K.

If the observations (i) and (ii) quoted above can be explained by an enhanced gas recirculation at higher temperature level operation, the observation (iii) seems to be associated to a combination of more complex mechanisms. To interpret the gas composition influenced results, several factors affecting the arc behavior and Al evaporation need to be taken into account. Plasma gas composition, arc dynamics, heat transfer to the metal bath, heat losses, and Al condensation in the plasma chamber are some of them. Their interdependence and effects are discussed next.

5.5.1.2.2. Influence of plasma gas composition

It was originally intended to use different compositions of hydrogen in the plasma gas to modify the arc voltage, gas enthalpy, and thermal conductivity to produce different Al concentrations at the same gas temperature. Experimental measurements demonstrated that in spite of hydrogen compositional changes, the Al concentration could not be significantly varied at the same gas temperature. The reasons are as follows:

a) Influence of plasma gas composition on gas temperature

The gas temperature is the result of the energy balance inside the plasma chamber and the gas enthalpy dictated by the gas composition. As observed from the data given in Table 5.1, Ar/10%H_2 gas mixture requires a higher power input to produce the same T1 than pure Ar plasma gas. The need for a higher energy input results from the H_2 addition, which promotes: (i) a higher gas enthalpy (a higher energy input is required to keep the plasma chamber off-gas temperature unchanged); and (ii) a higher gas thermal conductivity resulting in a higher energy losses through the walls and to the cathode nozzle (again, a higher energy input is required to cope with increased energy losses and keep the plasma chamber off-gas temperature unchanged).

Despite of the amount of thermal insulation used around the plasma chamber, an energy balance shows that almost 90% of the energy input is lost through the hot walls, water cooled cathode nozzle, and anode electrical contacts. Because of this large energy loss, as demonstrated by the power input data for different gas temperatures and plasma gas compositions given in Table 5.1, the gas temperature depends far more on power input than on gas composition.

b) Influence of plasma gas composition on Al evaporation rate

The evaporation rate of Al depends on the energy transfer from the arc to the anode (crucible and Al bath), which occurs in many forms as expressed by the equation:

$$q_a = q_c^I + q_r^I + j_e(\frac{5}{2}\frac{kT_e}{e} + V_a + \phi_a) \tag{5.7}$$

where: q_a is the total heat flux to the anode; q_c^I the convection and conduction heat flux from the plasma gas; q_r^I the radiation heat flux from the arc; j_e the electron flux (current density); T_e the electron temperature; e the electric charge of an electron; V_a the anode voltage fall; and ϕ_a the work function of the anode material. At steady state, this energy gain will be balanced by the heat losses from the anode, the equilibrium expressed as:

$$q_a = q_c^{II} + q_r^{II} + q_v \tag{5.8}$$

where: q_c^{II} is the heat loss to the gas flowing at the bottom of the crucible and to the crucible support by conduction and convection; q_r^{II} the heat loss by radiation from the crucible to the surrounding walls; and q_v the heat loss by evaporation of the metal in the crucible.

Arc current and plasma thermal conductivity can affect the heat transfer to the anode by many different mechanisms. The most pronounced effect of arc current occurs through the electron flux to the anode. It also affects the pumping effect on the surrounding gas exerted by an arc which is changing in cross section (Maecker effect[32]). This induced flow is directed towards the cross section augmentation and is typically present in the cathode region (cathode jet) and in short bell shaped arcs. Because this pumping effect is proportional to the product of the current intensity and current density, ultimately it changes with the square of the current intensity. The thermal conductivity directly affects the conduction heat transfer included in the first term of the right hand side of Equation (5.7). It also affects the induced gas flow above mentioned (Maecker effect) by promoting the constriction of the arc cross section, therefore increasing the current density. In any case, the net result of increase of either arc current and/or gas thermal conductivity is the increase of the heat transfer to the anode.

Radiation energy transfer from the arc to the anode might change with plasma gas composition. Above all, it will be a function of arc temperature and metal vapour content in the arc, since small amounts of metallic vapours substantially increase the radiative losses of a thermal plasma[32]. Increased arc temperature, as caused either by increased arc current or gas thermal conductivity (arc constriction), increases the radiative energy transfer to the anode.

c) Opposed effects of H_2 addition

To conclude, on one hand the addition of hydrogen increases the gas thermal conductivity, which, as discussed above, contributes to more Al evaporation. On the other hand, all the other parameters kept constant, the addition of hydrogen results in a higher arc voltage. Therefore, to achieve a given gas temperature (arc power) using an Ar/H_2 gas mixture, as opposed to pure Ar, requires lower arc current. As a consequence, the enhanced thermal conductivity of the Ar/H_2 mixture, which results in a better energy transfer to the anode and therefore in higher Al evaporation rates, is negated by the lower current required to maintaining the gas temperature level.

5.5.1.3. NH_3 decomposition

N_2 and NH_3 are the gases commonly used as a nitrogen source for the production of AlN powder. The higher reactivity of NH_3 over N_2 is well recognized for this purpose, and its use is preferred for carrying out short term reaction[11],[12],14],[15],[18].

At high temperatures, NH_3 dissociates into N_2 and H_2. For example, at a temperature of 700 K, typically attained at the exit of the tubular reactor, the equilibrium diagram of NH_3 [12] shows a decomposition higher than 99%. On the other hand, the modelling predictions, which were based on available kinetic data for the thermal decomposition of NH_3, showed that decomposition occurred at far lower levels than estimated by an equilibrium based prediction.

The amount of NH_3 present in the gas at the outlet of the reactor was measured using the procedure previously described. The results obtained for both radial and axial injection of NH_3 are shown in Table 5.2. In the axial injection at the top of the reactor, NH_3 was not mixed with quenching gas at its injection point, and had longer residence time at higher temperatures. For a same operating temperature level, the axial injection condition (compared with the radial injection) resulted in a greater decomposition of ammonia. Also, in the axial injection mode, it is observed that the higher the temperature, the greater the extent of ammonia decomposition.

5.5.2. Powder characterization

The powder composition was analyzed for AlN and free Al phases by XRD, for nitrogen content by wet chemical analysis (micro-Kjeldahl), and for oxygen by high temperature decomposition (LECO). Surface analysis was also carried out using FTIR and XPS analysis techniques. Particle size was evaluated by BET analysis and TEM. Particle morphology was analyzed using TEM.

For analysis, the powders produced were divided into two groups: (i) the white powder produced by axial injection of NH_3 upstream the quenching zone , whose XRD analysis exhibited only AlN peaks; and (ii) the powders with a colour ranging from light to dark gray, produced by radial injection of NH_3 at the quenching zone, whose XRD analysis exhibited AlN and Al peaks. The photograph of Figure 5.9 shows the white powder produced with the axial injection of NH_3. For illustration, one gray powder is also shown in this figure.

5.5.2.1. Powder composition

The typical XRD patterns of these two types of powders are shown in Figure 5.10. The diagram of the Al powder produced under non nitriding atmosphere [Figure 5.10(a)] is also included in this figure. The diffraction pattern characteristic of the gray powder is shown in Figure 5.10(b). The presence of both AlN and Al peaks are observed. The diffraction pattern of the white powder, shown in Figure 5.10(c), exhibits only hexagonal AlN peaks.

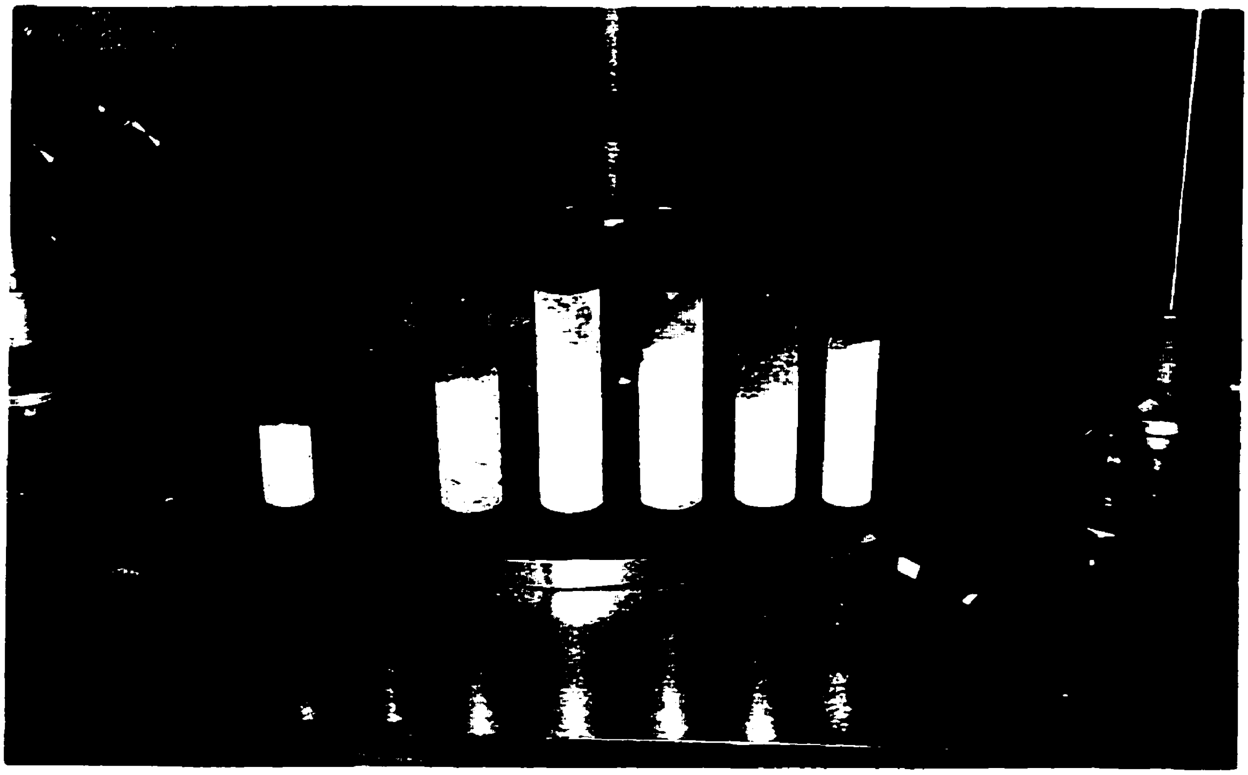

Figure 5.9 - White and grey AlN powder produced.

The results of the elemental analysis of Al, N, and O in the white powder are shown in Table 5.3. Although the powder is produced in a reducing oxygen-free atmosphere (Ar gas flowing stream and graphite crucible and walls), high levels of oxygen were found in all the powders analyzed. Such high contents were also observed in the previous works on plasma synthesis of AlN[12],[19],[20],[21]. Given that in these cases the powders were also produced in a similar oxygen-free atmosphere (limited to oxygen contamination from input gases and Al precursor), most of the authors concluded that large oxygen pickup occurs as the powder is handled in atmospheric air. The large scatter of the difference indicated in the last column of Table 5.3 is possibly the result of error accumulation and also contamination by C as detected in the XPS analysis discussed further on.

Table 5.2 - Ammonia concentration measured at the bottom of the reactor (exhaust line).

NH_3	Exp. nr.	Carrier gas	T(K)	NH_3 (lpm)	Quenching gas (lpm)		%NH3
		Ar			Ar	N_2	
Rad. inj.	26a	20	1957	2	5	-	43.7
Rad. inj.	26b	20	1953	2	7	-	50.5
Axial inj.	29a	25	1809	2	-	6	49.7
Axial inj.	29b	25	1955	3	-	6	21.4
Axial inj.	30	25	1853	2	-	6	45.1

Table 5.3 - Elemental analysis of the white powder produced by axial injection of NH_3.

Exp.	SSA(m2/g)	%N(1)	%Al(2)	%O(3)	Difference(4)
28.5	38.5	23.8	70.7	5.8	(−0.4)
21.3	46.5	23.5	63.4	6.3	6.7
32.4	69.4	25.4	69.3	10.4	(−5.2)
33.1	85.2	20.4	61.6	8.8	9.2
33.4	90.2	24.4	65.0	9.1	1.6
33.2	98.1	22.0	52.8	9.6	15.7
33.3	107.4	21.9	64.0	11.2	2.9
30.5	129.8	23.0	62.9	10.1	4.1
31.1	140.0	19.9	62.8	9.5	7.8
30.1	205.6	16.2	60.3	10.8	12.7

[1] Micro-Kejldahl.

[2] Atomic absorption.

[3] High temperature decomposition (LECO).

[4] Mass difference.

Table 5.4 - Chemical composition at the surface of the powder produced in experiment nr. 33.3, determined by XPS analysis.

Element	%At.	Comp.	%wt
Al	41.7	AlN	53.5
N	26.0	Al_2O_3	40.2
O	27.4	CO_2	4.4
C	5.0	C	1.9

The N, Al and O compositions are plotted as a function of the respective powder SSA in Figures 5.11 and 5.12. It is observed in Figure 5.11 that both Al and N content slightly decrease with increasing SSA. The plots of Figure 5.12 show the oxygen results obtained by high temperature decomposition analysis [LECO, graph (a)] and the oxygen content calculated as the difference from the nitrogen and aluminum analysis [graph (b)]. The dotted lines about the regression curves indicate the 95% confidence interval. Although a large amount of scatter is observed, the oxygen determined by mass difference shows a good agreement with the direct measurement (LECO) at lower SSA. Overall, it is observed that the oxygen content rises with SSA. Similar trends were also observed by Baba et al.[21] for AlN ultrafine powders and by Dransfield[9] for ultrafine titanium nitride powders produced in a plasma reactor. These results suggest that the oxygen is on the particle surface. The larger the SSA the higher is the reactivity of the powder.

The nature of the species present on the surface of the powder particles was analyzed using FTIR. A typical analysis result for the ultrafine AlN powder produced is shown in Figure 5.13(a). Analogous results were obtained by Moura[12] and Baba et al.[21]. Following the same procedure, three other powders were also analyzed for comparison: a commercial AlN powder, XUS 35548.00 (Dow Chemical); a high purity 0.3 μm polishing grade alumina (Al_2O_3); and high purity aluminum hydroxide ($Al(OH)_3$). Their respective FTIR spectra are shown in Figure 5.13 (c), (d), and (e). The curve shown in Figure 5.13(b) was obtained by the superimposition of the transmittances of the reference powders. The commercial AlN powder had a BET surface area of 2.8 m^2/g, and an oxygen content of 0.7 %wt. The great similarity observed between the experimental AlN powder and the combined profile (b) reflects the type of species found on its surface. The large absorption peak at approximately 650 cm^{-1} is characteristic of the AlN bond. Compared with the commercial AlN powder, the major difference appears to be the broad absorption peak around 3500 cm^{-1} which is found in the experimental AlN powder. This peak, characteristic of the $Al(OH)_3$ powder, is caused by OH bonds [21]. The H_2O peak, which occurs in the $Al(OH)_3$ diagram at about 1600 cm^{-1} [21], also occurs in the experimental AlN but at a much lower intensity, indicating that a small amount of H_2O might be absorbed on the surface of this powder.

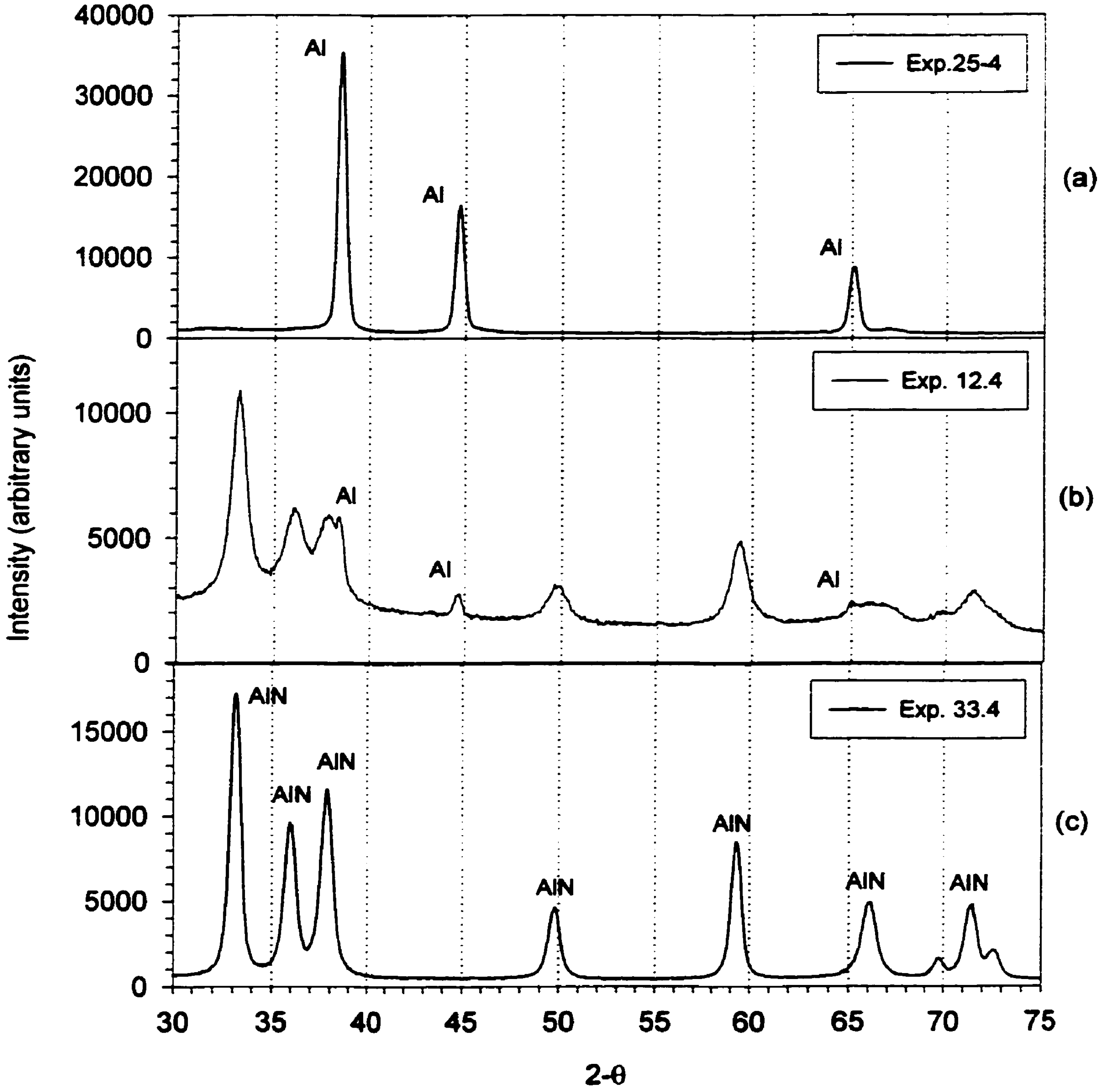

Figure 5.10 - Typical x-ray diffraction patterns of powders produced: (a) Al; (b) not fully converted AlN; and (c) AlN.

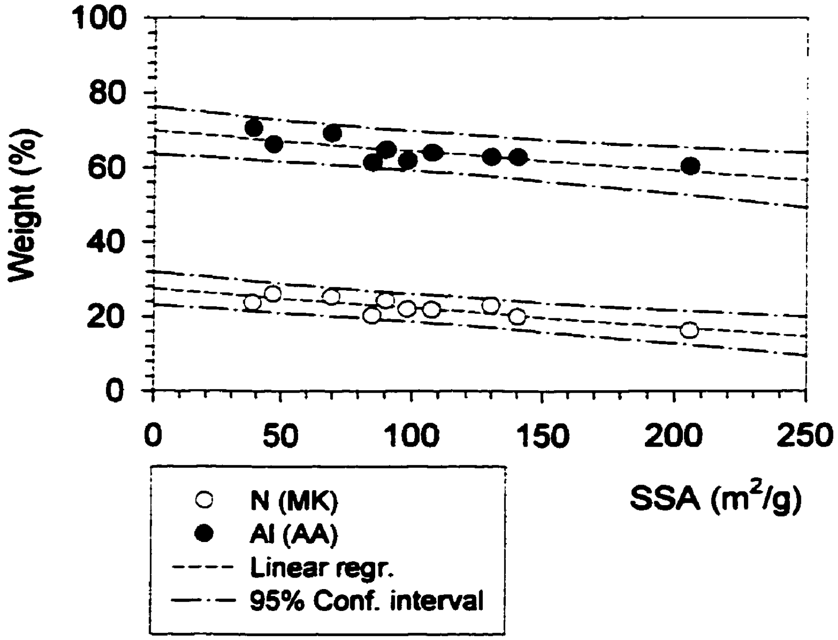

Figure 5.11 - N and Al contents plotted as a function of the powder specific surface area; MK=micro-Kejldahl, and AA=atomic absorption analysis.

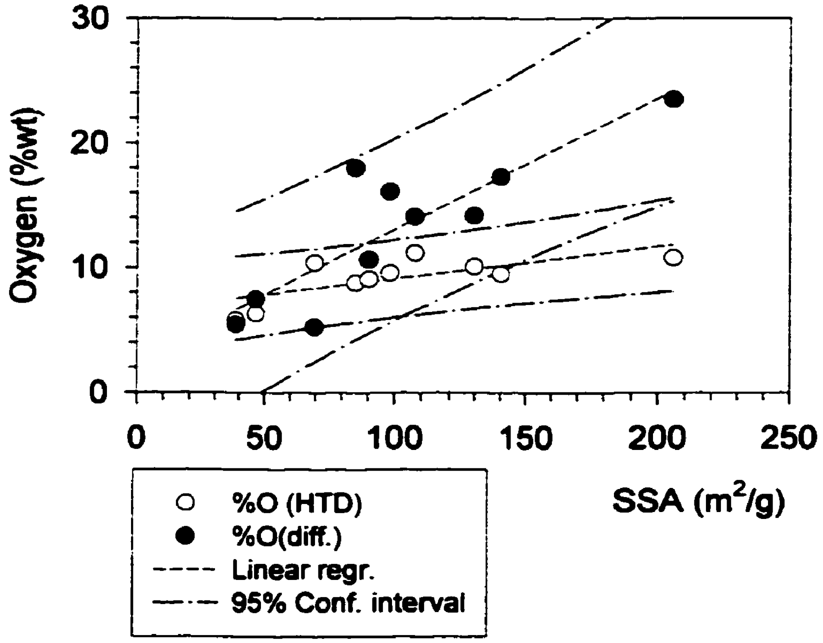

Figure 5.12 - Oxygen content plotted as a function of the powder specific surface area, determined by high temperature decomposition analysis (HTD), and as the difference from micro-Kejldahl and atomic absorption analysis.

The surface analysis of the white AlN powder was also carried out using the XPS technique. The graph of Figure 5.14 shows the peaks of Al, N, and O, and also the presence of C either in the form of C-C bond (or in solution) or in the form of adsorbed CO_2. The peak on the far left is the oxygen Auger peak. The XPS analysis cannot detect H. Also, given the closeness of Al-O and Al-OH oxygen electrons binding energies, and also to the fact that the specimen was charged (peaks displacement), these two O forms could not be differentiated. The atomic percentage of the elements found on the surface is shown in Table 5.4. Carbon contamination is thought to be partly due to the erosion of the graphite crucible, and partly due to CO_2 adsorption as the powder becomes exposed to atmospheric air. The correlation between the area under the C peaks gives 36% C in the CO_2 form and 64% in the form of dissolved C. From these results, if oxygen is assumed to be present in the form of oxide, the following stoichiometric composition is found for the surface of the particles: $Al_{4.82}N_3O_{3.17}C_{0.58}$ or $3AlN \cdot 0.907Al_2O_3 \cdot 0.222CO_2 \cdot C_{0.356}$. The correlation between the area under the C peaks of Figure 5.14 gives 36 % of the C in the CO_2 form and 64% in the form of dissolved or bonded C (the exact nature of the C bond could not be determined). These results give a total of 1.9 % C in the powder.

The possible reasons why XRD analysis does not dectect any oxygen compound related crystalline phase are that either the surface layer is too thin to be detected, or it does not have any ordered arrangement. Based on the total oxygen analysis of the powder and assuming the oxygen to be on the surface of the particle as a compact aluminum oxide film, the thickness of this film can be estimated to be of the order of 1 nm (corresponding at about two Al_2O_3 layers).

The nitrogen content of the powder produced by radial injection of NH_3 (second group) was also determined using the micro-Kejldahl method. The values found are given in Table 5.5. The amount of AlN, calculated based on the nitrogen content, is plotted in Figure 5.15 as a function of the quenching intensity. This figure shows four different operating conditions defined by combinations of the plasma gas composition and temperature. The data which are duplicated in Table 5.5 were plotted as average values. The quenching intensity was caracterized by the Ar flow rate radially injected mixed with a constant flow rate of NH_3 of 2 lpm. The SSA of each powder analyzed (also included in Table 5.5) is shown in this figure but will be discussed in another section. In all cases, it is observed that the more intense the radial jet, the higher is the AlN content in the powder. These results suggest that the increase of the AlN content of particles is caused by increased mixing of reagent: a greater Ar flow rate causes the increase of NH_3 concentration towards the tube centreline.

It should be noted that, due to oxidation the amount of AlN found is lower than the amount which could be found if powder had been handled in an oxygen free atmosphere. Using the oxygen analysis results of the first group of powders (assumed proportional to the SSA), the amount of oxygen and oxide composition were estimated assuming the oxygen content to be proportional to the SSA. The oxygen (and aluminum oxide) thus calculated is indicated in Table 5.5.

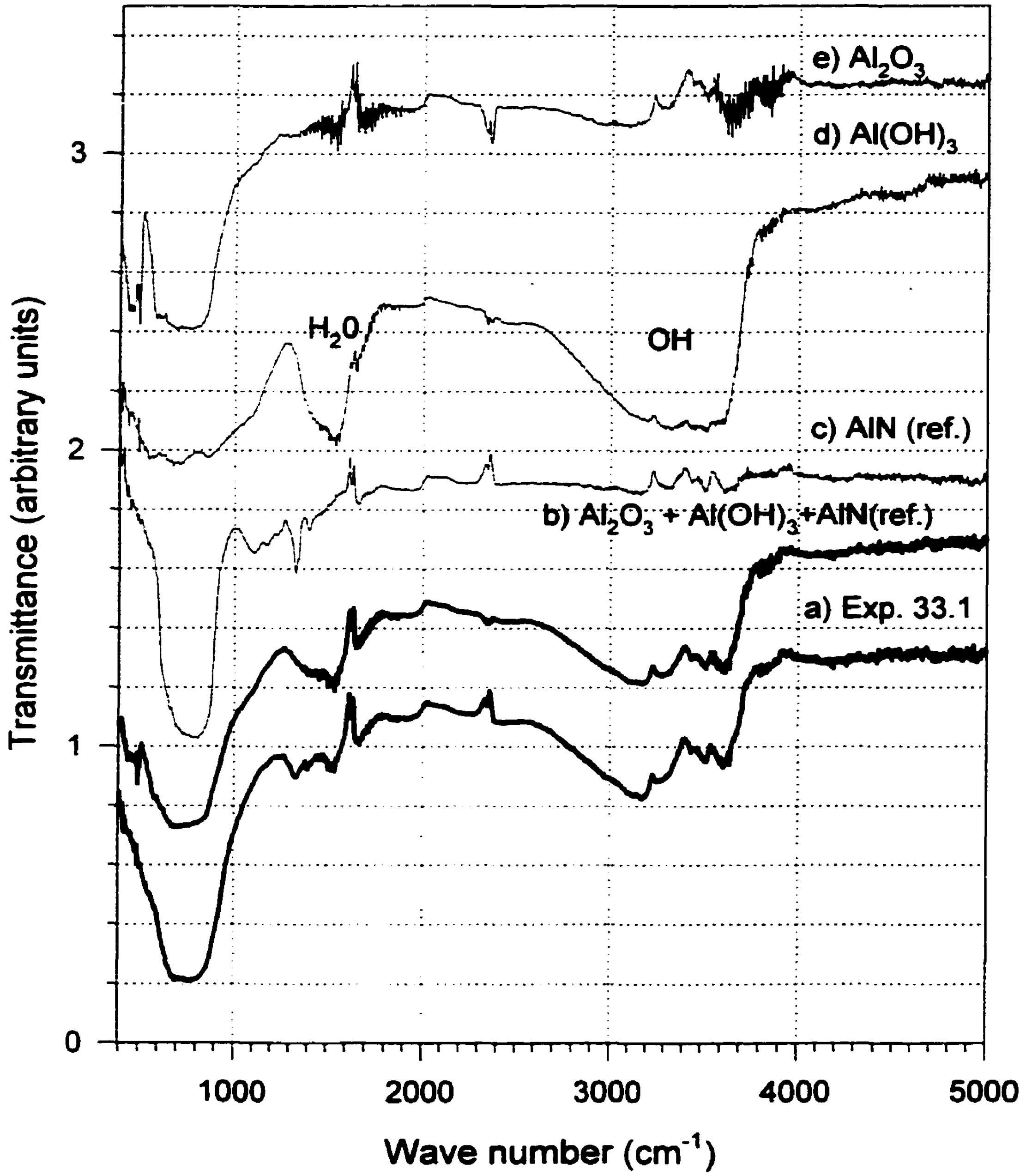

Figure 5.13 - FTIR spectra of powder samples. Diagram (b) obtained as the combination of (c), (d), and (e).

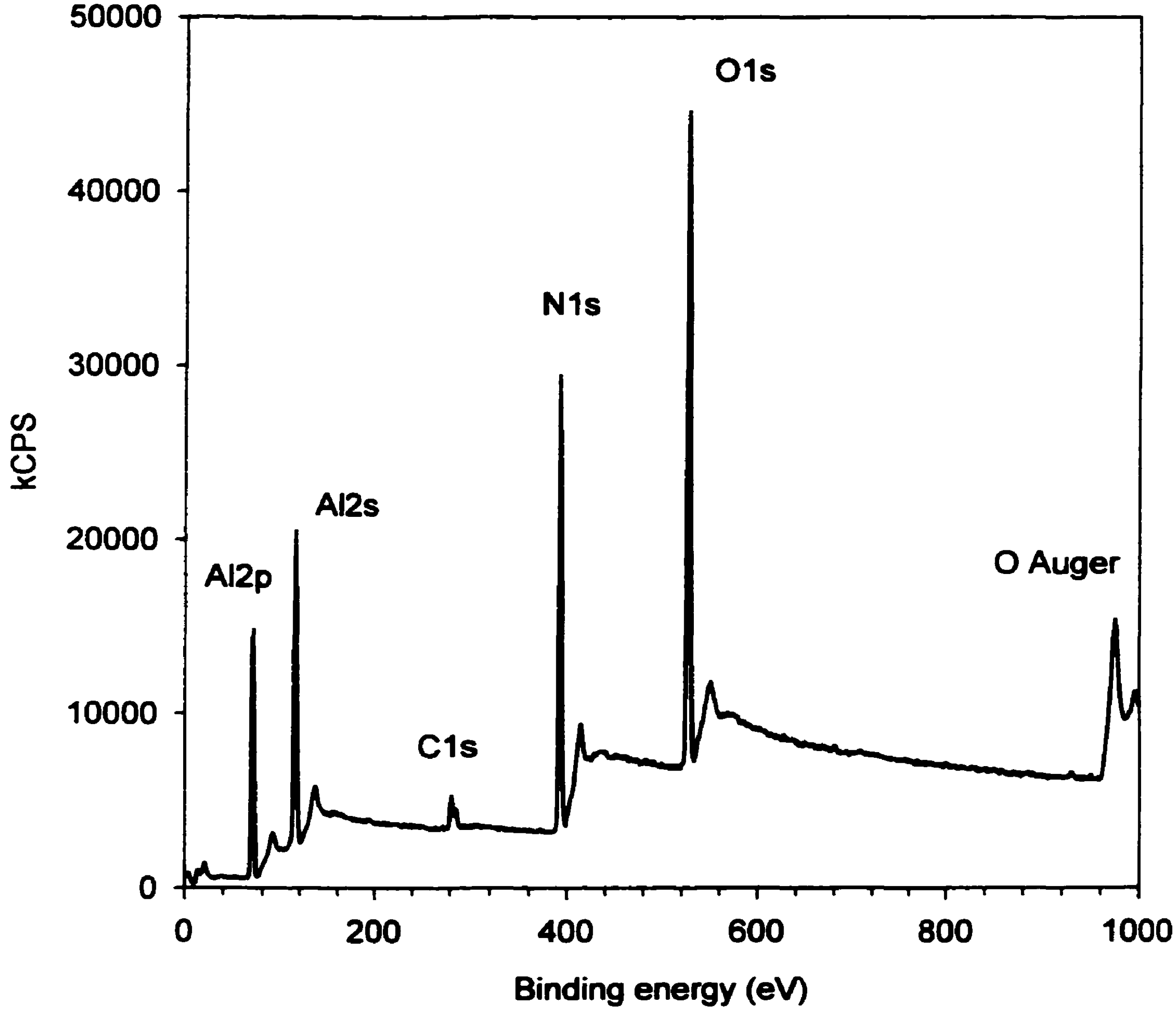

Figure 5.14 - XPS survey of AlN powder produced with the axial injection of NH_3 upstream the radial quenching point.

Table 5.5 - Specific surface area and elemental analysis of the powder produced by radial injection of NH_3. Q_{Ar} = flow rate of radially injected Ar; NH_3 = 2 lpm.

Plasma gas: Ar/H_2 (18/2 lpm) - T1 = 1800 K							
Exp.	Q_{Ar}(lpm)	SSA(m^2/g)	%N (1)	%O (2)	%Al (5)	%AlN (3)	%Al_2O_3 (4)
15/1.1	2	111.6	10.4	9.4	49.5	30.4	20.1
15/1.2	3	126.7	-	-	-	-	-
12/1	8	176.4	15.1	11.1	32.1	44.2	23.7
12/4	5	165.4	12.9	10.9	39.3	37.7	23.1
12/2	8	176.8	13.6	11.2	36.4	39.9	23.7
Plasma gas: Ar/H_2 (18/2 lpm) - T1 = 2000 K							
Exp.	Q_{Ar}(lpm)	SSA(m^2/g)	%N (1)	%O (2)	%Al (5)	%AlN (3)	%Al_2O_3 (4)
15/4.1	3	38.8	6.8	7.6	64.0	19.9	16.1
19/3.2	4	96.5	8.2	9.1	56.8	24	19.3
10/	5	93.5	15.4	9.0	35.8	45.1	19.1
19/3.3	6	125.5	15.4	9.8	34.0	45.1	20.9
11/3	7	157.2	15.3	10.6	32.5	44.9	22.6
Plasma gas: Ar (20 lpm) - T1 = 1800 K							
Exp.	Q_{Ar}(lpm)	SSA(m^2/g)	%N (1)	%O (2)	%Al (5)	%AlN (3)	%Al_2O_3 (4)
16/4	2	267.4	7.5	13.5	49.3	22.0	28.7
17/4.1	2	254.7	6.2	13.2	53.8	18.2	28.0
17/4.2	3	233.8	13.7	12.6	33.1	40.0	26.8
17/4.3	4	218.3	13.6	12.2	34.2	39.8	26.0
Plasma gas: Ar (20 lpm) - T1 = 2000 K							
Exp.	Q_{Ar}(lpm)	SSA(m^2/g)	%N (1)	%O (2)	%Al (5)	%AlN (3)	%Al_2O_3 (4)
18/6.2	2	242.3	16	12.9	25.9	46.8	27.3
26/7	2	233.7	17.4	12.6	22.2	51.0	26.8
13/5	3	206.9	13.1	11.9	36.4	38.2	25.4
26/1	3	238.1	14.5	12.7	30.6	42.3	27.1
13/6	4	196.5	15.0	11.7	31.2	44.0	24.8
18/6.3	4	194.7	19.2	11.6	19.2	56.1	24.7
18/6.4	5	191.6	17.8	11.5	23.3	52.2	24.5
26/2	5	200.9	15.4	11.8	29.9	45.0	25.0
18/6.1	7	177.5	16.9	11.2	26.9	49.4	23.7
26/3	7	170.8	13.9	11.0	36.0	40.7	23.4
Plasma gas: Ar (20 lpm) - T1 = 2000 K - Pure Al powder production experiments							
Exp.	14/5	26/5	25/2	25/3	25/4		
Q_{Ar}(lpm)(7)	4	4	5	7	9		
SSA(m^2/g)	16.9	31.9	28.6	29.6	28.4		

[1] Determined by micro-Kejldahl analysis.

[2] Estimated assuming O content proportional to SSA.

[3] Assuming all the N is bond to Al.

[4] Assuming all the O to be in the for of Al_2O_3.

[5] Determined by mass difference.

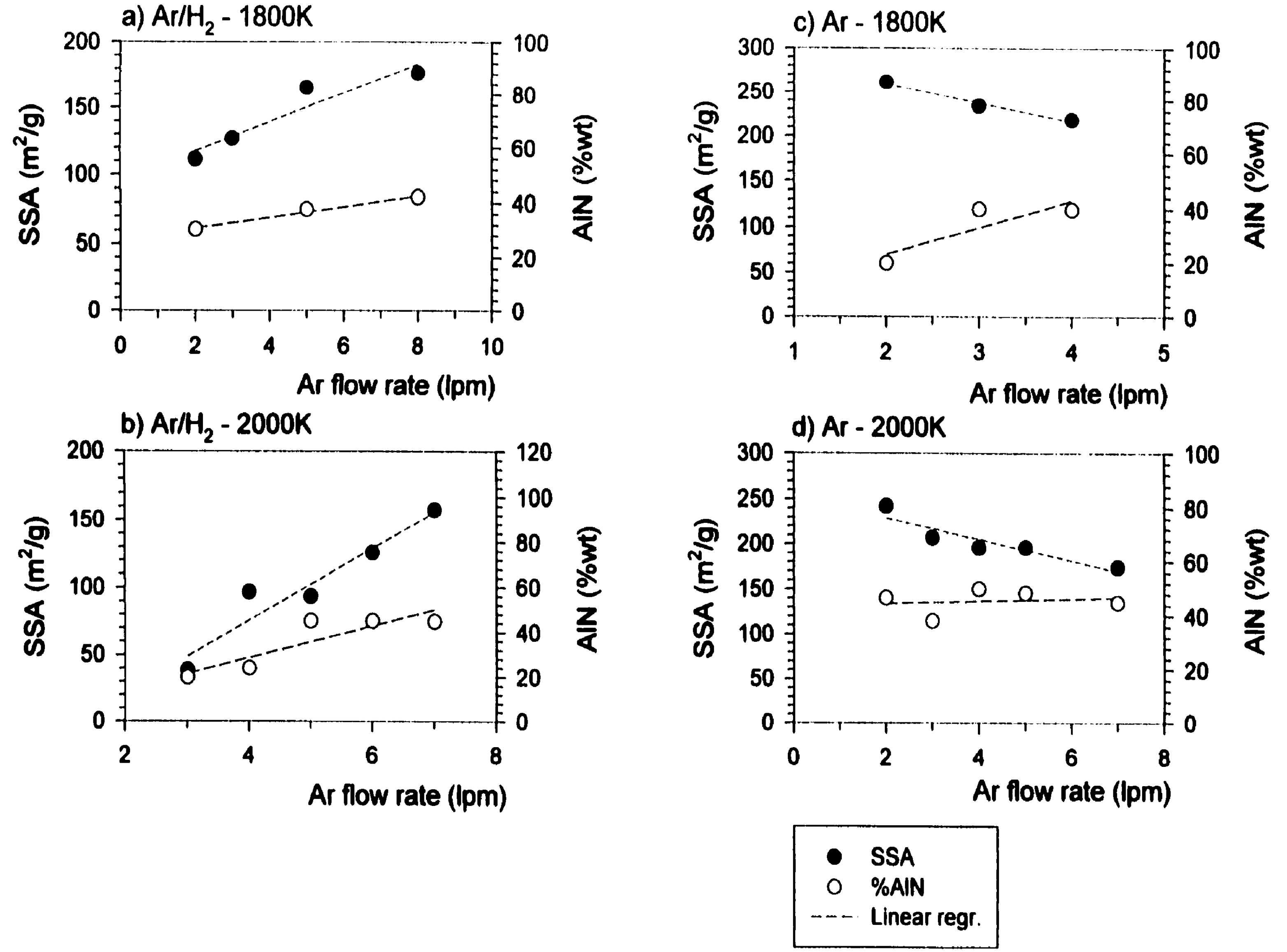

Figure 5.15 - Specific surface area and AlN content in the powder [group (ii)] as a function of the radial jet intensity (NH_3 flow rate of 2 lpm).

5.5.2.2. Particle size and morphology

Ultrafine particles were synthesized at different operating conditions with respect to carrier gas composition and temperature, using two different gas mixing geometries: radial nitriding/quenching jets of different intensities, and axial injection of NH_3 upstream the radial quenching point. In case of the radial injection of NH_3, depending on the composition of the plasma gas, two different trends were exhibited for the change of the specific surface area (SSA) with different intensities of the quenching jet. The results of SSA are included in Table 5.5, and are shown in the graphs of Figure 5.15.

Figure 5.15 (a) and 5.15 (b) show the effect of radial quenching intensity on the SSA of powders produced when a Ar/10% H_2 plasma gas mixture was used, at temperatures of 1800 K and 2000 K at the exit of the plasma chamber, respectively. In this case, at both temperature levels, an increase of the quenching intensity produced powders of greater SSA (smaller particle diameter).

However, under similar operating conditions, the experiments using pure Ar plasma gas resulted in a different trend. As shown in Figures 5.15(c) and 5.15(d), in this case, the increase of the quenching intensity produced powders of smaller SSA (greater particle diameter). In both Ar/H_2 and pure Ar carrier gases, the lower gas temperature resulted in smaller particle sizes (larger SSA).

A set of experiments was also conducted in order to evaluate the influence of chemical reaction on the particle size. This involved the production of powder in reacting and non-reacting atmospheres, under a broad range of cooling conditions. Except for NH_3 injection, all operating conditions were kept about the same. The results of these experiments are shown in Figure 5.16. It is observed that the specific surface area (SSA) of pure aluminum powders produced under inert atmosphere is far smaller than the SSA of the powders produced under the nitriding atmosphere. It is also observed that the quenching intensity produced little effect on the SSA of the Al powder.

The trend observed in the Ar/H_2 gas mixture is in agreement with the experimental[18] and modelling data previously reported in the literature[33],[34],[35]. Based on the homogeneous nucleation theory, this tendency is explained as being the result of greater supersaturation of the condensing species caused by the stronger quenching. Because under stronger cooling the supersaturation increases, a larger number of smaller size particles nucleate, resulting in a powder with greater SSA. However, this explanation does not fit the pure Ar carrier gas results. Based on the results shown in Figure 5.16 (Al vs. AlN experiments, using pure Ar plasma gas), two concurrent factors were considered as the possible cause for these results:

i. <u>Surface-reaction enhanced homogeneous nucleation</u>: if surface reaction occurs in the early stage of nucleation on the surface of subcritical nuclei, it might increase the nucleation rate by turning otherwise unstable clusters into stable particles.

ii. <u>Reduced particle coagulation under nitriding conditions</u>: pure aluminum particles which form in the absence of ammonia, and at temperatures higher than some minimum value, are in the form of spherical droplets which can coalesce upon collision with other particles. Under nitriding conditions, particles with a high content of AlN tend to be solid and therefore, although they may form agglomerates, they do not fuse together.

Using numerical modelling, the first hypothesis lead to the development of a new formulation of the nucleation rate equation which considers the effect of surface reaction in the initial stage of particle formation.

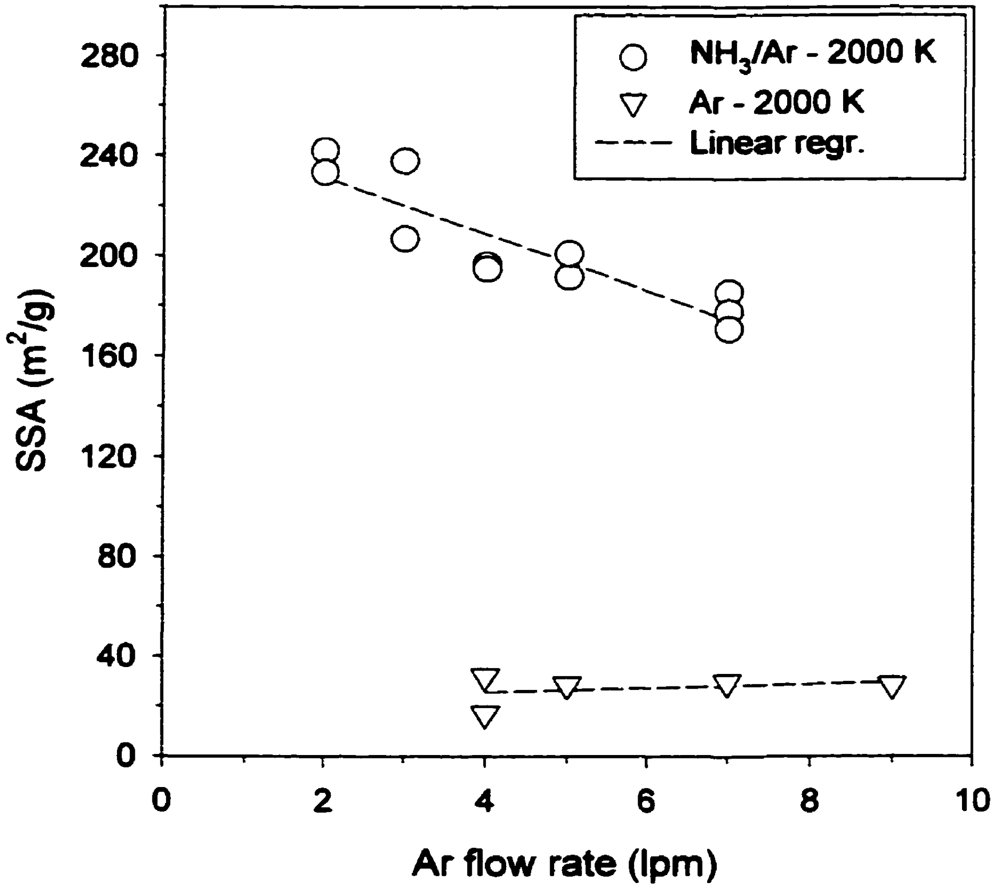

Figure 5.16 - Comparison of the specific surface area vs. quenching intensity plots of powders produced under nitriding and pure Ar quenching jets.

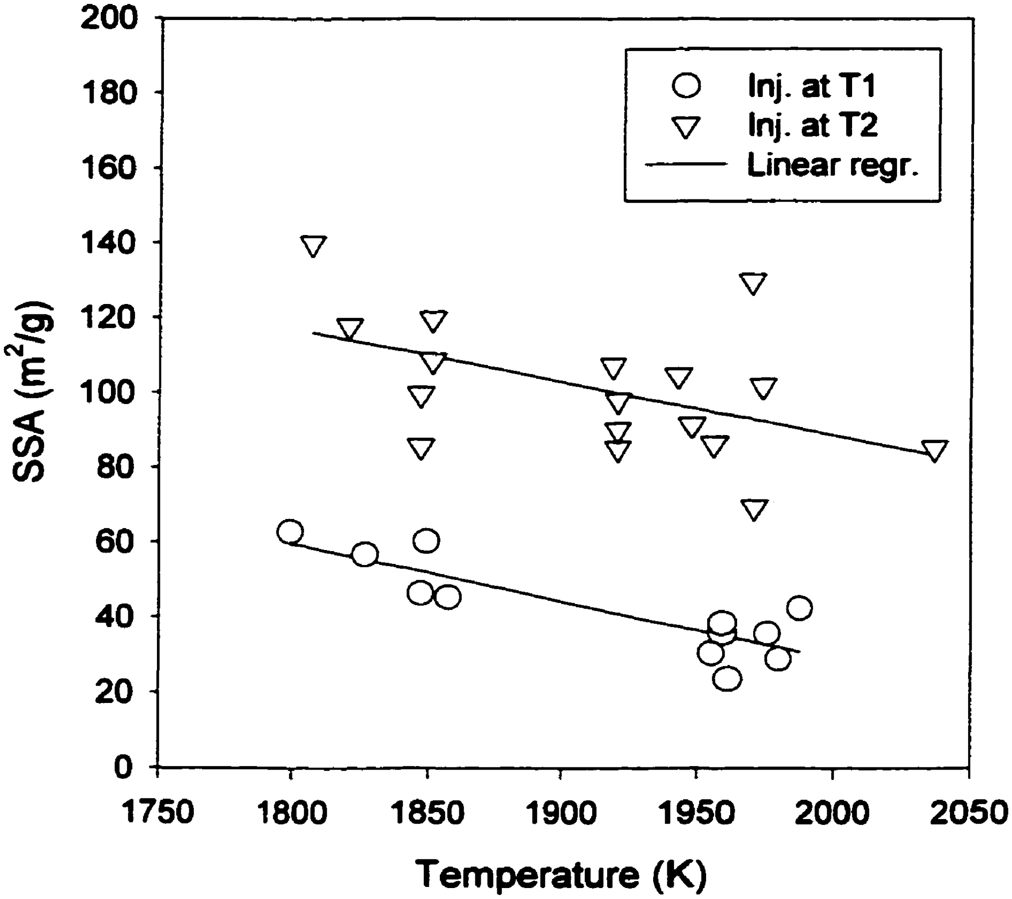

Figure 5.17 - Specific surface area as a function of plasma chamber off-gas temperature at T1, for axial injection of NH_3 at different feeding positions upstream of the quenching jet.

Because none of the experiments using radial injection of NH_3 succeeded in producing fully converted AlN powders, the ammonia injection was modified following the results of the modelling study. The simulation of the radial injection of NH_3 showed that the particles which form near the wall carry a high content of non-reacted Al. On the other hand, the simulation of the injection of NH_3 in the centreline upstream of the radial quenching predicted full convertion of Al at both temperature levels (1800 and 2000 K). These results will be discussed in more detail in the modelling chapter.

The modification introduced is indicated in the reactor layout shown in Figure 5.3(b). Injection at two different points was studied in individual experiments: (i) injection at the entrance of the tubular reactor; and (ii) at an upper point, about 40 mm above the entrance of the tubular reactor. The SSA results of these experiments are shown in Figure 5.17. In all cases, a 100% AlN powder was produced, identified by XRD analysis. Although the graph shows a large scatter of data, as in the radial injection experiments it is observed that in both injection positions a higher carrier gas temperature tends to produce a powder of larger particle size (smaller SSA).

The injection of NH_3 in the uppermost point resulted in larger particles for a same gas temperature. This is seen to result from a longer residence time of formed particles in a high temperature region. The uppermost point is located at the connical chamber before the entrace of the tube (see Figure 5.3), where a considerably high gas recirculation occurs.

Figure 5.18 shows the TEM micrographs typical of powders produced with the radial injection of NH_3. The flow rate conditions at which the powders shown in this figure were produced are: 2 lpm of NH_3; 2 lpm of quenching Ar; and 20 lpm of plasma gas. In both case, the plasma chamber off-gas temperature measured by the thermocouple located at T1 (Figure 5.3(a)) was approximately 1800 K. The micrograph shown in Figure 5.18(a) corresponds to a Ar/10%vol.H_2 carrier gas. The visual inspection of this figure shows that most of the particles are in a range of 15 to 20 nm. For this powder, the SSA = 111.6 m^2/g measured corresponds to an approximate average BET surface area particle diameter of 18.0 nm. Figure 5.18(b) corresponds to pure Ar carrier gas. The range of particle size inferred from the visual analysis of this figure is

5-10 nm. The corresponding SSA = 254.7 m^2/g results in an average particle diameter of 7.9 nm. In both cases, a 50% free Al content in the powder was assumed for the calculation of the BET average diameter. If the powder were considered as fully converted, these figures would be approximately 8 % smaller.

A typical micrograph of the powder produced with the axial injection of NH_3 upstream the radial quenching jet is shown in Figure 5.19. The specific powder shown had SSA = 37.1 m^2/g, corresponding to an average SSA diameter of 49.6 nm. Most of the particles observed are in the 20-100 nm range.

Figure 5.20 shows a typical micrograph of the Al powder produced in the absence of nitriding agent. Two types of particles can be observed: (i) spherical and dense particles; and (ii) large agglomerates of very small particles. The size of the first type of particles observed in this figure is in a broad range, from 100 to 700 nm, approximately. The BET surface area of the Al powder produced is in the range 16.9 - 31.9 m^2/g (Table 5.5), which corresponds to an average surface area particle diameter in the range of 70-130 nm, approximately. These average diameters seem to be largely influenced by the agglomerates of small particles. These agglomerates were possibly formed by collision of liquid or partially melted particles still in the quenching zone of the reactor, rather than formed by agglomeration during the TEM sample preparation. This type of powder was also observed by SEM, JEOL JSM 840A (Figure 5.21). As in the previous TEM micrographs (Figure 5.19), this figure shows a broad range of particle sizes. The particles observed have a spherical or near spherical morphology.

5.6. Conclusions

An experimental study of the vapour phase synthesis of ultrafine AlN particles using thermal plasma was carried out. AlN ultrafine powders were produced using a transferred-arc two-stage reactor: aluminum was evaporated by the transferred-arc in non nitriding conditions and reacted with ammonia in a separate tubular reactor. A new version of this reactor concept was built in which the transferred-arc chamber and tubular reactor were vertically aligned. This

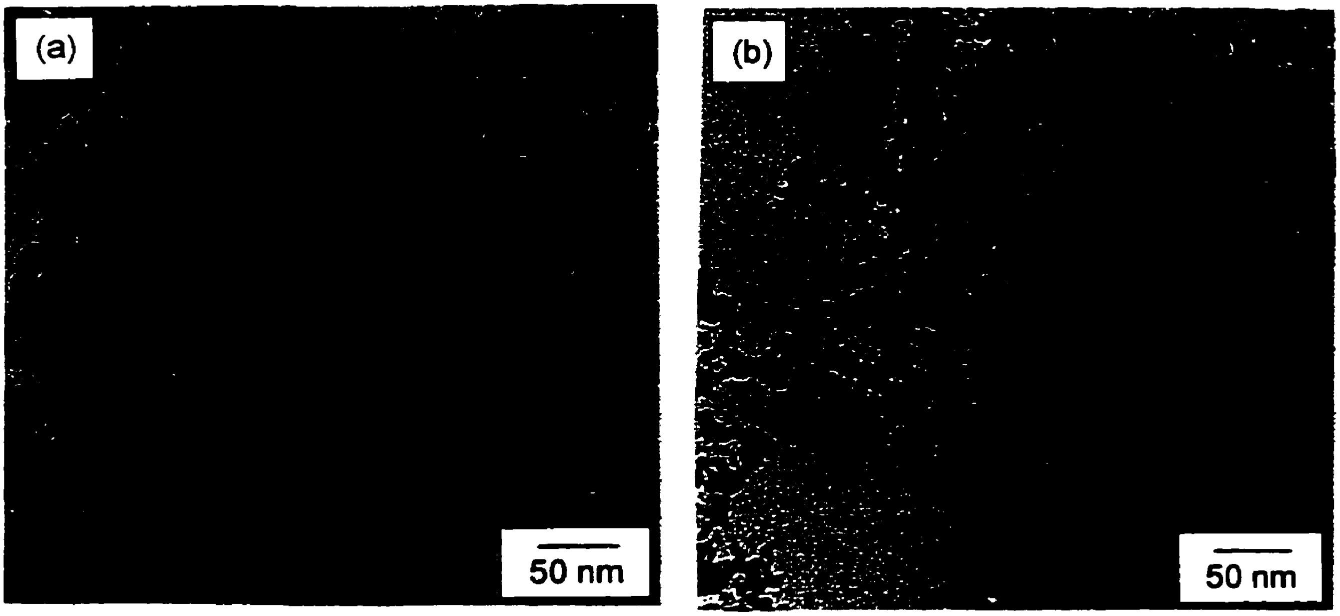

Figure 5.18 - TEM micrographs of powder produced with the radial injection of NH_3: a) Exp. 15/1.1, T1 = 1800 K, Ar/10%vol.H_2 plasma gas, SSA=111.6 m^2/g, average SSA particle diameter d_{BET} = 18.0 nm ; (b) Exp. 17/4.1, T1 = 1800 K, pure Ar plasma gas, SSA = 254.7 m^2/g, average SSA particle diameter d_{BET} = 7.9 nm. Magnification: x200K.

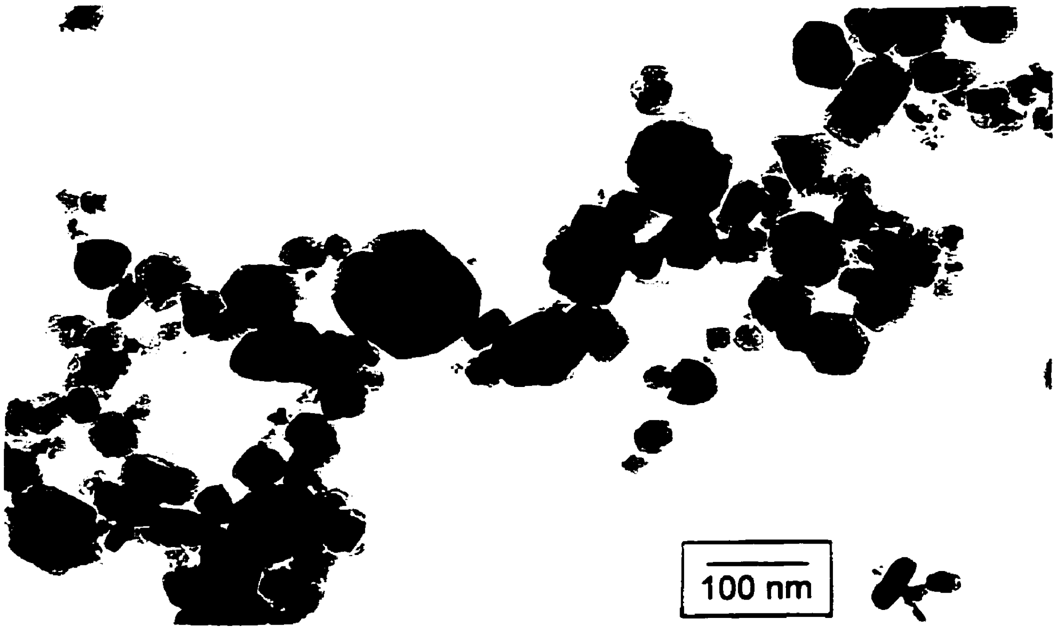

Figure 5.19 - Typical TEM micrograph of the ALN powder produced with the axial injection of NH_3. Exp. 29.5, SSA = 37.1 m^2/g, average SSA particle diameter d_{BET} = 49.6 nm. Magnification: x130K.

Figure 5.20 - TEM micrograph of the Al powder produced in non-nitriding condition. Magnification: x55K.

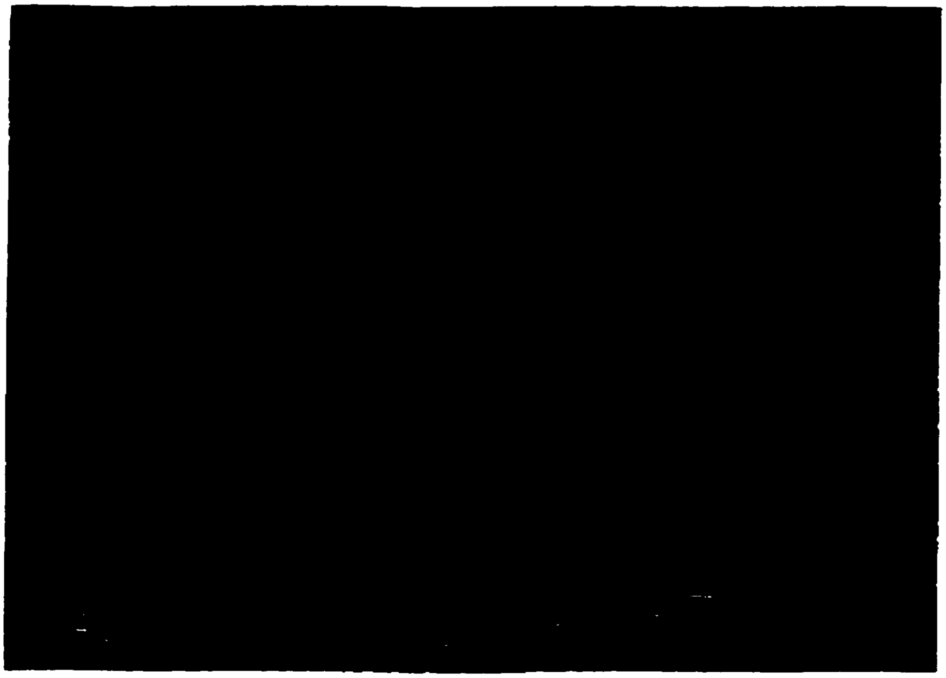

Figure 5.21 - SEM micrograph of the Al powder produced in non-nitriding condition.

reactor design allowed the study of both radial and axial mixing of NH_3 with plasma chamber off-gas. The main results observed are as follows:

Aluminum vapour concentration:

The concentration of Al vapour in the plasma chamber off-gas was measured using a gas suction probe. However, because gas temperature and gas composition could not be separated, the effect of concentration alone could not be carried out experimentally.

At 1800 K, the concentrations were of the same order of magnitude as the equilibrium concentrations. At 2000 K, the measured concentrations were lower than equilibrium. At temperatures lower than 1800 K, concentrations higher than equilibrium were observed. However, the production rate was small and little powder could be collected in the metal filter in the temperature range below 1800 K.

Radial injection of NH_3:

The first part of the work involved experiments with the radial injection of a NH_3/Ar mixture. Quenching intensity was changed by injecting different amounts of Ar with a constant amount of NH_3. The dependence of the particle size and composition on the reactor operating conditions (gas composition and temperature, and quenching intensity) was investigated. Powders were produced under different quenching intensities at two plasma chamber off-gas temperature levels: 1800 K and 2000 K; and two different plasma gas compositions: pure Ar and Ar/H_2 mixture.

The specific surface area of the powder produced with the radial injection ranged from 40 to 270 m^2/g, depending on the operating conditions. Two different trends were observed for the SSA vs. quenching intensity, depending on the composition of the plasma gas: with Ar/H_2

mixture, powders of smaller particle size (greater SSA) were produced when the quenching intensity increased; with pure Ar the opposite trend was observed.

Larger particles were produced at the higher temperature level, independent of the plasma gas composition. Higher AlN content in the powder was observed with increasing quenching intensities. However, none of the radial experiments produced a 100% AlN powder.

Axial injection of NH_3:

Pure NH_3 was injected at two different axial positions upstream of the quenching jet (at the entrance of the tubular reactor, or 40 mm upstream of this point). The same two temperature levels (1800 K and 2000 K) were tested. In this new configuration, fully converted powders (analyzed by x-ray diffraction) could be produced at both temperature levels.

The powder SSA ranged from 38 to 206 m^2/g, depending on gas temperature and NH_3 injection position. The uppermost injection resulted in particles of larger size. This was interpreted as resulting from a longer residence time. Also in this case, higher temperatures resulted in a powder of smaller SSA (larger particle size).

The oxygen analysis of the 100% AlN showed 5.8 - 11.2 %wt, depending on the SSA of the powder. It was observed that oxygen content is proportional to the powder SSA, thus suggesting that the oxygen is on particle surface. Because the powder is produced in an atmosphere in which oxygen is limited to process gases contamination, the large oxygen pick up observed is believed to occur during the powder handling in atmospheric air.

Surface chemical analysis (XPS) also showed the presence of carbon. The carbon content is believed to result from erosion of the graphite crucible, and from CO_2 contamination during handling in atmospheric air. The carbon content resulting from the synthesis process itself was estimated to be 1.9%.

Chapter 6

MODELLING

6.1. Introduction

The vapour synthesis of AlN in the reaction zone of the cylindrical reactor was simulated by means of a two dimensional numerical model. The development of this model was based on the procedure proposed by Bilodeau and Prouxl[36],[37] for the analysis of the production of ultrafine powders in thermal plasma reactors. According to this procedure, the several conservation equations are cast into the form of a general discretization equation for a control volume following the method developed by Patankar[38]. The solution of this set of equations is divided into two parts. First the velocity, temperature, and species concentration fields are determined. Following, the nucleation and growth of ultrafine Al/AlN particles is simulated by solving the particle population balance written in terms of the moments of the particle size distribution, using the formulation presented by Pratsinis[39]. Each group of discretization equations is simultaneously solved using the algorithm SIMPLER[38].

The calculation domain and its overall dimensions are shown in Figure 6.1. Given the axial symmetry of the reactor, the results to be presented in graphic form will show only half the diameter of the tube. Because gas-to-condensed phase transition is a strong function of temperature, special attention was dedicated to the calculation of the temperature distribution along the tubular reactor. In order to determine the most realistic boundary conditions for temperature at the tube wall, the energy transfer through the thermal insulation around the tube was also included in the model.

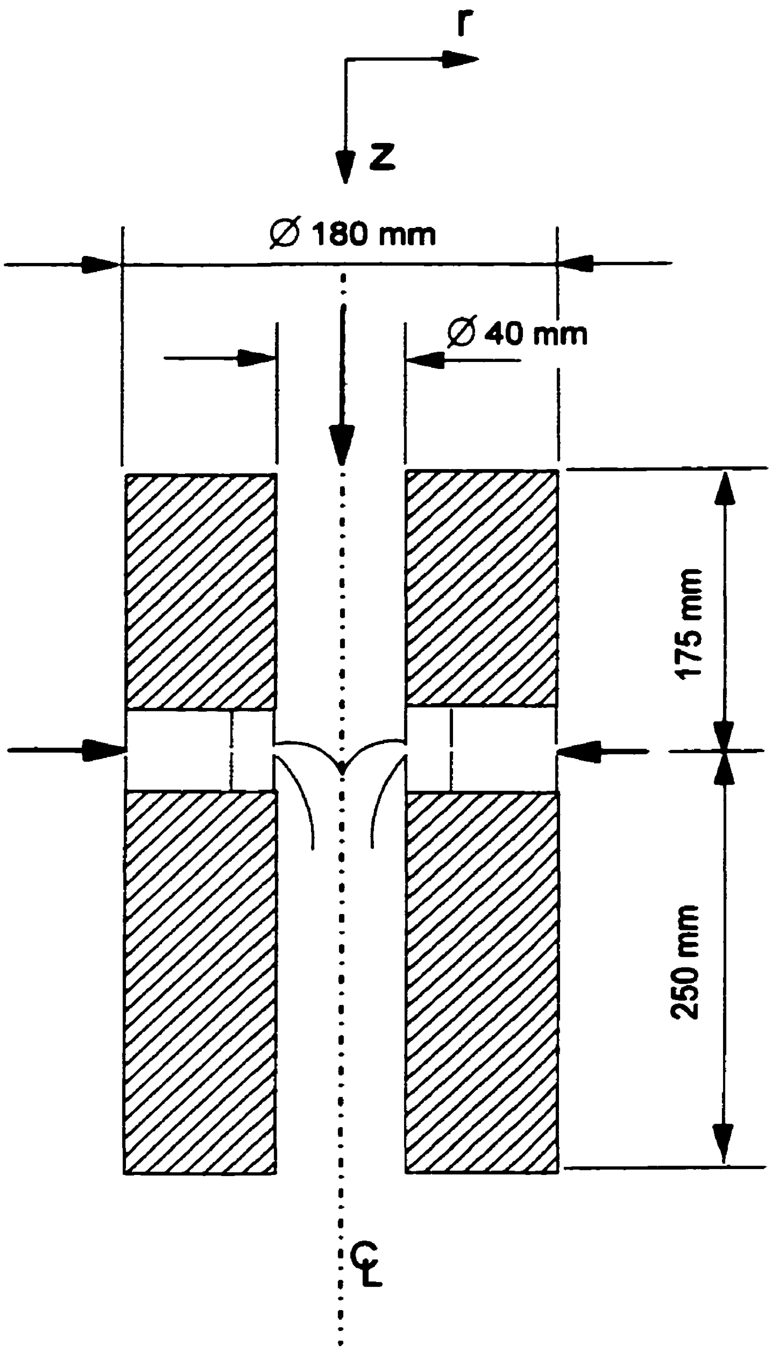

Figure 6.1 - Geometry and overall dimensions of the modelled region.

The simulation of the nucleation and growth of ultrafine particles considered the different mechanisms involved in the gas-to-condensed phase transition, i.e. homogeneous nucleation, condensation, and heterogeneous chemical reaction on the surface of particles. The formed particles were considered to be transported by bulk flow, Brownian diffusion, and thermophoresis. Experimental data on the flow conditions at the entrance of the tubular reactor were used as boundary conditions for the numerical simulation. Because the experimentally observed trends on the particle size (evaluated by specific surface area analysis) could not be explained using the commonly adopted homogeneous nucleation assumptions, a new formulation for the homogeneous nucleation of aluminum in the presence of a surface nitridation reaction was developed for this reacting system. This formulation was based on the work of Reiss[40] on homogeneous nucleation in binary systems, and on the work of Katz and Donohue[41] on nucleation with simultaneous chemical reaction.

6.2. Modelling of the vapour synthesis of ultrafine particles

A short literature review is presented on previous modelling work on the vapour synthesis of ultrafine particles using thermal plasmas and other high temperature systems.

Yoshida and Akashi (1981)[42] studied the injection of pure iron powder into an RF argon plasma, where it vaporized and recondensed. Using a simple Brownian collision-coalescence model for particle growth[43], they found a good agreement between the particle size calculated and the observed mean diameters (approx. 10 nm).

Okuyama et al. (1986)[44] studied the production of titania, silica and alumina powders by the thermal decomposition of metal alkoxide vapours. They used the numerical solution of the aerosol General Dynamic Equation (GDE) developed by Gelbard and Seinfeld (1978)[45] to predict particle size distribution, and compared calculation results with experimental data.

Girshick et al. published a series of studies on the synthesis of fine particles in thermal plasma reactors. In their initial study, they developed a simplified one-dimensional model[35] based on the assumption that any relevant chemical reaction leading to the formation of condensing species would be completed upstream of the nucleation region. They assumed that gas cooling occurred at a constant rate, and that particle growth occurred only by Brownian coagulation. Also, they assumed that coagulation might cease at a specified freezing temperature. In a later work[46], this study was extended to the formation of silicon carbide powder. Girshick et al.'s further work includes the numerical study of MgO powder synthesis[47], and the experimental study of ultrafine iron particles synthesis in a RF plasma reactor[48]. The MgO study neglected the heterogeneous reaction on the surface of particles and, as in their previous studies involving chemical reaction, they assumed that the chemical processes in the Mg-O system were complete before the nucleation event. Also this study assumed that particles nucleated as liquid droplets. As mentioned by the authors, previous experimental work demonstrated that phase transition in this system might occur to either a liquid phase or directly to a solid phase. Their experimental work on iron particles was supported by a two-dimensional model which combined the plasma conservation equations and the Aerosol General Dynamic equation (GDE) for the formation of iron particles. The GDE equation was written in terms of the method of moments as described by Pratsinis[39]. The nucleation rate of iron particles was described by the expression derived by Girshick et al.[49] based on Katz et al.'s[50],[51] arguments of a kinetic approach to the homogeneous nucleation theory.

Joshi et al.[34] developed a mathematical model to determine the effect of quenching conditions on the size characteristics of powders produced in reactive thermal plasma systems. They assumed that particle nucleation and growth was caused by both the condensation of gas phase reaction products and the surface reaction between adsorbed reactant species. However, particle growth was assumed to be due exclusively to condensation of homogeneous reaction product vapour. Considering the effect of surface reaction during the nucleation stage, Joshi et al. applied the nucleation rate expression for simultaneous chemical reaction and physical condensation proposed by Katz and Donohue[41]. The results of this study indicated that the particle size could be controlled by gradual quenching of the hot plasma gas.

Bilodeau and Proulx [36],[37],[52] carried out a progressive theoretical study of the nucleation and growth of ultrafine iron powders in a RF plasma reactor using a two-dimensional model. The model proposed by them accounts for particle formation by nucleation, and growth by condensation and Brownian coagulation. Nucleation and growth formulation is based on the method of moments of the particle size distribution. Also, it considers that transport of particles in the gas stream occurs by convection, Brownian diffusion, and thermophoresis. The modelling predictions were compared to those obtained by Girshick et al. (1993). This model was applied to the theoretical study of the synthesis of AlN in a RF reactor[33],[37], and to the simulation of the experiments conducted by Moura[53]. The model assumes that the AlN conversion is dominated by surface reaction. Moreover, it assumes that the homogeneous nucleation of pure aluminum, as described by the equation proposed by Girshick et al.[49], is the initial step in the gas-to-condensed phase transition, without the influence of heterogeneous nitridation reaction on the surface of subcritical clusters. Alike Girshick et al.[35],[46], Bilodeau and Proulx[36],[37],[52] also assume in their studies the existence of a certain temperature bellow which coagulation ceases. In the AlN case, it was assumed[33],[37] that this temperature would be equal to the Al solidification temperature.

All these previous modelling studies verified the strong effect of process parameters such as cooling rate and concentration of condensing species on particle size definition. In general, these models predicted that the stronger the cooling rate the smaller the particles which are produced. Also they predicted that the higher the concentration of condensing species, the larger the particles which are produced.

6.3. Particle generation and transport

Particle generation involves nucleation and growth by condensation and coagulation processes. These processes, referred to as internal processes[54], result in the movement of particles in the particle size space. The particle generation processes are described by the Aerosol General Dynamic Equation. Particle transport results from processes such as bulk flow, Brownian diffusion and effects of external force fields. These are referred as external processes since they involve the movement of particles across the wall of an elemental volume. The particle transport processes are described by the particle-number continuity equation, in the spatial coordinate system. In this equation, the internal processes are written as source terms.

6.3.1. The aerosol general dynamic equation

The GDE for simultaneous nucleation, condensation, and coagulation is written as [39]:

$$\begin{aligned}\frac{\partial n(v,t)}{dt} &= J\delta(v, v_{cr}) - \frac{\partial}{\partial v}\Big(Gn(v,t)\Big) + \\ &\frac{1}{2}\int_0^v \beta_{v-\overline{v},\overline{v}}\, n(v-\overline{v},t)\, n(\overline{v},t)\, d\overline{v} - n(v,t)\int_0^\infty \beta_{v,\overline{v}}\, n(\overline{v},t)\, d\overline{v}\end{aligned} \tag{6.1}$$

The term of the left hand side describes the rate of change of the concentration $n(v,t)$ of particles whose volume is in the interval $v+dv$. On the right hand side, the first term represents the formation of new particles of critical volume v_{cr} by nucleation at a rate J (δ is the Kronecker delta which is equal to 1 when v is equal to v_{cr}, and otherwise equal to 0); the second term accounts for the loss or gain of particles due to condensation of monomers at a rate G ; the third term accounts for the formation of particles of volume v by collision of particles of volumes $\overline{v}$ and $v-\overline{v}$; and the last term represents the loss of particles of volume v due to collision with any other particle.

6.3.2. Particle-number continuity equation

Particles are assumed to be spherical, and transported by gas convection, Brownian diffusion, and thermophoresis. The particle volume v is chosen as the internal coordinate in the particle-size space. Assuming a spatially distributed particulate process, described in terms of one internal coordinate in the particle size space. The population balance can be written as[55]:

$$\frac{\partial n}{dt} + \nabla \cdot (U + U_{th}) n = \nabla \cdot \left(D_p \nabla n \right) - \frac{\partial}{\partial v}(Gn) + (B - D) \qquad (6.2)$$

where U is the gas velocity vector; U_{th} the thermophoresis velocity vector; D_p is the particle diffusivity; and B and D stand for the birth and death of particles due to Brownian coagulation.

6.3.3. Moments of the particle-size distribution

The kth-moment of the particle size distribution is defined as:

$$M_k = \int_0^{\infty} v^k n dv \qquad (6.3)$$

The conservation equation for the kth-moment, derived from the particle-number continuity equation by multiplying both sides of Equation (6.2) by $v^k dv$ and integrating over the particle size range, is written as:

$$\frac{\partial M_k}{dt} + \nabla \cdot (U + U_{th}) M_k = \nabla \cdot (D_p \nabla M_k) - \int_0^{\infty} v^k \frac{\partial}{\partial v}(Gn) dv + (B - D)_k \qquad (6.4)$$

If it is assumed that the particle size distribution follows a log-normal distribution, which is a two parameter equation: the geometric standard deviation σ_g and the geometric mean particle size v_g, then it suffices to solve the three first integer moments (order 0, 1, and 2) for the determination of the particle size distribution.

6.3.3.1. The log-normal distribution function

The use of the log-normal distribution in the aerosol science has no theoretical background[56]. Its wide application to this field is rather based on empiricism, since it fits well the shape of most of the aerosol size distributions. Typically, particulate processes such as comminution and precipitation produce particle distributions which, on a weight basis, are asymmetric and skewed toward the larger sizes[55]. The log-normal distribution is a normal distribution of frequencies as a function of the log of the variable considered. Using the particle volume to express the particle size characteristic, this distribution is given as:

$$f(\ln v) = \frac{1}{\sqrt{2\pi}\,\ln\sigma_g}\exp\left[-\frac{\ln^2\left(v/v_g\right)}{2\ln^2\sigma_g}\right] \tag{6.5}$$

where v_g and σ_g are its two parameters, the geometric mean and the geometric standard deviation, respectively. These parameters are defined as:

$$\ln v_g = \int_0^\infty f(\ln v)\ln v(d\ln v) \tag{6.6}$$

and

$$\ln^2\sigma_g = \int_0^\infty f(\ln v)\ln^2\left(v/v_g\right)(d\ln v) \tag{6.7}$$

This distribution function has the property that:

$$\int_0^\infty f(\ln v)(d\ln v) = 1 \tag{6.8}$$

The concentration of particles of a given size v is defined as[39]:

$$n(v,t) = \frac{1}{3\sqrt{2\pi}\,\ln\sigma_g}\exp\left[-\frac{\ln^2\left(v/v_g\right)}{2\ln^2\sigma_g}\right]\frac{1}{v} \tag{6.9}$$

and the geometric average particle volume v_g and the geometric standard deviation σ_g can be expressed in terms of the first three moments of the log-normal size distribution as:

$$v_g = \frac{M_1^2}{M_0^{3/2} M_2^{1/2}} \tag{6.10}$$

$$\ln^2\sigma_g = \frac{1}{9}\ln\left(\frac{M_0 M_2}{M_1^2}\right) \tag{6.11}$$

Fractional moments can be expressed in terms of M_0, v_g, and σ_g as:

$$M_k = M_0 v_g^k \exp\left[\frac{9}{2}k^2 \ln^2\sigma_g\right] \tag{6.12}$$

6.3.4. Particle diffusion

Particle diffusivity caused by Brownian motion is related to particle size by the following equation[54] :

$$D_p = \frac{k_B T}{3\pi\mu}\left(\frac{1}{d_p} + \frac{2\lambda}{d_p^2}\left(A_1 + A_2 \exp\left(-A_3 \frac{d_p}{\lambda}\right)\right)\right) \tag{6.13}$$

where A_1=1.257; A_2=0.4; A_3=0.55; d_p is the particle diameter; and λ is the mean free-path length of the gas species. Because the nonlinear form of this equation represents a major difficulty in the formation of the moment equations, the diffusivity is approximated by the simplified expression [57]:

$$D_p = \frac{k_B T}{3\pi\mu}\left(\frac{1}{d_p} + \frac{3.314\lambda}{d_p^2}\right) \tag{6.14}$$

It is observed that the diffusion coefficient is inversely proportional to both the particle diameter and its square. Compared to Equation (6.13), Equation (6.14) over predicts the particle diffusivity by 2%-11% for 0.1<Kn<10 and by less than 2% for all other Knudsen numbers[57].

6.3.5. Thermophoresis

Thermophoresis is the mechanism by which particles are transported by the effect of thermal gradients. The more energetic collisions of gas molecules on the higher temperature side of the particle causes it to move in the direction of the negative temperature gradient. Comparing Brock's equation[58] for the thermophoretic force with the Millikan drag force, and considering the situation when $Kn \to \infty$, Talbot et al.[59] derived the following equation for the thermophoretic velocity:

$$u_{th} = -K\frac{\mu}{\rho T}\nabla T \qquad (6.15)$$

with the dimensionless thermophoretic coefficient K related to particle size by the expression:

$$K = 2C_s\left(\frac{k_g}{k_p} + 2C_t\frac{\lambda}{d_p}\right)\frac{1 + 2\lambda\left(A + B\exp\left(-Cd_p/2\lambda\right)\right)/d_p}{\left(1 + 6C_m\lambda/d_p\right)\left(1 + 2k_g/k_p + 4C_t\lambda/d_p\right)} \qquad (6.16)$$

where C_s=1.17, C_m=1.14, and C_t=2.18, and the coefficients for the Millican drag force equation are given as A=1.2, B=0.41, and C=0.88 [59]. As in the case of the particle diffusivity coefficient, the non-linearity of this expression also represents a major difficulty for the moments formulation. For particles smaller than 1 μm, $K \cong 0.55$. Since particles smaller than 1 μm are subjected to stronger thermophoretic forces than larger particles, Phanse and Pratsinis[57] suggested the adoption of the value $K = 0.55$ over the entire particle size spectrum, which would result in a conservative estimate of the thermoporetic effect if particles grow larger than 1 μm.

6.4. Assumptions

The following are the main assumptions which were used for the solution of the two sets of conservation equations.

6.4.1. Velocity, temperature and Ar, NH_3, H_2, and N_2 concentration fields

- Steady state, axi-symmetric laminar flow. The highest Reynolds number (based on the tube diameter) observed in a typical simulation condition is of the order of 400.
- The radial gas injector holes were approximated by a thin slit of equal cross section area; the study of gas mixing using radial injection by Njah[60] demonstrated the validity of this approximation when the number of injection holes is greater than 8.
- The latent heat of phase transition and heat of nitridation reaction were neglected (dilute system).
- Viscous dissipation in the energy equation is neglected.
- The possible influence of Al vapour on the physical properties of the gas is neglected.
- Momentum transfer between the gas and particles is neglected. Particles are assumed to travel at the gas velocity.
- The solution of the momentum, energy and gaseous species concentrations assumes that no Al vapour and condensed phase is present (dilute system).
- Radiative losses due to the presence of Al(v) in the gas were neglected; a conservative estimation at a 2000 K operating condition indicates that the gas enthalpy change is less than 0.5% at the upper potion of the tubular reactor.

6.4.2. Al and AlN vapour concentrations, and nucleation and growth related variables

- Nucleation does not occur inside the plasma chamber. In the temperature range in which the modelling study is carried out, the Al mole fraction, plotted as a function of the temperature measured immediately after the plasma chamber in Figure 5.7. shows that the carrier gas Al concentration is below saturation. Also, the fact that no condensation or particle deposition on the walls of the chamber preceding the entrance of the tubular reactor was observed in any of the experiments carried out, is evidence that the carrier gas was free from nuclei which could have formed inside the plasma chamber.

- For the computation of particles volume, the particles (including Al atoms and AlN "molecules") are assumed to be spherical and structureless. The calculation of the volume of Al atoms and AlN "molecules" is based on the density of the material (liquid Al or crystalline AlN).
- Particles are assumed to be in thermal equilibrium with the gas phase.
- The Kelvin effect[54], which considers the increase of vapour pressure on liquid surfaces of small curvature is neglected.
- The decomposition of the condensed phase AlN is neglected.
- The gas phase formation of AlN is considered for the purpose of evaluation of the respective reaction rate, and AlN(g) is considered to condense on the surface of existing particles. Unless otherwise indicated, its participation on the nucleation process is neglected.
- Sub-critical clusters are short lived and, therefore, their transport is neglected (nucleation phenomenon is treated as instantaneous).
- Sub critical clusters scavenging by larger stable particles is neglected.
- Particle coalescence is considered to be dependent on the average local particle composition as follows: (i) free-Al mole fraction $\geqslant 0.5$: particles fully coalesce if local temperature is equal to or higher than the Al melting point; otherwise no coalescence occurs; (ii) free-Al mole fraction < 0.5 : particles fully coalesce if local temperature is higher than 1650K; otherwise no coalescence occur.
- Surface reaction is assumed to stop if the temperature is lower than the Al melting point.
- When taken into account under the above restrictions, particle coagulation is assumed to occur in the free molecule regime.

- Particle size distribution at any location can be represented by a log-normal distribution.
- The effect of small curvature radius on the surface tension of Al was not considered; capillarity approximation.

6.5. Gas-to-condensed phase transition mechanisms

The three routes which make possible the gas-to-condensed phase conversion are[35] :

i. Homogeneous nucleation;
ii. Condensation on an existing particle;
iii. Heterogeneous chemical reaction on the surface of particles.

Each of these routes will be formulated next. The nucleation equation that considers the influence of surface reaction is briefly introduced in this section. Its detailed deduction is further presented in a separate section.

6.5.1. Homogenous nucleation

The experimental results given in Figure 5.16 show that, under similar cooling conditions, the SSA of a powder produced in nitriding atmosphere is by far greater than the SSA of a powder produced in inert atmosphere. Heterogeneous reaction on the surface of sub critical clusters was pointed out as one of two possible factors responsible for these results. As observed in the short literature review presented in the introduction of this section, most of the earlier workers[34],[36],[44],[46] treated this problem in systems which involve chemical reaction by applying the nucleation formulation of a single component, with different assumptions depending on the particular chemical system. Accordingly, it has been assumed that either the reaction is completed before the onset of the nucleation event[34],[44],[46] in case of a dominating gas phase reaction, or that one of the reacting species first nucleates before a dominating heterogeneous reaction can take place[37]. This last assumption was initially applied to the present study, using, as did Bilodeau[37], the equation of the kinetic theory for homogeneous nucleation proposed by Girshick[49]:

$$J_{kin} = \frac{n^{e}_{Al}\beta_{Al}s_{Al}}{3}\sqrt{\frac{\theta}{\pi}}\,\exp\left[\theta - \frac{4}{27}\frac{\theta^{3}}{\ln^{2}S_{Al}}\right] \tag{6.17}$$

where n^{e}_{Al} is the number density of Al atoms in the gas phase at equilibrium, β_{Al} is the aluminum impingement rate (or collision frequency), s_{Al} the aluminum atom surface area, S_{Al} the Al supersaturation ratio, and $\theta = \sigma s_1 / k_B T$ the dimensionless surface energy of liquid Al, σ is the surface tension, and s_1 is the surface of a monomer (in this case, the Al atom).

The comparison of results of experimental data and the numerical analysis based on this assumption, carried out in the early stage of this work, did not provide a good agreement with respect to both the powder characteristics and the main trends observed experimentally. Following these results, a new development for the nucleation rate is proposed which considers the surface-reaction enhanced nucleation and that sub critical cluster may have both free Al and AlN in their composition. The detailed development of this formulation is presented later in a separate section. At this point only the resulting equation is introduced:

$$J = \frac{n(v_1,\overline{X_c})\beta^{*}s_1}{3S_{Al}}\sqrt{\frac{\overline{\theta}}{\pi}}\,\exp\left[-\frac{4}{27}\frac{\overline{\theta}^{3}}{\left(\ln S_{Al} - (1-\overline{X_C})\left(\frac{\Delta G_r}{k_B T}\right)_L\right)^{2}}\right] \tag{6.18}$$

where $n(v_1,\overline{X_c})$ is the particle number density written as a function of an equivalent monomer-size v_1 and the free-Al molar fraction $\overline{X_c}$ in a cluster, $\overline{\theta}$ is an average dimensionless surface energy considering the cluster composition, ΔG_r is the free energy change associated with the AlN heterogeneous reaction, and β^{*} is an equivalent impingement rate defined as:

$$\beta^{*} = \frac{1}{v_1}\left[(a\beta_{AlN} + R^{s,c}_{AlN})v_{AlN} + (a\beta_{Al} - R^{s,c}_{AlN})v_{Al}\right] \tag{6.19}$$

where β_{AlN} is the AlN(g) impingement rate, v_{AlN} and v_{Al} respectively the AlN(g) molecule and Al atom volumes, a the mass accommodation coefficient (in this case, the fraction of the total number of collisions that result in condensation), and $R^{s,c}_{AlN}$ is the reaction rate on the surface of a cluster.

In the absence of nitriding reagent, Equation 6.18 reduces to the equivalent of the nucleation equation which is deduced from the classical theory (J_{cl}) using Blander and Katz[61] arguments regarding the Gibbs free energy change to form a cluster of the condensed phase from the gaseous state:

$$J = J_{cl} = \frac{n^{e}_{Al}\beta_{Al}S_{Al}}{3}\sqrt{\frac{\theta}{\pi}}\exp\left[-\frac{4}{27}\frac{\theta^{3}}{\ln^{2}S_{Al}}\right] \tag{6.20}$$

The ratio between Equations (6.17) and (6.20) results in:

$$\frac{J_{kin}}{J_{cl}} = e^{\theta} \tag{6.21}$$

Therefore, in case of pure Al nucleation, Equation (6.20) predicts a considerably smaller nucleation rate than Equation (6.17).

The exponential term of the newly proposed nucleation rate equation [Equation (6.18)] results in a strong dependence of the nucleation rate not only on aluminum supersaturation and surface energy, but also on the free-energy change resulting from reaction. In the case of particle nucleation in nitriding conditions, the greater surface energy of binary particles (as compared with pure Al particles) contributes to the decrease of the nucleation rate (the newly formed particles have to overcome a greater barrier imposed by the creation of a surface of higher energy). On the other hand, because of the addition of the reaction free energy term to the denominator (the free energy change involved in the AlN reaction is negative), a stronger driving force towards the phase transition arises. This contributes to an increase of the nucleation rate. Based on the modeling results using this new formulation which will be presented later on, it is observed that the net balance between these two opposed forces favours the second trend (an increased nucleation rate).

6.5.2. Surface growth

It is considered that surface growth might result from condensation and surface reaction processes. The growth rate G resulting from $Al_{(g)}$ and $AlN_{(g)}$ and surface nitridation is developed using the collision frequencies of gaseous phase Al and AlN in the free-molecule regime (β_i) :

$$\beta_i = \frac{p_i}{\sqrt{2\pi k_B T m_i}} \tag{6.22}$$

where p_i is the partial pressure of the species i, and m_i the species atomic or molecular mass. The collision frequency expresses the number of species i which collide on a unit surface area of a given particle per unit time.

Three different regimes can be defined for the collision among particles[62], depending on the Knudsen number defined by:

$$Kn = \frac{2\lambda}{d_p} \tag{6.23}$$

where d_p is the particle diameter, and λ is the mean free path length of the gas molecules, which is evaluated using the Chapman-Enskog's viscosity equation for hard sphere molecules[63]:

$$\lambda = 1.256\left(\frac{M}{RT}\right)^{1/2}\frac{\mu}{p} \tag{6.24}$$

- continuum regime: $Kn < 10^{-3}$
- transition regime: $10^{-3} \leq Kn < 10$
- free molecule regime: $10 \leq Kn$

Fuchs and Sutugin[62] suggested the use of the following interpolation formula for the calculation of the growth rate over the entire range of Knudsen numbers:

$$G = G_{fm}\left(\frac{1.333Kn(1+Kn)}{1+1.71Kn+1.333Kn^2}\right) \tag{6.25}$$

If the volume of a particle is taken as the sum of the volumes of free Al and AlN phases:

$$v = v^{Al} + v^{AlN} \tag{6.26}$$

then the surface growth rate can be written:

$$G = \frac{dv}{dt} = \frac{dv^{Al}}{dt} + \frac{dv^{AlN}}{dt} \tag{6.27}$$

Formulating a detailed balance for the surface growth of each of those components as:

$\frac{dv^{Al}}{dt} =$	(nr. of Al atoms that collide and stay with a particle size-v, per unit time)	x (volume of Al atom)
$-$	(nr. of Al atoms that evaporate from a particles size-v, per unit time)	x (volume of Al atom)
$-$	(nr. of free-Al that react with NH_3 at the surface, per unit time)	x (volume of Al atom)

(6.28)

and

$\frac{dv^{AlN}}{dt} =$	(nr. of NH_3 molecules that collide and react with free-Al at the surface of a particle size-v, per unit time)	x (vol. of AlN molecule)
+	(nr. of AlN molecules that collide and stay with a particle size-v, per unit time)	x (vol. of AlN molecule)

(6.29)

the growth rate in the free-molecule regime becomes:

$$G_{fm} = (36\pi)^{1/3}[v_{Al}\alpha\beta_{Al}^{e}(S_{Al} - 1) - (v_{Al} - v_{AlN})R_{AlN}^{s,p} + v_{AlN}\alpha\beta_{AlN}]v^{2/3} \tag{6.30}$$

where $R_{AlN}^{s,p}$ is the AlN reaction rate on the surface of a particle, $S_{Al} = p_{Al}/p_{Al}^{e}$ is the Al supersaturation ratio, p is the pressure and the superscript e refers to the Al saturation. The mass accommodation coefficient α is assumed equal to unity for Al(g) and AlN(g) species.

The substitution of the collision frequencies (β_i) in Equation (6.30) using Equation (6.22) and the relation:

$$p_i = n_i k_B T \tag{6.31}$$

gives:

$$G = f_{FS}[B_1(S_{Al} - 1) - B_2 + B_3]v^{2/3} \tag{6.32}$$

where the coefficients B_i are defined as:

$$B_1 = (36\pi)^{1/3} n_{Al}^{e} v_{Al} \sqrt{\frac{k_B T}{2\pi m_A}} \tag{6.33}$$

$$B_2 = (36\pi)^{1/3}(v_{Al} - v_{AlN})R_{Al}^{s,p} \tag{6.34}$$

$$B_3 = (36\pi)^{1/3} n_{AlN} v_{AlN} \sqrt{\frac{k_B T}{2\pi m_{Al}}} \tag{6.35}$$

and f_{FS} is the Fucks-Sutugin factor, derived from Equation (6.25):

$$f_{FS} = \frac{G}{G_{fm}} = \frac{1.333Kn(1+Kn)}{1+1.71Kn+1.333Kn^2} \tag{6.36}$$

Integrating by parts, the second term in the right hand side of Equation (6.4) is developed as:

$$f = v^k \rightarrow df = kv^{k-1}dv \tag{6.37a}$$

$$dg = \frac{\partial}{\partial v}(Gn)dv \rightarrow g = Gn \tag{6.37b}$$

$$\begin{aligned}\int_0^\infty v^k \frac{\partial}{\partial v}(Gn)dv &= \int_0^\infty fdg \\ &= \int_0^\infty d(f.g) - \int_0^\infty gdf \\ &= f.g\,\Big|_0^\infty - \int_0^\infty gdf\end{aligned}$$

$$= v^k(Gn)\,\Big|_0^\infty - \int_0^\infty (Gn)kv^{k-1}dv \tag{6.37}$$

The first term on the right hand side of Equation (6.37) gives[55]:

$$v^k(Gn)\,\Big|_0^\infty \simeq \infty^k Gn(\infty) - v_{cr}^k Gn(v_{cr}) \simeq 0 - v_{cr}^k J \simeq -v_{cr}^k J \tag{6.38}$$

With the substitution of Equation (6.32), the second term is developed as:

$$\int_0^\infty (Gn)kv^{k-1}dv = f_{FS}\left[B_1(S_{Al}-1) - B_2 + B_3\right]k\int_0^\infty v^{(k-1/3)}ndv \tag{6.39}$$

which, using the definition of the k^th^-moment, Equation (6.3), is written:

$$\int_0^\infty (Gn)kv^{k-1}dv = f_{FS}\left[B_1(S_{Al}-1)-B_2+B_3\right]kM_{k-1/3} \tag{6.40}$$

With the substitution of Equations (6.38) and (6.40) in (6.37), the surface growth term is finally written:

$$\int_0^\infty v^k \frac{\partial}{\partial v}(Gn)dv = -v_{cr}^k J + f_{FS}\left[B_1(S_{Al}-1)-B_2+B_3\right]kM_{k-1/3} \tag{6.41}$$

6.5.3. Coagulation

The birth and death terms associated with Brownian coagulation in Equation (6.4) are evaluated assuming free molecule regime for particle collisions. Using the procedure presented by Pratsinis[39], the collision frequency between particles of size v and $\overline{v}$ in this regime is expressed as:

$$\beta_{fm} = B_4\left(\frac{1}{v}-\frac{1}{\overline{v}}\right)^{1/2}\left(v^{1/3}+\overline{v}^{1/3}\right)^2 \tag{6.42}$$

where:

$$B_4 = \left(\frac{3}{4\pi}\right)^{1/6}\left(\frac{6k_BT}{\rho_p}\right)^{1/2} \tag{6.43}$$

Because the particle volume v was adopted to represent the particle size characteristic, of the three moments necessary to describe the log-normal particle size distribution, only the zeroth and second moments, M_0 and M_2, are affected by particle coagulation. The moment order 1 represents the volume of particles per unit volume of gas and therefore remains unchanged by the consolidation of particles.

The calculation of the birth and death difference terms for each moment is based on the expressions derived by Lee et al.[64],[65] as a function of fractional moments:

$$(B-D)_0 = b_0B_4(M_{2/3}M_{-1/2}+2M_{1/3}M_{-1/6}+M_{1/6}M_0) \tag{6.44}$$

$$(B-D)_2 = 2b_2B_4(M_{5/3}M_{1/2} + 2M_{4/3}M_{5/6} + M_{7/6}M_1) \tag{6.45}$$

These equations are based on the approximation in each of the two moments of the collision square term in Equation (6.42) by the expression:

$$\left(\frac{1}{v} - \frac{1}{\overline{v}}\right)^{1/2} = b_k\left(\frac{1}{v^{1/2}} - \frac{1}{\overline{v}^{1/2}}\right) \tag{6.46}$$

Using the values of b_k, $k = 0$ or 2 (the moment order index), tabulated by Lee et al.[64],[65] for various σ_g, Pratsinis[39] obtained the following polynomial expressions:

$$b_0 = 0.633 + 0.092\sigma_g^2 - 0.022\sigma_g^3 \tag{6.47}$$

$$b_2 = 0.39 + 0.5\sigma_g - 0.214\sigma_g^2 + 0.029\sigma_g^3 \tag{6.48}$$

6.5.4. Set of differential equations

The SIMPLER algorithm[38] numerically solves partial differential equations which are written in the following general form:

$$\frac{\partial}{\partial t}(\rho\Phi) + \nabla.(\rho U\Phi) = \nabla.(\Gamma\nabla\Phi) + S_C + S_P\Phi \tag{6.49}$$

where Φ is a general variable to be solved; ρ is the density; Γ is the diffusivity coefficient; and S_C and S_P are the linearization coefficients of the source term for the respective equation. For the moment equations to fit this form, the kth-moment was calculated as:

$$M_k' = \frac{M_k}{\rho} \tag{6.50}$$

where ρ is then the gas density. Performing the appropriate changes, the set of differential equations to be simultaneously solved for the nucleation and growth of particles is given as:

Moment order 0:

$$\begin{aligned}\frac{\partial}{\partial t}(\rho M'_0) + \nabla.[\rho(U+U_{th})M'_0] = \nabla.(\rho D_p \nabla M'_0) + \\ J - \rho^2 b_0 B_4 (M'_{2/3}M'_{-1/2} + 2M'_{1/3}M'_{-1/6} + M'_{1/6}M'_0)\end{aligned} \tag{6.51}$$

Moment order 1:

$$\begin{aligned}\frac{\partial}{\partial t}(\rho M'_1) + \nabla.[\rho(U+U_{th})M'_1] = \nabla.(\rho D_p \nabla M'_1) + \\ v_{cr}J + \rho[B_1(S_{Al}-1) - B_2 + B_3]M'_{2/3}\end{aligned} \tag{6.52}$$

Moment order 2:

$$\begin{aligned}\frac{\partial}{\partial t}(\rho M'_2) + \nabla.[\rho(U+U_{th})M'_2] = \nabla.(\rho D_p \nabla M'_2) + \\ v_{cr}^2 J + 2\rho[B_1(S_{Al}-1) - B_2 + B_3]M'_{5/3} + \\ 2\rho^2 b_2 B_4 (M'_{5/3}M'_{1/2} + 2M'_{4/3}M'_{5/6} + M'_{7/6}M'_1)\end{aligned} \tag{6.53}$$

In order to calculate the particle composition, the moments order 1 in Al and AlN are defined as:

Moment order 1 in Al:

$$\begin{aligned}\frac{\partial}{\partial t}(\rho M_1'^{Al}) + \nabla.[\rho(U+U_{th})M_1'^{Al}] = \nabla.(\rho D_p \nabla M_1'^{Al}) + \\ v_{cr}^{Al}J + \rho[B_1(S_{Al}-1) - B_{2a}]M'_{2/3}\end{aligned} \tag{6.54}$$

Moment order 1 in AlN:

$$\begin{aligned}\frac{\partial}{\partial t}(\rho M_1'^{AlN}) + \nabla.[\rho(U+U_{th})M_1'^{AlN}] = \nabla.(\rho D_p \nabla M_1'^{AlN}) + \\ v_{cr}^{AlN}J + \rho[B_{2b} + B_3]M'_{2/3}\end{aligned} \tag{6.55}$$

were the coeficients B_{2a} and B_{2b} are defined as:

$$B_{2a} = (36\pi)^{1/3} v_{Al} R_{Al}^{s,p} \tag{6.54a}$$

$$B_{2b} = (36\pi)^{1/3} v_{AlN} R_{AlN}^{s,p} \tag{6.55b}$$

At this step, the conservation equations for Al(g) and AlN(g) species written in terms of their mole fraction w_{Al} and w_{AlN} are also included:

$$\begin{aligned}\frac{\partial}{\partial t}(\rho w_{Al}) + \nabla.(\rho U w_{Al}) = \nabla.(\rho D_{Al,Ar} \nabla w_{Al}) - \\ \rho_{Al} v_{cr}^{Al} J - \rho p_{Al} B_1 (S_{Al} - 1) M'_{2/3} - R_{AlN}^{g} \overline{M}_{Al}\end{aligned} \tag{6.56}$$

$$\begin{aligned}\frac{\partial}{\partial t}(\rho w_{AlN}) + \nabla.(\rho U w_{AlN}) = \nabla.(\rho D_{AlN,Ar} \nabla w_{AlN}) - \\ \rho_{Al} v_{cr}^{Al} J - \rho p_{AlN} B_3 M'_{2/3} + R_{AlN}^{g} \overline{M}_{AlN}\end{aligned} \tag{6.57}$$

where R_{AlN}^{g} is the gas phase AlN reaction rate in (moles/m^3/s), and $\overline{M}_{Al}$ and $\overline{M}_{Al}$ are the molecular weight of Al and AlN, respectively.

6.5.5. Particle composition

The average particle composition $\overline{X_p}$ is specified as the mole fraction of free Al in the particle. The volume v of a particle which has free Al and AlN in its composition was defined by Equation (6.26) as the sum of total free Al and AlN. For the calculation of particle composition, substitution of this equation in the equation of the first-moment of the particle size distribution (total volume of particles per unit volume of gas) gives:

$$M_1 = \int_0^\infty v n dv = \int_0^\infty (v^{Al} + v^{AlN}) n dv = \int_0^\infty v^{Al} n dv + \int_0^\infty v^{AlN} n dv = M_1^{Al} + M_1^{AlN} \tag{6.58}$$

where M_1^{Al} and M_1^{AlN} are defined as first-moments of Al and AlN, respectively, by the following equations:

$$M_1^{Al} = \int_0^{\infty} v^{Al} n dv \tag{6.59}$$

$$M_1^{AlN} = \int_0^{\infty} v^{AlN} n dv \tag{6.60}$$

Using the above definitions, the following expression for the average mole fraction of the ensemble of particles, at a given reactor location, can be derived:

$$\overline{X_p} = \frac{M_1^{Al} v_{AlN}}{M_1^{AlN} v_{Al} + M_1^{Al} v_{AlN}} \tag{6.61}$$

where v_{Al} and v_{AlN} are the hard sphere model volumes of Al atoms and AlN molecules, respectively.

6.6. Homogeneous nucleation modified by surface reaction

A short review is presented of the different theories for the nucleation in vapour condensation processes, with emphasis on their applicability to systems which involve chemical reaction. Following the discussion of the possible effects of surface reaction on the kinetics of the Al/AlN phase transition, a new development of the formulation of the nucleation equation is presented for this system.

6.6.1. Nucleation theories and heterogeneous chemical reaction

The classical theory of homogeneous nucleation applied to vapour condensation processes[66], and also the more recent kinetic approach to the theory of homogeneous nucleation proposed by Katz et al.[50],[51], refer to systems involving one condensable species - hereafter referred to as one (or single) component systems, as opposed to systems involving two and more condensable species, to be referred to as two (or binary) and multicomponent systems, respectively. When these theories are applied to plasma synthesis and other high temperature related synthesis processes in chemically reacting systems, it has been usually assumed that either the reaction occurs only in the gas phase and it is fast compared to the condensation rate[47], or one of the condensable species first nucleates before heterogeneous reaction can take place [33],[37],[53].

Katz and Donohue[41] presented a theory which takes into account the effect of simultaneously occurring nucleation and chemical reaction. They considered the situation in which two (or more) volatile species react to form a nonvolatile product, in a processes represented by the equation:

$$\text{A(gas)} + \text{B(gas)} \rightarrow \text{C(liquid or solid)} \tag{6.62}$$

and demonstrated that when the reaction occurs both homogeneously in the gas phase and heterogeneously on the surface (or in the bulk) of clusters, the nucleation rate can be greatly increased. Their work was developed on the assumption that only one component nucleates. In this case, vapour clusters are characterized by the number of reaction product species they contain (species C). As observed by Katz and Donohue[41], this assumption is valid if the reactants are far more volatile than the product, in which case it is reasonable to consider that the average number of reacting species adsorbed (or dissolved) in a cluster will be small compared to the number of product species.

Bilodeau and Prouxl[33],[37] carried out a theoretical study of the nucleation and growth of ultrafine AlN powders in an inductive plasma reactor. They considered that aluminum nucleates without the influence of surface nitridation, and used the equation for the homogeneous nucleation proposed by Girshick et al.[49]. In the present work, the results of experiments involving nitridation reaction and pure aluminum condensation in similar cooling conditions (Figure 5.14) show a large difference in the particle size characteristic of the powder produced. Much larger particle sizes are produced in the absence of nitridation, clearly suggesting that aluminum nucleation is strongly influenced by heterogeneous reaction. Also, the Al-N-H-Ar equilibrium diagram (Figure 4.2) indicates that heterogeneous reaction might be the most important mechanism for the AlN conversion: AlN(s) is the predominant aluminum containing phase below 2200 K, and very little AlN(g) is present at equilibrium.

These facts suggest that the vapour phase synthesis of AlN would better be treated as a nucleation with simultaneous chemical reaction process, in the light of Katz and Donohue's theory. However, the intrinsic characteristics of the AlN system precludes the direct application of this theory. Because of its relatively low vapour pressure, aluminum cannot be considered a far more volatile species than aluminum nitride, especially in the temperature range pertaining to the present study (maximum of 2000 K). Indeed, given the reduced amount of gaseous aluminum nitride that is observed at equilibrium, it is expected that aluminum will have to condense in first place in order to provide the surface necessary for the heterogeneous reaction to proceed. In this case, this system can not be visualized as a single component one. In addition to their size characteristic, vapour clusters need also to be identified by their composition, i.e. their Al and AlN content.

Reiss[40] presented a theory for the homogeneous nucleation in a system containing two components. Later, this theory was extended to a multi component system by Hirchfelder[67]. This theory applies to vapour-to-liquid and liquid-to-liquid phase transitions but does not include chemical reaction effects.

In the following, a new development for the nucleation in the AlN system is presented. This formulation combines the Katz and Donohue's[41] theory of nucleation in the presence of chemical reaction, with Reiss'[40] theory of nucleation in binary systems. A major simplification is made by assuming that subcritical cluster composition is determined by the rate at which Al and AlN species are added to their surface. This simplification allows the development to be cast in the form used in the classical theory while preserving its binary characteristic.

6.6.1.1. The classical theory

Detailed reviews of the classical theory of homogeneous nucleation of liquid drops in supersaturated vapours were presented by Hirth and Pound[68], Feder et al.[66], Zettlemoyer[69], and Abraham[70]. Also Kotake and Glass[71] presented a survey on this subject with emphasis on flows with nucleation and condensation. In order to introduce the development of the nucleation equation that considers both the condensation of Al(g) and AlN(g), and formation of AlN(s) by surface reaction, some of the concepts related to the classical theory will be briefly reviewed, as outlined in the work of Katz et al.[41],[50],[51].

A supersaturated vapour produces small clusters of the new phase which can contain two or more atoms or molecules, hereafter also referred to as monomers, and which exist for a short period of time since they grow and shrink rapidly as a result of fluctuations in the condensation and evaporation processes. Nucleation occurs when clusters of two or more monomers fluctuate in size and overcome the barrier imposed by the surface energy associated with the creation of the new phase. When the growth rate equals the decay rate, the cluster is said to have a critical size (critical nucleus). Clusters that fluctuate in size beyond the critical size will have the tendency to continuously grow rather than shrink.

The development of the classical theory is based on the assumptions that clusters as well as monomers are spherical and charge neutral, that London-van der Waals forces can be neglected, and that the surface tension of clusters are the same as in bulk (capillarity approximation). Because the concentration of sub-critical clusters is much lower than the concentration of monomers, the probability that two of such clusters will collide to form a larger cluster is small compared with the growth resulting from monomer-cluster collision. Therefore, it is assumed that clusters grow by addition of single atoms or molecules.

The nucleation rate is equal to the number of clusters per unit volume of gas and unit time that grow larger than the critical size. Adopting the number "i" of monomers in a cluster to express the characteristic cluster size, the net rate at which clusters of size-i grow to size-(i+1) is the difference between the rate at which clusters of size-i have monomers added by condensation and the rate at which clusters of size-(i+1) lose monomers by evaporation. This net rate is expressed by the following equation:

$$J(i) = f(i)n(i) - b(i+1)n(i+1) \tag{6.63}$$

where $f(i)$ is the forward rate (the rate of addition of monomers to a cluster), $b(i)$ is the backward rate (the rate of loss of monomers from a cluster), and $n(i)$ is the number density of clusters of size-i. These quantities are not only a function of cluster size, temperature, and pressure, but also can be a function of time. Using the kinetic theory of gases, the forward rate is determined as:

$$f(i) = \alpha\beta s(i) \tag{6.64}$$

where a is the condensation coefficient, s(i) the cluster surface area., β the rate at which monomers impinge on the cluster's surface which is given by Equation (6.22).

In order to develop an equation for the nucleation rate, the classical theory makes use of two concepts: (i) the constrained equilibrium condition in which, for all i, $J(i) = 0$; and (ii) the steady state condition in which, for all i, $J(i) = J$, or in other words, $J(i)$ becomes a constant, independent of i. Thus, to eliminate the backward rate from Equation (6.63), the classical theory invokes the constrained equilibrium concept and writes:

$$b(i+1) = \frac{a\beta s(i)N(i)}{N(i+1)} \tag{6.65}$$

where instead of $n(i)$, the number density of clusters size-i is indicated by $N(i)$ in this hypothetical system. The theory makes the additional assumption that the cluster distribution in the constrained-equilibrium obeys a Boltzmann like distribution given as:

$$N(i) = \overline{N} \exp\left[-\frac{\Delta G(i)}{k_B T}\right] \tag{6.66}$$

where $\overline{N}$ is a normalization constant, and $\Delta G(i)$ the free energy change associated with the formation of a cluster size-i. Following, it invokes the steady state condition, when the net rate of growth becomes constant (i.e., independent of cluster size). Applying the mathematical procedure found in [49], the equation for the nucleation rate can be written in the form of the classical expression of Becker and Döring[66] as:

$$J = \frac{\overline{N}s(1)\beta}{3}\sqrt{\frac{\theta}{\pi}} \exp\left[-\frac{\Delta G(i^*)}{k_B T}\right] \tag{6.67}$$

where $\theta = s_1\sigma/k_B T$ is the dimensionless surface energy, σ the surface energy of the condensed phase, s_1 the surface area of a monomer. i^* is the critical particle size given as:

$$i^* = \left(\frac{2}{3}\frac{\theta}{\ln S}\right)^3 \tag{6.68}$$

where $S = n(1)/n_S$ is the supersaturation ratio, $n(1)$ the vapour concentration, and n_S the saturation vapour concentration.

6.6.1.2. Al nucleation modified by surface nitridation

The processes that can result in the formation of AlN are summarized by the following set of equations:

$$Al_{(g)} + NH_{3(g)} \rightarrow AlN_{(g)} + 3/2H_2 \tag{6.69.a}$$

$$AlN_{(g)} \rightarrow AlN_{(s)} \tag{6.69.b}$$

$$Al_{(g)} \rightarrow Al_{(l)} \tag{6.69.c}$$

$$NH_{3(g)} \rightarrow NH_{3(ad)} \tag{6.69.d}$$

$$Al_{(l)} + NH_{3(ad)} \rightarrow AlN_{(s)} + 3/2H_2 \tag{6.69.e}$$

As discussed before, Equation (6.69.b) might represent a minor contribution to the whole phase transition. Nevertheless, it has been included in this formulation so its importance can be better evaluated. The assumptions of the classical theory are maintained: clusters as well as monomers are spherical and charge neutral, that London-van der Waals forces can be neglected, and that the surface tension of clusters are the same as in bulk (capillarity approximation). The probability that two clusters will collide to form a larger cluster is neglected (clusters grow by addition of single atoms or molecules).

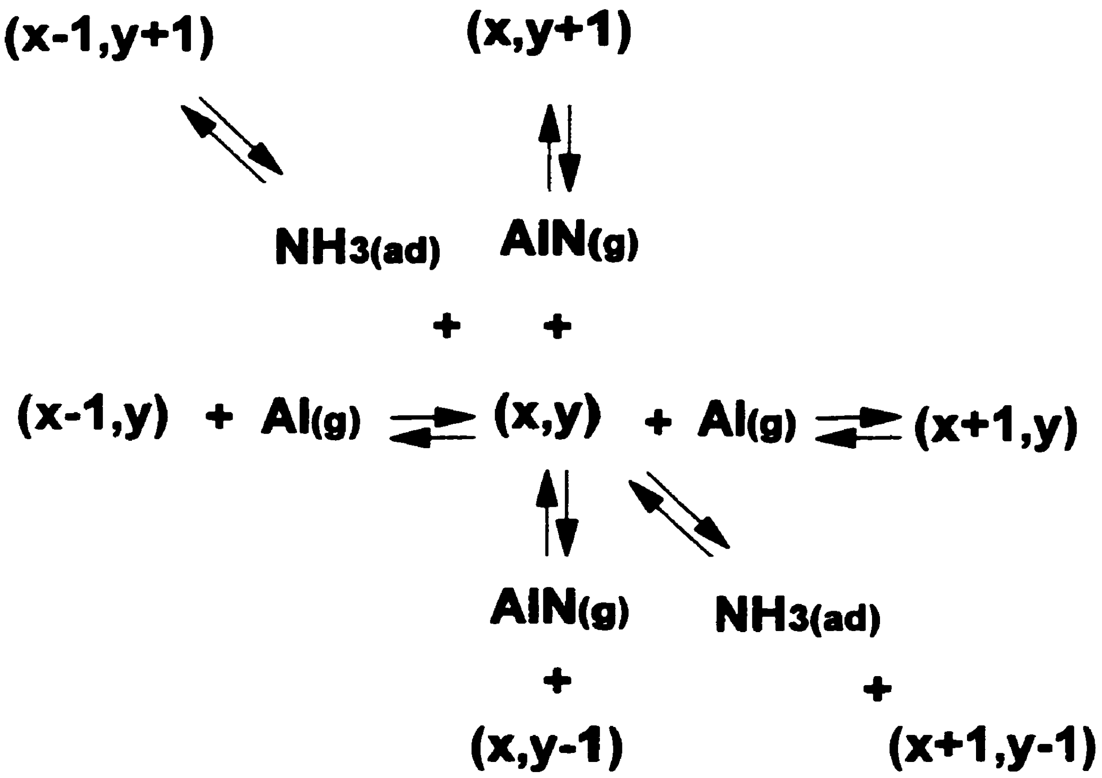

Figure 6.2 - Schematic representation of the six possible elementary reactions that a cluster size-(x,y) can undergo.

Adjusting the notation used by Reiss[40] to represent the possible reactions that a cluster can undergo in a binary composition system to the above ensemble of reactions, a cluster composed by "x" atoms of free Al and "y" AlN "molecules", and referred as an embryo (x,y), can theoretically undergo the six reactions sketched in Figure 6.2. The processes which will contribute to the growth of a cluster size-(x,y) are Al(g) condensation, AlN(g) condensation, and surface reaction between free Al and adsorbed NH_3.

Using the Reiss' planar representation of a binary system[40] in which clusters of different sizes are indicated as contiguous grid points, the growth and decay rates associated with these reactions can be visualized as shown in Figure 6.3. The coordinates represent the number of Al atoms and AlN molecules a cluster would contain. In this framework, the growth rate components are represented by vectors pointing to the growth direction. The growth (or decay) resulting from Al condensation (or evaporation) will cause a cluster to move in composition along the horizontal direction, while AlN(g) condensation will cause a cluster to move in the vertical direction. Because surface reaction "removes" an Al atom and "adds" an AlN molecule, its related vector forms an angle of 135° with the Al axis.

In principle, Al can condense anywhere on the surface of a cluster, whether this surface is formed by free Al or AlN. Al evaporation on the other hand, if it can occur from a portion of the surface formed by AlN, it would be expected to do so in a much lower rate than from a portion formed only by free Al. However, to maintain the principle of microscopic reversibility (at equilibrium, each elementary process and its reverse proceed at the same rate) it will be assumed that like condensation, Al evaporation can occur on the entire surface, independent of its composition. The net rate of growth is given by the resultant vector J(x,y) which forms an angle θ with the Al axis.

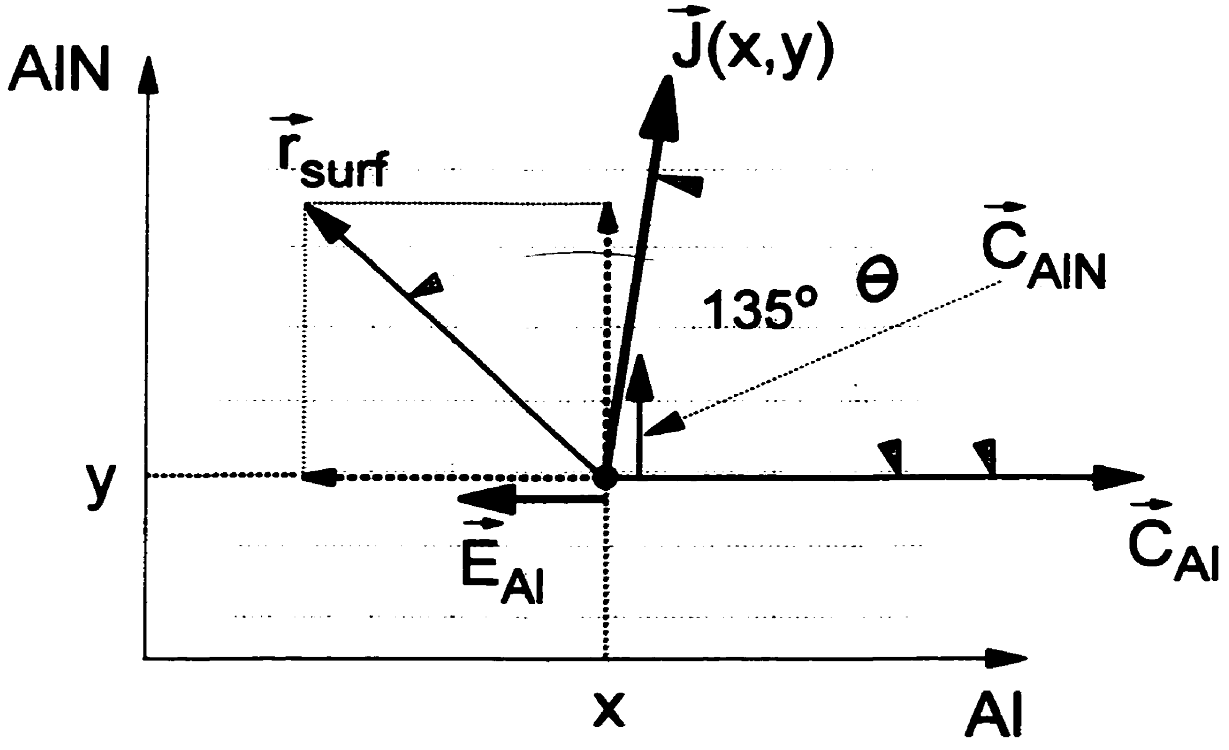

Figure 6.3 - Vectorial representation of cluster growth.

J(x,y) = net growth rate
C_{Al} = Al condensation rate
E_{Al} = Al evaporation rate
C_{AlN} = AlN(g) condensation rate
r_{surf} = surface reaction rate

$$\vec{J}(x,y) = \vec{C}_{Al} + \vec{E}_{Al} + \vec{C}_{AlN} + \vec{r}_{surf}$$

In a multicomponent system, a cluster is not only characterized by its size but also by its composition. It is a characteristic of the present reactor that the composition of the reactant species changes with the space coordinates. This occurs as a consequence of phase transition and also as a consequence of the mixing process employed. At one extreme, there are regions like the entrance of hot gas where Al concentration is high and practically no NH_3 is present, and on the other, regions like the vicinity downstream of the quenching gas injection where NH_3 concentration is high and Al species have practically vanished. Written in terms of the free-Al molar fraction present in a cluster, the cluster composition $\overline{X_c}$ is expressed as:

$$\overline{X_c} = \frac{x}{x+y} \tag{6.70}$$

An equivalent monomer-size v_1 is defined as:

$$v_1 = \frac{v}{(x+y)} \tag{6.71}$$

which can be written as a function of the cluster concentration as:

$$v_1 = \overline{X_c} v_{Al} + (1 - \overline{X_c}) v_{AlN} \tag{6.72}$$

where v_{Al} and v_{AlN} are respectively the volumes of Al atoms and AlN molecules. Using the cluster volume as the size characteristic, and with the additional assumption that individual species, as well as clusters, can be treated as spherical particles, the surface area of a cluster can be calculated as:

$$s(v) = (x+y)^{2/3} s_1 \tag{6.73}$$

where s_1 is the equivalent-monomer surface area given by:

$$s_1 = 4\pi \left(\frac{3v_1}{4\pi} \right)^{2/3} \tag{6.74}$$

At a given location, the growth rate of a cluster size-v and composition $\overline{X}_c$ is given by:

$$\frac{dv}{dt} = \frac{dx}{dt} v_{Al} + \frac{dy}{dt} v_{AlN} \tag{6.75}$$

Observation of the equilibrium diagram of Figure 4.2 and the maximum possible AlN conversion shown in Figure 4.3, shows that in the temperature range concerning the present study (≤ 2000 K), AlN decomposition is unlike to occur. Therefore, neglecting the rates at which AlN can decompose or evaporate from the cluster surface, the rates of change of number of free Al and AlN in a cluster are given as:

$$\frac{dx}{dt} = \left[a\beta^{e}_{Al}(S_{Al} - 1) - R^{s,c}_{AlN}\right](x+y)^{2/3} s_1 \tag{6.76}$$

$$\frac{dy}{dt} = \left[a\beta_{AlN} + R^{s,c}_{AlN}\right](x+y)^{2/3} s_1 \tag{6.77}$$

where β^{e}_{Al} is the Al(g) impinging rate at saturation, $S_{Al} = n_{Al}/n^{e}_{Al}$ is the Al(g) supersaturation, n_{Al} is the Al(g) number density, n^{e}_{Al} is the Al(g) number density at saturation, and $R^{s,c}_{AlN}$ is the nitridation reaction rate on the surface of a cluster.

In order to develop a general equation that takes into account the mentioned fact that reagent species concentrations change with the space coordinates, and at the same time, to introduce important simplifications that will allow this development to be cast in a form that resembles the one used by the classical theory, at this point a major assumption is made concerning cluster composition: the composition of any subcritical cluster is assumed to be determined by the rates at which Al and AlN species are added to its surface. Under this assumption the cluster composition becomes dependent only on local gas composition, which is a function of the space coordinates. Also, it is a direct consequence of this assumption that at a given location, all subcritical clusters will have the same composition.

The expressions in brackets in Equations (6.76) and 6.77) are replaced by:

$$A_x = a\beta^{e}_{Al}(S_{Al} - 1) - R^{s,c}_{AlN} \tag{6.78}$$

and

$$A_y = a\beta_{AlN} + R^{s,c}_{AlN} \tag{6.79}$$

Because neither A_x nor A_y depend on cluster composition (the surface reaction rate as further formulated depends only on the impinging rates of reacting species and not on the cluster composition), the Al to AlN number ratio in sub critical clusters can be calculated as:

$$\frac{x}{y} = \frac{dx}{dy} = \frac{A_x}{A_y} \tag{6.80}$$

and the free-aluminum mole fraction as:

$$\overline{X_c} = \left[1 + \frac{A_y}{A_x}\right]^{-1} \tag{6.81}$$

Analogous to Equation (6.63), the net rate of growth [vector $J(x, y)$ in Figure 6.3] can be expressed as the number of clusters of a given size-v that grow to size-(v+dv), per unit time, per unit volume of gas. This net rate, equal to the difference between the rate at which clusters of size-v have free-Al and AlN added by condensation and heterogeneous nitridation reaction, and the rate at which clusters of size-(v+dv) decay in size due to the reverse reactions, is given as:

$$J(v, \overline{X_c}) = f(v)n(v, \overline{X_c}) - b(v + dv)n(v + dv, \overline{X_c}) \tag{6.82}$$

For the sake of simplification, the dependence of the nucleation rate on spatial coordinates will not be indicated. In this case, the forward term $f(v)$ is written as:

$$f(v) = s(v)\left[a\beta_{AlN}v_{AlN} + a\beta_{Al}v_{Al} + R^{s,c}_{AlN}v_{AlN} - R^{s,c}_{AlN}v_{Al}\right] \tag{6.83}$$

where $s(v)$ is the surface area of the cluster, the first term in brackets is the rate of volume change due to AlN(g) condensation, the second term the rate of volume change due to Al(g) condensation, and the last two terms the rate of volume change due to surface reaction. Equation (6.83) can be written in a simplified form:

$$f(v) = s(v)\beta^{*} v_1 \tag{6.84}$$

after rearranging its right hand side terms to give:

$$\beta^{*} = \frac{1}{v_1}\left[(a\beta_{AlN} + R^{s,c}_{AlN})v_{AlN} + (a\beta_{Al} - R^{s,c}_{AlN})v_{Al}\right] \tag{6.85}$$

If, as in the classical theory, the system is arbitrarily constrained to be in equilibrium, when as a result of the microscopic reversibility principle, for all v:

$$J(v, \overline{X_c}) = 0 \tag{6.86}$$

and, if the concentration of clusters of size-v is represented by $N(v, \overline{X_c})$, the backward rate can be determined as:

$$b(v + dv) = \frac{s(v)\beta^{*} v_1 N(v, \overline{X_c})}{N(v + dv, \overline{X_c})} \tag{6.87}$$

Substituting Equation (6.87) in equation (6.82), and dividing both sides by $s(v)\beta^{*} v_1 N(v, \overline{X_c})$ results in:

$$\frac{J(v, \overline{X_c})}{s(v)\beta^{*} N(v, \overline{X_c})} = \frac{n(v, \overline{X_c})}{N(v, \overline{X_c})} - \frac{n(v + dv, \overline{X_c})}{N(v + dv, \overline{X_c})} \tag{6.88}$$

This equation can be multiplied by dv on both sides and integrated in the interval $(v_1, \overline{v})$ as:

$$\int_{v_1}^{\overline{v}} \frac{J(v,\overline{X_c})dv}{s(v)\beta^* v_1 N(v,\overline{X_c})} = \int_{v_1}^{\overline{v}} \left[\frac{n(v,\overline{X_c})}{N(v,\overline{X_c})} - \frac{n(v+dv,\overline{X_c})}{N(v+dv,\overline{X_c})} \right] dv \tag{6.89}$$

If the term in brackets on the right hand side is approximated by a summation, it is easier to see that successive terms cancel resulting in a difference of the last and first terms of the summation.

At steady state, $J(v,\overline{X_c})$ becomes constant for all v, and since β^* is independent of cluster size, Equation (6.89) can be written as:

$$\frac{J}{\beta^* v_1} \int_{v_1}^{\overline{v}} \frac{dv}{s(v)N(v,\overline{X_c})} = \frac{n(v_1,\overline{X_c})}{N(v_1,\overline{X_c})} - \frac{n(\overline{v},\overline{X_c})}{N(\overline{v},\overline{X_c})} \tag{6.90}$$

Following, it is observed that for a sufficiently large $\overline{v}$ it results that $n(\overline{v},\overline{X_c}) \to 0$, and consequently the last term on the right hand side of Equation (6.90) becomes nil. By defining:

$$H(v,\overline{X_c}) = \ln\left[s(v)N(v,\overline{X_c}) \right] \tag{6.91}$$

Equation (6.90) can then be written:

$$J = \frac{n(v_1,\overline{X_c})\beta^* v_1}{N(v_1,\overline{X_c})} \left[\int_{v_1}^{\overline{v}} \exp\left[-H(v,\overline{X_c}) \right] dv \right]^{-1} \tag{6.92}$$

The next step in this development consists of expanding $H(v,\overline{X_c})$ around the critical cluster size, identified as $(v^*,\overline{X_c})$, in a Taylor series truncated at the second derivative. In doing so, it is observed that because the equilibrium distribution $N(v,\overline{X_c})$ has a minimum when $v = v^*$, the first derivative equals zero:

$$H'(v^*,\overline{X_c}) = 0 \tag{6.93}$$

The resulting expanded function is then written:

$$H(v,\overline{X_c}) = H(v^*,\overline{X_c}) + \frac{(v-v^*)^2}{2}H''(v^*,\overline{X_c}) \tag{6.94}$$

With Equation (6.94) substituted in (6.92), making the change of variables and using the definition of the error function [see Appendix A(1)] gives:

$$J = \frac{n(v_1,\overline{X_c})\beta^* v_1}{N(v_1,\overline{X_c})}\exp\left[H(v^*,\overline{X}_c)\right]\left[\frac{H''(v^*,\overline{X_c})}{2\pi}\right]^{1/2} \tag{6.95}$$

It was shown by Reiss[40] that in a binary system at equilibrium, the simultaneous solution of the set of equations formed by the free-energy change of the system and the species conservation equations is a Boltzmann type of distribution. Adapted to the present nomenclature this distribution can be expressed as:

$$N(v,\overline{X_c}) = F\exp\left[-\frac{\Delta G(v,\overline{X_c})}{k_B T}\right] \tag{6.96}$$

where $\Delta G(v,\overline{X_c})$ is the Gibbs free energy of formation of a cluster size-v and composition $\overline{X_c}$, and in Reiss' theory F is the total number of species, including clusters. Reiss argued that this distribution remains valid when the system is constrained to a metastable equilibrium, and the kinds of clusters that exist in this condition are arbitrarily limited. This is essentially the condition on which the classical theory is built[51].

The substitution of Equations (6.71), (6.73), and (6.96) in (6.91) gives:

$$H(v,\overline{X_c}) = \ln s_1 + \frac{2}{3}\ln\frac{v}{v_1} + \ln F - \frac{\Delta G(v,\overline{X_c})}{k_B T} \tag{6.97}$$

Considering only the initial and final states in the gas-to-condensed phase transition, and neglecting the free-energy change associated with the mixing of two components, after the Blander and Katz observation[61] the free energy change to form a cluster size-(x,y) is written as:

$$\frac{\Delta G(v,\overline{X_c})}{k_B T} = -(\frac{v}{v_1} - 1)\ln S_{Al} + \frac{v}{v_1}(1 - \overline{X_c})\left(\frac{\Delta G_r}{k_B T}\right)_L + \left(\frac{v}{v_1}\right)^{2/3}\theta \tag{6.98}$$

where ΔG_r is the free energy change associated with the nitridation reaction, assumed to occur only in the liquid phase (subscript L). The substitution of Equation (6.98) in (6.97) gives:

$$H(v,\overline{X_c}) = \ln s_1 + \frac{2}{3}\ln\frac{v}{v_1} + \ln F + (\frac{v}{v_1} - 1)\ln S_{Al} - \frac{v}{v_1}(1 - \overline{X_c})\left(\frac{\Delta G_r}{k_B T}\right)_L - \left(\frac{v}{v_1}\right)^{2/3}\theta \tag{6.99}$$

The first derivative of Equation (6.91) is then written:

$$H'(v,\overline{X_c}) = \frac{2}{3}v^{-1} + \frac{1}{v_1}\ln S_{Al} - \frac{(1 - \overline{X_c})}{v_1}\left(\frac{\Delta G_r}{k_B T}\right)_L - \frac{2}{3}\frac{v^{-1/3}}{v_1^{2/3}}\theta \tag{6.100}$$

and the second derivative is written:

$$H''(v,\overline{X_c}) = -\frac{2}{3}v^{-2} + \frac{2}{9}\frac{v^{-4/3}}{v_1^{2/3}}\theta = -\frac{2}{3}v^{-2}\left[1 - \frac{1}{3}\left(\frac{v}{v_1}\right)^{2/3}\theta\right] \tag{6.101}$$

By realizing that:

$$\frac{1}{3}\left(\frac{v}{v_1}\right)^{2/3}\theta \gg 1 \tag{6.102}$$

Equation (6.101) can be approximated to:

$$H''(v,\overline{X_c}) = \frac{2}{9}\frac{v^{-4/3}}{v_1^{2/3}}\theta \tag{6.103}$$

The fact that the first derivative of Equation (6.91) equals zero when a cluster reaches the critical size is used to calculate the critical cluster size. Thus, after Equation (6.93), the following expression is derived [see Appendix A(2)]:

$$\frac{2}{3}\left(\frac{v}{v_1}\right)^{2/3}\theta = \frac{v}{v_1}\left[\ln S_{Al} - (1-\overline{X_c})\left(\frac{\Delta G_r}{k_B T}\right)_L\right] \tag{6.104}$$

Observing that:

$$\left(\frac{v}{v_1}\right)^{2/3}\theta \gg 1 \tag{6.105}$$

it results [see Appendix A(3)]:

$$v = \left[\frac{2}{3}\frac{\theta}{\mathrm{LnS}}\right]^3 v_1 \tag{6.106}$$

where, for simplification "LnS" is defined as:

$$\mathrm{LnS} = \ln S_{Al} - (1-\overline{X_c})\left(\frac{\Delta G_r}{k_B T}\right)_L \tag{6.107}$$

Substitution of Equations (6.91) and (6.103) in (6.95) gives:

$$J = \frac{n(v_1,\overline{X_c})\beta^* v_1}{N(v_1,\overline{X_c})} s(v) N(v,\overline{X})\left(\frac{1}{9}\frac{v^{-4/3}}{v_1^{2/3}}\theta\right)^{1/2}\frac{1}{\sqrt{\pi}} \tag{6.108}$$

After substitution of the Equations (6.71), (6.73), and (6.96) in (6.108), it results in:

$$J = \frac{n(v_1,\overline{X_c})\beta^* s_1 F}{3N(v_1,\overline{X_c})}\sqrt{\frac{\theta}{\pi}}\exp\left[-\frac{\Delta G(v^*,\overline{X_c})}{k_B T}\right] \tag{6.109}$$

Developing the free energy contained in the argument of the exponential term according to Equation (6.98) and using Equations (6.103) and (6.115) gives:

$$\frac{\Delta G(v^{*},\overline{X_c})}{k_B T} = -(\frac{v}{v_1})\left[\ln S_{Al} - (1-\overline{X_c})\left(\frac{\Delta G_r}{k_B T}\right)_L\right] + \left[\frac{2}{3}\frac{\theta}{\mathrm{LnS}}\right]^2 \theta + \ln S_{Al} \qquad (6.110)$$

Next, replacing the term in the first brackets by **LnS** as defined by Equation (6.107), and using Equation (6.106), and making the needed rearrangements it results [see Appendix A(3)]:

$$\frac{\Delta G(v^{*},\overline{X}_c)}{k_B T} = \frac{4}{27}\frac{\theta^3}{(\mathrm{LnS})^2} + \ln S_A \qquad (6.111)$$

With the use of Equation (6.111), after substituting back LnS, Equation (6.108) is written:

$$J = \frac{n(v_1,\overline{X_c})\beta^{*} s_1 F}{3N(v_1,\overline{X_c})S_{Al}}\sqrt{\frac{\theta}{\pi}}\exp\left[-\frac{4}{27}\frac{\theta^3}{\left(\ln S_{Al} - (1-\overline{X_c})\left(\frac{\Delta G_r}{k_B T}\right)_L\right)^2}\right] \qquad (6.112)$$

In the classical theory, the development of Equation (6.67) following the procedure used above gives the nucleation rate written in the form of Equation (6.109):

$$J = \frac{n(1)\beta s_1 \overline{N}}{3N(1)}\sqrt{\frac{\theta}{\pi}}\exp\left[-\frac{\Delta G(i^{*})}{k_B T}\right] \qquad (6.113)$$

where $n(1)$ and $N(1)$ are the concentrations of monomers in the real condition and at the constrained equilibrium, respectively. The further development of Equation (6.113) depends on which definition of the free energy to form a cluster is used. The classical theory[66] defines this free energy as:

$$\frac{\Delta G(i)}{k_B T} = -i \ln S + \theta i^{2/3} \tag{6.114}$$

Blander and Katz[61] noted a misconception in the derivation of the above equation. Following a strict thermodynamic formulation they derived a more precise definition written as:

$$\frac{\Delta G(i)}{k_B T} = -(i-1)\ln S + \theta i^{2/3} \tag{6.115}$$

The normalization constant $\overline{N}$ in Equation (6.113) is taken equal to $N(1)$, the number density of monomers at the constrained equilibrium. The final expression of the nucleation rate resulting from these two definitions of free energy to form a cluster differs by the number density of monomers used in the numerator of the first term in the right hand side: $n(1)$ in the classical theory and $n^e(1)$ after Blander and Katz's correction, where the superscript e refers to the saturated condition. In the last case, the nucleation rate is written as:

$$J = \frac{n^e(1)\beta s_1}{3}\sqrt{\frac{\theta}{\pi}}\exp\left[-\frac{4}{27}\frac{\theta^3}{\ln^2 S}\right] \tag{6.116}$$

The similarities between the forms of Equations (6.112) and (6.116) are obviously a consequence of casting the net flux of cluster growth in the form of Equation (6.63) by means of the simplifications introduced in the present development.

Resuming the development of Equation (6.112), an assumption has to be made about the normalization constant F and the monomer number density $n(v_1, \overline{X_c})$. In a multicomponent system, F is taken as the summation of the condensable chemical species which are present in the gas phase[67]. In the present case, because of the adoption of the equivalent monomer volume v_1, following the steps of the classical theory and taking F as $N(v_1, \overline{X_c})$ seems a straight forward procedure. If it is recalled that both F and $N(v_1, \overline{X_c})$ refer to a pseudo-equilibrium situation, and are unknown, the adoption of this procedure adds the convenience of eliminating these terms from the nucleation rate equation.

In the case of the monomer number density, two possibilities were considered. Invoking the low amount of AlN(g) present at equilibrium, a straight forward procedure would be to assume that $n_{Al} \gg n_{AlN}$, where n_{Al} and n_{AlN} are the Al and AlN gaseous species number densities, and approximate $n(v_1, \overline{X_c})$ by n_{Al}. The other possibility would be to define $n(v_1, \overline{X_c})$ in terms of the total volume of Al and AlN species and leave the numerical calculation to proceed according to locally calculated number densities. The second possibility was adopted and $n(v_1, \overline{X_c})$ was defined by the expression:

$$n(v_1, \overline{X_c}) = \frac{n_{Al} v_{Al} + n_{AlN} v_{AlN}}{v_1} \tag{6.117}$$

After these considerations, Equation (6.112) is finally written:

$$J = \frac{n(v_1, \overline{X_c}) \beta^* s_1}{3 S_{Al}} \sqrt{\frac{\theta}{\pi}} \exp\left[-\frac{4}{27} \frac{\theta^3}{\left(\ln S_{Al} - (1 - \overline{X_c}) \left(\frac{\Delta G_r}{k_B T} \right)_L \right)^2} \right] \tag{6.118}$$

The computation of the nucleation rate still requires the determination of the heterogeneous reaction rate, the free energy change associated with the AlN surface reaction, and the surface energy associated with the binary cluster.

The free energy of the AlN heterogeneous reaction was determined from thermodynamic data[29] for the overall reaction:

$$Al_{(l)} + NH_3 \rightarrow AlN + \frac{3}{2} H_2 \tag{6.119}$$

The surface reaction rate and the surface energy were estimated as described next.

6.7. Reaction rates

The inclusion of chemical reaction in the treatment of the nucleation and growth process certainly requires knowledge of the specific reaction rates. For the Al-N system, no information is presently available in the literature. To proceed with the present study, assumptions had to be made concerning the possible reaction mechanisms.

It was mentioned before that, according to the Al-N-H-Ar equilibrium diagram (Figure 4.2), the heterogeneous reaction might be by far the most important mechanism for the AlN production. However, in order to better evaluate the importance of the gas phase reaction compared with the surface reaction mechanism, the net rate of formation of AlN(g) was also included in the numerical simulation.

Because the determination of the homogeneous reaction rate requires the calculation of the concentration of atomic nitrogen, the compilation of available kinetic data on the thermal decomposition of NH_3 has been included in this section.

6.7.1. The thermal decomposition of NH_3

As described in the experimental section, the total NH_3 decomposition was evaluated by measuring its concentration in the gas at the exit of the reactor using a simple analytical procedure. Decomposition in a broad range was measured, depending on the operating conditions (Table 5.2).

For numerical simulation of the particle nucleation and growth in the present reacting system, the NH_3 concentration distribution in the calculation domain has to be determined. For this reason, the data available in the literature on the kinetics of the thermal decomposition of NH_3 is briefly reviewed.

The thermal decomposition of NH_3 has been studied using shock wave experiments since the early 60's. Not withstanding the amount of data collected, it still seems a contentious matter, with two different reactions proposed as the rate limiting step. Yumura and Asaba[72] determined the rate constants of several steps in the process by monitoring the concentration of atomic hydrogen using a NH_3/Ar mixture. Table 6.1, compiled primarily from their work, shows the rate parameters for the several elementary reactions involved in the ammonia thermal decomposition mechanism. They assumed the initiation and rate controlling reaction to be the NH_3/Ar collision, Equation (1a). On the other hand, Holzrichter and Wagner[73] studied the unimolecular decomposition, Equation (1b), considering this reaction as the initial and limiting step. Because the unimolecular reaction predicts a greater decomposition rate, it was adopted as the ammonia decomposition limiting step.

Table 6.1 - Elementary reactions and rate parameters for the thermal decomposition of ammonia, $k = AT^n \exp(-E/RT)$. Units: reaction (1a): (sec^{-1}); all others: ($\text{cm}^3.\text{mole}^{-1}.\text{sec}^{-1}$).

nr.(1)	Reaction	A	n	E (kJ/mole)	Equation nr.	Ref.
1a	$NH_3 + Ar \rightarrow NH_2 + H + Ar$	1.78E+016	0	385.6	(6.120*a*)	[72]
1b	$NH_3 \rightarrow NH_2 + H$	5.50E+015	0	451.0	(6.120*b*)	[73]
2	$NH_3 + H \rightarrow NH_2 + H_2$	1.26E+014	0	90.0	(6.121)	[72]
3	$NH_2 + H \rightarrow NH + H_2$	3.02E+013	0	35.8	(6.122)	[72], [74]
4	$2NH \rightarrow N_2 + 2H$	2.45E+013	0	0.0	(6.123)	[75]
5	$NH_2 + M \rightarrow NH + H + M$	2.04E+014	0	289.4	(6.124)	[72]
6	$NH + M \rightarrow N + H + M$	3.23E+012	0.5	290.8	(6.125)	[76]
7	$NH_3 + NH_2 \rightarrow N_2H_3 + H_2$	7.94E+011	0.5	90.3	(6.126)	[77]
8	$N_2H_3 + M \rightarrow NH_2 + NH + M$	6.31E+012	0	41.9	(6.127)	[77]
9	$2NH_2 \rightarrow NH + NH_3$	6.31E+012	0	41.9	(6.128)	[77]
10	$H_2 + M \rightarrow 2H + M$	2.34E+014	0	410.0	(6.129)	[78]

[1] Reaction number, used for indexation.

6.7.2. The gas phase aluminum nitride reaction

The calculation of the gas phase reaction rate was based on the following reactions:

(Reaction nr. 11) $$Al_{(g)} + N + M \rightleftarrows AlN(g) + M \qquad (6.130)$$

(Reaction nr. 12) $$N_2 + M \rightleftarrows 2N + M \qquad (6.131)$$

plus the ammonia decomposition reactions involved in the formation of atomic nitrogen given in Table 6.1. The general species M is considered to be Ar. The reactions involving NH_3 or any of its radicals were discarded. From equilibrium thermodynamic analysis, it is seem that such reactions have considerably smaller equilibrium constants than the reactions involving atomic nitrogen. The reaction numbers indicated on the left side of Equations (6.130) and (6.131) are used for indexation.

From Equation (6.130), the net rate of formation of AlN(g) is written:

$$R^{g}_{AlN} = \frac{d[AlN]}{dt} = k^{f}_{11}[Al][N][M] - k^{b}_{11}[AlN][M] \qquad (6.132)$$

where k^{f}_{11} and k^{b}_{11} are respectively the forward and backward rates for this reaction, and the terms in square brackets refer to species concentrations given in (moles/cm^3). Neither the forward or backward rate for this reaction is known. Therefore, these rates were estimated using the reaction equilibrium constant:

$$K_{C,11} = \frac{k^{f}_{11}}{k^{b}_{11}} \qquad (6.133)$$

The equilibrium constant was obtained from thermochemistry data[29] as:

$$\log K_{P,11} = -5.1761 + \frac{1.4972x10^4}{T} - \frac{6.8425x10^5}{T^2} \qquad (6.134)$$

with $K_{P,11}$ given in (atm^{-1}) units. Therefore:

$$K_{P,11} = K_{C,11}\frac{[M]}{p} = \frac{k_{11}^f}{k_{11}^b}\frac{[M]}{p} \qquad (6.135)$$

Because in the present case the pressure (p) is numerically equal to 1, it was excluded from the formulation. The rate constant for the AlN(g) dissociation was estimated using the collision theory for gas phase dissociation-recombination reactions[79]. According to this theory, the rate corresponding to the dissociation equation (backward direction of Equation (6.130)) can be written as:

$$\left(\frac{d[AlN]}{dt}\right)_b = P\left(\frac{\varepsilon_o}{k_B T}\right)^{s-1}\frac{\exp\left(\frac{-\varepsilon_o}{k_B T}\right)}{(s-1)!}\sqrt{8\pi k_B T\left(\frac{1}{m_{AlN}}+\frac{1}{m_M}\right)}\,(r_{AlN}+r_M)^2[AlN][M]N_{Av} \qquad (6.136)$$

where: P is the steric factor; s is the number of squares terms; ε_o is the AlN(g) dissociation energy (activation energy); m and r, are the mass and atomic or molecular radius, respectively, of the colliding species; N_{Av} is the Avogrado number; and T is the absolute temperature. In this case, P , s and ε_o had to be evaluated. The steric factor, which expresses the fact that the colliding species may not have the proper orientation relative to each other, was assumed to be 0.01 by considering an atom-linear molecule collision based reaction[80]. The number of square terms was adopted as 2, considering an atom-molecule interaction[79] (a square term meaning a term expressing the molecular energy which is quadratic in some appropriate variable used to describe the energy; $s = 1$ meaning that only translation energy along the line of centers of gravity is considered). The AlN(g) dissociation energy was estimated as the molecular enthalpy change for the reaction:

$$AlN(g) \rightarrow Al(g) + N(g) \qquad (6.137)$$

Using thermochemistry data[29] for the temperature range considered in this study, the dissociation energy is written after regression analysis as:

$$\varepsilon_0 = \frac{\left(274.3674 + 0.2934 \times \sqrt{T}\right)}{N_{Av}} \tag{6.138}$$

This gives for the backward reaction rate:

$$k_{11}^{b} = P\left(\frac{\varepsilon_o}{k_B T}\right)^{s-1} \frac{\exp\left(\frac{-\varepsilon_o}{k_B T}\right)}{(s-1)!} \sqrt{8\pi k_B T\left(\frac{1}{m_{AlN}} + \frac{1}{m_M}\right)}\,(r_{AlN} + r_M)^2 N_{Av} \tag{6.139}$$

With the use of Equation (6.135), Equation (6.132) becomes:

$$\frac{d[AlN]}{dt} = k_{11}^{b}\left(K_{P,11}[Al][N] - [AlN][M]\right) \tag{6.140}$$

The concentration of atomic nitrogen is determined from the balance of the rate of change of the ammonia radicals (indexes are as defined in Table 6.1):

$$\frac{d[NH_2]}{dt} = k_{1b}[NH_3] + k_2[NH_3][H] - k_3[NH_2][H] - k_5[NH_2][M] \tag{6.141}$$

$$\frac{d[NH]}{dt} = k_3[NH_2][H] + k_5[NH_2][M] - k_6[NH][M] \tag{6.142}$$

$$\frac{d[N]}{dt} = k_6[NH][M] + 2k_{12}^{f}[N_2][M] + k_{11}^{b}[AlN][M] - 2k_{12}^{b}[N]^2[M] - k_{11}^{f}[Al][N][M] \tag{6.143}$$

Assuming that the concentrations of the intermediates NH_2, NH, N, and H are small compared to NH_3, N_2 and H_2 concentrations, and making use of the steady state approximation (the low concentration intermediates are destroyed as rapidly as they are formed[81], and therefore their rates are nil), Equations (6.141) to (6.143) are summed to give:

$$k_{1b}[NH_3]+k_2[NH_3][H]+2k^f_{12}[N_2][M]+k^b_{11}[AlN][M]-2k^b_{12}[N]^2[M]-k^f_{11}[Al][N][M]=0 \tag{6.144}$$

After realizing that:

$$k_{1b}[NH_3]+k_2[NH_3][H] \gg 2k^f_{12}[N_2][M] \tag{6.145}$$

and that, because of the relatively low concentration of $Al_{(g)}$ if compared to the general species M, the reaction of Equation (130) represents a minor contribution to the atomic N equilibrium, Equation (6.144) can be simplified to:

$$k_{1b}[NH_3]+k_2[NH_3][H]-2k^b_{12}[N]^2[M]=0 \tag{6.146}$$

In other words, the atomic nitrogen resulting from the reaction of Equation (6.125), Table 6.1, is assumed to be mostly consumed by the recombination reaction, the reverse of Equation (6.131).

The atomic hydrogen concentration is determined from the assumption that steady state hydrogen is dictated by the balance of the reactions of Equations (6.120b) and (6.121)[72]:

$$\frac{d[H]}{dt}=k_{1b}[NH_3]-k_2[NH_3][H]=0 \tag{6.147}$$

which results in:

$$[H]=\frac{k_{1b}}{k_2} \tag{6.148}$$

The backward rate of the N_2 dissociation (Equation (6.131)), was calculated as:

$$k_{12}^{b} = \frac{k_{12}^{f}}{K_{C,12}} = \frac{p}{[M]}\frac{k_{12}^{f}}{K_{P,12}} \tag{6.149}$$

with the equilibrium constant $K_{P,12}$ obtained from thermochemistry tables[29] approximated by a polynomial equation using regression analysis:

$$\log K_{P,12} = 6.9049 - \frac{5.0071\times10^{4}}{T} + \frac{1.2818\times10^{5}}{T^{2}} \tag{6.150}$$

For the same reason as in Equation (6.135), the pressure factor was excluded from the formulation. The substitution of the atomic hydrogen concentration and the backward rate of the nitrogen decomposition equation in Equation (6.147) gives:

$$k_{1b}[NH_3] - \frac{k_{12}^{f}}{K_{P,12}}[N]^{2} = 0 \tag{6.151}$$

and therefore:

$$[N] = \sqrt{\frac{K_{P,12}k_{1b}[NH_3]}{k_{12}^{f}}} \tag{6.152}$$

And finally, with the substitution of (6.152) in (6.141), the net rate of formation of AlN(g) is written:

$$R_{AlN}^{g} = k_{11}^{b}\left(K_{P,11}[Al]\sqrt{\frac{K_{P,12}k_{1b}[NH_3]}{k_{12}^{f}}} - [AlN][M]\right) \tag{6.153}$$

(moles/cm^{3}s)

Because AlN(g) can condense on the surface of forming particles, the net change of its concentration, to be considered as the source term for the respective conservation equation, is given by:

$$S_{AlN} = R_{AlN}^{g} - R_{AlNcon} \tag{6.154}$$

6.7.3. The surface reaction rate

The kinetics of the heterogeneous reaction between aluminum and ammonia (or any of its radicals) is unknown. For this reason, two simple reaction mechanisms were considered. Although they might be identical in nature, heterogeneous reaction on the surface of sub critical clusters and on the surface of stable particles were formulated on different basis, according to the assumptions presented next.

6.7.3.1. Sub-critical particles

It was assumed that the AlN surface reaction can consume all or part of the aluminum which condenses on the cluster surface; whatever happens depends on the local gas-phase concentrations of aluminum vapour and ammonia.

If the local concentration of ammonia is low, and does not allow the ammonia adsorption rate to overcome the rate of aluminum condensation on the surface of a cluster, ammonia adsorption was considered as the reaction limiting step. On the other hand, if local gas-phase concentration is such that the ammonia adsorption rate could be larger than the rate of aluminum deposition, then it was considered that the net aluminum condensation becomes the surface reaction limiting step. The adsorption of ammonia was estimated from the rate of incidence of ammonia molecules on the surface of the cluster and a mass accommodation coefficient. The above stated dependence is expressed by the following relations:

In case $a'\beta_{NH_3} \leqslant a\beta^{e}_{Al}(S_{Al}-1)$, the reaction rate is calculated as:

$$R^{s,c}_{AlN} = a'\beta_{NH_3} \tag{6.155}$$

If otherwise $a'\beta_{NH_3} > a\beta^{e}_{Al}(S_{Al}-1)$, the reaction rate is calculated as:

$$R^{s,c}_{AlN} = a\beta^{e}_{Al}(S_{Al}-1) \tag{6.156}$$

where the incidence/condensation rates of ammonia and aluminum are calculated as:

$$\beta_{NH_3} = \frac{p_{NH_3}}{\sqrt{2\pi k_B m_{NH_3} T}} \tag{6.157}$$

and

$$\beta^e_{Al} = \frac{p^e_{Al}}{\sqrt{2\pi k_B m_{Al} T}} \tag{6.158}$$

were β^e_{Al} is the aluminum condensation rate at saturation and S_{Al} the aluminum supersaturation:

$$S_{Al} = \frac{p_{Al}}{p^e_{Al}} \tag{6.159}$$

and p_{Al} and p^e_{Al} are respectively the partial and saturation vapour pressures of Al.

The mass accommodation coefficient a for Al was assumed to be 1.0. In case of NH_3, considering that unlike Al, ammonia is a volatile species adsorbed on the particle surface, a mass accommodation coefficient $a' = 0.01$ was assumed.

6.7.3.2. Stable particles

The above assumption of a surface reaction rate controlled either by NH_3 adsorption or Al condensation - ultimately depending on their local concentrations - may be plausible when applied to subcritical particles which can grow or decay in size in very short periods of time, as is the case of homogeneous nucleation. In case of surface growth of stable particles, which flow along with the gas stream, this situation may change. Particles which nucleate and grow in the presence of little or no NH_3 (and therefore have excess Al in their composition) may travel to regions where the NH_3 concentration can be high. Therefore, not only newly condensed Al but also the free Al already present in the particle may react.

In this case, it was assumed that the surface reaction is controlled by the rate of incidence of NH_3 molecules on the surface of particles, and that its rate was proportional to the reactive fraction of the particle surface[37]. This surface fraction was approximated by the average volumetric fraction of free-Al in the whole particle $\overline{X}_v$:

$$R_{AlN}^{s,p} = a'\beta_{NH_3}\overline{X}_v \tag{6.160}$$

Assuming that individual particles have the average composition calculated for the powder, the surface fraction is determined as:

$$\overline{X}_v = \frac{\overline{X}_p v_{Al}}{v_{AlN} + \overline{X}_p(v_{Al} - v_{AlN})} \tag{6.161}$$

As in the case of reaction on the surface of clusters, a mass accomodation coefficient $a' = 0.01$ was assumed.

6.8. Physical properties

6.8.1. Aluminum vapour pressure

The Al vapour pressure was taken from tabulated thermochemistry data[29]. These data are comparable to the less recent vapour pressure data given by Kubaschewsky[82].

6.8.2. The surface energy

The surface energy of a cluster which has Al and AlN in its composition was calculated as the sum of the surface energies corresponding to the surface area of the cluster occupied by each species. Considering a cluster size-$(v,\overline{X_c})$, the surface areas corresponding to Al and AlN were approximated as being proportional to the fraction of volume they occupy in the cluster. Under these assumptions, the average surface energy is written as

$$\sigma = \frac{\overline{X_c} v_{Al} \sigma_{Al} + (1-\overline{X_c}) v_{AlN} \sigma_{AlN}}{v_1} \tag{6.162}$$

The surface energy of liquid aluminum was taken as its surface tension which is a function of temperature expressed by[83]

$$\sigma_{Al} = 0.914 - 3.5 \times 10^{-4}(T - 933) \tag{6.163}$$

Because there is no evidence that AlN is present as a liquid phase[23], it was assumed that its condensation occurs directly to the solid phase, in crystalline form. Its surface energy was estimated as the energy of unsatisfied bonding of surface atoms[84], based on the AlN crystal structure which is shown in Figure 4.1. Because packing density depends on plane direction, the surface energy of each crystal plane is different. Also, because growth is governed by Al pickup (if there is no Al condensation, clusters do not grow simply by NH_3 adsorption), considering only

Al-N bonds, the surface energy of AlN was estimated as the bond strength of the total number of unsatisfied bonding of surface Al atoms on a basal plane (planes A or C). Al occupies tetrahedral sites, which results in one unsatisfied bond left on the crystal surface. Referred to a unit cell basal plane, the surface energy is written:

$$\sigma_{AlN} = \frac{n(D_{Al-N}/2)}{A} \tag{6.164}$$

where n is the number of Al atoms in the basal plane, D_{Al-N} the dissociation energy of the Al-N bond, $A = [a_o(1 + \alpha\Delta T)]^2 \cos 30^\circ$ the basal plane surface area, α the AlN thermal expansion[25], and $\Delta T = T - 298$ the temperature difference. The thermal expansion coefficient of AlN as a function of temperature is given in Table 4.1. Division of the dissociation energy by two results from the fact that each bond is shared by two atoms.

Although bond dissociation energies may differ considerably from mean bond energies calculated solely from thermochemical data, a good agreement is found between the value of 297.2 ± 96.3 kJ/mol at 298 K tabulated for the Al-N bond[85] and the bond strength evaluated as the mean bond energy to be added to separate components into neutral free atoms at the given temperature and pressure. Using thermodynamic data[29] in a broad range of temperature for the reaction:

$$AlN \rightarrow Al(g) + N(g) \tag{6.165}$$

and a regression analysis, the temperature dependence of the surface tension of aluminum nitride is written:

$$\sigma_{AlN} = 2.8191 - 6.7217 \times 10^{-5} T + 3.1225 \times 10^{-9} T^2 - 2480.5715/T^2 \tag{6.166}$$

A comparison of the surface energy of AlN calculated as above and the one of liquid Al is shown in Figure 6.4.

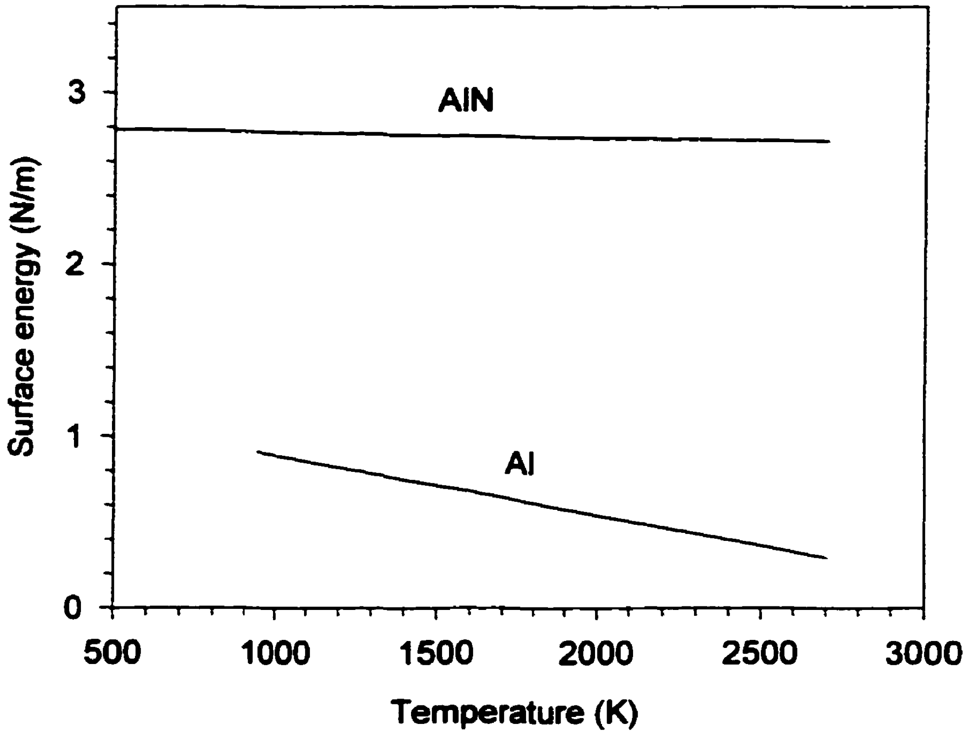

Figure 6.4 - Surface energy of Al and AlN as a function of temperature.

6.9. Gas flow

The momentum, energy, and species conservation equations were solved in order to determine the fields of velocity, temperature, and species concentration along the reaction zone. All chemical species but Al were considered at this step.

6.9.1. Conservation equations

The following is the set of differential equations, written in cylindrical coordinates, which were simultaneously solved at this stage:

Continuity:

$$\frac{1}{r}\frac{\partial}{\partial r}\left(\rho r v\right) + \frac{\partial}{\partial z}\left(\rho u\right) = 0 \tag{6.167}$$

r-Momentum:

$$\frac{\partial}{\partial r}\left(\rho v v\right) + \frac{\partial}{\partial z}\left(\rho u v\right) = \frac{\partial}{\partial z}\left(\mu\frac{\partial v}{\partial z}\right) + \frac{2}{r}\frac{\partial}{\partial r}\left(r\mu\frac{\partial v}{\partial r}\right) + \frac{\partial}{\partial z}\left(\mu\frac{\partial u}{\partial z}\right) - \frac{\partial p}{\partial r} \tag{6.168}$$

z-Momentum:

$$\frac{\partial}{\partial r}\left(\rho v u\right) + \frac{\partial}{\partial z}\left(\rho u u\right) = \frac{1}{r}\frac{\partial}{\partial r}\left(r\mu\frac{\partial u}{\partial r}\right) + \frac{1}{r}\frac{\partial}{\partial r}\left(r\mu\frac{\partial v}{\partial z}\right) + 2\frac{\partial}{\partial z}\left(\mu\frac{\partial u}{\partial z}\right) - \frac{\partial p}{\partial z} \tag{6.169}$$

Energy:

$$\begin{aligned}\frac{\partial}{\partial r}\left(\rho v h\right) + \frac{\partial}{\partial z}\left(\rho u h\right) = {} & \frac{1}{r}\frac{\partial}{\partial r}\left(\rho\frac{k}{C_p}\frac{\partial h}{\partial r}\right) + \frac{\partial}{\partial z}\left(\rho\frac{k}{C_p}\frac{\partial h}{\partial z}\right) + \\ & \frac{1}{r}\frac{\partial}{\partial r}r\sum_i\left[h_i\left(\Gamma_i - \frac{k}{C_p}\right)\frac{\partial w_i}{\partial r}\right] + \\ & \frac{\partial}{\partial z}\sum_i\left[h_i\left(\Gamma_i - \frac{k}{C_p}\right)\frac{\partial w_i}{\partial r}\right] + S_n\end{aligned} \tag{6.170}$$

Chemical species:

$$\frac{\partial}{\partial r}\left(\rho v w_i\right)+\frac{\partial}{\partial z}\left(\rho u w_i\right)=\frac{1}{r}\frac{\partial}{\partial r}\left(\rho D_{i,Ar}\frac{\partial w_i}{\partial r}\right)+\frac{\partial}{\partial z}\left(\rho D_{i,Ar}\frac{\partial w_i}{\partial z}\right)+S_i \qquad (6.171)$$

Energy (thermal insulation):

$$\frac{1}{r}\frac{\partial}{\partial r}\left(rk\frac{\partial T}{\partial r}\right)+\frac{\partial}{\partial z}\left(\rho k\frac{\partial T}{\partial z}\right)=0 \qquad (6.172)$$

At each iteration step, the temperature field was calculated by interpolation using the calculated gas enthalpy and gas composition, and tabulated values for the enthalpy of the species in the gas mixture.

6.9.2. Thermodynamic and transport properties

The thermodynamic and transport properties (enthalpy, thermal conductivity, and viscosity) of the gaseous species Ar, N_2, H_2, and NH_3 were obtained from tabulated data[32],[86],[29]. The viscosity of the gas mixture was calculated using the method of Wilke[87], and its thermal conductivity calculated using similar prediction equations[88].

The mass diffusivities of the several gas species in the mixture were calculated using the Chapman-Enskog theory[88]. Because argon is by far the gas with the highest concentration, the mass diffusivities were calculated considering a binary system gas species-argon.

6.10. Boundary conditions

6.10.1. Fluid flow, species concentrations and temperature

Figure 6.5 shows the boundary conditions used in the calculation of the velocity, species concentration, and temperature fields inside the tubular reactor, in the radial and axial injection of NH_3. Temperature and species concentrations at the boundaries were defined according to the typical operating conditions which were simulated.

6.10.2. Moments and Al and AlN gaseous species concentrations

Figure 6.6 shows the boundary conditions used in the calculation of the moments of the particle size distribution and Al(g) and AlN(g) species concentrations. The Al vapour concentration was specified according to the measured value for each of the operating conditions which were simulated.

6.11. Numerical solution procedure

The solution of the several conservation equations describing the fluid flow, energy, species conservation, and nucleation and growth of ultrafine particles was carried out using the computational method (SIMPLER algorithm) developed by Patankar[38]. According to this method, the consevation equations are discretized in the form of algebraic equations using a control-volume formulation.

Following the procedure used by Bilodeau[37], three sucessive grid levels where used. With the exception of the coarsest level (level 0), each grid level was obtained from the next lowest level by equi-dividing the dimensions of each volume element. In each direction, starting from the injection point and from the tube wall, the volume element dimensions were changed progressivelly in order to cope with the sharper gradients expected for these regions.

The solution for the coarsest grid considered a cold reactor as initial guess. In the higher levels, the convergence of the next lowest level was used as initial guess. In this case, each new grid point variable was determined from the interpolation of its nearest neighbors. This procedure minimizes the number of iterations required, and avoids divergence at the finest grid levels. Because of the strong dependence of the nucleation event and related physical properties on temperature, the steady state solution of the nucleation and growth step was achieved via an unsteady state formulation. In this approach, a small time step is choosen in order to assure the convergence of the solution.

Convergence at each level was verified by carrying overall balances (over the calculation domain). In the solution of the first group of equations (fluid flow, energy, and species concentration), the mass balance difference for two consecutive iterations was verified to be better than 10^{-5}. Also, the change of the sum of the temperature in all grid points was verified to be better than 1 K for two consecutive iterations. In the solution of the nucleation and growth, the aluminum mass balance was verified to a change better than 10^{-5}, and the change of the average SSA at the outlet of the calculation domain to be better than 10^{-5}. In both cases, the maximum change to be observed refers to the difference between sucessive iteractions.

a) Radial injection of NH_3

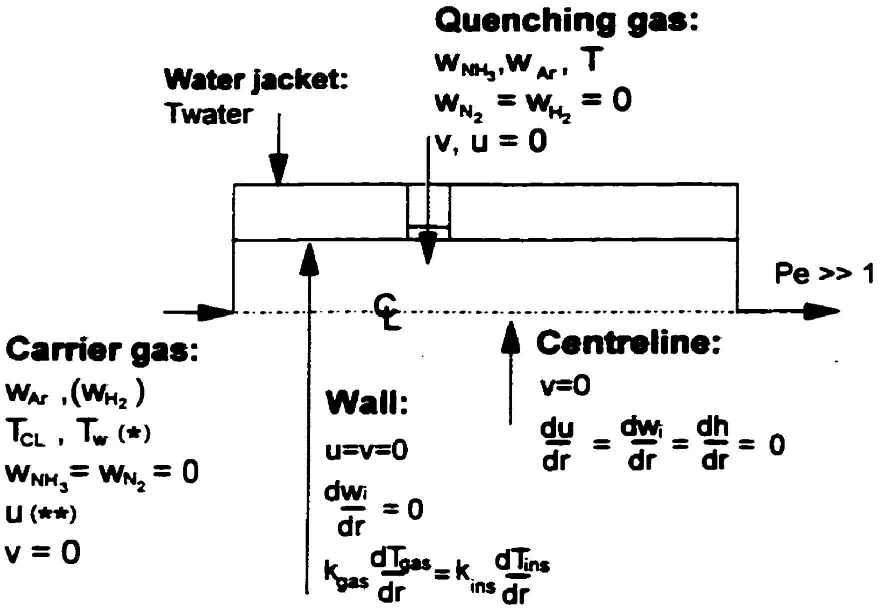

b) Axial injection of NH_3

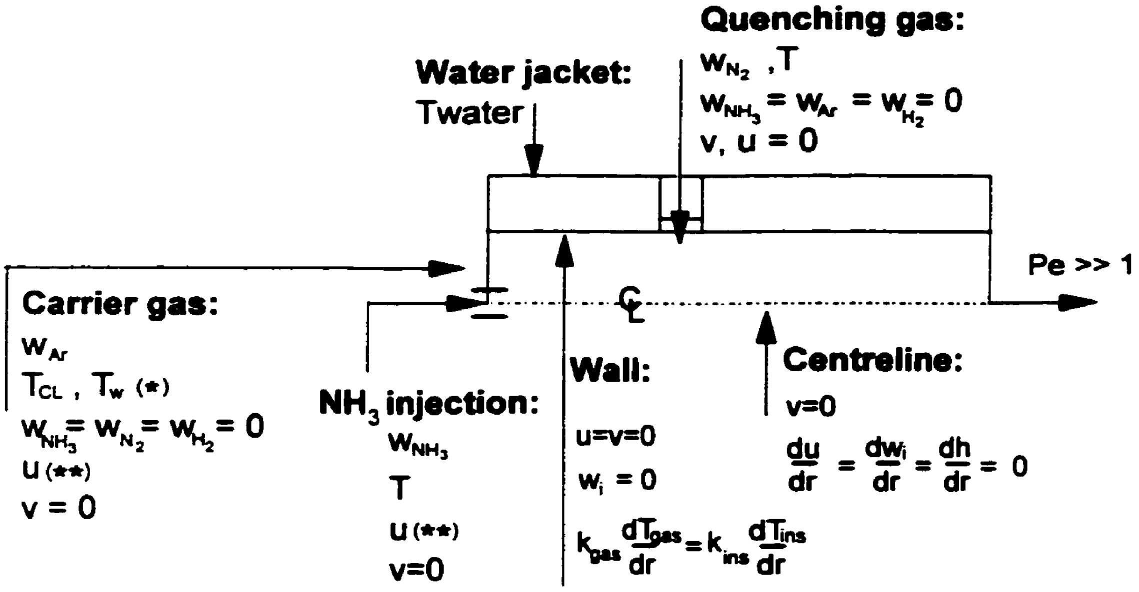

*) Parabolic profile (T)

**) Determined from specified flow rate.

Figure 6.5 - Boundary conditions used in the solution of the momentum, energy, and species conservation equations.

a) Radial injection of NH_3

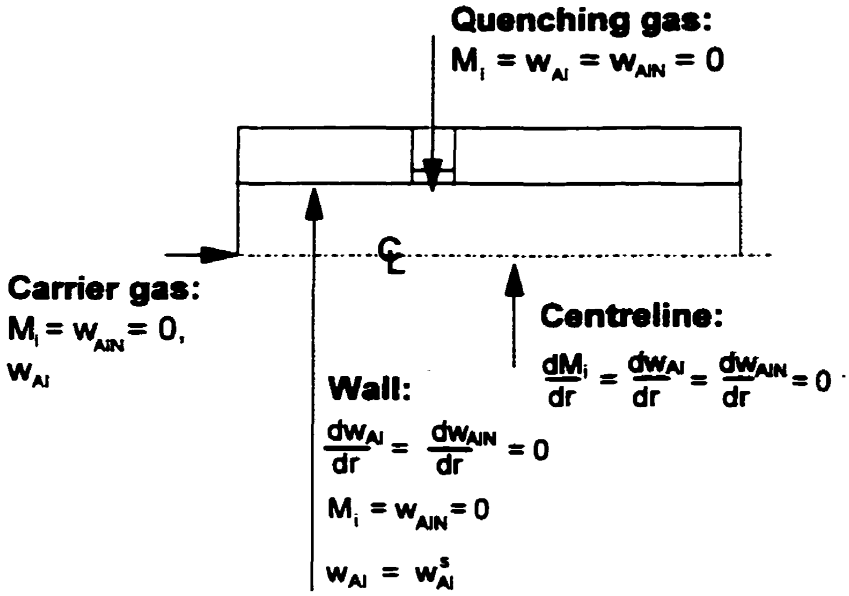

b) Axial injection of NH_3

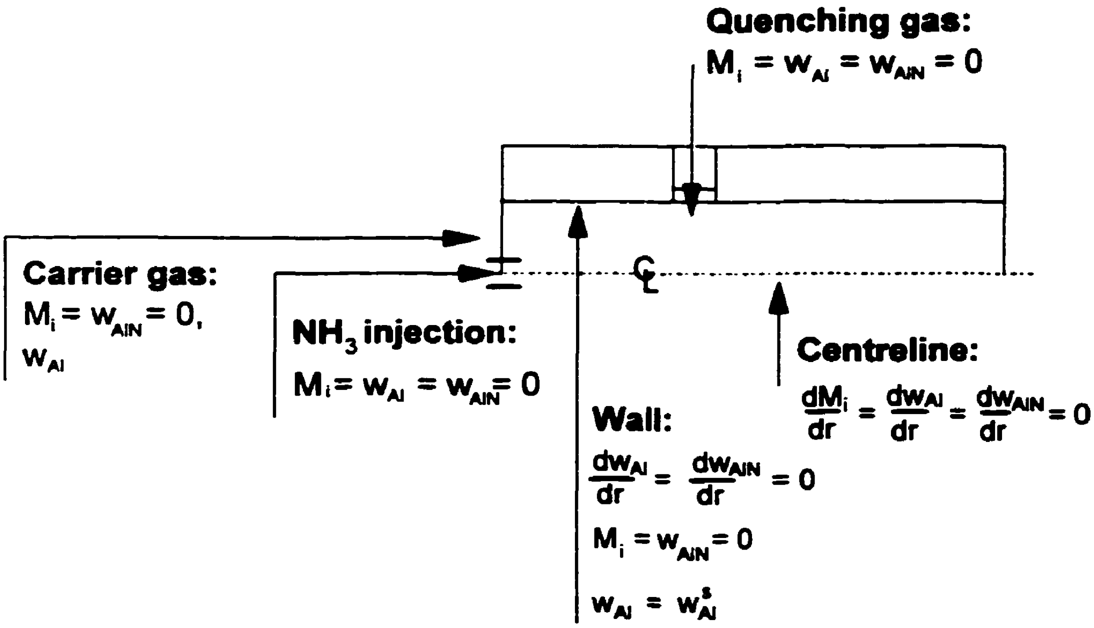

Figure 6.6 - Boundary conditions used in the solution of the moments of the particle size distribution, and Al(g) and AlN(g) especies conservation equations.

6.12. Moments related variables

The powder related variables which can be determined directly from the moments of the particle size distribution are:

Suspended particle number density: M_0

Suspended particle volume per unit volume of gas: M_1

Specific surface area average diameter:

$$d_{BET} = \frac{6}{\rho_p(SSA)} = \left(\frac{6}{\pi}\right)^{1/3}\left(\frac{M_{2/3}}{M_0}\right) \tag{6.173}$$

Number mean particle diameter:

$$d_{NM} = \left(\frac{6}{\pi}\right)^{1/3}\left(\frac{M_{1/3}}{M_0}\right) \tag{6.174}$$

The particle density (ρ_p) used in the equations above is calculated as:

$$\rho_p = \frac{\overline{X}_p m_{Al} + (1 - \overline{X}_p) m_{AlN}}{\overline{X}_p v_{Al} + (1 - \overline{X}_p) v_{AlN}} \tag{6.175}$$

where m_{Al} and m_{AlN} are the mass of the Al atom and of the AlN molecule, respectively.

6.13. Modelling results

The model developed above will be used to examine the main experimental results. In the first part, the experiments with radial injection of the nitriding gas are examined. A comparison is made between the newly developed nucleation model, in which the stability of nuclei is assumed to be influenced by surface reaction, and the model which assumes that single phase stable nuclei form before surface reaction can take place. Next, the relative importance of the mechanisms involved in the gas-to-condensed phase transition is analyzed. This is followed by a study of the influence of cooling conditions for pure argon and argon/hydrogen plasma gases as well as the possible effect of Al vapour concentration on particle size and composition. A sensitivity analysis is made on the main parameters used in the model. Finally, the axial injection of ammonia at the entrance of the tubular reactor is modeled.

Unless otherwise indicated, the simulation neglects the participation of AlN(g) in the nucleation event. However, the homogeneous reaction was included and the AlN(g) thus formed was assumed to condense on the surface of the forming particles whether they were stable or not. This is discussed in detail in the sensitivity analysis.

6.13.1. Comparison of SREN and OSN approaches

The surface-reaction enhanced nucleation (SREN) formulation results are compared with the results of the one-species nucleation (OSN) formulation using as reference the experimental data on powder synthesis in reacting and non-reacting conditions. The operating conditions and results of powder SSA and composition for the two experimental cases considered, together with the predictions of each modelling approach, are shown in Table 6.2.

The experimental results for the production of Al powder (Figure 5.16) showed little effect of the quenching jet intensity on SSA. To compare the modelling results, the quenching gas flow rate of the pure Al experiment was chosen to produce a temperature field equivalent to the AlN experiment. The isothermal curves shown in Figure 6.7 reveal very strong temperature gradients in the mixing region, resulting from the quenching effect of the cold jet. Upstream of the injection point, gradients are not as strong and are the result of heat losses to the walls.

Table 6.2 - Experimental and modelling data on the synthesis of AlN and pure Al powder using radial gas quenching and introduction of reacting gas.

Conditions	Non-reacting system			Reacting system		
Carrier gas	Ar			Ar		
Flow rate (lpm)	20			20		
Al mole fraction	2×10^{-3}			2×10^{-3}		
Carrier gas temp., T1 (K)	2,000			2,000		
Quenching gas	Ar			NH_3 / Ar		
Flow rates (lpm)	9			2 / 5		
Powder properties	Exp.25/4	OSN(1)	SREN(1)	Exp.26/2	OSN(1)	SREN(1)
SSA (m^2/g)	28	192	63	201	355	210
AlN (wt %)	0	0	0	95	95.3	95.8

OSN = One-species nucleation model.
SREN = Surface-reaction enhanced nucleation model.
[1] Grid refinement level 2.

Temperature (K)

a) Non-reacting system.

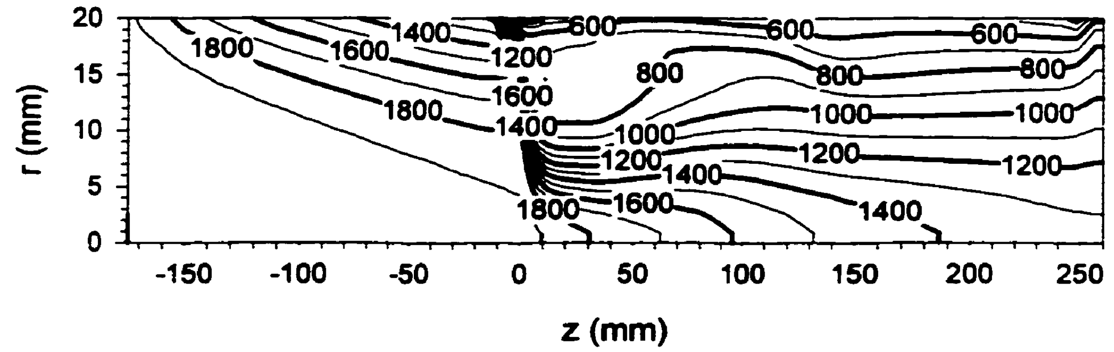

b) Reacting system.

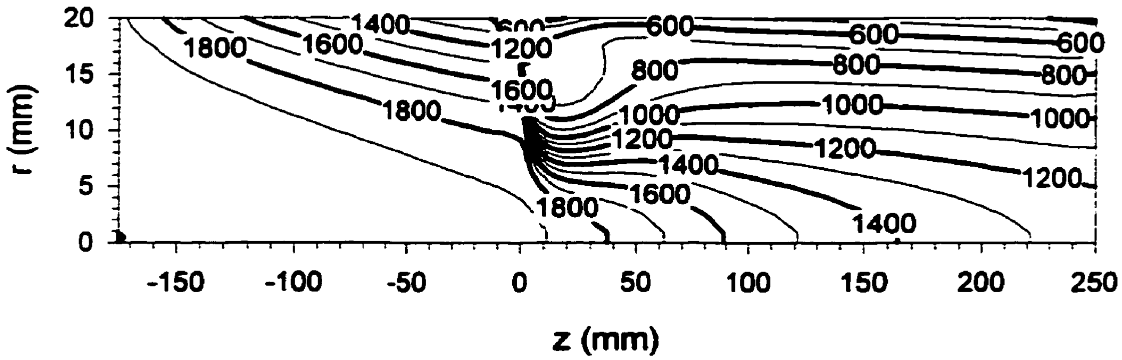

Figure 6.7 - Temperature fields predicted for pure Ar carrier gas in non-nitriding and nitriding conditions. Simulation data as shown in Table 6.2.

The predicted distributions of the variables used for comparison of the non-reacting and reacting cases are shown in the following figures, respectively: nucleation rate, Figures 6.8 and 6.10; average BET particle size and number density of particles, Figures 6.9 and 6.11.

It is observed in Figures 6.8 and 6.10 that, in both models, nucleation starts near the wall upstream of the injection point, where the temperature drops below 1600 K. As the hot gas stream is quenched by the cold jet, a more pronounced nucleation develops.

The examination of the non-reacting condition (pure Al case, Figure 6.8) shows that the nucleation rate peak predicted by the OSN model, at the core of the injection zone, is greater than the one predicted by the SREN model by approximately 4 orders of magnitude. This is due to the fact that, as it was observed in the introduction of the nucleation equation (Section 6.4.1), the use of Girshick's formulation [Equation (6.17)] predicts a considerably greater nucleation rate. As a result, in the OSN model, the large number of small particles which are blown towards the tube centre line (and also along the carrier gas flow direction) by the cold gas injection allows the condensation growth to take over and prevent any further nucleation. Therefore, the nucleation event is limited to a small region in this model. By comparison, in the SREN model the nucleation event is distributed over a larger volume. As can be observed from the graphs shown in Figure 6.9, a smaller number of nuclei results in a smaller number density of particles of greater size. The final result is that in case of a non-reacting system, the SREN (which for this specific condition represents the classical theory formulation adjusted according to Blander and Katz[61] observation concerning the free energy change to form a nucleus) predicts a smaller average SSA for the ensemble of particles at the outlet of the calculation domain, in better agreement with the experimental result.

Figure 6.8 - Nucleation rate field, pure Al powder case.

a) Nucleation rate (1/m^3/s), OSN model.

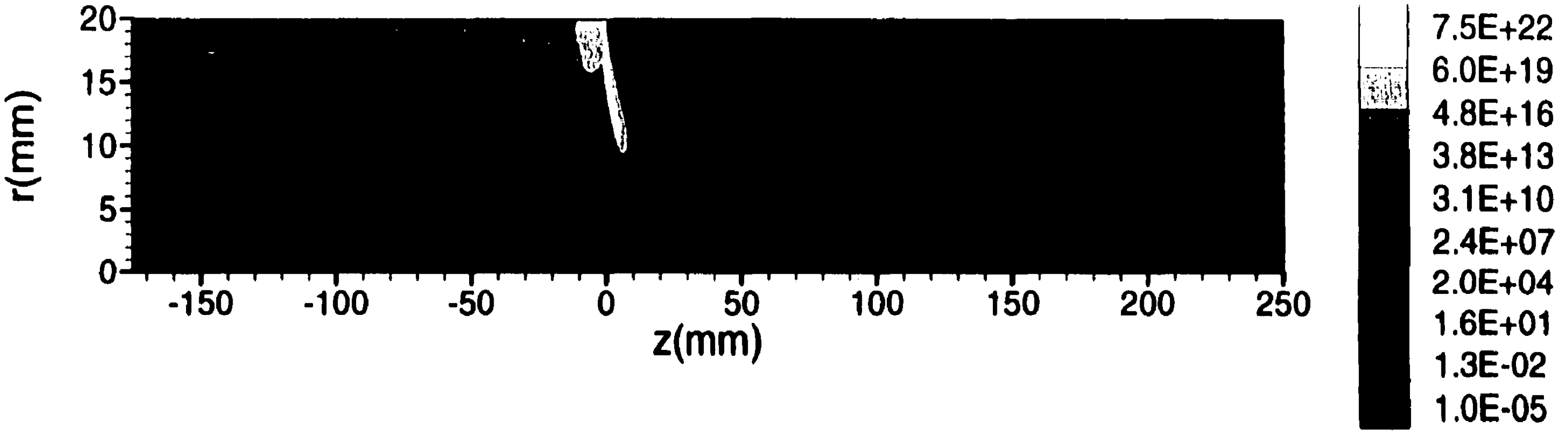

b) Nucleation rate (1/m^3/s), SREN model.

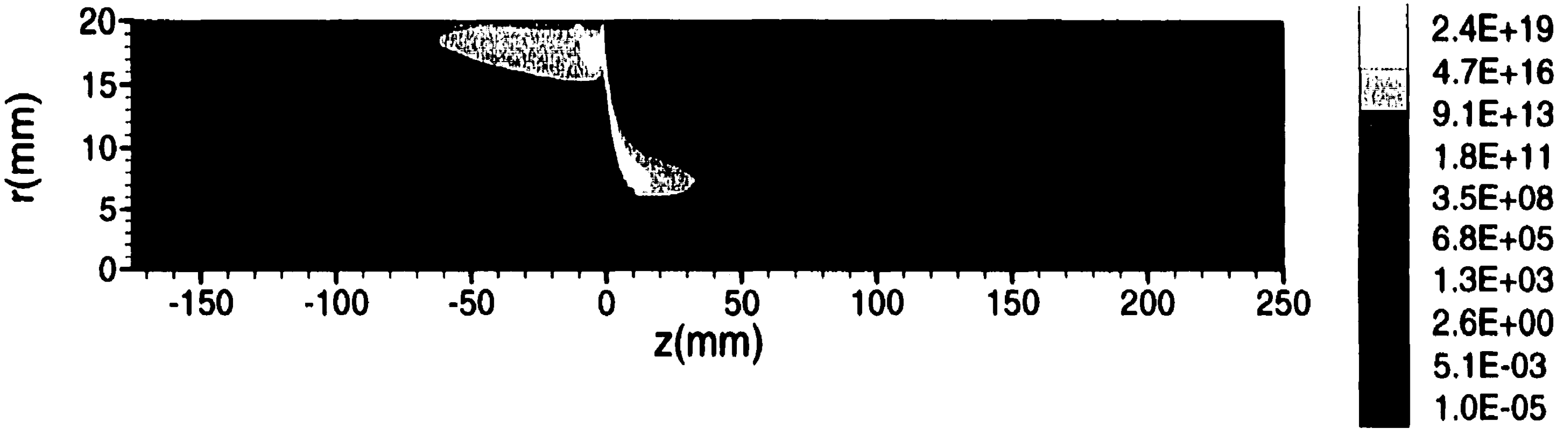

Non-reacting system, radial quenching

Figure 6.9 - Average BET diameter and particle number density as a function of the reactor radius at different axial positions, pure Al case.

a) dBET (nm), OSN model.

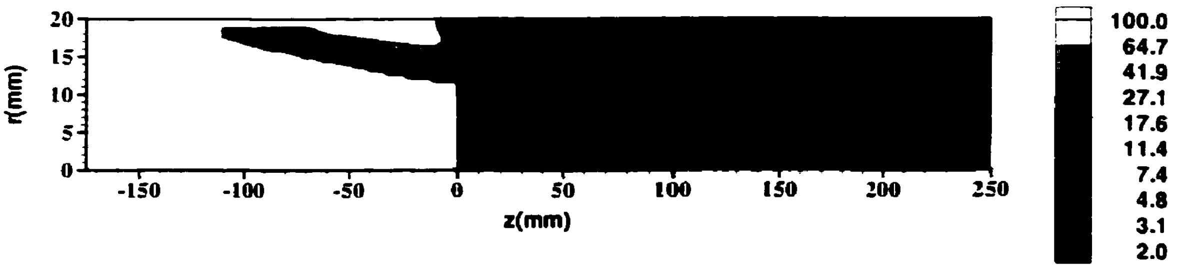

b) Part. number density (1/m^3), OSN model.

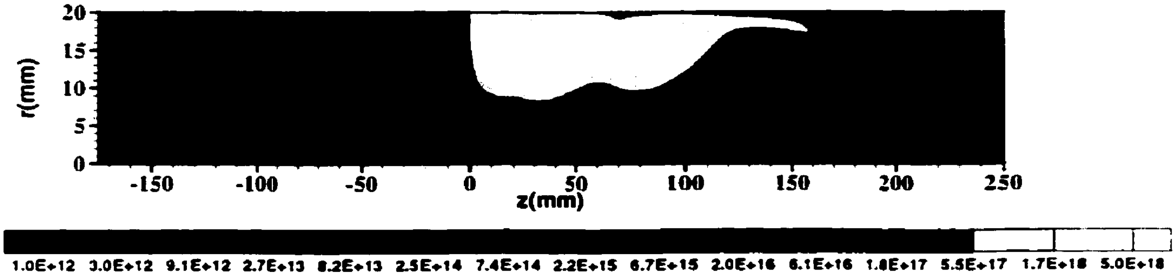

c) dBET (nm), SREN model.

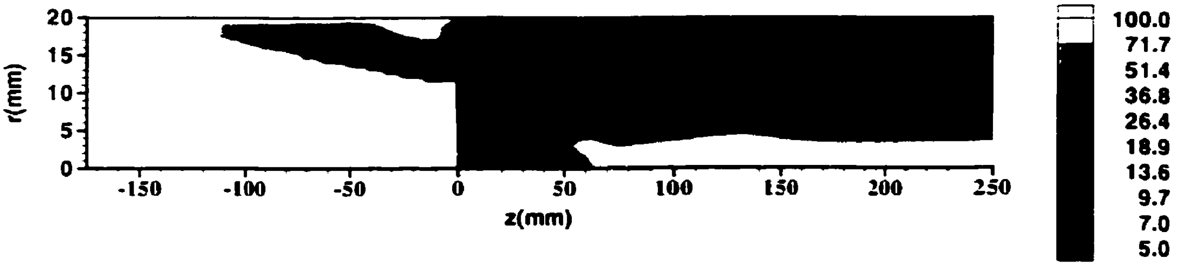

d) Part. number density (1/m^3), SREN model.

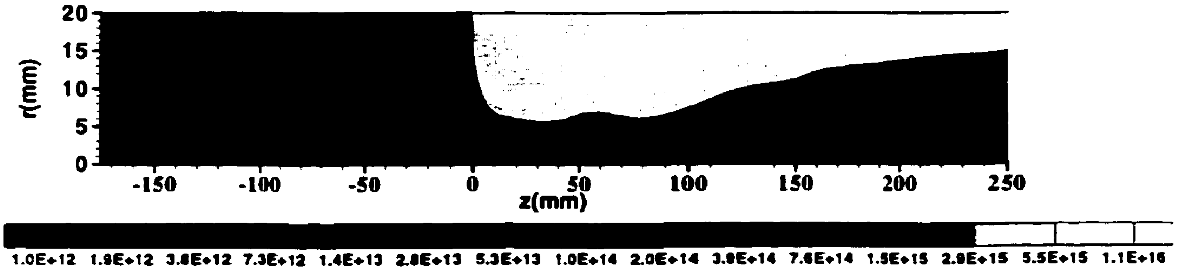

Non-reacting system, radial quenching

Figure 6.10 - Nucleation rate field, AlN powder case.

a) Nucleation rate ($1/m^3/s$), OSN model.

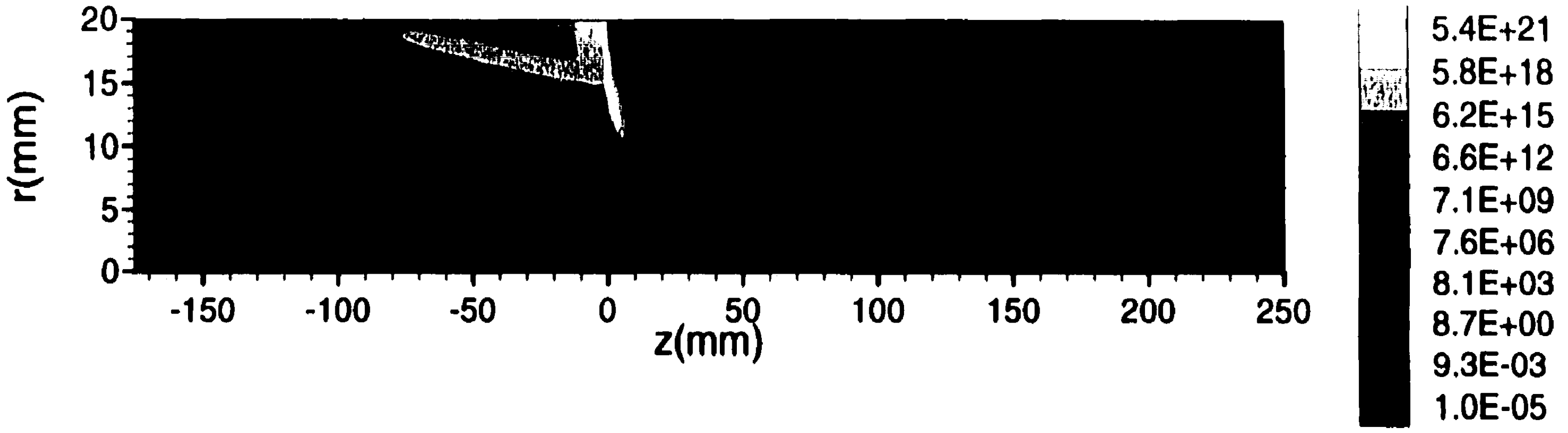

b) Nucleation rate ($1/m^3/s$), SREN model.

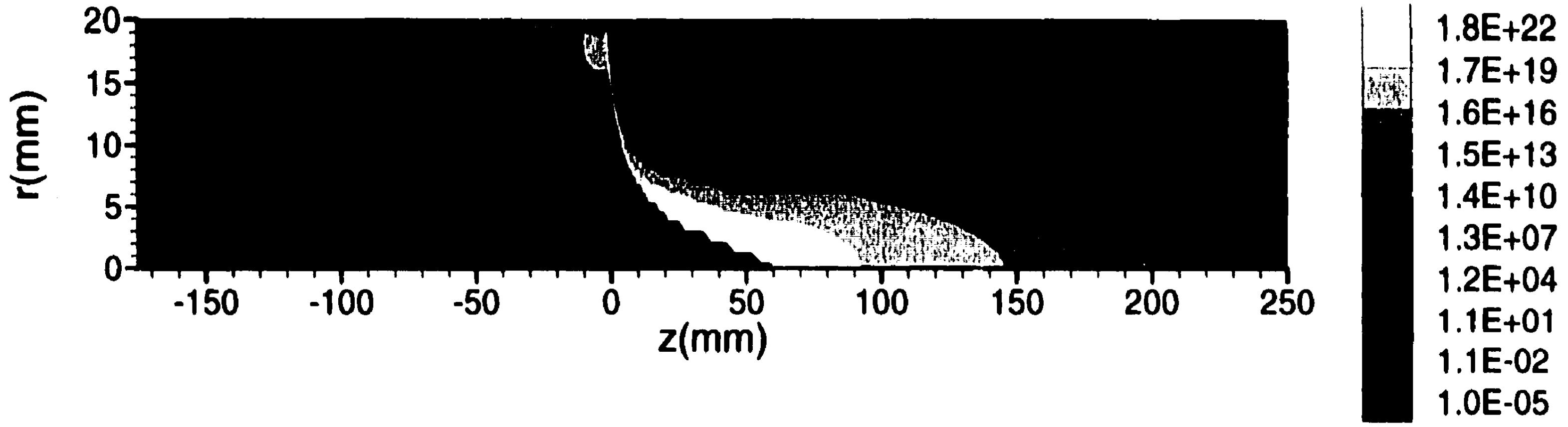

Reacting system, radial injection of NH_3

Figure 6.11 - Average BET diameter and particle number density as a function of the reactor radius at different axial positions, AlN case.

a) dBET (nm), OSN model.

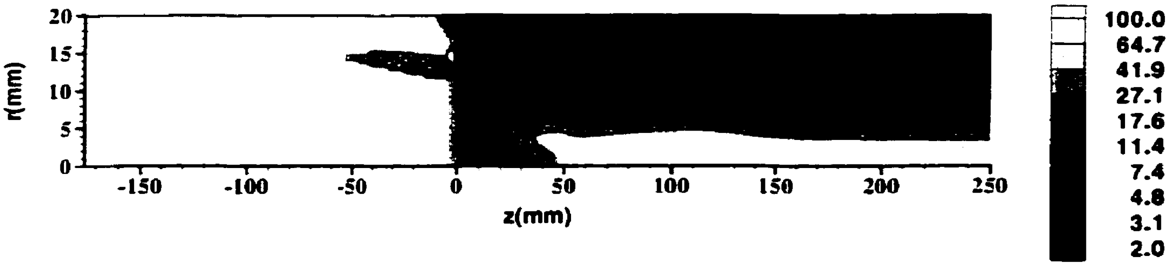

b) Part. number density ($1/m^3$), OSN model.

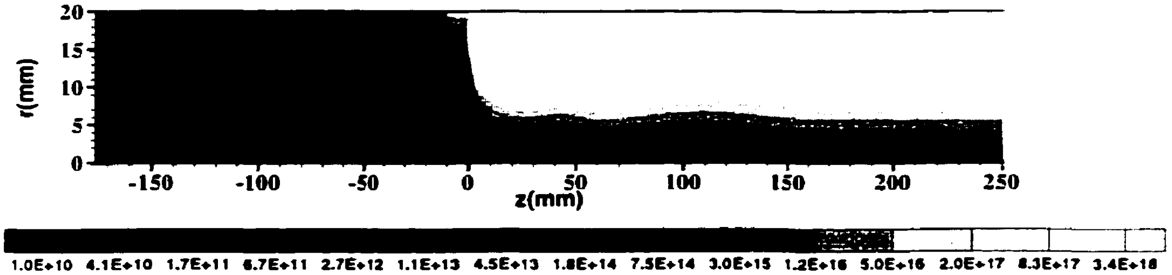

c) dBET (nm), SREN model.

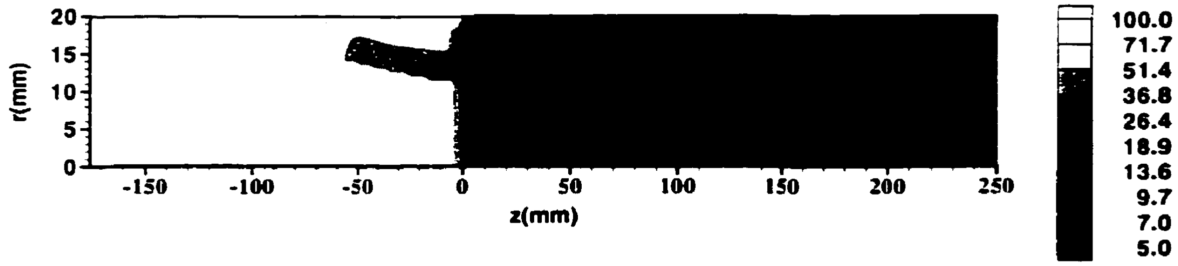

d) Part. number density ($1/m^3$), SREN model.

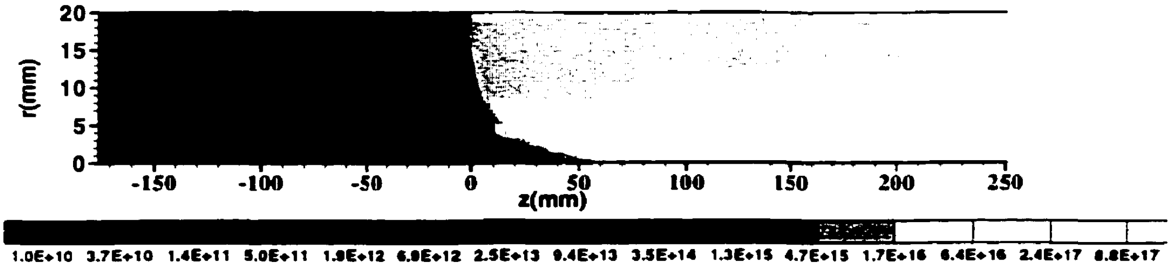

Reacting system, radial injection of NH_3

In the presence of reaction (Figure 6.10), except for the peak intensity, the OSN prediction remains practically unchanged; the nucleation zone is constricted to a small region near the injection point, rapidly vanishing towards the reactor centreline. On the other hand, the SREN model predicts a totally different scenario in which the nucleation extends over a broader region. The smaller nucleation peak in the OSN model results from the partial consumption of Al vapour by the AlN gas phase reaction included in both simulations (less Al vapour is left for the single component nucleation). In the SREN model, because of the effect of nitridation reaction on the surface of otherwise unstable nuclei, a greater nucleation rate peak occurs over a larger volume.

6.13.2. The mechanisms involved in the gas-to-condensed phase transition

The relative importance of the mechanisms for the gas-to-condensed phase transition in the AlN system which were considered in this work were evaluated using the modelling conditions shown in Table 6.2 (reacting system, SREN model) as reference. The respective rates were quantified in terms of mass of condensed phase formed per unit volume of gas. The resulting distributions are shown in Figure 6.12. The total rate of condensed phase generation [Figure 6.12(f)] was determined as the sum of individual contributions resulting from nucleation, condensation [Al and AlN(g)], and surface reaction.

The nucleation mechanism is responsible for the initiation of the phase-transition process. The final characteristic of particle size and size distribution is to a great extent determined by the nucleation rate. In general, the higher the nucleation rate, the smaller are the particles which are formed in the final process. However, as shown in Figure 6.12(a), the amount of condensed phase generated by nucleation represents a comparatively small contribution to the whole phase transition process.

Figure 6.12 - Mass rates corresponding to the various phase transition mechanisms involved in the formation of AlN ultrafine particles.

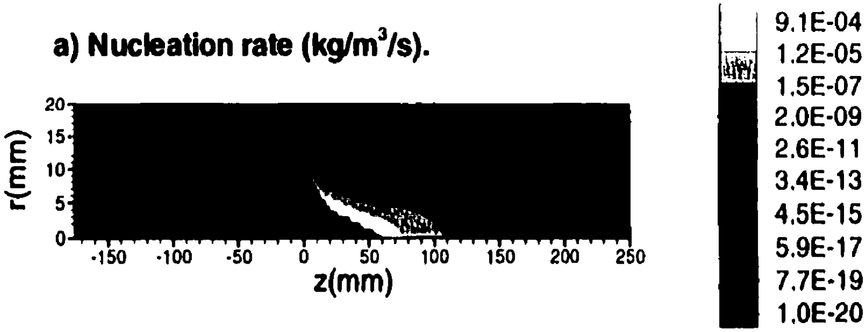

a) Nucleation rate (kg/m^3/s).

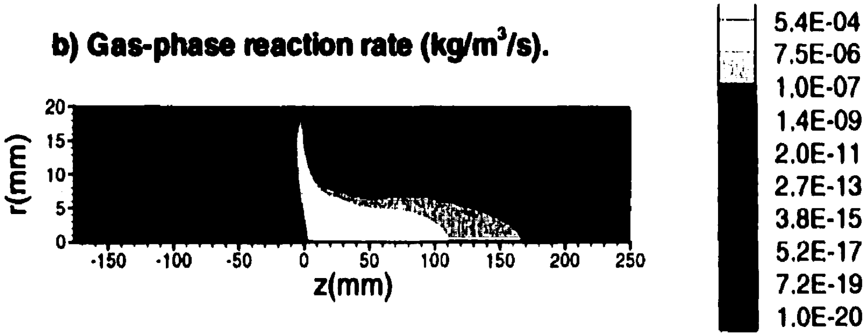

b) Gas-phase reaction rate (kg/m^3/s).

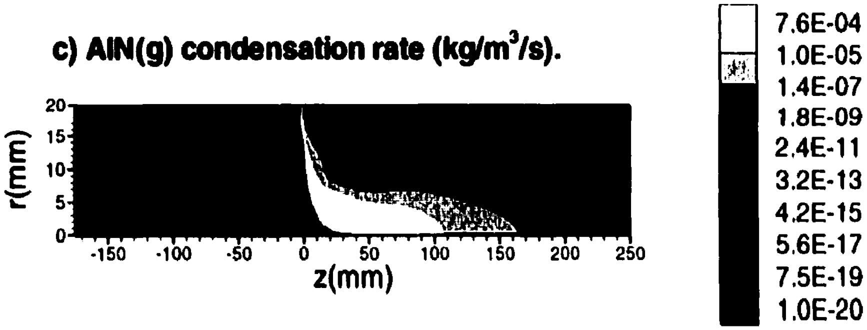

c) AlN(g) condensation rate (kg/m^3/s).

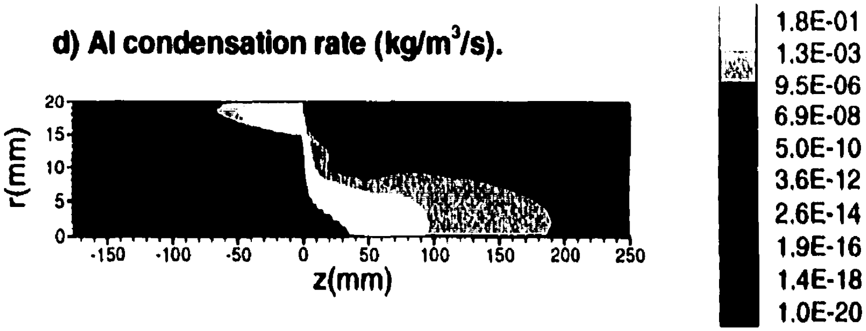

d) Al condensation rate (kg/m^3/s).

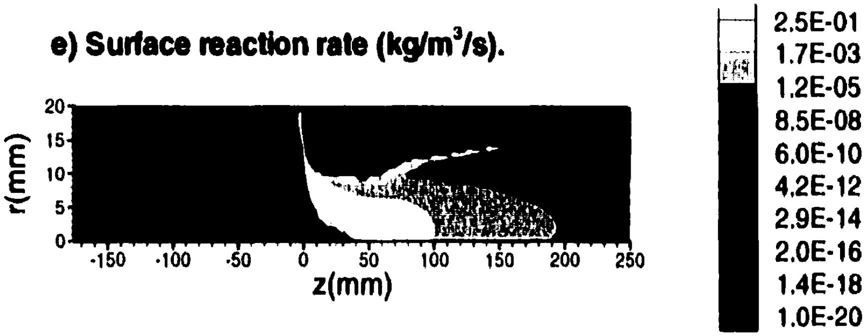

e) Surface reaction rate (kg/m^3/s).

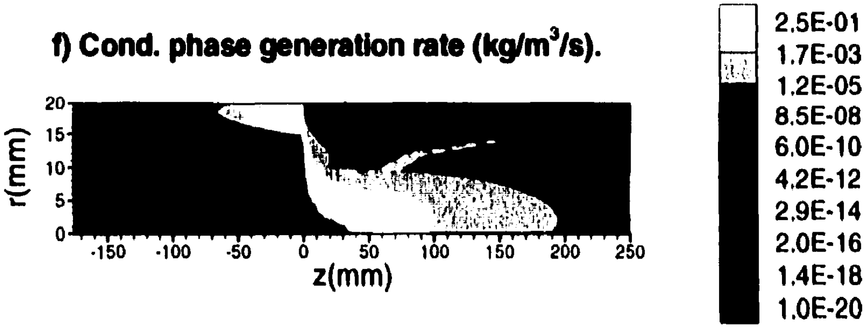

f) Cond. phase generation rate (kg/m^3/s).

SREN - Reacting system, radial injection of NH_3

As initially predicted from the analysis of the Al-N-H-Ar equilibrium diagram, the modelling results confirm that surface reaction is the dominating mechanism for the vapour phase synthesis of AlN. Because reaction depends on the presence of free-Al in the particle, Al condensation is seen as the rate limiting step in this process.

The observation regarding the amount of AlN(g) in equilibrium also led to the development of a nucleation rate equation (SREN) based on the initial assumption that gas-phase AlN could be neglected in the homogeneous nucleation process. However, based on the parameters assumed for the AlN(g) dissociation equation [Equation (6.139)], Figure 6.12(b) shows that, although of feeble intensity, AlN gas phase reaction, presents a mass rate of the same order of magnitude as nucleation. For the modelling input conditions considered, it is observed that the nucleation peak is about twice as high the reaction peak. However, the homogeneous reaction rate peak extends to a broader region than nucleation, including upstream sites, near the reactor's centreline, where no nucleation is taking place.

Although the prediction of both rates was based on the use of the kinetic theory of gases, nucleation and gas-phase reaction rates were developed using different arguments. The nucleation may include a broad range of nucleus size, which can vary from a single atom or molecule to large clusters, depending on local temperature and gas composition. The stability of these nuclei is determined by the Gibbs free-energy function, and their generation rate is computed as the number of nuclei which surpass a given critical size. On the other hand, the gas-phase reaction to AlN molecules was based on reaction kinetic data, partially experimental (NH_3 thermal decomposition) and partially theoretical (predicted using the kinetic theory of gas-phase dissociation-recombination reactions). In the mixing region, because of the high cooling rates present, very high supersaturation ratios can arise which ultimately result in a high nucleation rate of nuclei which approach the AlN(g) molecule size. In such condition, AlN(g) molecules themselves might act as nuclei.

6.13.3. Influence of cooling intensity, radial injection of NH_3

Next, the trends which were observed in the experimental part of this work concerning the powder SSA changes as a function of quenching intensity are reviewed in the light of the simulation results using the SREN model.

6.13.3.1. SSA as a function of quenching intensity, pure Ar carrier gas

It was observed in the experiments using pure Ar as carrier gas, quenched by radial jets of NH_3/Ar mixture, that increasing quenching intensity produced larger particles when all other operating variables were kept unchanged. In these experiments, the quenching intensity was characterized by the amount of Ar mixed with a fixed amount of NH_3. This result opposes the general trend observed in experimental and theoretical work involving AlN and other systems in which increasing the quenching rate resulted in a more intense nucleation, and the formation of smaller particles.

However, in agreement with the present experimental results, the simulation based on the SREN model also predicted a decrease in SSA when quenching is intensified. Two temperature levels were simulated, 1800 K and 2000 K, at the conditions used for the experiments. Because the results and trends were essentially the same, only the 2000 K level is presented and discussed here.

Figures 6.13 and 6.14 show the graphical simulation results of the general conditions of the reacting system given in Table 6.2, using two different quenching intensities. To better distinguish the effect of different jet intensities, two extremes were chosen: a radial jet formed by 2 lpm of NH_3 and 2 lpm of Ar in one case, and 2 lpm of NH_3 and 6 lpm of Ar in the other.

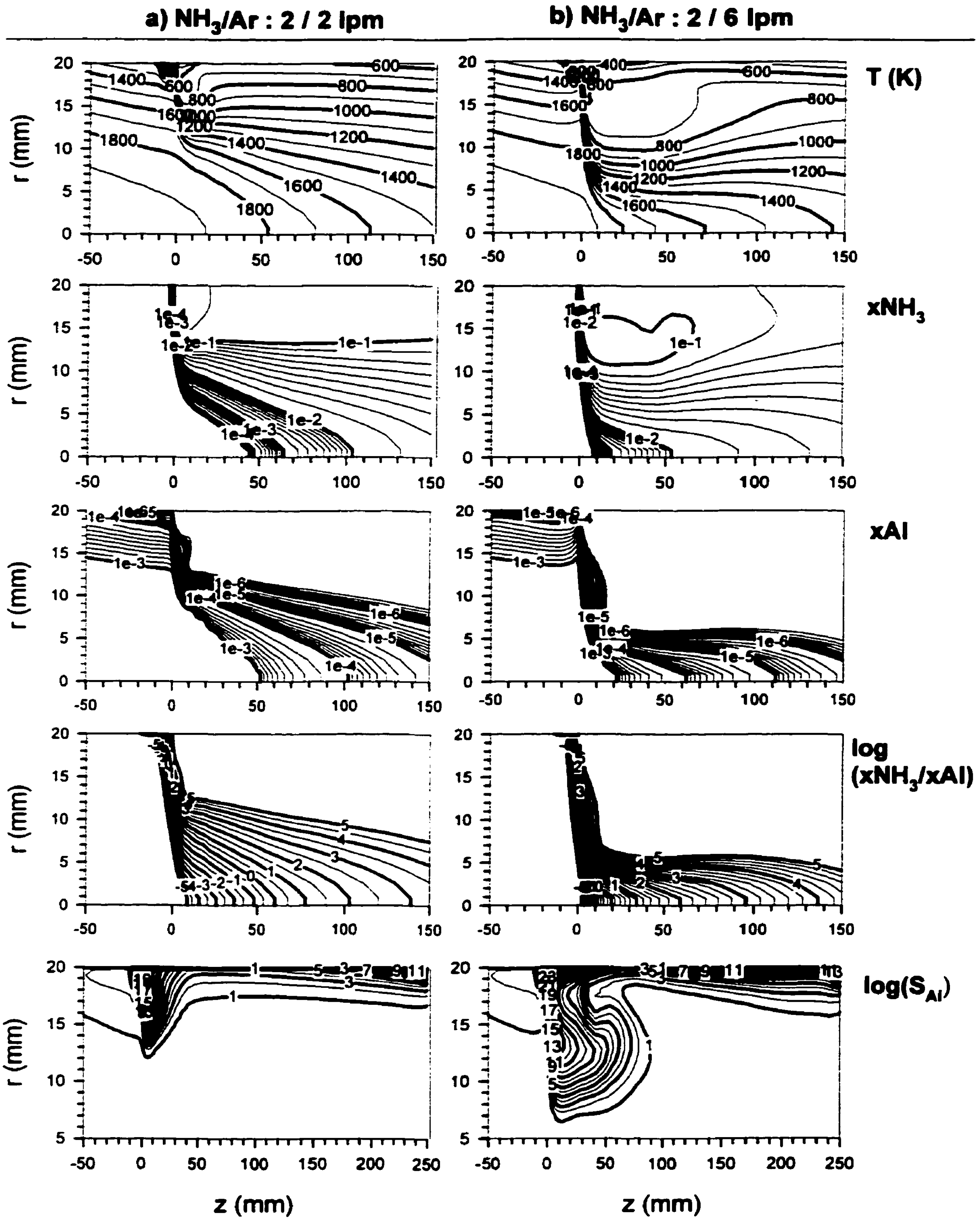

Figure 6.13 - Simulated fields of temperature, NH$_3$ and Al mole fractions, NH$_3$ to Al mole fraction ratio, and Al supersaturation ratio, for pure Ar carrier gas quenched by two different radial jet intensities.

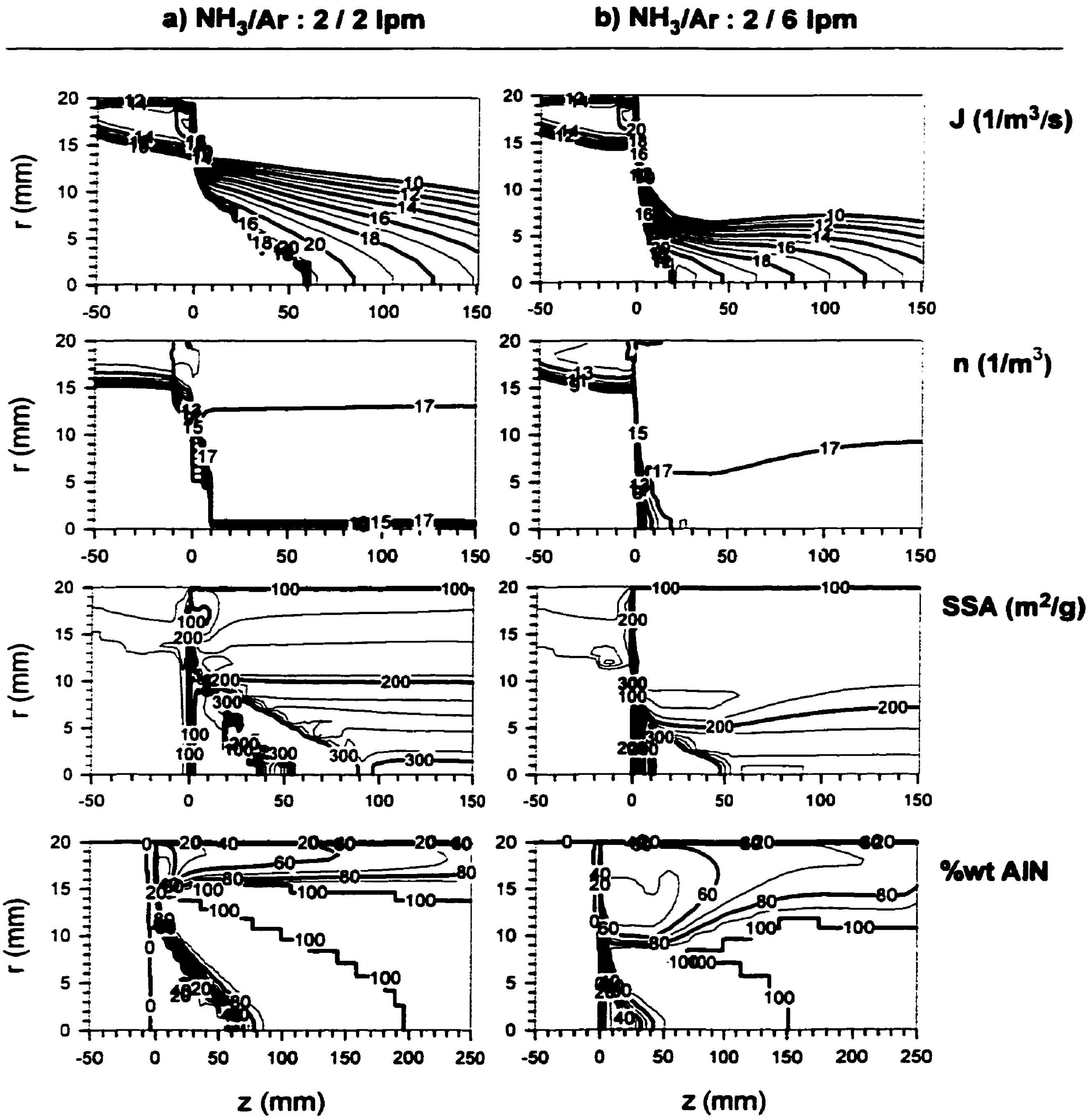

Figure 6.14 - Simulated fields of nucleation rate, particle number density, specific surface area, and weight percentage of AlN of pure Ar carrier gas quenched by two different radial jet intensities.

As the hot stream reaches the cold radial jet region, sharp temperature and reacting species concentration gradients develop. The quenching effect promotes high supersaturation ratios in this region. The more intense the jet, the more NH_3 is brought to the tube centreline. Because of the intensified nucleation and subsequent condensation, the Al vapour concentration is also sharply reduced in this zone. All these features are sequentially shown in Figure 6.13. Increased jet intensity produces stronger cooling and deeper penetration of the reacting species.

As can be observed in Figure 6.14, as a consequence of these events, a strong nucleation develops in the injection region. Comparing the two jets, it is seen that in the lower intensity case the nucleation extends to a broader region. This results from the fact that in the SREN model the nucleation equation [Equation (6.18)] is influenced by both Al supersaturation and heterogeneous reaction on the surface of subcritical clusters. The coupling of heat and mass transfer seems to exert different effects in each case. The stronger jet having the tendency to favour the Al nucleation component, as observed from the Al supersaturation distribution in Figure 6.13. Supersaturation is the driving force for nucleation. Because Al is consumed faster in the stronger jet, there is a less pronounced effect of a surface-reaction enhanced nucleation in this case. Although the isocontour lines shown for both cases in Figure 6.14 indicate about the same order of magnitude of the particle number density and SSA variables, it is observed that they extend to a broader region in the lower quenching intensity case. As a final result, the less intense jet develops a larger number of smaller particles for the average of the powder leaving the reaction zone.

The change of the simulated average SSA at the exit of the calculation domain plotted as a function of quenching intensity in the 2-6 lpm Ar flow rate interval, for the 2000 K hot gas temperature level, is shown in Figure 6.15 (a), pure Ar carrier gas. Except for the curvature, these results are in good agreement with the experimental data for similar operating conditions shown in Figure 5.15(d). The curvature differences possibly result from the fact that the ideal conditions assumed in the model are not experimentally verified. The impingement of a cold gas on a hot stream might result in turbulence and enhanced mixing not predicted in the laminar model.

Figure 6.15(b) also shows the equivalent results for the average SSA and powder composition in the Ar/H_2 carrier gas case. These results are discussed at the end of the next section.

6.13.3.2. SSA as a function of quenching intensity, Ar/H_2 carrier gas

Under the same operating temperature of the plasma chamber off-gas and gas flow rate, the use of Ar/H_2 plasma gas produced a powder of smaller SSA and lower AlN content than the powder produced using pure Ar plasma gas. Also, contrary to the trend previously discussed, as shown in Figures 5.13 (a) and (b), in the Ar/H_2 case the powder SSA increased with the quenching intensity. In the light of the modelling results, this trend appears to be associated with an increased gas cooling in the portion of the tube preceding the radial gas injection. This is a consequence of the higher thermal conductivity of the Ar/H_2 gas mixture.

Three simulated temperature distributions are shown in Figure 6.16. Except for the indicated plasma gas composition, these results were obtained using the basic operating conditions given in Table 6.2, reacting system. Figure 6.16(a) shows the temperature field of a pure Ar carrier condition simulated assuming a parabolic temperature profile at the entrance of the tube calculated from the measured gas temperature T1=2000 K, and tube wall temperature T2=1937 K. This same profile was used as temperature boundary condition for the cases which were discussed so far. Figure 6.16(b) shows the temperature field using a plasma gas mixture formed by 18 lpm of Ar and 2 lpm of H_2. The remaining conditions were kept unchanged.

In comparing Figure 6.16(a) with Figure 6.16(b), it is observed that the Ar/H_2 mixture develops a higher temperature gradient upstream the injection point. The corresponding graphs showing the distributions of the nucleation rate are shown in Figure 6.17. The Ar/H_2 mixture [Figure 6.17(b)], shows that a larger nucleation volume starts to develop near the wall, upstream of the injection point. The resulting powder SSA and composition of the Ar/H_2 case were 158.3 m^2/g and 94.6 %wt of AlN. In the pure Ar case, the equivalent results were 210.4 m^2/g and 95.1 %wt AlN. Also, there is a drop of about three orders of magnitude of the nucleation peak from the pure Ar to the Ar/H_2 mixture case, again, meaning that larger particles are formed at a smaller number density.

The heat loss profiles at the tube wall predicted by the model for the simulations (a) and (b) are shown in Figure 6.18. Because of its higher thermal conductivity, a higher heat loss profile results for the Ar/H_2 gas mixture. It thus seems reasonable to assume that, for a same bulk gas temperature measured at the point T1, the temperature at the wall of the chamber preceding the entrance of the tubular reactor would be lower in the Ar/H_2 case. Accordingly, if a more pronounced temperature gradient is assumed for the Ar/H_2 gas mixture at the entrance of the tube (by making T2=1800 K), a new temperature distribution is obtained as shown in Figure 6.16(c). The corresponding nucleation rate is shown in Figure 6.17(c). In this case, even larger particles and lower conversion were predicted for the powder at the outlet of the calculation domain; the average SSA and powder composition were calculated as 85.2 m^2/g and 83.7 %wt AlN, respectively.

The change of the simulated average SSA at the exit of the calculation domain plotted as a function of quenching intensity in the 2-6 lpm Ar flow rate interval, for the 2000 K hot gas temperature level, is shown in Figure 6.15(b), for Ar/H_2 carrier gas. The trend of an increasing SSA with quenching intensity is observed. If compared with the experimental results shown in Figure 5.15(b), a lower slope of the SSA is observed in case of the simulation result. Again, the laminar condition assumed for the model might not be fully satisfied, specially at higher quenching intensities.

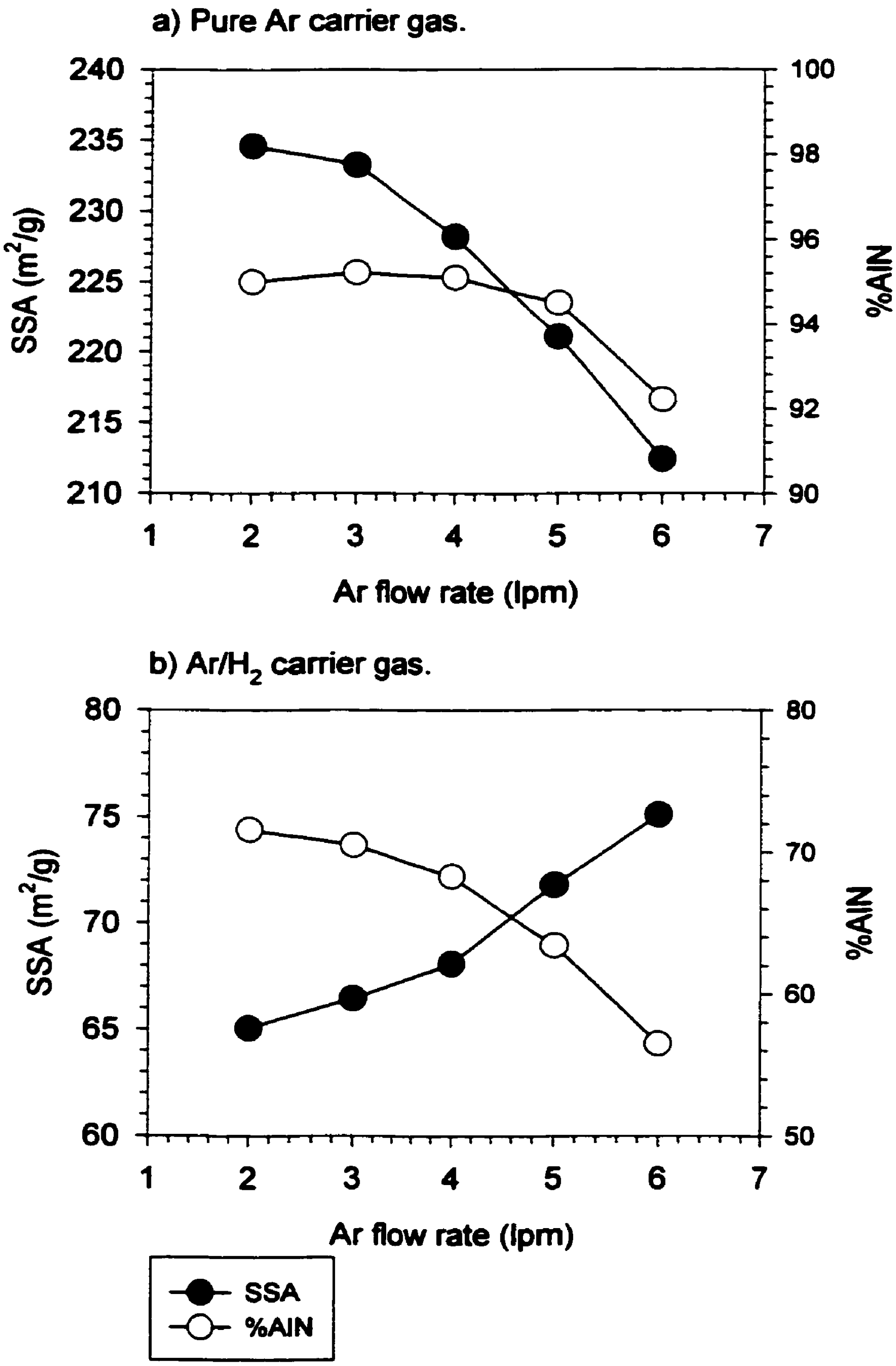

Figure 6.15 - Average specific surface areas and compositions predicted at the exit of the calculation domain, as a function of quenching intensity. Inlet carrier gas temperature of 2000 K, and mole fraction of Al vapour of $2X10^{-3}$.

a) Pure Ar carrier gas, T2 =1937 K.

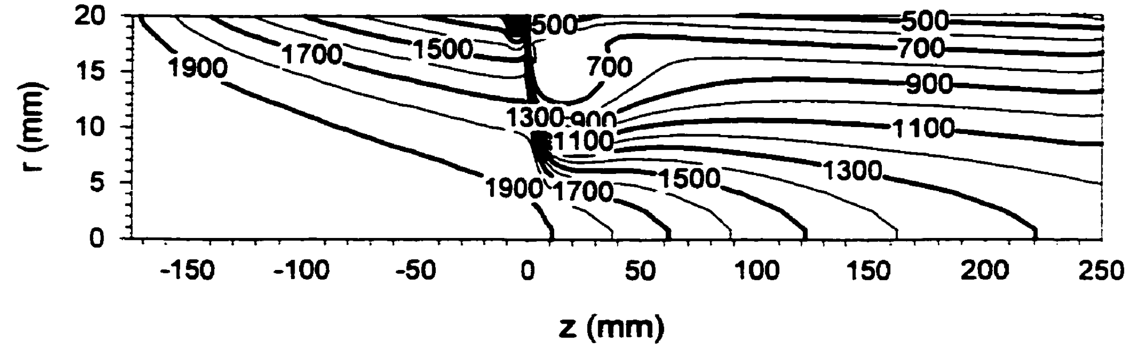

b) Ar/10%vol.H2 carrier gas, T2 =1937 K.

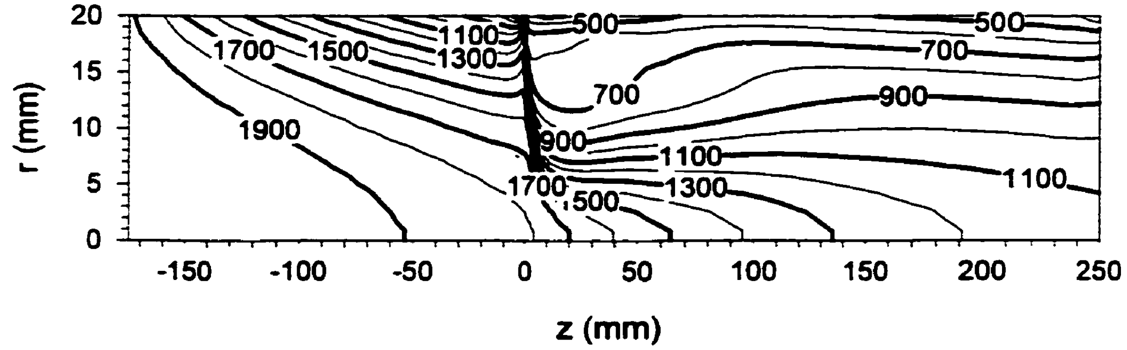

c) Ar/10%vol.H2 carrier gas, T2 =1800 K.

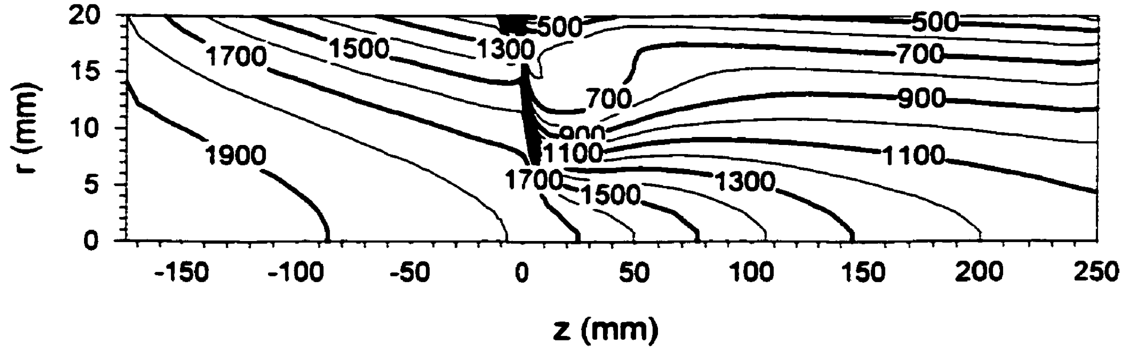

Figure 6.16 - Temperature fields predicted for Ar and Ar/H_2 carrier gas compositions assuming different temperature profiles at the entrance of the tubular reactor.

Figure 6.17 - Nucleation rate ($1/m^3/s$) predicted for different carrier gas compositions and temperature profiles at the entrance of the tubular reactor.

Nucleation rate (1/m^3/s) predicted for different carrier gas composition and temperature profile at the entrance of the tubular reactor.

a) Pure Ar carrier gas, T2=1937K.

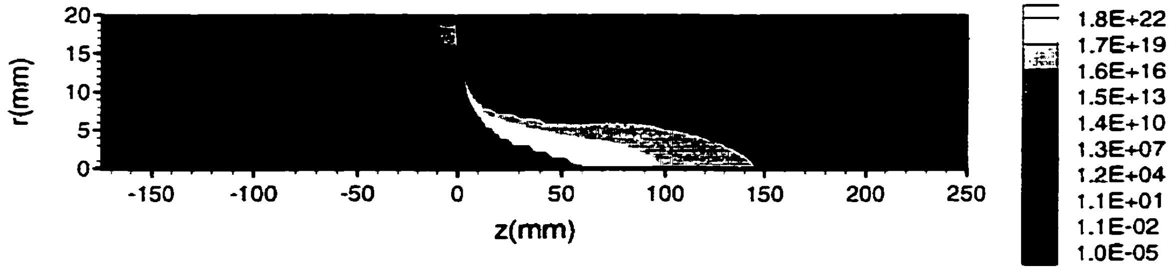

b) Ar/10%vol.H_2 carrier gas, T2=1937K.

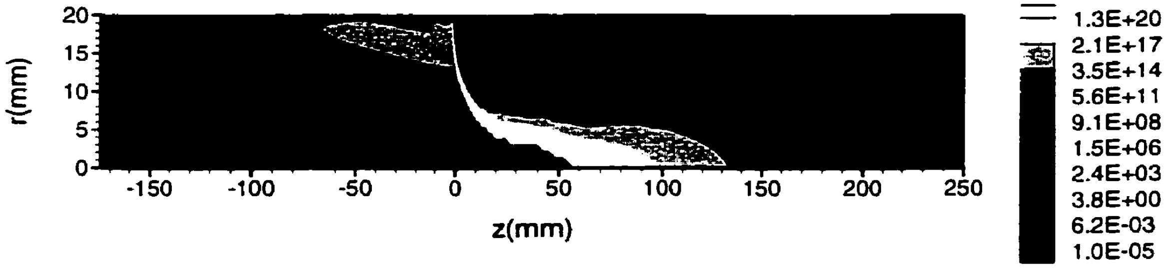

c) Ar/10%vol.H_2 carrier gas, T2=1800K.

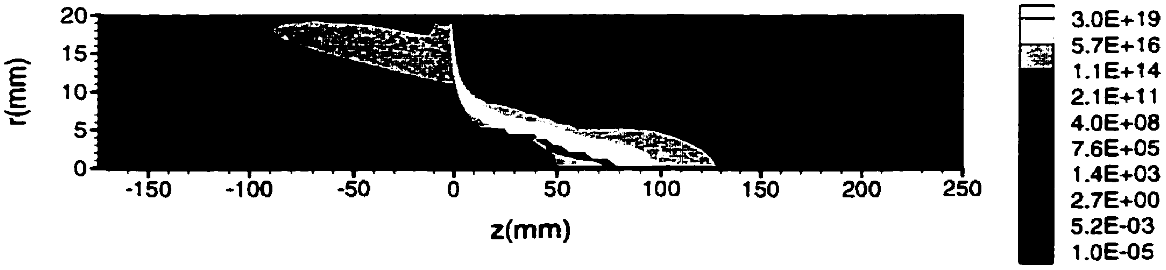

SREN-Reacting system, radial injection of NH_3

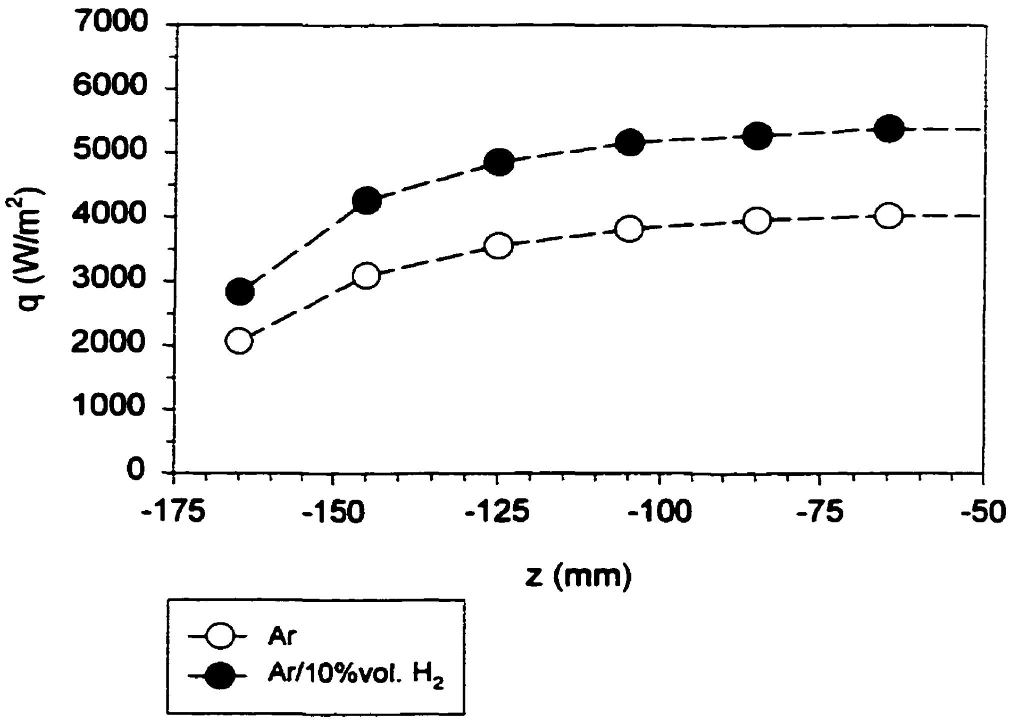

Figure 6.18 - Simulated energy loss through the reactor wall at different carrier gas compositions.

6.13.4. Powder composition

In the present vertically aligned reactor configuration, none of the experiments in which NH_3 was radially injected succeeded in producing a 100% AlN powder. The difference was always unreacted Al. Similarly all the modelled radial injection cases showed partially converted powder.

According to the modelling results, the particles which form near the wall carry a large amount of free-Al. Upstream of the jet, particles which nucleate near the wall, do so in practically total absence of NH_3. Those particles which pass the injection point and remain near the wall where the NH_3 concentration is high, but temperature and Al concentration are rather low, have their already condensed Al only partially converted to AlN. Those particles which form in the higher temperature central portion, will become fully nitrided far before the end of the exit of the calculation domain.

As observed in the graph showing the %wt AlN in Figure 6.14, for pure Ar carrier gas, a higher intensity jet results in full conversion occurring locally at a shorter distance from the injection point at the centreline. However, with the lower intensity jet full conversion is extended to a greater radius. In both cases there are still regions of low conversion near the tube wall.

In the Ar/H_2 carrier gas case, a large nucleation of particles occurs before the hot gas stream reaches the quenching zone, as shown in Figure 6.17(c). Therefore, a large fraction of the Al vapour condenses in locations with little or no NH_3. Conversion of these high free-Al content particles will have to proceed by liquid phase nitridation. In this case, the model assumes the simplified proposition made by Bilodeau[37], in which the reaction rate is proportional to fraction of the particle surface coated with free-Al, considered to be equal to the volume fraction of free-Al in the bulk of the particle, and to the impinging rate of NH_3 molecules on the particle surface [Equation (6.157)] multiplied by an accommodation factor. Also, the model assumes that the reaction stops if the local temperature is lower than the Al solidification temperature. A more realistic and complex scenario is that in which nitridation of free-Al in the particle requires that either Al diffuses to the particle surface or N diffuses toward the core of the particle. In either case this process might be accelerated by internal flow in the liquid core of a partially nitrided particle, or by exposure resulting from cracks on the forming AlN solid layer.

The average results for the powder composition at the exit of the calculation domain shows higher AlN content than observed experimentally. A decreasing AlN content is predicted when the quenching intensity increases. These results oppose the trend observed experimentally in which an increasing quenching intensity produces a powder of higher AlN content (Figure 5.15). Although modelling and experimental results do not fully agree quantitatively, qualitatively they show that full conversion to AlN using the radial injection of reagent in this reactor design is difficult to achieve.

6.13.5. Sensitivity analysis

The assessment of the importance of gas phase AlN(g) as a "condensation site" when local conditions reduce the critical nuclei size to atomic/molecular dimensions, obviously depends on the accuracy with which nucleation and reaction rates are predicted. In addition to the many assumptions which had to be made for the various physical properties needed for the computation of the nucleation rate, there is a high degree of uncertainty involved in the evaluation of the AlN(g) reaction rate, especially the rate law assumed for the AlN(g) dissociation [backward direction of Reaction nr. 11, Equation (6.130)].

The influence of the AlN gas phase reaction on the nucleation mechanism, and the influence of the minimum temperature limit imposed for high AlN content particle to coagulate upon collision were analyzed. Also, in the case of nucleation, a sensitivity analysis was done on the influence of the AlN surface energy used for the SREN formulation, Equation (6.18).

In all cases, the predicted average powder properties (SSA and %wt AlN) at the exit of the calculation domain were used as indicators. The sensitivity analysis results were expressed as the percent change relative to a base case defined as follows:

(i) the overall conditions for the reacting system given in Table 6.2 were adopted as representative of most of the trends observed in the experiments involving the radial injection of reagent;

(ii) the parameters whose sensitivity was analyzed had their value fixed in the base case according to the initial assumptions made. To recall, these assumptions were: the participation of AlN(g) in the nucleation event can be neglected; the steric factor (P) assumed as 0.01; the AlN(g) dissociation energy (ε_0) as defined by Equation (6.138); and a minimum temperature limit above which particles having more than a 0.5 free-Al mole fraction can coagulate arbitrarily assumed as 1650 K.

The finest grid level (level 2) is the one which most closely approximates the true solution for the set of differential equations describing the nucleation and growth process. However, because of the large number of parameters involved in such an analysis, the use of such a refined grid is extremely time consuming. Therefore, after a comparison of the results of the three grid levels for the base case as shown in Table 6.3, the sensitivity analysis was carried out using the coarsest grid level (level 0).

Table 6.3 - Comparison of powder properties predicted at the exit of the reactor for the three progressive grid levels used. AlN(g) not considered in the nucleation process.

Grid level	Specific surface area		AlN conversion	
	(m^2/g)	difference (%)	%wt AlN	difference (%)
2[1]	210.4	-	95.1	-
1	215.2	2.3	94.0	-1.0
0	234.7	11.5	93.7	-1.5

[1] The finest grid is used as reference.

The overall results of this analysis are given in Table 6.4 and individually plotted in the graphs of Figure 6.19. The analysis criteria and results for each of the mechanisms analyzed are discussed in sections 6.13.5.1 to 6.13.5.3. The conclusions of the sensitivity analysis are included in the conclusion section, at the end of this chapter.

6.13.5.1. Gas-phase reaction

The analysis of the influence of homogenous reaction considered the inclusion of AlN(g) in the nucleation formulation as described next. Two of the parameters used for the computation of AlN(g) dissociation reaction, Equation (6.145), were analyzed: the steric factor P and the AlN(g) dissociation energy ε_o. The respective sensitivity analysis results are shown in the graphs (a) and (b) of Figure 6.19. The dissociation energy is modified according to a multiplier (f_ε), defined as the ratio between the dissociation energy used in the calculation and the one defined according to Equation (6.164).

The results shown in Figure 6.12 demonstrate that Al condensation followed by surface reaction is the dominating process in the gas-to-condensed phase transition for the vapour phase synthesis of AlN. However, for the gas-to-condensed phase transition to occur, initial stable nuclei are required. These nuclei may be thought to form the first surface area available for Al condensation.

To evaluate the influence of the homogeneous reaction on the phase transition, by considering the possibility of AlN gaseous species acting as nuclei when critical particles predicted by the SREN model approaches the AlN molecule size, an equivalent nucleation rate (J_{eq}) was defined.

The concept of “first surface area” (A_o) available for condensation is expressed as the sum of the surface areas created by the nucleation and gas-phase reaction per unit volume of gas as follows:

$$A_o = (36\pi^2)^{1/3}\left[v_{cr}^{2/3} J + v_{AlN}^{2/3}\left(R_{AlN}^{g} - R_{AlNcond}\right)\right] \tag{6.176}$$

and made equal to the surface area which would be generated if an equivalent nucleation rate (J_{eq}) were considered, maintaining the critical particle size as calculated according to Equation (6.106):

$$A_o = (36\pi^2)^{1/3} v_{cr}^{2/3} J_e \tag{6.177}$$

this gives:

$$J_{eq} = J + \left(R_{AlN}^{g} - R_{AlNcond}\right)\left(\frac{V_{AlN}}{V_{cr}}\right)^{2/3} \tag{6.178}$$

It is observed from the graphs (a) and (b) of Figure 6.19 that the increase of the reaction rate brought about either by an increase of one order of magnitude in the steric factor or the decrease of the dissociation energy by 10% produces an increase of the order of 300% in the predicted average SSA of the powder. The decrease of the reaction rate by a decrease of the steric factor of one order of magnitude, or the increase of the dissociation energy of 10%, produces an increase of the order of 20% in the predicted average SSA of the powder. Increasing the dissociation energy of the AlN(g) molecule 20% or more has no further effect on the nucleation rate or SSA.

To better visualize the kind of changes caused in the simulated nucleation rate by the assumed homogeneous reaction, their respective rate fields are shown in Figure 6.20. Figure 6.20(a) shows simulation results for the base case. Figure 6.20(b) shows results for a simulation case which considers AlN(g) as nucleation site, at an homogeneous reaction rate which produces an average SSA equivalent to the base case ($f_c = 1.3$). Coherently with the 'first surface area' concept introduced above, the rates were expressed in [surface area created/unit volume/unit time] units. The comparatively higher reaction rate predicted under the base case assumptions produces a field which has about the same order of magnitude as the respective nucleation rate.

Because reaction consumes a considerable amount of Al(v), which would otherwise nucleate. Figure 6.20(a1) does not register nucleation in the tube centreline near the radial injection coordinate. Eventhough the less intense reaction rate predicted for the modified case [Figure 6.20(a2)] did not change considerably the nucleation rate field for isocontours having a value lower than 10^2 $m^2/m^3/s$, a considerably higher nucleation rate is observed at the centreline closer to the injection coordinate [Figure 6.20(b1)]. However, this result did not affect the average SSA determined at the exit of the calculation domain.

Because of the dominant role of the surface reaction mechanism in the formation of AlN. the powder purity is only slightly affected by these changes (see Table 6.4). In any of the combinations of the two parameters, the changes observed are less than 4%.

Table 6.4 - Sensitivity analysis of the influence of the steric factor, the AlN dissociation energy. the temperature limit for the coalescence of high content AlN particles, and the AlN surface energy on the average powder properties at the exit of the reactor.

Parameters analyzed				Specific surface area		AlN content	
Gas phase reaction		Coalescence (AlN rich part.)	AlN Surf. energy				
P	f_ε (1)	T_{lim}	f_σ (2)	m^2/g	% change	%wt	% change
0.1	1.0	1650	0.77	970.0	313.6	95.9	3.2
0.01	1.0	1650	0.77	417.4	78.0	95.4	2.7
0.001	1.0	1650	0.77	274.9	17.2	92.8	-0.1
0.0001	1.0	1650	0.77	235.8	0.6	92.8	-0.1
0.01	0.9	1650	0.77	868.7	270.4	95.6	2.9
0.01	1.0	1650	0.77	417.4	78.0	95.4	2.7
0.01	1.1	1650	0.77	290.5	23.9	92.8	-0.1
0.01	1.2	1650	0.77	238.6	1.7	92.7	-0.2
0.01	1.3	1650	0.77	233.7	-0.3	92.8	-0.1
0.01	1.4	1650	0.77	234.2	-0.1	92.9	0.0
0.01	1.0	1000	0.77	76.1	-67.5	92.8	-0.1
0.01	1.0	1200	0.77	101.8	-56.6	92.8	-0.1
0.01	1.0	1400	0.77	136.3	-41.9	92.8	-0.1
0.01	1.0	1500	0.77	149.3	-36.3	92.9	0.0
0.01	1.0	1600	0.77	185.7	-20.8	92.9	0.0
0.01	1.0	1650	0.77	234.5	0.0	92.9	0.0
0.01	1.0	1700	0.77	281.8	20.2	92.9	0.0
0.01	1.0	1800	0.77	442.3	88.6	92.8	-0.1
0.01	1.0	1850	0.77	639.5	172.7	92.8	-0.1
0.01	1.0	1900	0.77	640.6	173.2	92.8	-0.1
0.01	1.0	2000	0.77	639.4	172.7	92.8	-0.1
0.01	1.3	1650	0.70	502.6	114.3	94.3	1.5
0.01	1.3	1650	0.75	293.5	25.2	93.3	0.4
0.01	1.3	1650	0.77	233.7	-0.3	92.8	-0.1
0.01	1.3	1650	0.80	168.7	-28.1	92.2	-0.8
0.01	1.3	1650	0.90	90.7	-61.3	89.9	-3.2
0.01	1.3	1650	1.00	81.0	-65.5	87.2	-6.1

[1] $f_\varepsilon = \overline{\varepsilon_0}/\varepsilon_0$, ε_0 dissociation energy given by Equation (6.138); $\overline{\varepsilon_0}$ is the modified parameter;

[2] $f_\sigma = \overline{\sigma}/\sigma$, σ surface energy of the AlN crystal defined by Equation (6.162); $\overline{\sigma}$ is the modified parameter.

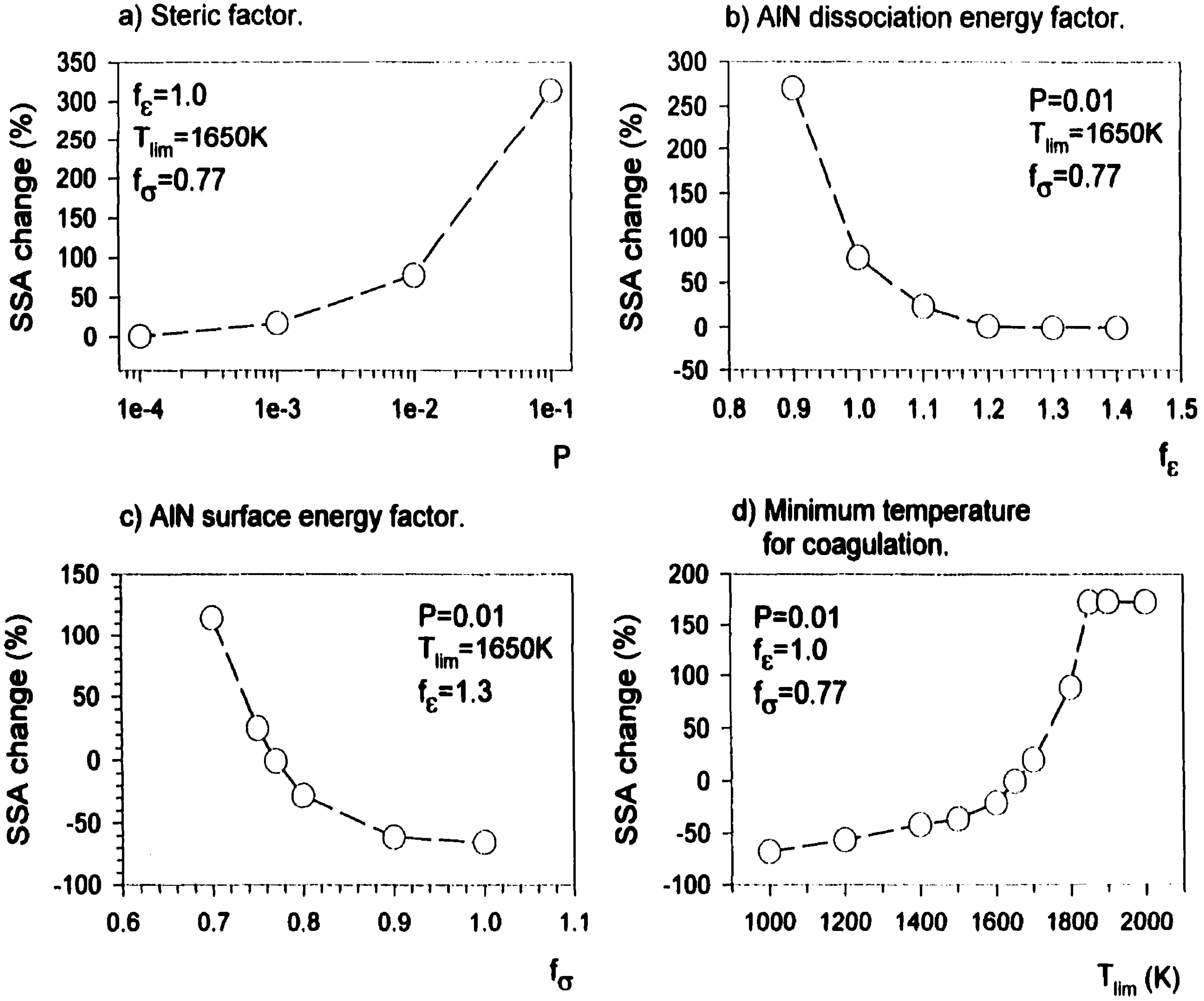

Figure 6.19 - Sensitivity analysis on the parameters affecting the AlN gas phase reaction, nucleation, and coagulation of AlN rich particles.

a) Base case

b) Modified as specified

1) Nucleation rate ($m^2/m^3/s$).

1) Nucleation rate ($m^2/m^3/s$).

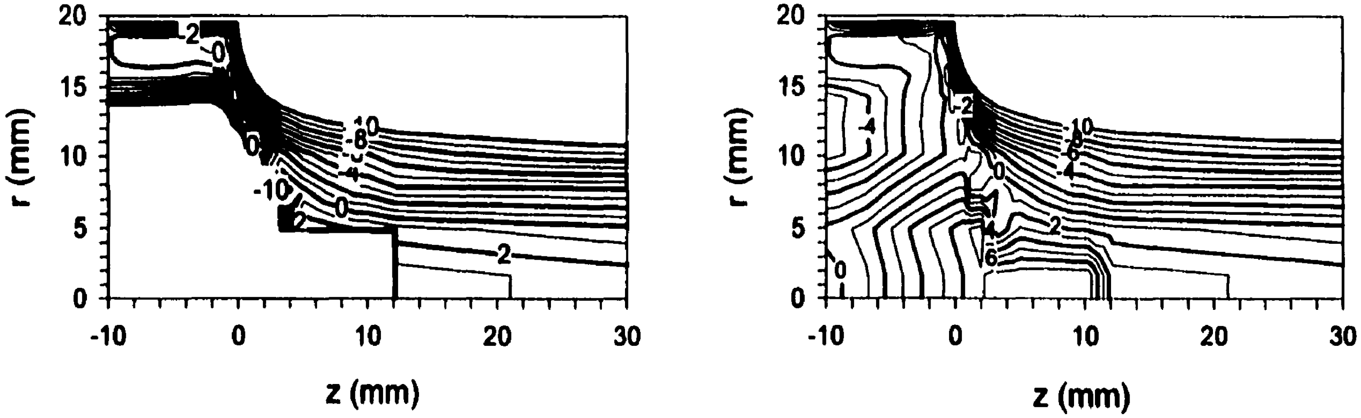

2) Gas-phase reaction rate ($m^2/m^3/s$).

2) Gas-phase reaction rate ($m^2/m^3/s$).

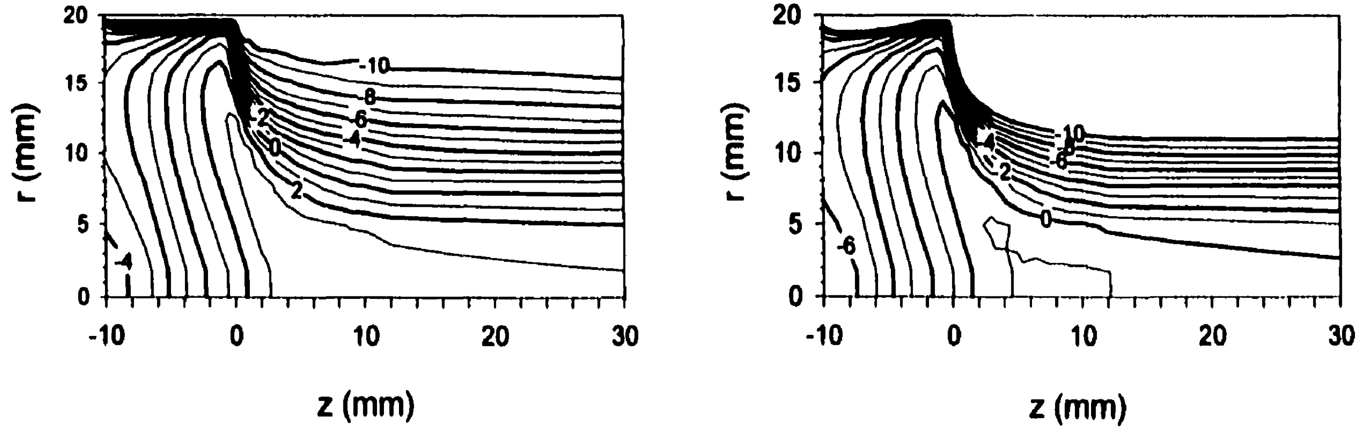

Figure 6.20 - Logarithm of the rates of surface area generation per unit volume of gas by nucleation and gas-phase reaction; right hand side results from the modification of the base case by the inclusion of AlN(g) in the nucleation equation and use of a AlN(g) dissociation energy factor (f_ε) of 1.3.

6.13.5.2. AlN surface energy

The change of the powder SSA due to changes in the surface energy estimated for the AlN crystal is shown in Figure 6.19(c). Again, a multiplier (f_σ) is defined as the ratio between the surface energy of AlN used in the calculation and the one given by Equation (6.164). The strong influence of the surface energy results from the exponential dependence of the nucleation rate [Equation (6.18)] on the dimensionless surface tension. It has to be remembered at this point that an average surface energy was considered [Equation (6.162)], accounting for the binary cluster composed by Al and AlN. In case of Al, the assumption of the capillarity approximation (the surface tension of small liquid droplets is the same as the surface tension of a macroscopic flat film) is itself contentious; according to Rao and McMurry[89], a considerable debate exists concerning the order of magnitude of the effects of this assumption, and even whether the surface energy of smaller droplets is larger or smaller than the values for flat surfaces.

A small surface energy reduces the barrier to be overcome for a cluster to become stable, thus promoting a larger nucleation rate of smaller nuclei, and therefore, producing a powder of larger SSA. The reverse is true if the surface energy is increased. The 0.77 factor was adopted considering that small clusters might not be perfectly crystallized, and therefore would present a lower surface energy than the one predicted by Equation (6.162).

Again, because of the weak dependence of phase transition on the amount of condensed phase formed by nucleation, the large changes on the nucleation rate cause comparatively small changes on the powder composition.

6.13.5.3. Minimum temperature for the coalescence of AlN rich particles

Whether ultrafine particles having a high AlN content coalesce upon collision is open to speculation. Such particles tend to be solid. Although such particles might remain together after colliding they may not coalesce. In spite of the strong driving force towards sintering, represented by the large free-energy associated with their large specific surface area, this process would require a residence time far larger than it is available in this reactor. Nevertheless, because of the strong condensation component, very small particles which collide and remain together for some time in the early stage post-nucleation, might be rapidly coated by condensing vapour followed by surface reaction. This process is illustrated in Figure 6.21. In addition to the temperature dependence, this process suggests also a dependence of coalescence on variables such as local Al vapour composition and particle size.

The minimum temperature at which coalescence of AlN rich particles is "allowed" lacks a physical meaning and, therefore, can only be arbitrarily established, subject to an arbitrary particle composition. The temperature dependence shown in Figure 6.19(d) is interpreted as an expression of the existence of high temperature regions inside the reactor, where AlN rich particles are present. The fact that the SSA reaches a constant value above 1800K results from the absence of nucleation, and therefore of particles below this temperature in the present Al concentration conditions.

Because coalescence does not affect reaction, the small changes observed relative to the AlN content of the powder result from numerical approximations in the algorithm.

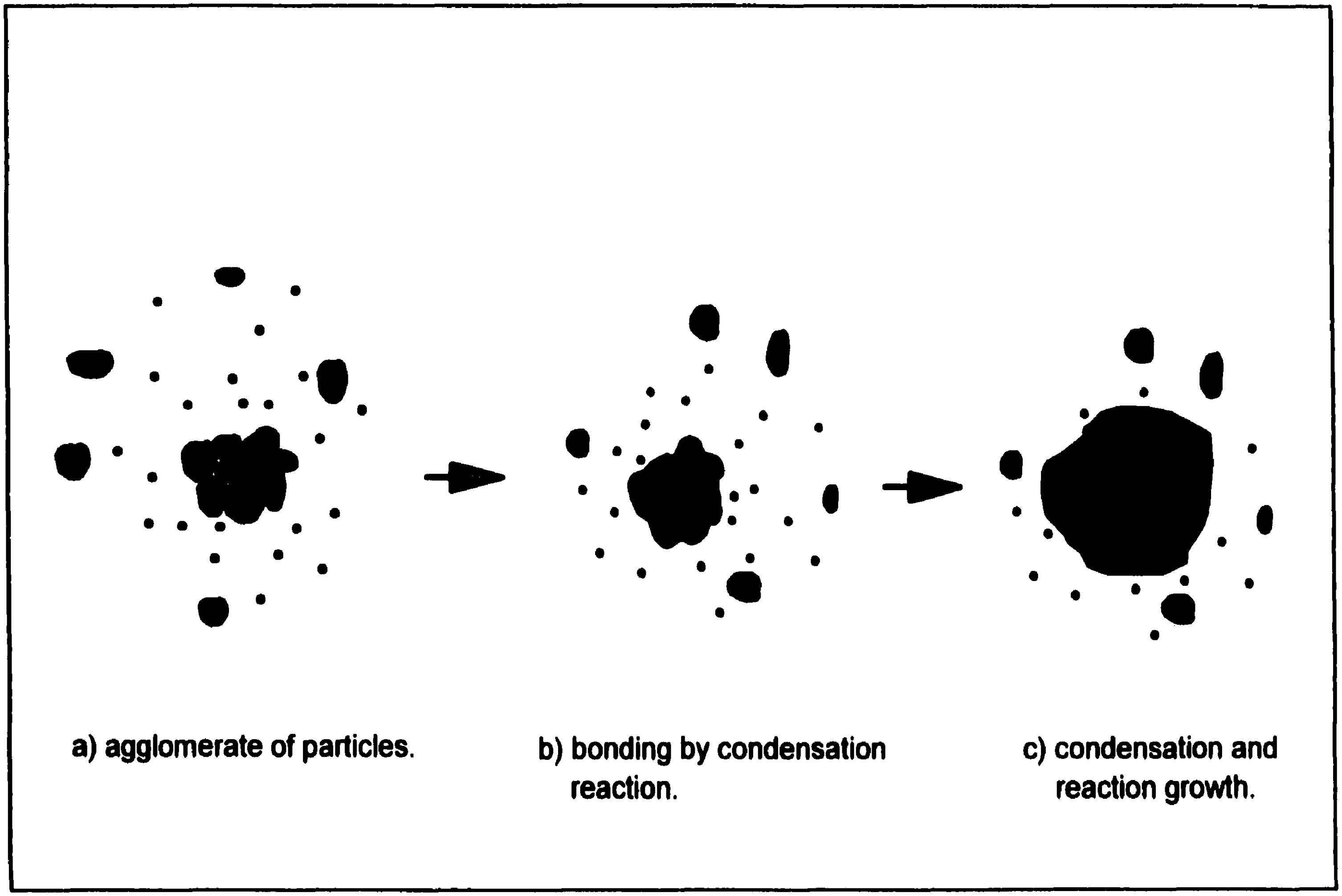

a) agglomerate of particles.

b) bonding by condensation reaction.

c) condensation and reaction growth.

Figure 6.21 - Ilustration of a possible mechanism leading to the sintering of high AlN content particles in the early stage after nucleation.

6.13.6. Influence of Al concentration

Because the gas temperature and Al vapour concentration variables could not be separated, the influence of the concentration of Al vapour in the hot gas at the entrance of the tubular reactor on the powder characteristics could not be experimentally studied.

The possible trends resulting from changes in this variable were analyzed using the SREN model. As a study case, the pure Ar carrier gas (2000 K temperature level and radial injection of NH_3 according to the conditions shown in Table 6.2) was adopted. Using the level 1 grid refinement, the results of the powder SSA and composition as a function of the mole fraction of Al vapour (xAl) is shown in the graphs of Figure 6.22. The values plotted are averages calculated over the cross section at the exit of the calculation domain. A maximum for both SSA and AlN content is observed.

In the SSA case, the existence of a maximum reflects both (i) the competition between the nucleation and condensation followed by surface reaction as the dominating mechanism for the gas-to-condensed phase transition and (ii) and nucleation of pure Al upstream the quenching jet point. At very low concentrations, nucleation occurs under relatively low supersaturation ratios as the hot flow reaches the quenching zone. This results in a comparatively small number density of particles of large sizes. Because the concentration is low, after the onset of nucleation, little or none metal vapour is left for condensation growth and surface reaction. As the concentration of metal vapour increases, for concentrations lower than the one corresponding to the maximum in the SSA curve, higher supersaturations develop which result in increasing nucleation rates and decreasing particle sizes. At the same time, condensation growth keeps increasing. Provided that sufficient surface area is created by nucleation, the balance between both processes starts to favour condensation (and surface reaction) growth. As the concentration of Al(v) increases, nucleation upstream of the quenching jet near the tube wall is also increased. High Al(v) concentrations (beyond the concentration corresponding to the maximum of the curve) promotes a more intense nucleation followed by condensation growth before the gas can reach the radial jet region. This results in particles of larger size (and smaller SSA).

In case of powder composition, two major trends are observed depending on Al vapour concentration. The balance of these two trends causes the curve to inflect:

(i) At lower concentrations, the phase transition dominated by nucleation rather than condensation is also seen as the reason for the reduced conversion. Because the values are averages calculated over the cross section at the exit of the calculation domain, in case of low Al vapour concentration this average is greatly influenced by the larger nucleation that occurs near the wall in the mixing region. Little nucleation occurs at the small supersaturations found in the hot core. Although the ammonia concentration is high in the jet zone near the wall, the temperature is too low to promote reaction. As an internal boundary condition, the model assumes that surface reaction proceeds only if the temperature is higher than the Al melting point. For Al concentrations lower than the maximum of the powder composition (%wt AlN) curve, as Al vapour concentration increases, increased nucleation and condensation followed by surface reaction occurs in the hot core. This brings up the average results.

(ii) At very high Al vapour concentrations, higher supersaturations enhance nucleation upstream of the jet. Contrary to the lower concentration case, a high Al vapour condensation occurs where little NH_3 is present (absence of surface reaction). The higher the Al vapour concentration the greater is the amount of phase transition which occurs upstream of the injection point in the absence of NH_3. As a result the lower is the AlN content of the powder produced.

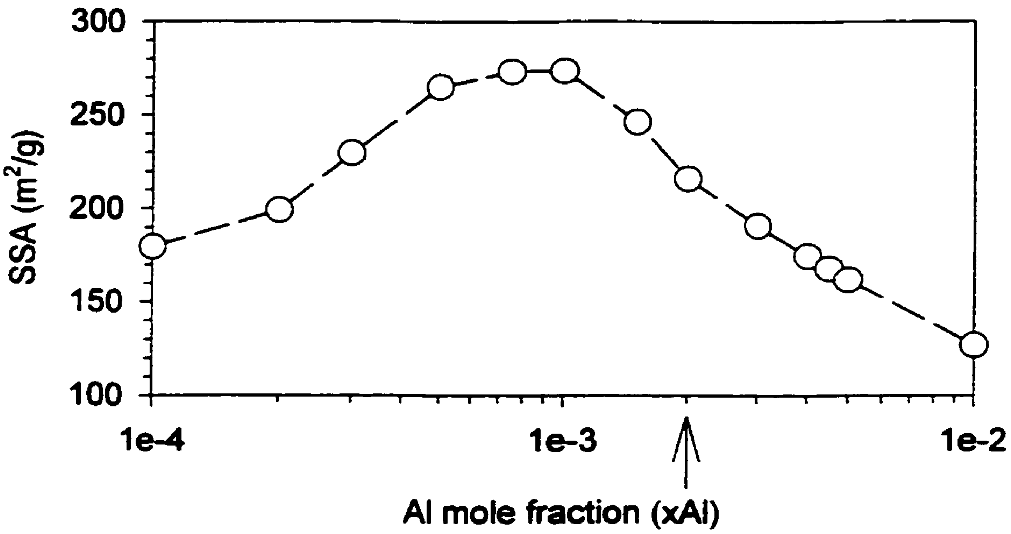

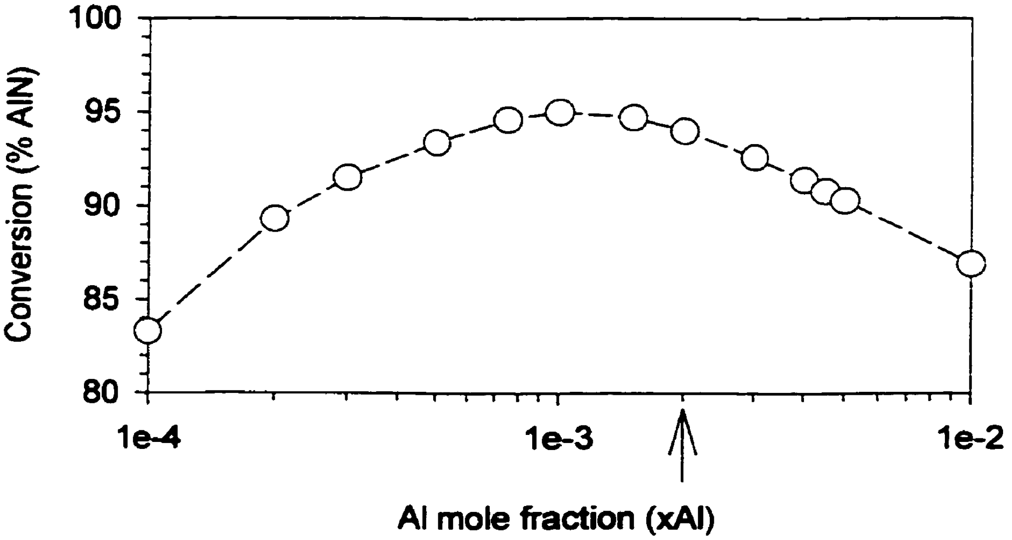

Figure 6.22 - Specific surface area and AlN content of powder at the exit of the tubular reactor, predicted as a function of the Al vapour concentration, for pure Ar carrier gas. Overall conditions as indicated in Table 6.2. The arrows indicate the concentration which was produced experimentaly.

6.13.7. Axial injection

The axial injection of NH_3 at the entrance of the tubular reactor was simulated for two temperatures (1800 and 2000 K) of the plasma chamber off-gas. The overall conditions which were used in the simulations are shown in Table 6.5. Because the main trends and field patterns predicted for the two temperatures were similar, only the results pertaining to the 2000 K level are shown in graphic form. The temperature field predicted is shown in Figure 6.23. The fields of the nucleation rate, BET diameter, and number density for the higher temperature case are shown in Figure 6.24.

Table 6.5 - Modelling data on the synthesis of AlN using axial injection of NH_3.

Carrier gas		Ar	Ar
Carrier gas temp., T1 (K)		1,800	2,000
Flow rate (lpm)		25	25
Al mole fraction		$7x10^{-4}$	$2x10^{-3}$
NH_3 flow rate (lpm)		2	3
NH_3 temperature (K)		700	900
N_2 quenching gas flow rate (lpm)		6	6
Powder properties	SSA (m^2/g)	158.8	117.7
	Al (wt %)	100	99.9

Figure 6.24(a) shows that an intense nucleation occurs at the periphery of the axial jet as NH_3 mixes with the plasma chamber off-gas. Because most of the Al vapour is consumed in this region, no nucleation activity is observed in the high NH_3 concentration core. For the same reason, the downstream radial injection of quenching gas do not promote nucleation. Where the nucleation peak occurs, the average SSA particle diameter (d_{BET}) is of the order of 2 nm. Due to the intense surface growth, the average particle diameter becomes about ten times greater in a few millimeters downstream the nucleation peak.

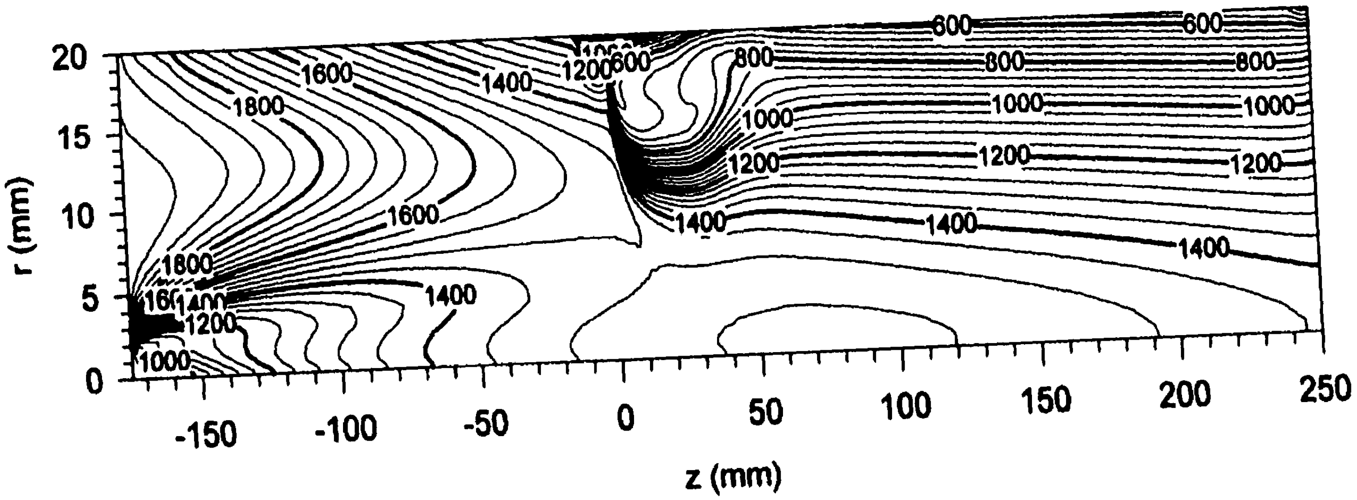

Figure 6.23 - Temperature field predicted for the axial injection of NH_3 (3 lpm) upstream of the radial injection. T1=2000 K, carrier gas flow rate = 25 lpm (pure Ar), radial gas flow rate = 6 lpm (N_2).

Figure 6.24 - Modelling predicted nucleation rate, equivalent specific surface area mean diameter, and particle number density distributions of powder produced when NH_3 is axially injected at the entrance of the reaction zone. Pure Ar carrier gas, T1 = 2000 K.

a) Nucleation rate (1/m^3/s).

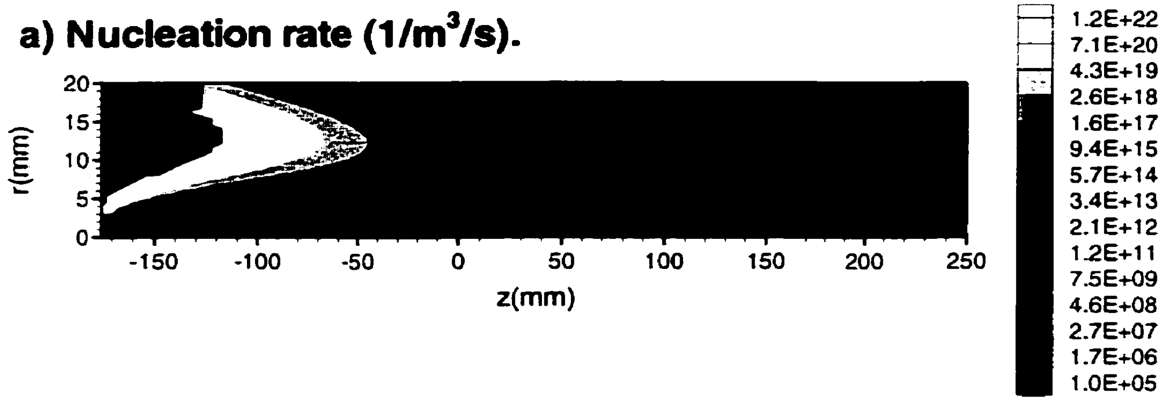

b) dBET (nm).

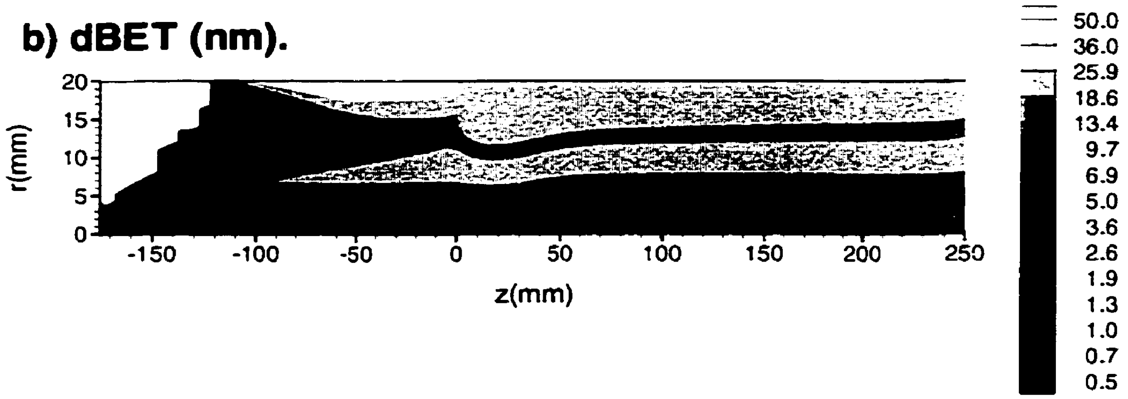

c) Part. number density (1/m^3).

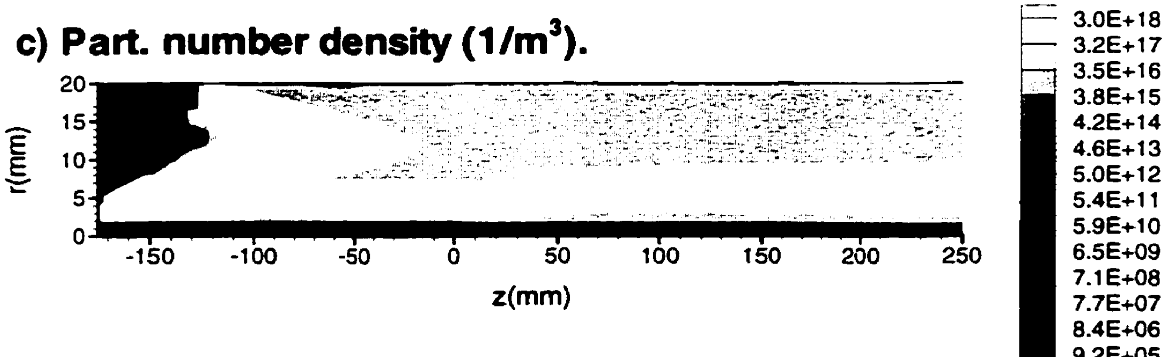

Reacting system, axial injection of NH_3

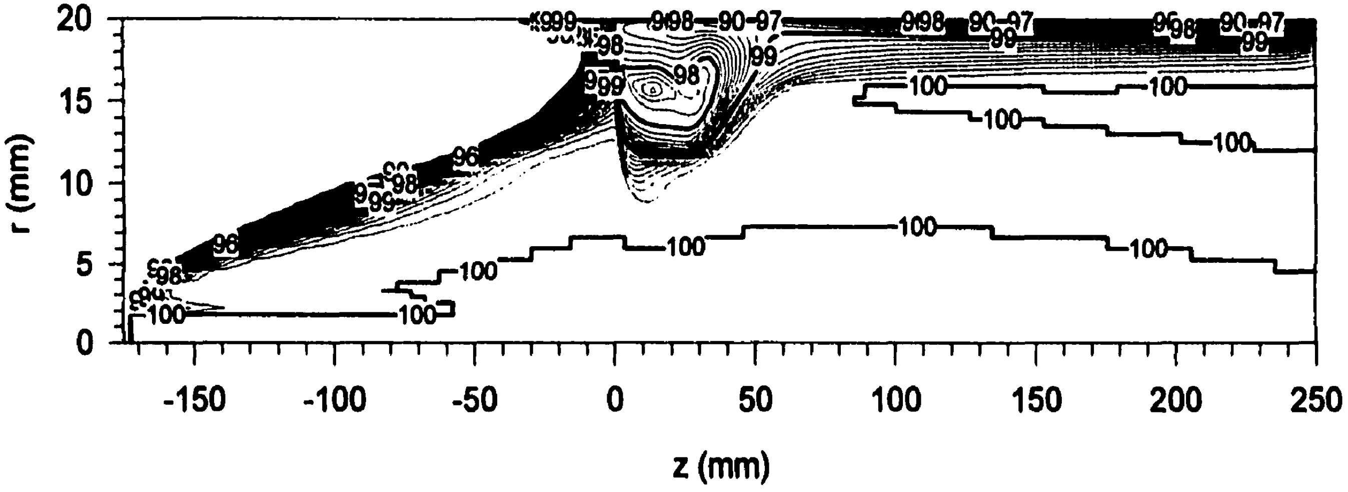

Figure 6.25 - AlN content of particles predicted for the axial injection of NH_3 (3 lpm) upstream of the radial injection. T1 = 2000 K, carrier gas flow rate = 25 lpm (pure Ar), radial gas flow rate = 6 lpm (N_2).

The distribution of the percentage of AlN in the condensed phase predicted by the model is shown in Figure 6.25. It is observed that full conversion is readily achieved in the high temperature and high NH_3 concentration core. Because of the lower temperatures near the tube wall, the particles which form in this region are difficult to be fully nitrided. However, in this injection configuration, the conversion at this region is better than 96 %. Since most of the gas-to-condensed phase transition occurs in the hot core, a conversion of 99.9 % was predicted for average of the powder at the exit of the calculation domain in the 2000 K temperature level. In case of the 1800 K temperature level, 100 % conversion was predicted for the average of the powder. These results, which are in full agreement with the experiments, confirm the importance of avoiding too high cooling rates in the mixing zone.

6.14. Conclusions

A two-dimensional numerical model was developed for the nucleation and growth of ultrafine particles in the tubular reactor. Based on thermodynamic equilibrium analysis, the small amount of AlN(g) predicted led to the assumption that the gas-to-condensed phase transition would be dominated by surface reaction.

Initially, it was assumed that nucleation of pure Al had to occur before surface reaction could take place. The simulation results produced using this assumption were not satisfactory. Specifically, the model could not explain the observed trends resulting from the use of different plasma gas compositions.

The hypothesis of a surface-reaction enhanced nucleation was examined. The results of experiments involving the production of pure Al particles in inert atmosphere, which resulted in powders with considerably larger particle sizes, were considered strong evidence for this assumption. A new formulation for the nucleation rate equation for the AlN system was developed. This formulation considers the effect of reaction on the surface of very small clusters of the new phase. This new modelling approach is in good agreement with the experimental results.

The different trends of the SSA vs. quenching intensity, caused by the different gas compositions, result from a greater cooling upstream of the quenching jet for the Ar/H_2 mixture. This was caused by the higher thermal conductivity of hydrogen.

The negative slope of the SSA vs. quenching intensity curve for pure Ar results from the coupling of heat and mass transfer as the jet becomes stronger. The more intense cooling caused by a stronger jet favours the Al nucleation component.

The relative importance of the mechanisms involved in the gas-to-condensed phase transition was examined. It was observed that, for the concentrations which were obtained experimentally, condensation of Al followed by surface reaction is by far the most important mechanism for the vapour phase synthesis of AlN.

A sensitivity analysis of the gas-phase AlN reaction rate, the coalescence of high AlN content particles, and the nucleation rate was carried out. Specifically, it was observed that the modelling results for the average SSA would strongly increase if the gas-phase reaction rate were high. The good agreement between model and experiment, when the homogeneous reaction is neglected, shows that the initial assumption of neglecting the gas-phase AlN reaction is justified.

The numerical study of the effect of concentration on particle size shows the existence of a maximum for both SSA and AlN content curves. Both maxima are caused by the modification of the balance between nucleation and condensation/surface reaction growth as the Al(v) concentration changes.

In the radial injection of NH_3, the model shows that the particles which form near the wall carry a large amount of unreacted Al. The simulation of the axial injection shows far better results for the powder composition. In full agreement with the experimental results, it shows that higher particle sizes are produced at the higher temperature level. The simulation results show that to reach full conversion, excessive cooling rates in the mixing zone must be avoided.

To study the sintering behaviour of the AlN powder produced in this work, cylindrical green compacts were prepared without additives from the powder whose XRD showed only the AlN phase. The samples were fired for 3 hours at temperatures ranging from 1250° to 1750 °C. The sintered compacts were analyzed for composition using XRD and XPS, for microstructure using TEM, for density using the Archimedes principle, and for linear shrinkage by measuring the sample diameter.

7.1. Background

Sintering is the process by which compacts of metal and/or ceramic particles are densified[1] at high temperatures. For most of the ceramic materials, sintering occurs by solid-state and/or liquid-phase material transport mechanisms. Solid-state sintering, generally associated with the densification of highly covalent materials like AlN, involves material transport by volume diffusion. It includes neck formation by evaporation-condensation and surface diffusion mechanisms. Densification occurs by bulk diffusion. The driving force for sintering is the reduction of the total free-energy of the system (ΔG_T) formed by[2]

$$\Delta G_T = \Delta G_V + \Delta G_B + \Delta G_S \qquad (7.1)$$

where ΔG_V , ΔG_B, and ΔG_S represent the change in free-energy associated with the volume, boundaries, and surface of the particles, respectively. Because the surface energy of a bulk ceramic is negligible, it may be assumed that the surface free-energy of the powder is the major driving force. The excess surface energy that a material possesses when in the form of a powder is particle size dependent, and becomes very significant for particle sizes < $1\mu m$.

Generally, AlN is sintered with the addition of an oxide (most commonly yttrium oxide, Y_2O_3). Pressureless sintering of AlN with sintering aids progresses by a liquid phase sintering mechanism. At high temperature, the oxide usually present on the particle surface of AlN powders reacts with the sintering aid to form an aluminate compound which is liquid at the sintering temperature. This liquid phase allows the material transfer which is essential for densification. This procedure is specially suitable for preparing high thermal conductivity AlN. For most of the ceramic materials, heat is primarily transferred by lattice vibrations. In analogy with the photons in the radiation theory, in the theory for the thermal conduction process, since the elastic vibrations are nearly harmonic, wave like solutions for the motion of atoms in a crystalline lattice can be quantized in amounts of energy called phonons[1]. Phonon scattering by impurities, specially oxygen, is seen as the main reason for the low conductivity observed in AlN ceramics, as compared with its theoretical value of 320 W/m.K[3]. If the sintering aid composition does not wet the AlN grains, it migrates to grain triple points. Thus, most of the grain interface can be kept clean, free from phonon-scattering impurities. The sintering aid located at the triple points does not significantly interfere with the thermal conduction[13].

Sintering and phase equilibria of Al_2O_3 and AlN compositions were studied by McCauley and Corbin[90]. They determined a relatively wide range of stable compositions roughly centered at 35.7 %mol AlN. This composition is equivalent to the stoichiometric composition $Al_{23}O_{27}N_5$ or $5AlN.9Al_2O_3$, which McCauley and Corbin refer to as ALON (nitrogen stabilized cubic aluminum oxide). They have also shown that this composition when pressureless sintered to nearly full density exhibits transparency in visible light. The phase diagram for the Al_2O_3-AlN composition proposed by McCauley and Corbin[91] is shown in Figure 7.1. This figure shows an eutectic at 25 %mol AlN (1850°C).

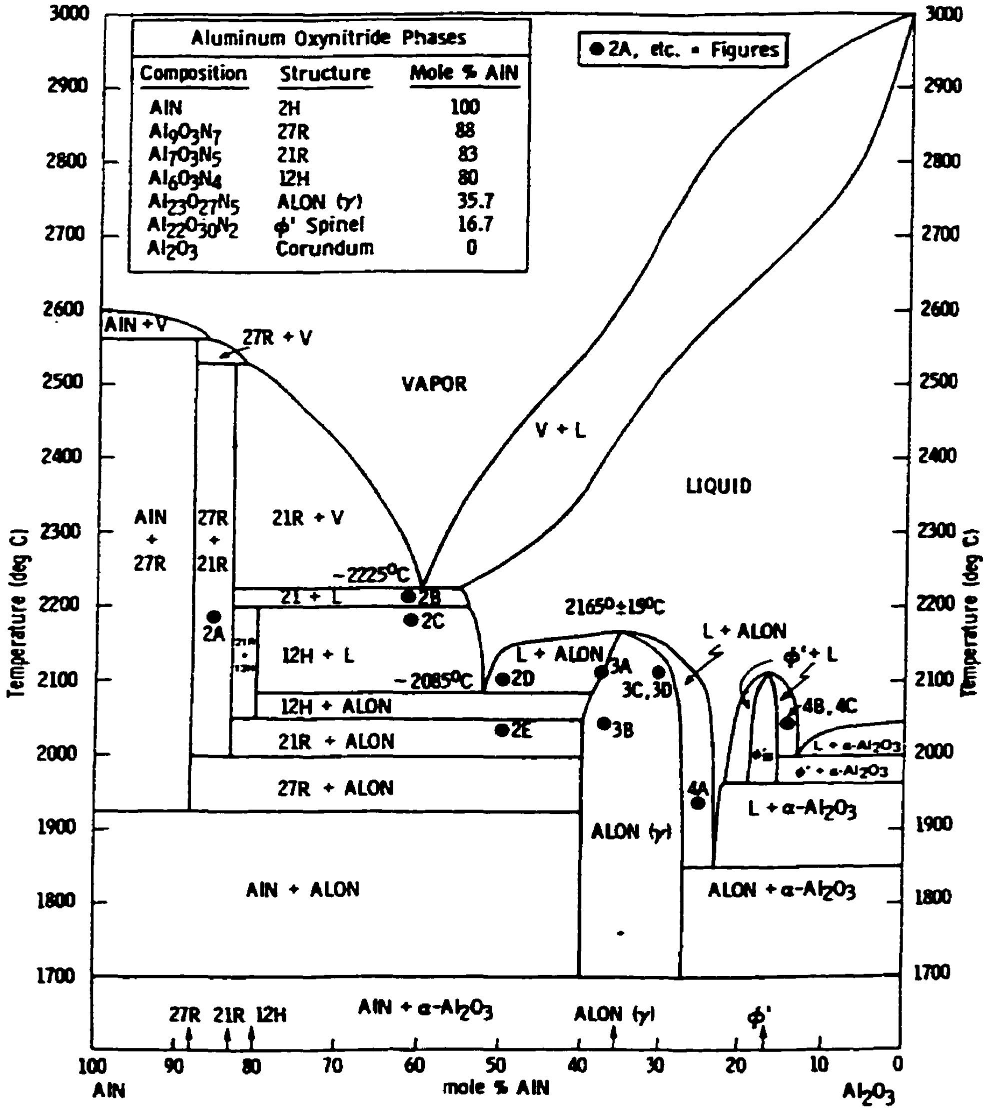

Figure 7.1 - Phase diagram for the Al_2O_3-AlN composition join in the one atmosphere of flowing nitrogen proposed by McCauley and Corbin[91].

Hashimoto and Yoden[92] investigated the densification behaviour of AlN as a function of particle size and oxygen composition of powders with a specific surface area in the range 3.2-22.8 m^2/g. They observed that smaller particle sizes increase densification and little influence of oxygen content. They reported that AlN powder without additives reached theoretical density at 1700 °C. The addition of 2 %wt Y_2O_3 decreased the temperature required for full densification to 1600 °C.

Experiments involving the sintering of AlN powders synthesized by plasma were conducted by Wehling et al.[20] and Ageorges et al.[11]. These authors reported the preparation of full density AlN ceramics by pressureless sintering of AlN ultrafine powders at lower temperatures than commonly used for commercially available powders.

Wehling et al.[20] reported that cylindrical samples (6 mm dia. x 7 mm height) prepared from AlN powders without use of additives could be sintered at 1530 °C to a density of 3.30 g/cm^3. The samples were prepared from RF plasma synthesized AlN powders with a specific surface area of 115 m2/g. The sintering experiments were carried out under atmospheric pressure of N_2. The use of different additives (1.5 %wt $CaCO_3$ and 5.0 %wt Y_2O_3) showed that the maximum sintering temperature could be further reduced. A maximum linear shrinkage of 21 % was reported.

Ageorges et al.[11] reported that samples prepared with the addition of 1 %wt Y_2O_3, pressureless sintered at 1850 °C for 3 hrs in N_2 atmosphere, had a density of 3.26 g/cm^3 and were translucent. They also reported that the same powder sintered without additives had a density of 3.15 g/cm^3.

Baik[93] studied the pressureless sintering of commercial AlN with Y_2O_3 as additive in several compositions. This study showed that full density of commercially available powder is achieved above 1850 °C. The commercial powder used in these experiments (Tokuyama Soda, Grade F) had a specific surface area of 3.3 m^2/g.

7.2. Experimental procedure

To minimize the influence of particle size and oxygen composition on the sintering process, only powders which had a SSA in the 85 to 110 m^2/g range were used. The oxygen content of these powder samples ranged from 8.8 to 11.2 %wt, directly proportional to the specific surface area of the powder as shown in Figure 7.2. Amounts of about 0.5 g of powder were compacted at 5000 psi into cylindrical green compacts of 9.6 diameter x 5.0 mm height. The powder was compacted as produced, without the use of binders or additives. A minimum of two green compacts were prepared for each firing temperature.

A graphite resistance furnace (Bullet), which operates either in vacuum (maximum of 50 mmHg) or inert atmosphere, was used for these experiments. Internally, the furnace is insulated with graphite felt. Its walls are water cooled. The green compacts were arranged on top of a BN plate placed in the center of the cylindrical electrical resistance (100 mm internal diameter).

The air inside the furnace was purged by successively filling its space with N_2 and producing vacuum. For degassing, a vacuum better than 100 mmHg was kept until the temperature reached 1000 °C. After reaching this temperature, the furnace was filled with N_2, and typically kept at 1 atm pressure. Heating took from 2 to 3 hours, depending on the specific firing temperature. Once the firing temperature was reached, it was maintained in a ±10 °C range for 3 hours. After that, the furnace was let to cool to room temperature before it was opened.

7.3. Results and discussion

The sintering experiment data are shown in Table 7.1. Figure 7.3 shows the X-ray diffraction patterns of compacts sintered at 1250 °C and 1650 °C. A small peak of a second phase is observed at approximately 46° for the sample sintered at 1250 °C. This phase becomes more pronounced at 1650 °C. This new phase was identified as an aluminum oxynitride of a general composition $Al_{8/3-x/3}O_{4-x}N_x$ (JCPD card 18-52).

Table 7.1 - Sintering experiment data.

Sample	SSA (m^2/g)	Firing T (°C)	density (g/cm^3)	relative density (%)	linear shrinkage(%)
#33.1(a)	85.2	1250	3.23	97.2	3.1
#33.2(b)	98.1	1250	3.24	97.5	3.0
#33.1(a)	85.2	1350	3.21	96.5	8.8
#33.2(b)	98.1	1350	3.25	97.6	8.6
#33.1(a)	85.2	1450	3.24	97.5	17.2
#33.2(b)	98.1	1450	3.24	97.6	17.2
#33.3(a)	107.4	1550	3.28	98.7	23.7
#33.4(b)	90.2	1550	3.28	99.1	16.8
#31.4(c)	105.0	1550	3.28	98.7	22.0
#31.5(d)	87.0	1550	3.27	98.7	19.3
#30.4(a)	101.9	1650	3.29	99.2	24.1
#31.4(b)	105.0	1650	3.32	100.0	19.3
#32.5(c)	91.5	1650	3.29	99.2	16.9
#32.5(d)	91.5	1650	3.33	100.6	23.2
#33.4(a)	90.2	1750	3.28	98.8	23.3
#33.4(b)	90.2	1750	3.31	99.5	20.4

Table 7.2 - Chemical composition at the surface of the powder particles and of fragments of sintered compacts determined by XPS surface analysis.

	Powder	Sinter	Sinter	
Sint. T (oC)	-	1,650	1,550	
Powder	#33.3	#30.4	#33.3	
Al	41.7	36.8	42.2	%At
N	26.0	21.2	26.2	
O	27.4	26.0	25.4	
C	5.0	16.1	6.2	
AlN	53.52	45.84	54.21	%wt
Al_2O_3	40.39	39.53	38.21	
Al	0.00	1.21	1.43	
C	1.88	8.99	2.86	
CO_2	4.21	4.43	3.30	

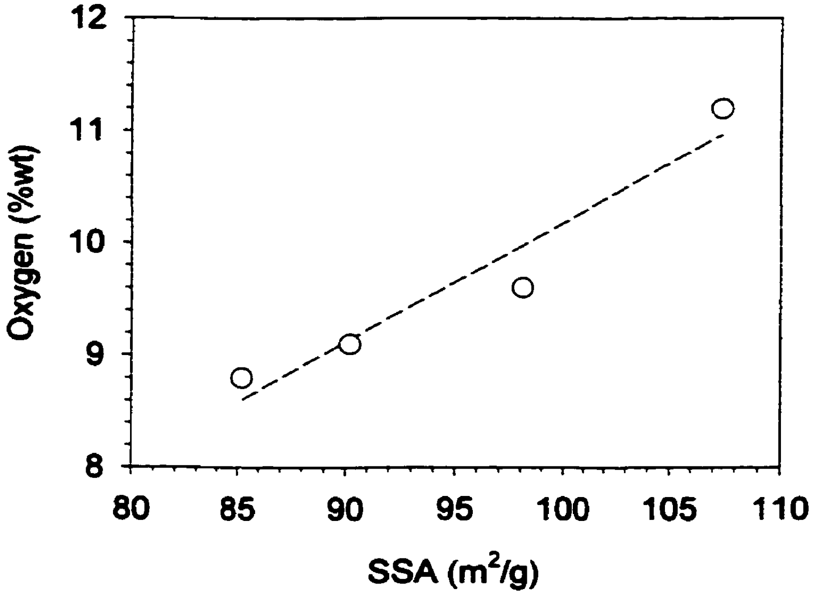

Figure 7.2 - Oxygen content determined by high temperature decomposition (LECO) representative of the powders used for the sintering experiments.

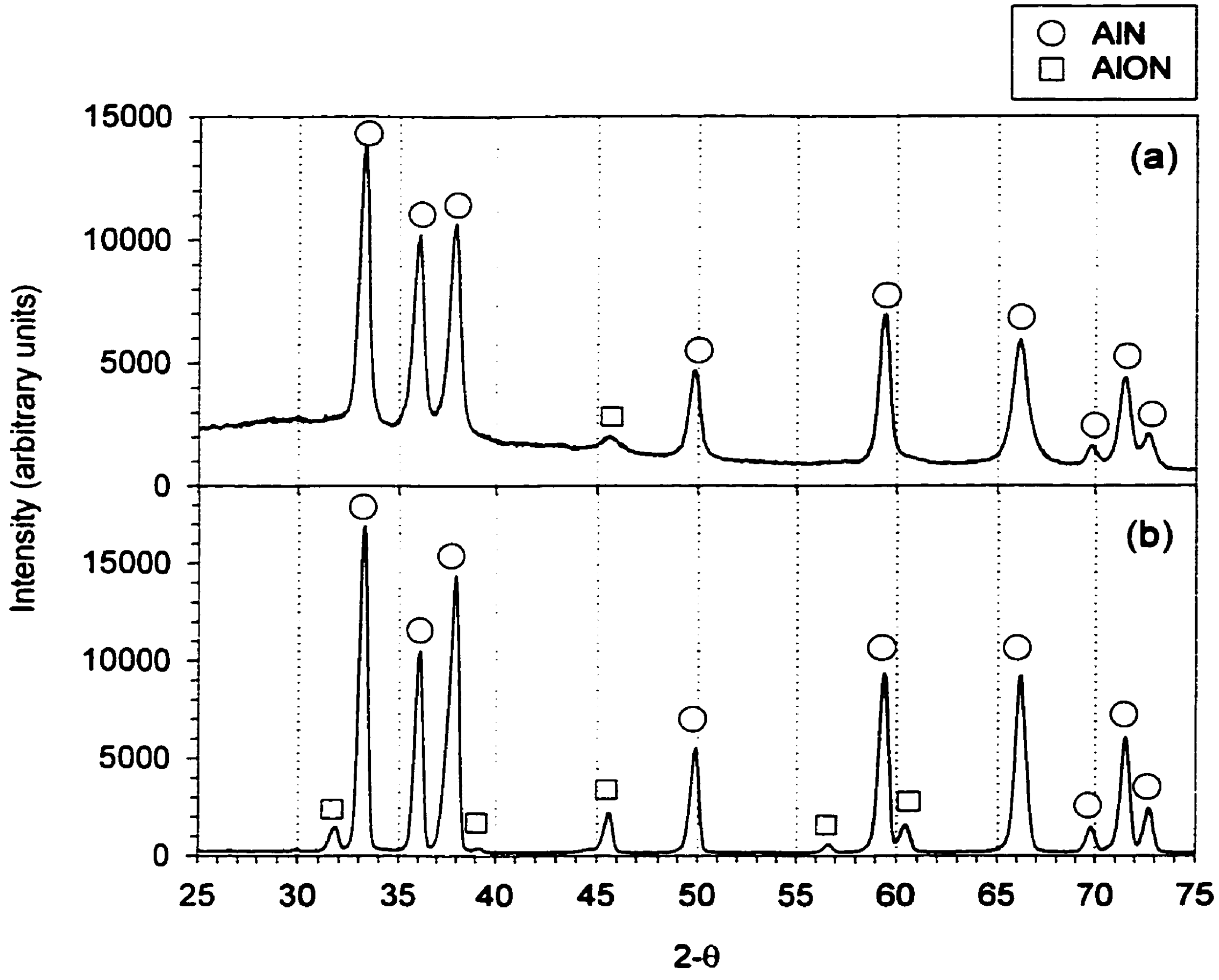

Figure 7.3 - X-ray diffraction pattern of sintered compacts: a) powder sintered at 1250 °C; b) powder sintered at 1650 °C.

The peaks of the elements found by the XPS survey of the AlN powder and fragments of sintered compacts are shown in Figure 7.4. The corresponding chemical compositions are shown in Table 7.2. With the exception of the samples fired at 1550 °C, all samples were fired in non-flowing N_2 atmosphere (10^5 Pa). Larger C contents were observed for the samples treated in this condition than for the initial powder. The hypothesis that higher C content resulted from C pick up from the furnace atmosphere (as a result of the large reactivity of the starting powder caused by its large specific surface area) was confirmed by the special preactions taken when sintering samples at 1550 °C. These samples were treated in flowing N_2, and with small pellets of titanium sponge placed around them to minimize their contact with C and CO eventually present in the furnace atmosphere. The detailed XPS C peaks of samples treated in these two different furnace preparations, and of the initial powder are shown in Figure 7.5. The small peak to the right was attributed to CO_2 which generally represents contamination by atmospheric air. The carbon content of the samples (left peak) is observed to increase with sintering treatment. Sample #30.4, which presents the highest C content was treated at stagnant N_2 atmosphere, without titanium sponge pellets. As shown in Table 7.2, C reduces the oxide forming free-Al.

The surface morphology and microstructure of compacts fired at 1350° and 1750 °C were examined by TEM. The sintered samples were fractured and fragments were analyzed using Pt/C replica technique[94] of the exposed surface. The replicas consisted of thin platinum/carbon (Pt/C) film (95 %wt Pt) film, 1-2 nm thick, deposited on the sample surface. The replicas were detached from the sample surface using concentrated HF solution and transferred to a 200 mesh copper grid coated with supporting carbon film (20 - 30 nm thick). Figure 7.6 shows the internal microstructure of a fracture surface of a compact fired at 1350 °C. This represents an intermediate stage of the sintering process in which fine grains of the starting powder and a new phase are observed. The higher magnification shows a plate like microstructure which resembles the coarser microstructure which was observed by McCauley and Corbin[90] in nitrogen stabilized cubic aluminum oxide (AlON) at a 35.7 %mol AlN. The observation of this new phase agrees with the small peak observed at 46° in the XRD shown in Figure 7.3(a). This phase seems to result from the incorporation of the oxygen present on the surface of the starting powder into the AlN lattice.

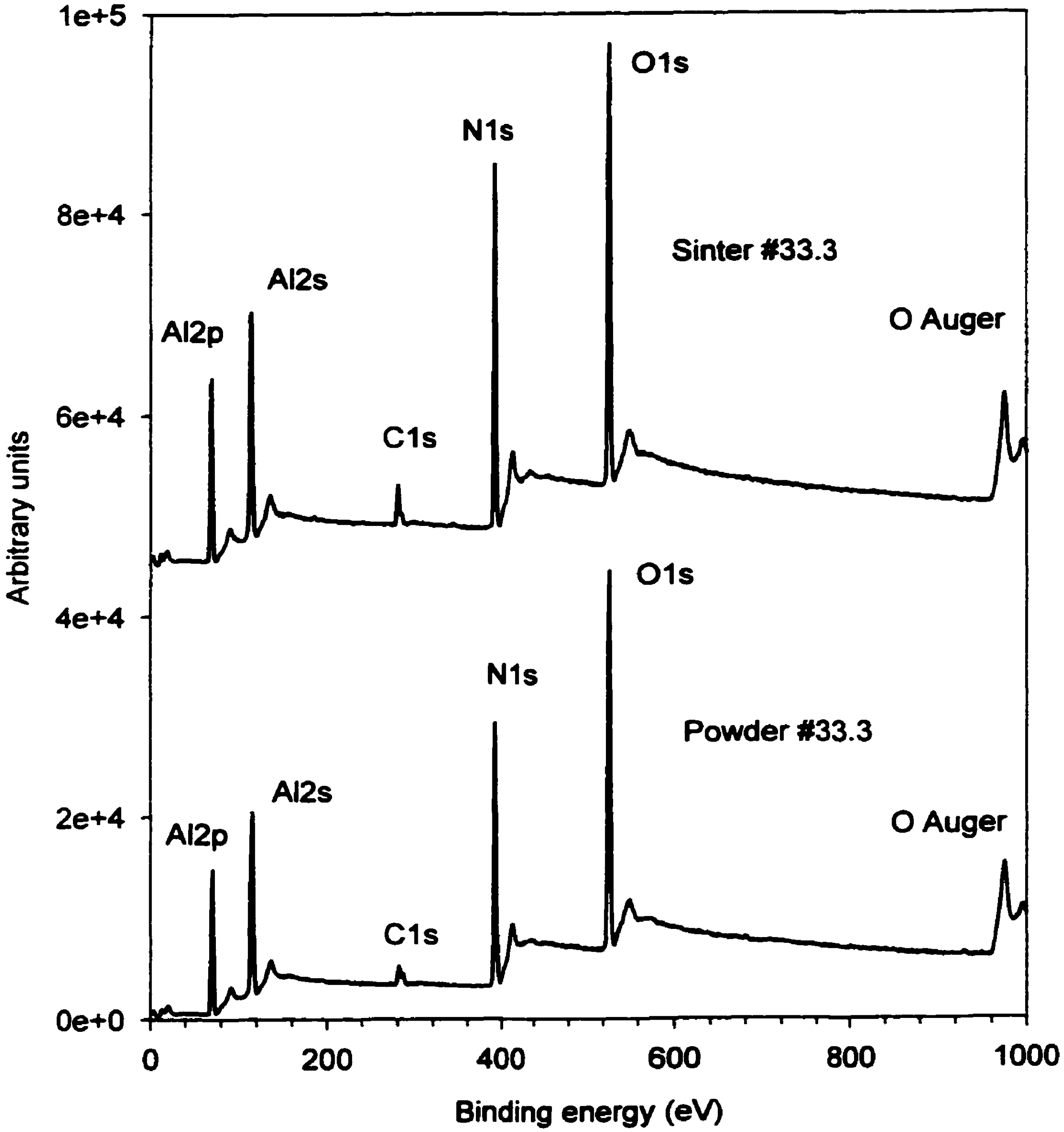

Figure 7.4 - XPS survey on AlN powder and fragment of a compact sintered at 1550 °C.

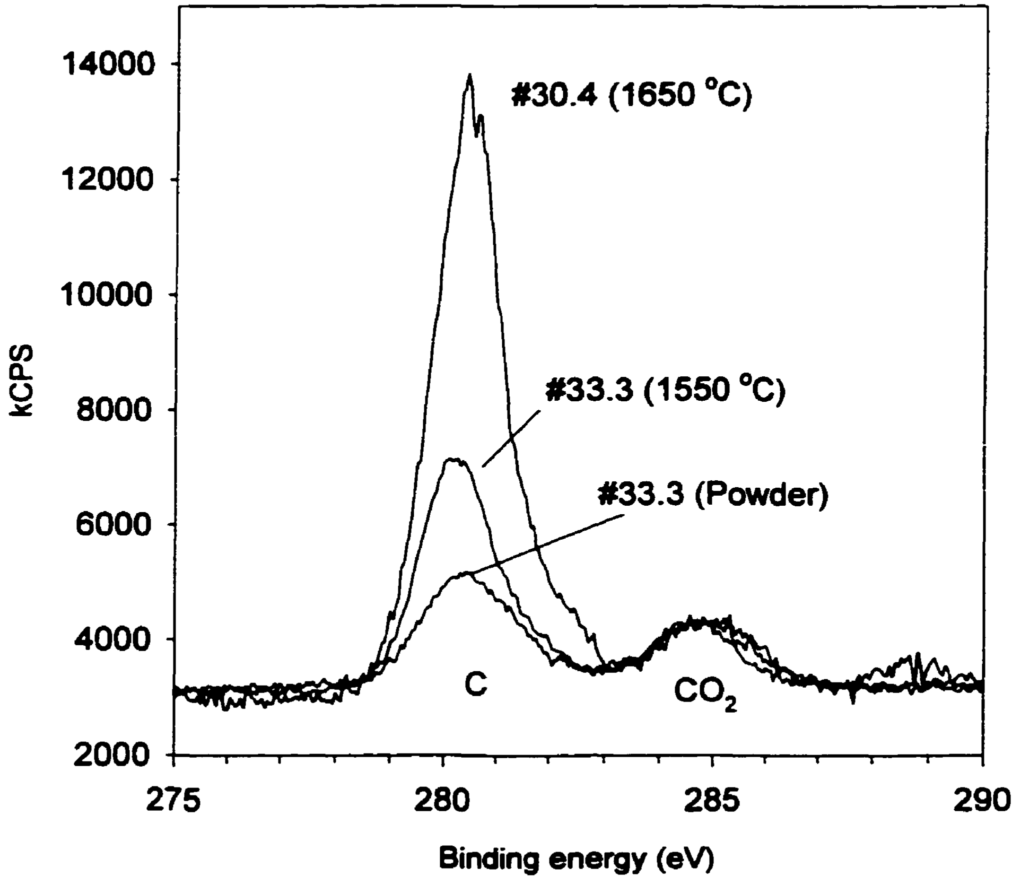

Figure 7.5 - Carbon 1s peaks of AlN powder and sintered compacts determined by XPS surface analysis.

The internal microstructure exposed by the fracture surface of a compact sintered at 1750°C is shown in Figure 7.7. A dense structure with coarse grains is observed (compared with the particles size of the starting powder shown in Figure 7.6). The brighter areas observed are the result of shadowing effect. This microstructure is similar to the one observed by Hashimoto and Yoden[92] in sintered compacts of coarser powders (14.6 m^2/g) sintered without additives for 3 hours at 1800 °C.

The effect of the sintering temperature on powder densification is represented in Figure 7.8. In this figure, the average of the densities and linear shrinkages, and their respective minimum and maximum ranges, as given in Table 7.1, are shown as a function of the sintering temperature. The linear shrinkage is referred to the green compact diameter of 9.6 mm. Because of the presence of oxygen in the AlN structure, densities which are higher than the AlN theoretical density (3.26 g/cm^3) are observed above 1550 °C. The density of the compact was determined using the Archimedes principle, with the samples immersed in isopropanol (0.785 specific density). Because no precaution was taken to avoid impregnation of the open structure of the samples sintered at lower temperatures by the isopropanol, the measurement resulted in a density higher than their true density (which could be evaluated from the dimensions and weight of the sintered samples). The tight microstructure observed in Figure 7.7 for the samples sintered at 1750 °C shows that full density has been attained at this temperature.

7.4. Conclusions

The sinterability of the powder produced was studied. Green compacts of the powder produced were sintered at temperatures ranging from 1250° to 1750 °C. Sintering to full density was achieved at temperatures lower than needed for commercially available powders in similar firing conditions.

Because of the high oxygen content of the powder, a second phase identified as aluminum oxynitride (ALON) was observed to form. The microstructure of the compacts sintered to full density was similar to the microstructure of compacts sintered with coarser powders reported in the literature[92]. The finer microstructure observed in the present case seems to result from the use of a finer powder.

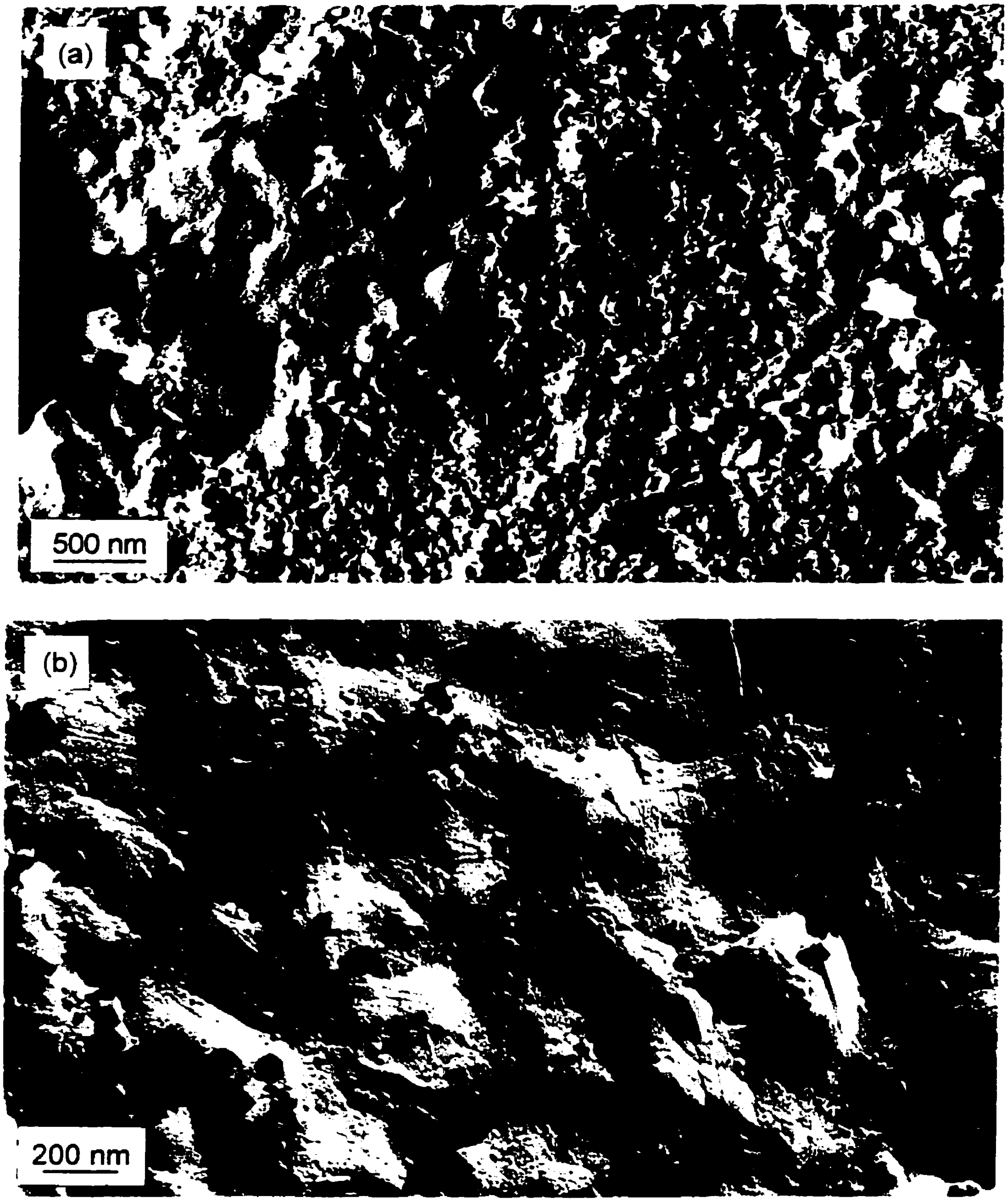

Figure 7.6 - TEM Pt/C replica of a compact fired at 1350 °C, shown in progressive magnification.

Figure 7.7 - TEM Pt/C replica of a compact sintered at 1750 °C, shown in progressive magnification. The arrow indicates the shadowing direction.

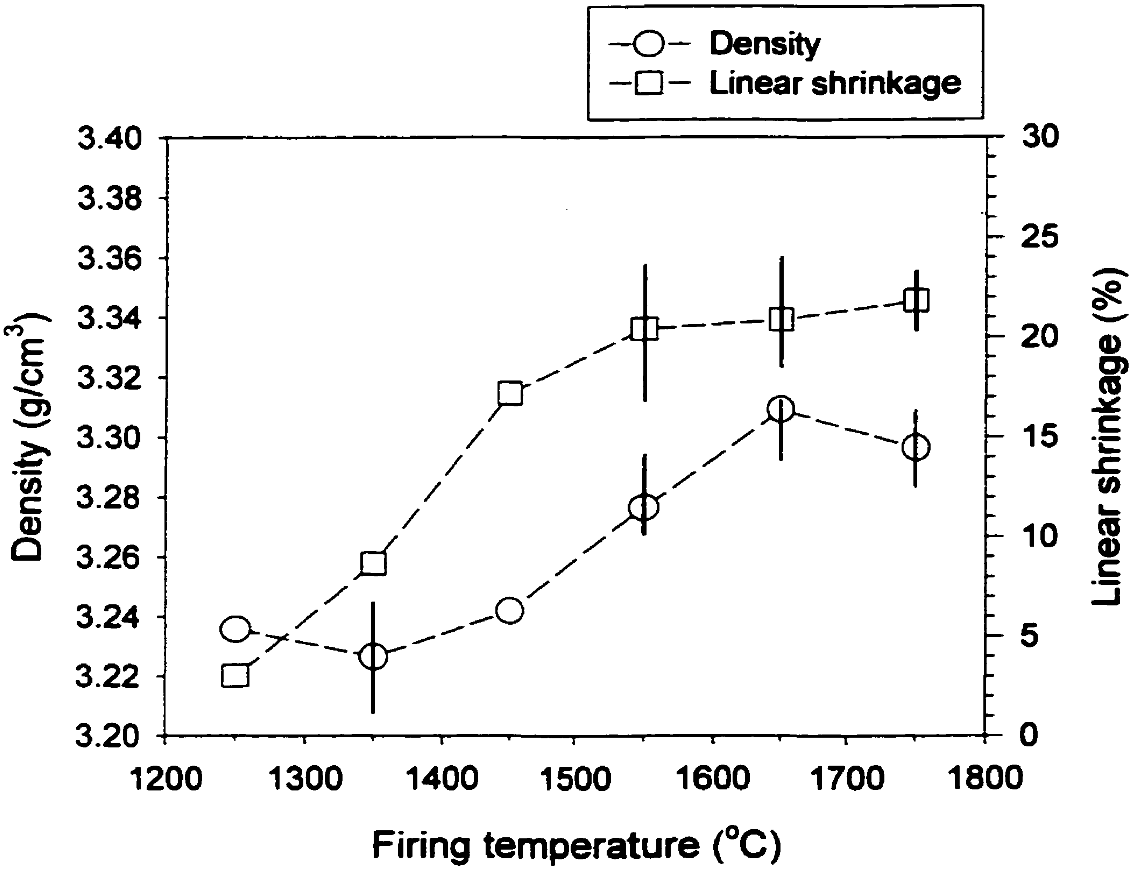

Figure 7.8 - Effect of firing temperature on powder densification. Simbols indicate average value and bars the minimum and maximum range.

Chapter 8

CONCLUSIONS AND RECOMMENDATIONS FOR FUTURE WORK

8.1 Conclusions

In the following, the overall and most relevant conclusions of this work are presented. Specifically, the observations and conclusions concerning both experimental and modelling developments were summarized in their respective chapters.

1. An experimental and theoretical study of the fundamentals of the vapour phase synthesis of ultrafine AlN particles using thermal plasma was carried out. The methodology followed in this research involved the simultaneous experimentation and development of a numerical model for the mixing region of the reactor. The synergism of these two approaches strongly contributed to a better understanding of the gas-to-condensed phase transition in this reacting system.

2. The first part of the work involved the radial injection of a NH_3/Ar mixture. The experimental investigation of the dependence of the particle size and composition on the reactor operating conditions was carried out. The numerical simulation was used to interpret the several trends observed experimentally. Since many of the physical properties needed for this development are not presently available, a large number of estimates and assumptions had to be made. To this respect, the experimental results were used for the validation and/or guidance along the model development.

3. A new equation for the nucleation rate for the AlN system was proposed. Its formulation was based on the observation of the experimental trends of SSA vs. quenching intensity, and results for pure Al nucleation. This formulation considers the effect of reaction on the surface of clusters of the new phase, which can greatly increase the nucleation rate.

4. In the present reactor design, none of the experiments with the radial injection of NH_3 produced a 100% AlN powder. This resulted from excessive cooling caused by the radial injection. The model results showed that particles which form near the wall carry a large amount of unreacted Al.

5. The model initially developed for the radial injection was adapted to study the axial injection of NH_3 upstream of the quenching jet. Its results showed that more than 99.9% AlN powder would be produced in this new configuration. The experimental results fully confirmed these predictions.

6. With the axial injection, a broad range of particles sizes were produced (SSA ranging from 38 to 206 g/m^2). A high oxygen contamination (5.8-11.2%) was observed since no special care was taken during handling of the powder. Carbon content was estimated to be 1.9%. Carbon results from erosion of the graphite crucible, and also from contamination by atmospheric CO_2.

7. The study demonstrated that the control of particle size and composition depends on the proper combination of process variables. The following is a summary of the major trends observed with respect to the influence of process variables such as gas temperature, metal vapour concentration, and cooling intensity on particle size and composition in this system:

a) Particle size:

(i) Metal vapour concentration: higher concentrations, for the same gas composition and cooling intensity, favours the formation of larger particle sizes. Because higher vapour concentrations are achieved when temperature is increased, high temperature operation results in larger particle sizes.

(ii) Cooling intensity: because higher cooling intensity favours the Al nucleation component of the nucleation rate, larger particle sizes form upon increased quenching. This observation opposes the usual trend observed in other systems according to which higher cooling rates produce smaller particles. In the present reactor design, because of the modification of the gas thermal conductivity, cooling condition is associated with gas composition.

The experiments with the axial injection of NH_3 at different positions upstream the quenching jet showed the possible influence on particle size of the residence time at high temperatures (the longer the residence time the larger the particles which are expected to form).

b) AlN content:

Although experimental and modelling results did not show a good quantitative agreement for particle composition for the radial injection of NH_3, the following trends could be observed:

(i) Al particles which nucleate and grow before the mixing zone near the wall do not fully react (modelling observation).

(ii) Conversion is improved (although to a limited amount) by increased mixing; a higher Ar flow rates causes the increase of NH_3 concentration towards the tube centreline (experimental observation).

For the axial injection, modelling and experiment were in full agreement: provided that the temperature is kept high enough to avoid nucleation of Al particles, full conversion occurs if there is good mixing of NH_3 with the hot gas.

8. The sinterability of the powder produced was studied. Sintering to full density was achieved at 1550 °C. Because of the high oxygen content of the powder, a second phase identified as aluminum oxynitride (ALON) was observed to form.

8.2. Contributions to knowledge

The following are the original contributions resulting from this research:

1. Design and application of a new version of a transferred-arc reactor for producing ultrafine particles.
2. Experimental and theoretical study of the effect of temperature and cooling conditions on particle size and composition characteristics of ultrafine AlN powder produced by vapour-phase synthesis.
3. Development of a new equation for nucleation in the AlN system which considers the effect of surface reaction.
4. Better understanding of the nucleation and growth mechanisms of ultrafine particles in the plasma synthesis of AlN.
5. Ability to produce ultrafine AlN powders with a wide range of specific surface areas.
6. Study of the sintering and development of the microstructure during the sintering of ultrafine AlN powder produced by plasma vapour synthesis.

8.3. Recommendations for future work

1. Modification of the operating conditions and/or mixing zone to produce larger particle sizes [the SSA range between 3 m^2/g (maximum produced commercially) and 38 m^2/g (minimum produced in the present experiments) was not covered by this work]. This can be accomplished by improving Al evaporation (higher arc currents and/or better thermal insulation of the plasma chamber). In this case, operating temperature will be higher than the maximum produced in this work (2000 K). Another possibility would be to improve the residence time by carrying out mixing and reaction with gas recirculation in a chamber having larger volume, immediately after the plasma chamber [the axial injection (experimental results) of NH_3 inside the chamber above the tubular reactor suggests that particle size can be controlled by controlling the residence time of particles at the high temperature].

2. In order to avoid powder contamination by C it is recommended to study the mechanisms by which the graphite crucible becomes eroded; this would require the investigation of different crucible materials, possibly a combination of graphite and a high temperature ceramic or the use of molibdenum.

3. Continuous feeding of Al to allow longer operating times and reduce the time consuming and costly experiment preparation. In this case, use of a bigger filter is recommended for long term operation (collection of large amounts of powder), while using a small metal filter for short term powder sampling.

4. The present model can be improved by using more precise reaction kinetic data as these became available. Because of the unavailability of data, many assumptions had to be made concerning physical properties and reaction kinetics.

5. Study of other systems which might involve surface-reaction using the developed mathematical model.

6. Inclusion of a turbulence model.

7. Study of the sintering properties of plasma produced powders for electronic applications. This will involve the production of larger amounts of powder and handling the powder in an oxygen free environment.

NOMENCLATURE

a_o = coefficient for the linear expansion equation.
A = pre-exponential factor (reaction rate equation).
A = AlN unit cell basal plane surface area (m^2).
A_o = "first surface area" available for condensation (m^2).
A_x, A_y = coefficients defined by Equations (6.78) and (6.79), respectively.
b = coefficient used on the approximation of the birth and death terms by the sum of fractional moments.
b = backward rate (s^{-1}).
B = birth term in the population balance equation.
$(B - D)$= birth and death term.
$B_1, B_2, B_{2a}, B_{2b}, B_3, B_4$ = coefficients used in the formulation of the surface growth rate.
C_p = specific heat (J/kg·K)
d_{BET} = BET surface area average particle diameter (m).
d_N = number mean particle diameter (m).
d_p = particle diameter (m).
D = death term in the population balance.
D_{Al-N} = dissociation energy of the Al-N bond (kJ/mol).
$D_{i,Ar}$ = mass diffusivity (m^2/s).
D_p = particle diffusivity (m^2/s).
d_p = particle diameter (m).
E = activation energy (kJ/mole).
e = electron charge.
f = log-normal distribution defined by Equation (6.5).
f = integration variable.
f = forward rate (s^{-1}).
f_ε = AlN dissociation energy related multiplier defined for sensitivity analysis.
f_σ = surface energy related multiplier defined for sensitivity analysis
f_{FS} = Fuchs-Sutugin factor, defined by Equation (6.25).

F = normalization constant.

g = integration variable.

G = surface growth (m^3/s);

G = Gibbs free energy (J/kg).

G_{fm} = surface growth in the free-molecule regime (m^3/s)

G_r = Gibbs free energy for the surface nitridation reaction (J/kg).

h = gas enthalpy (J/kg).

H = function defined by Equation (6.91).

i_e = electron flux.

J = nucleation rate ($1/m^3/s$).

J_{cl} = nucleation equation which is deduced from the classical theory ($1/m^3/s$).

J_{eq} = equivalent nucleation rate ($1/m^3/s$).

J_{kin} = Girshick's homogenous nucleation equation formulation ($1/m^3/s$).

J_{SREN} = surface-reaction enhanced nucleation rate ($1/m^3/s$).

k = thermal conductivity (W/m·K).

k = reaction rate.

K = thermophoretic coefficient.

K_C = equilibrium constant, concentration.

K_P = equilibrium constant, partial pressure.

k_B = Boltzmann constant (1.38×10^{-23} J/K).

Kn = Knudsen number.

LnS = expression defined by equation (6.116).

m_{Al} = mass of the Al atom (kg).

m_{AlN} = mass of the AlN molecule (kg).

M_k = k^{th}-moment of particle size distribution (m^k/m^3).

M_k' = k^{th}-moment of particle size distribution as used in SIMPLER algorithm, defined by equation (6.50) (m^k/kg).

$\overline{M}$ = molecular weight.

n = particle number density (1/m^3).

n = number of moles per unit volume (moles/m^3).

n = number of moles per unit volume (moles/m^3)

n_{Al}^{e} = number density of Al atoms in the gas phase at equilibrium.

N = particle number density at the constrained equilibrium (1/m^3).

N_{Av} = Avogrado number (=6.02x10^{23})

$\overline{N}$ = normalization constant.

p = pressure.

P = steric factor.

Pe = Peclet number $\left(\rho uL/\Gamma\right)$, where Γ is the diffusion coefficient.

q = energy flux (W/m^2·s).

r = radius (m).

R = gas constant (8.3192 kJ/kmol·K).

R_{AlNcon} = AlN(g) condensation rate.

R_{AlN}^{g} = AlN gas-phase reaction rate (moles/cm^3/s).

$R_{AlN}^{s,c}$ = AlN surface reaction rate on a cluster surface (1/m^2/s).

$R_{AlN}^{s,p}$ = AlN surface reaction rate on a particle surface (1/m^2/s).

s = particle (cluster) surface area (m^2);

s = number of square terms.

s_1 = monomer surface area (m^2).

S = supersaturation ratio.

S_{Al} = Al vapour supersaturation ratio.

S_C = linearization coefficient for the source term in the SIMPLER algorithm general partial differential equation.

S_P = linearization coefficient for the source term in the SIMPLER algorithm general partial differential equation.

t = time (s).

t = variable defined by Equation (6.96).

T = temperature (K).

u = velocity (m/s).

U = velocity vector.

U_{th} = thermophoretic velocity vector.

v = particle volume (m^3).

v = velocity (m/s).

$\overline{v}$ = particle volume satisfying the relation $\overline{v} + (v - \overline{v}) = v$ (m^3).

v_{Al} = volume of an Al atom (m^3).

v_{AlN} = volume of an AlN "molecule" (m^3).

v^{Al} = volume of free-Al in a particle (m^3).

v^{AlN} = volume of AlN "molecules" in a particle (m^3).

v_{cr} = volume of critical-particle (m^3).

v_g = geometric average particle volume.

V_a = anode voltage drop.

x = number of Al atoms in a cluster.

x_{Al} = aluminum vapour mole fraction.

$\overline{X_c}$ = average sub critical-cluster free-Al mole fraction.

$\overline{X_p}$ = average stable-particle free-Al mole fraction.

$\overline{X_v}$ = average stable-particle free-Al volumetric fraction.

y = number of AlN "molecules" in a cluster.

w = mass fraction.

z = axial coordinate (m).

Greek symbols

α = mass accommodation coefficient.

α = linear expansion coefficient (cm/cm/°C).

β_i = condensation (or impingement) rate of species i (1/m^2/s).

$\beta_{v,\overline{v}}$ = collision frequency between particle sizes v and $\overline{v}$ (1/s).

β_{fm} = collision frequency between particle sizes v and $\overline{v}$ in the free-molecule regime (1/s).

β^* = equivalent impingement rate, defined by Equation (6.19).

δ = Kronecker delta (equals 1 or 0 depending on if indexes are equal or different, respectively).

ε_o = dissociation energy (J/molecule).

θ = dimensionless surface energy.

λ = mean free-path length (m).

ρ = gas density (kg/m^3).

ρ_p = particle density (kg/m^3).

μ = viscosity (kg/m·s).

σ = surface energy (N/m).

σ_g = geometric standard deviation.

ϕ_a = work function of the anode material.

Φ = general variable in the SIMPLER algorithm equation.

Subscripts

a = anode.

c = convection.

r = radiation.

i = chemical species.

k = moment order.

L = liquid.

s = saturation.

v = evaporation.

Superscripts

e = equilibrium.

REFERENCES

[1] Kingery, W. D., Introduction to Ceramics, John Wiley and Sons, New York, 1976.

[2] Richerson, D. W., Modern Ceramic Engineering, Marcel Dekker, Inc., New York, 1992.

[3] Sheppard, L. M., International trends in powder technology, Ceramic Bulletin. Vol. 68, No. 5, p. 979, 1989.

[4] Selvaduray, G. and Sheet, L., Aluminum nitride: review of synthesis methods, Materials Science and Technology, Vol. 9, pp. 463-473, 1993.

[5] Fauchais, P., Bourdin, E., Coudert, J. F., and McPherson, R., High pressure plasmas and their application to ceramic technology, in Topics in Current Chemistry, F. L. Boschke (ed.), Plasma Chemistry IV, Springer-Verlag, pp. 59-183, Berlin, 1983.

[6] Kong, P. C. and Lau, Y. C. , Plasma synthesis of ceramic powders, Pure and Applied Chemistry, Vol. 62, No. 9, pp. 1809-1816, 1990.

[7] Hamblyn, S. M. L., and Reuben, B. G., Use of radio-frequency plasma in chemical synthesis, Advances in Inorganic Chemistry and Radiochemistry 17, p. 89, 1975.

[8] Akashi, K., Application of plasma to processing for ceramics, Techno Japan, Vol. 20, No. 3, pp. 7-26, 1987.

[9] Dransfield, G., Plasma production and novel processing of ultrafine ceramic powders, in Ceramic Technology International, Ian Birkby (ed.), pp. 71-74, Sterling Publication Ltd., Malasia, 1992.

[10] Etemadi, K., Formation of aluminum nitrides in thermal plasmas, Plasma Chemistry and Plasma Processing, Vol. 11, No. 1, p. 41-56, 1991.

[11] Ageorges, H., Megy, S., Chang, K., Baronnet, J. M., Williams, J. K., and Chapman, C., Synthesis of aluminum nitride in transferred arc plasma furnaces, Plasma Chemistry and Plasma Processing, Vol. 13, No. 4, p. 613-632, 1993.

[12] Moura, F.J, Vapour Phase Synthesis of AlN using a Transferred Arc Plasma System, Ph.D.. Thesis, McGill University, Montreal, 1993.

[13] Mroz, T. J., Aluminum nitride, American Ceramic Society Bulletin, Vol. 72, No. 6, pp. 78-80, 1993.

[14] Kimura, I., Ichiya, K., Ishii, M., Hotta, N., and Kitamura, T., Synthesis of fine AlN powder

by a floating nitridation technique using N_2/NH_3 gas mixture, Journal of Materials Science Letters, Vol. 8, pp. 303-304, 1989.

[15] Chang, A.J., Rhee, S.W., and Baik, S., Nitridation characteristics of floating aluminum powder, Journal of Material Science., Vol. 30, pp. 1180-1186, 1995.

[16] Kimura, I., Hotta, N., Nukui, H., Saito, N., and Yasukawa, S., Synthesis of fine AlN powder by vapour-phase reaction, Journal of Material Science Letters, Vol. 7, pp. 66-68, 1988.

[17] Adjaottor, A. A. and Griffin, G. L., Aerosol reactor design for aluminum nitride powder synthesis, 3rd International Conference on Powder Processing Science, San Diego. Selected Papers on Ceramic Synthesis, Ceramic Transactions, Vol. 12, pp. 299-304, 1990.

[18] Pratsinis, S. E., Wang, G., and Panda, S., Aerosol synthesis of AlN by nitridation of aluminum vapor and clusters, J. Mater. Res., Vol. 10, No. 3, pp. 512 - 520, 1995.

[19] Canteloup, J. and Mocellin, A., Synthesis of ultrafine nitrides and oxynitrides in an R.F. plasma, Special Ceramics, Vol. 6, pp. 209 - 222, 1974.

[20] Wehling, C., Heitz, F., and Hausner, H., Synthesis of ceramic powders from metals in an inductively coupled plasma, International Symposium on Plasma Chemistry 10, Brochum, p. 1.4-5 p.1, 1991.

[21] Baba, K., Shohata, N., and Yonezawa, M., Preparation of ultrafine AlN powder using RF plasma, International Symposium on Plasma Chemistry 8, Tokyo, pp. 2034-2039, 1987.

[22] Godin, M. F., Chevallier, F., Amouroux, J., and Morvan, D., Synthesis of aluminum nitride powders by thermal plasma, International Symposium on Plasma Chemistry 10, Brochum, p. 1.4-4 p.1, 1991.

[23] Slack, G. A. and McNelly, T. F., Growth of high purity AlN crystals, Journal of Crystal Growth, Vol. 34, pp. 263-279, 1976.

[24] Verma, R.A., and Krishna, P., Polymorphism and Polytypism in Crystals, John Wiley & Sons, New York, 1966.

[25] Taylor, K. M. and Lenie, C., Some properties of aluminum nitride, Journal of the Electrochemical Society, Vol. 107, No. 4, pp. 308-314, 1960.

[26] Kuramoto, N., Taniguchi, H., and Aso, I., Development of translucent aluminum nitride ceramics, American Ceramic Society Bulletin, Vol. 68, No. 4, pp. 883-887, 1989.

[27] Hashman, T. W., and Pratsinis, S. E., Thermodynamics of vapor synthesis of AlN by nitridation of aluminum and its halides, Journal of the American Ceramic Society, Vol. 75, No. 4, pp. 920-928, 1992.

[28] HSC - Chemistry, Equilibrium Compositions, V. 2.03, Outokumpu.

[29] JANAF Thermochemical Tables, Journal of Physical and Chemical Reference Data. Supplement, Vol. 14, No. 1, The American Chemical Society and the American Institute of Physics, 1986.

[30] Streuli, C.A., and Averell, P.R., The Analytical Chemistry of Nitrogen and Its Compounds, Part 1, Wiley-Interscience, Chemical Analysis Vol. 28, New York, 1970.

[31] Moulder, J. F., Hand Book of X-ray Photoelectron Spectroscopy, Perkin Elmer Corp., Minnesota, 1992.

[32] Boulos, M. I., Fauchais, P., and Pfender, E., Thermal Plasmas: Fundamentals and Applications, Vol. 1, Plenum Press, New York, 1994.

[33] Bilodeau, J. F. and Proulx, P., Analysis of the synthesis of ultrafine AlN powder in an induction plasma reactor, International Symposium on Plasma Chemistry 13, PG.2.01, pp. 1201-1206, Minnesota, 1995.

[34] Joshi, S. V., Liang, Q., Park, J. Y., and Batdorf, J., Effect of quenching conditions on particle formation and growth in thermal plasma synthesis of fine powders, Plasma Chemistry and Plasma Processing, Vol. 10, No. 2, pp. 339-358, 1990.

[35] Girshick, S.L., Chiu, C.-P., and McMurry, P., A model for particle formation and growth in a plasma synthesis reactor, International Symposium on Plasma Chemistry 18, pp.2052-2057, Tokyo, 1987.

[36] Proulx, P., and Bilodeau, J.-F., A model for ultrafine powder production in a plasma reactor, Plasma Chemistry and Plasma Processing, Vol. 11, No. 3, 1991.

[37] Bilodeau, J. F., Modelisation de la croissance des poudres ultrafines en reacteur a plasma thermique, Ph.D. Thesis, Sherbrooke University, Sherbrooke, 1994.

[38] Patankar, S. V., Numerical Heat Transfer and Fluid Flow, McGraw-Hill, 1980.

[39] Pratsinis, S.E., Simultaneous nucleation, condensation, and coagulation in aerosol reactors, Journal of Colloid and Interface Science, Vol. 24, No. 2, pp. 416-427, 1988.

[40] Reiss, H., The kinetics of phase transition in binary systems, The Journal of Chemical Physics, Vol. 18, No. 6, pp. 840-848, 1950.

[41] Katz, J. L., and Donohue, M. D., Nucleation with simultaneous chemical reaction, Journal of Colloids and Interface Science, Vol. 85, No. 1, pp. 267-277.

[42] Yoshida, T. and Akashi, K., Preparation of ultrafine iron particles using an RF plasma, Transations of the Japan Institute of Metals, Vol. 22, pp. 371-378, 1981.

[43] Ulrich, G.D., Theory of particle formation and growth in oxide synthesis flames, Combustion Science and Technology, Vol. 4, pp. 47-57, 1971.

[44] Okuyama, K., Kousaka, Y., Tohge, N., Yamamoto, S., Wu, J.J., Flagan, R.C., and Seinfeld, J.H., Production of ultrafine metal oxide aerosol particles by thermal decomposition of metal alkoxide vapors, AIChE Journal, Vol. 32, pp. 2010-2019, 1986.

[45] Gelbard, F. and Seinfeld, J.H., Numerical solution of the dynamic equation for particulate systems, Journal of Computational Physics, Vol.28, pp. 357-375, 1978.

[46] Girshick, S.L., Chiu, C.-P., and McMurry, P., Modelling particle formation and growth in a plasma synthesis reactor, Plasma Chemistry and Plasma Processing, Vol. 8, No. 2, pp. 145-157, 1988.

[47] Girshick, S.L. and Chiu, C.-P., Numerical study of MgO powder synthesis by thermal plasma, Journal of Aerosol Science, Vol. 21, No. 5, pp. 641-650, 1990.

[48] Girshick, S.L., Chiu, C.-P., Muno, R., Wu, L.Y., Singh, S.K., and McMurry, P.H., Thermal plasma synthesis of ultrafine iron particles, Journal of Aerosol Science, Vol. 24, No. 3, pp. 367-382, 1993.

[49] Girshick, S.L. and Chiu, C.-P., Kinetic nucleation theory: a new expression for the rate of homogeneous nucleation from an ideal supersaturated vapor, Journal of Chemical Physics, Vol. 93, No. 2, pp. 1273-1277, 1990.

[50] Katz, J.L. and Wiedersich, H., Nucleation theory without Maxwell demons, Journal of Colloid and Interface Science, Vol. 61, No. 2, pp. 351-355, 1977.

[51] Katz, J.L. and Donohue, M.D., A Kinetic Approach to Homogeneous Nucleation Theory, in Advances in Chemical Physics, Vol. 40, Prigogine, I., and Rice, A. S., editors, John Willey and Sons, New York, pp. 137-154, 1979.

[52] Bilodeau, J.F., and Proulx, P., A mathematical model for ultrafine iron powder growth in a thermal plasma, Aerosol Science and Technology, Vol. 24, pp. 175-189, 1996.

[53] Bilodeau, J. F., Proulx, P., Moura, F. J., and Munz, R. J., A study of the nucleation and growth of ultrafine AlN powders in a plasma reactor, International Symposium on Plasma Chemistry 11, pp. 356-361, 1993.

[54] Friedlander, S. K., Smoke, Dust, and Haze: Fundamentals of Aerosol Behavior, Wiley-Interscience, New York, 1981.

[55]Randolph, A.D. and Larson, M. A., Theory of Particulate Processes, Academic Press, New York, 1971.

[56] Hinds, W. C., Aerosol Technology: Properties, Behavior, and Measurement of Airborne Particles, John Wiley & Sons, New York, 1982.

[57] Phanse, G. M., and Pratsinis, S. E., Theory of aerosol generation in laminar flow condensers, Aerosol Science and Technology, 11, pp. 100-119, 1989.

[58] Brock, J. R., On the theory of thermal forces acting on aerosol particles, Journal of Colloid Science, Vol. 17, pp. 768-780, 1962.

[59] Talbot, L., Cheng, R. K., Schefer, R. W., and Willis, D. R., L., Title ???, J. Fluid Mech., Vol. 101, 737-758, 1980.

[60] Njah, Z., Etude Laminaire et Turbulent du Melange d'un ou Plusieurs Jets Lateraux avec un Ecoulement a Haute Temperature, Ph.D. Thesis, Sherbrooke University, Sherbrooke, 1992.

[61] Blander, M., and Katz, J.L., The thermodynamics of cluster formation in nucleation theory, Journal of Statistical Physics, Vol. 4, No. 1, 1972.

[62] Fucks, N. A., and Sutugin, A. G., High-Dispersed Aerosols, in Topics in Current Aerosol Research, G. M. Hidy and J. R. Brock (eds.), Vol. 2, pp. 1 -60, Pergamon Press, Oxford, 1971.

[63] Pendlebury, J. M., Kinetic Theory, Adam Hilder Ltd., Bristol, 1985.

[64] Lee, K. W., and Chen, H., and Gieseke, J. A., Log-normally preserving size distribution for Brownian coagulation in the free-molecule regime, Aerosol Science and Technology, Vol. 3, pp. 53-62, 1984.

[65] Lee, K. W., and Chen, H., Coagulation rate of polydisperse particles, Aerosol Science and Technology, Vol. 3, pp. 327-334, 1984.

[66] Feder, J., Russell, K.C., Lothe, J., and Pound, G.M., Homogeneous nucleation and growth of droplets in vapours, Advances in Physics, Vol. 15, pp. 111-178, 1966.

[67] Hirschfelder, J.O., Kinetics of homogeneous nucleation on many-component systems, The Journal of Chemical Physics, Vol. 61, No. 7, pp. 2690-2694, 1974.

[68] Hirth, J.P. and Pound, G.M. Condensation and evaporation, nucleation and growth kinetics, Progress in Materials Science, 11, 1963.

[69] Zettlemoyer, A.C., Nucleation, Marcel Dekker, New York, 1969.

[70] Abraham, F.F., Homogeneous Nucleation Theory, Academic Press, New York, 1974.

[71] Kotake, S., and Glass, I.I., Flows with nucleation and condensation, Progress in Aerospace Science, Vol. 19, pp. 129-196, Pergamon Press, London, 1981.

[72] Yumura, M., and Asaba, T., Rate constants of chemical reactions in the high temperature pyrolysis of ammonia, 18th Symposium (International) on Combustion, The Combustion Institute, pp. 863-872, 1981.

[73] Holzrichter, K. and Wagner, H. GG., On the thermal decomposition of ammonia behind shock waves, 18th Symposium (International) on Combustion, The Combustion Institute, pp. 769-775, 1981.

[74] Roose, T.R., Hanson, R.K., and Kruger, C.H., Proceedings of the 12th International Symposium on Shock Tube and Waves, pp. 476-485, Jerusalem, 1979.

[75] Kajimoto, O., Yamamoto, T., and Fueno, Kinetic studies of the thermal decomposition of hydrazoic acid in shock waves, Journal of Physical Chemistry, Vol. 83, No. 4, pp. 429-437, 1979.

[76] Bahn, G.S., Reaction Rate Compilation for the H-O-N System, Gordon and Breach, New York, 1967.

[77] Dove, J.E. and Nip, W.S., A shock-tube study of ammonia pyrolysis, Canadian Journal of Chemistry, Vol. 57, pp. 689-701, 1979.

[78] Baulch, D.L., Drysdale, D.D., Horne, D.G., and Lloyd, A.C., Evaluated Kinetic Data for High Temperature Reactions, Vol. 1, Butterworth, London, 1972.

[79] Vincenti, W. G., and Kruger, C. H., Introduction to Physical Gas Dynamics, John Wiley and Sons, New York, 1965.

[80] Benson, S.W., The Foundations of Chemical Kinetics, McGraw-Hill, New York, 1960.

[81] Mahan, B. H., University Chemistry, Addison-Wesley, New York, 1966.

[82] Kubaschewsky, O., and Alcock, C.B., Metallurgical Thermochemistry, Pegamon Press, New York, 1979.

[83] Smithells, C.J., Metals Reference Handbook, Butterworths, London, 1978.

[84] Lewis, B., Nucleation and Growth Theory, in Crystal Growth, B.R. Pamplin (ed.), Pergamon Press, New York, 1975.

[85] CRC Handbook: Materials Science and Engineering, CRC Press, Boca Raton, 1994.

[86] Stephan, K., and Lucas, K., Viscosity of Dense Fluids, Plenum Press, New York, 1979.

[87] Wilke, C. R., A viscosity equation for gas mixtures, Journal of Chemical Physics, Vol. 18, No. 4, pp. 517-519, 1950.

[88] Bird, B. R., Stewart, W. E., and Lightfoot, E. N., Transport Phenomena, John Wiley & Sons, New York, 1960.

[89] Rao, N.P., McMurry, P.H., Effect of the Tolman surface tension correction on nucleation in chemically reacting systems, Aerosol Science and Technology, Vol. 13, pp. 183 - 195 (1990).

[90] McCauley, J.W., and Corbin, N.D., Phase relations and reaction sintering of transparent cubic aluminum oxynitride spinel (ALON), Journal of the American Ceramic Society, Vol. 62, pp. 476-479, 1979.

[91] McCauley, J.W., and Corbin, N.D., High temperature reactions and microstructures in the Al_2O_3-AlN system, in Progress in Nitrogen Ceramics, F.L. Riley (Ed.), Martinus Nijhoff Publishers, Boston, pp. 111-118, 1983.

[92] Hashimoto, N., and Yoden, H., Sintering behavior of fine aluminum nitride powder synthesized from aluminum polynuclear complexes, Journal of the American Ceramic Society, Vol. 75, No. 8, pp. 2098-2106, 1992.

[93] Baik, Y., Sintering of Aluminum Nitride with Y_2O_3 by Secondary Phase Composition Control, Ph.D. Thesis, McGill University, Montreal, 1995.

[94] Vali, H., Allahverdi, M., Drew, R.A.L., TEM study of the surface morphology of extracted ZrO_2-Al_2O_3 fibres, Journal of Materials Science, Vol. 31, pp. 6177-6184, 1996.

APPENDIX A

Detailed development of equations from Chapter 6, Section 6.6 (homogeneous nucleation modified by surface reaction)

1) Development of Equation (6.92) by the substitution of Equation (6.94), making the change of variables, and making use of the definition of the error function:

Equation (6.94) substituted in (6.92) gives

$$J = \frac{n(v_1, \overline{X_c})\beta^* v_1}{N(v_1, \overline{X_c})} \exp\left[H(v^*, \overline{X_c})\right]\left[\int_{v_1}^{\overline{v}} \exp\left(-\frac{(v-v^*)^2}{2} H''(v^*, \overline{X_c})\right) dv\right]^{-1} \tag{A.1}$$

Making the change of variables:

$$t = (v - v^*)\left[\frac{H''(v^*, \overline{X_c})}{2}\right]^{1/2} \tag{A.2}$$

and

$$dt = \left[\frac{H''(v^*, \overline{X_c})}{2}\right]^{1/2} dv \tag{A.3}$$

and changing the limits of integration such as:

$$v = v_1 \Rightarrow t = -(v^* - v_1)\left[\frac{H''(v^*, \overline{X_c})}{2}\right]^{1/2} \tag{A.4}$$

$$v = \overline{v} \Rightarrow t = (\overline{v} - v_1)\left[\frac{H''(v^*, \overline{X_c})}{2}\right]^{1/2} \tag{A.5}$$

the integral in Equation (A.1) is written:

$$\int_{v_1}^{\overline{v}} \exp\left[-\frac{(v-v^*)^2}{2}H''(v^*,\overline{X_c})\right]dv = \left[\frac{H''(v^*,\overline{X_c})}{2}\right]^{-1/2} \int_{-(v^*-v_1)A}^{(\overline{v}-v_1)A} \exp[-t^2]dt \tag{A.6}$$

where $A = [H''(v^*,\overline{X_c})/2]^{1/2}$. It is observed that the term in the integral has the form of the error function:

$$\mathrm{erf}(y) = \frac{2}{\sqrt{\pi}}\int_0^y e^{-t^2}dt \tag{A.7}$$

which has the property that when $y \rightarrow \infty$, $\mathrm{erf(y)} \rightarrow 1$. Being that:

$$\int_{-(v^*-v_1)A}^{(\overline{v}-v_1)A} \exp[-t^2]dt < \int_{-\infty}^{\infty} \exp[-t^2]dt = \sqrt{\pi} \tag{A.8}$$

Equation (A.6) is approximated by:

$$\int_{v_1}^{\overline{v}} \exp\left[-\frac{(v-v^*)^2}{2}H''(v^*,\overline{X_c})\right]dv \cong \left[\frac{H''(v^*,\overline{X_c})}{2}\right]^{-1/2} \int_{-\infty}^{\infty} \exp[-t^2]dt \tag{A.9}$$

Substitution of Equation (A.9) in (A.1) then gives:

$$J = \frac{n(v_1,\overline{X_c})\beta^* v_1}{N(v_1,\overline{X_c})}\exp\left[H(v^*,\overline{X}_c)\right]\left[\frac{H''(v^*,\overline{X_c})}{2\pi}\right]^{1/2} \tag{6.95}$$

2) Detailed development of the calculation of the critical cluster size [Equation (6.106)]:

The fact that the first derivative of Equation (6.91) equals zero when a cluster reaches the critical size is used to calculate the critical cluster size. Thus, after Equation (6.93), the following expression is derived:

$$H'(v^*,\overline{X_c}) = 0 \;\therefore \tag{A.10}$$

$$\frac{2}{3}v^{-1} + \frac{1}{V_1}\ln S_{Al} - \frac{(1-\overline{X_c})}{V_1}\left(\frac{\Delta G_r}{k_B T}\right)_L - \frac{2}{3}\frac{v^{-1/3}}{V_1^{2/3}}\theta = 0 \;\therefore \tag{A.11}$$

$$\frac{2}{3} + \frac{v}{V_1}\ln S_{Al} - \frac{v(1-\overline{X_c})}{V_1}\left(\frac{\Delta G_r}{k_B T}\right)_L - \frac{2}{3}\left(\frac{v}{V_1}\right)^{2/3}\theta = 0 \;\therefore \tag{A.12}$$

$$\frac{2}{3}\left[1-\left(\frac{v}{V_1}\right)^{2/3}\theta\right] + \frac{v}{V_1}\left[\ln S_{Al} - (1-\overline{X_c})\left(\frac{\Delta G_r}{k_B T}\right)_L\right] = 0 \;\therefore \tag{A.13}$$

$$\frac{2}{3}\left(\frac{v}{V_1}\right)^{2/3}\theta = \frac{v}{V_1}\left[\ln S_{Al} - (1-\overline{X_c})\left(\frac{\Delta G_r}{k_B T}\right)_L\right] \tag{6.104}$$

Observing that:

$$\left(\frac{v}{V_1}\right)^{2/3}\theta \gg 1 \tag{6.105}$$

$$\left(\frac{v}{V_1}\right)^{-1/3}\theta = \frac{3}{2}\left[\ln S_{Al} - (1-\overline{X_c})\left(\frac{\Delta G_r}{k_B T}\right)_L\right] \tag{A.14}$$

it results:

$$v = \left[\frac{2}{3}\frac{\theta}{\mathrm{LnS}}\right]^3 V_1 \tag{6.106}$$

where, for simplification "LnS" is defined as:

$$\mathrm{LnS} = \ln S_{Al} - (1-\overline{X_c})\left(\frac{\Delta G_r}{k_B T}\right)_L \tag{6.107}$$

3) Development of Equation (6.111):

By replacing the term in the first brackets of Equation (6.110) by LnS as defined by Equation (6.107), and using Equation (6.106):

$$\frac{\Delta G(v^{*},\overline{X_{c}})}{k_{B}T}=-\left[\frac{2}{3}\frac{\theta}{\mathrm{LnS}}\right]^{3}[\mathrm{LnS}]+\left[\frac{2}{3}\frac{\theta}{\mathrm{LnS}}\right]^{2}\theta+\ln S_{Al}\;\therefore \qquad \text{(A.15)}$$

$$\frac{\Delta G(v^{*},\overline{X_{c}})}{k_{B}T}=-\left[\frac{8}{27}\frac{\theta^{3}}{(\mathrm{LnS})^{2}}\right]+\left[\frac{4}{9}\frac{\theta^{3}}{(\mathrm{LnS})^{2}}\right]+\ln S_{Al}\;\therefore \qquad \text{(A.16)}$$

$$\frac{\Delta G(v^{*},\overline{X}_{c})}{k_{B}T}=\frac{4}{27}\frac{\theta^{3}}{(\mathrm{LnS})^{2}}+\ln S_{A} \qquad \text{(6.111)}$$